Summer 2014

Functionally graded Ti6Sl4V and Inconel 625 by laser metal deposition

Syamala Rani Pulugurtha

Department: Materials Science and Engineering

FUNCTIONALLY GRADED Ti6Al4V AND INCONEL 625 BY LASER METAL DEPOSITION

by

SYAMALA R PULUGURTHA

A DISSERTATION

Presented to the Faculty of the Graduate School of the

MISSOURI UNIVERSITY OF SCIENCE AND TECHNOLOGY

In Partial Fulfillment of the Requirements for the Degree

DOCTOR OF PHILOSOPHY

in

MATERIALS SCIENCE AND ENGINEERING

2014

Approved
Joseph Newkirk, Advisor
Frank. W. Liou
Ronald Kohser
Caizhi Zhou
David. C. Van Aken

ABSTRACT

The objective of the current work was to fabricate a crack-free functionally graded Ti6Al4V and Inconel 625 thin wall structure by Laser Metal Deposition (LMD). One potential application for the current material system is the ability to fabricate a functionally graded alloy that can be used in a space heat exchanger. The two alloys, Inconel 625 and Ti6Al4V are currently used for aerospace applications. They were chosen as candidates for grading because functionally grading those combines the properties of high strength/weight ratio of Ti6Al4V and high temperature oxidation resistance of Inconel 625 into one multifunctional material for the end application. However, there were challenges associated with the presence of Ni-Ti intermetallic phases (IMPs). The study focused on several critical areas such as (1) understanding microstructural evolution, (2) reducing macroscopic cracking, and (3) reducing mixing between graded layers. Finite element analysis (FEA) was performed to understand the effect of process conditions on multilayer claddings for simplified material systems such as SS316L and Inconel 625 where complex microstructures did not form. The thermo-mechanical models were developed using Abaqus^{TM} (and some of them experimentally verified) to predict temperature-gradients; remelt layer depths and residual stresses. Microstructure evolution along the functionally graded Ti6Al4V and Inconel 625 was studied under different processing and grading conditions. Thermodynamic modeling using Factsage (v 6.1) was used to construct phase diagrams and predict the possible equilibrium major/minor phases (verified experimentally by XRD) that may be present along the functionally graded Ti6Al4V and Inconel 625 thin wall structures.

ACKNOWLEDGMENTS

There are many individuals who have supported me in my program that I would like to thank while I was at Missouri S&T.

Firstly, I would like to thank my husband Parishram whose constant support made me undertake this course and complete it successfully. And, also I would like to thank my 2 and half years old daughter Samviti whose birth brought not only joy but pushed me to achieve my goal faster. I would also like to thank my dear parents Kirti and Radha whose prayers for my success helped me achieve whatever I dreamed of in my life so far. I would also like to thank my in-laws Parthasarathy and Prema for their prayers and support during the 4–year program.

Next, I would like to thank my mentor, the late Dr. Deepak G Bhat (MS academic advisor at the University of Arkansas), for encouraging me to work towards my PhD program. I would also like to thank my PhD advisor Dr. Joseph Newkirk and co-advisor Dr. Frank Liou. My sincere thanks to the other members of the dissertation committee: Dr. David C. Van Aken, Dr. Ronald Kohser and Dr. Caizhi Zhou. Special words of appreciation have to be extended to Dr. Wayne Huebner for providing me with financial support through the department in the last stages of my PhD program. Many thanks to my fellow students (Nilesh Kumar and Todd Sparks) and lab specialists (Eric Bohannan and Clarissa Wisner) at MS&T. The research was initially supported by U.S. Air Force Research Laboratory contract # FA8650-04-C-5704. Support from Missouri S&T Intelligent Systems Center is also greatly appreciated.

"This thesis is a tribute to my mother who is the most inspiring woman that I have ever known."

TABLE OF CONTENTS

Page

LIST OF ILLUSTRATIONS

LIST OF TABLES

NOMENCLATURE

Symbol	Description
FGM	Functionally Graded Material
LMD	Laser Metal Deposition
DMD	Direct Metal Deposition
Ti6Al4V	Titanium alloy 6% weight Aluminum 4% weight Vanadium
Inconel 625	Ni-based alloy
FEA	Finite Element Analysis
FEM	Finite Element Modeling
IMPs	Intermetallic Phases
LRF	Laser Rapid Forming
CTE	Coefficient of Thermal Expansion
SCCM	Standard Cubic Centimeter per Minute
atm.	Atmosphere
α	Alpha Phase Titanium
β	Beta Phase Titanium
ρ	Density
c_p	Specific Heat
k	Thermal Conductivity
h	Convective Heat Transfer Coefficient
ϵ	Emissivity
ε	Strain
$\frac{\partial T}{\partial t}$	Cooling Rate
σ	Stress

1. INTRODUCTION

Functionally graded materials (FGMs) [1] are a new generation of high performance multi-functional material-systems in which the properties of a component are spatially tailored to meet service requirements. This is achieved by doing a smooth transition between layers with varying compositions of chosen alloys. Some of the older manufacturing methods for FGMs used wasteful subtractive or forming processes to shape parts. This was accomplished by melting and time-consuming heat-treatment processes to join dissimilar materials and improve bulk microstructures. With the introduction of additive rapid prototyping techniques such as *Laser Metal Deposition* (LMD) the process allows the ability to deposit any alloy into near-net shape parts in a single processing step [2, 3]. Heat transfer between meltpool and workpiece is extremely localized allowing accurate deposition, low dilution and a small heat affected zone.

Although FGMs potentially offer attractive application-specific alternatives to conventional materials, several aspects important to their design, development and functionality (not investigated in this thesis) using LMD processes warrant further investigation. These include:

1. Thermo-physical property mismatch of material-systems such as density, coefficient of thermal expansion, thermal diffusivity, etc., results in generation of residual internal stress, segregation in the melt pool and de-lamination of layers during processing.
2. Material-systems compatibility, an issue when reaction between components results in unwanted intermetallic phases (IMPs, brittle compounds).
3. Uncontrolled process parameters, which can cause the melt pool to get

superheated and result in high temperature gradients. This will enhance unwanted mixing between layers and create residual stresses.

Poorly defined FGM deposition strategies manifest themselves as poorly controlled microstructural features that adversely impact the desired mechanical properties of the end component [4]. The major challenge in fabricating FGMs by LMD is cracking as a result of accumulation of internal stresses due to multiple heat-cool cycles and formation of un-wanted intermetallic phases (IMPs).

1.1 AIM AND MAJOR CHALLENGES

The goal of this research project was to develop an alloy combination that can potentially solve two inter-related problems: (1.) Achieve a high strength/low weight and high-temperature oxidation resistant functional material and (2.) Solve processing issues associated with generating the aforementioned material-system. Bi-metallic joining or laser claddings were not considered as suitable processes for this application. This was because of the inability to bring incompatible or functional materials together without encountering problems such as de-bonding and cracking due to sharp transitions such as hardness or microstructure variation at the interface. It was recognized that functionally grading disparate alloys would reduce such sharp transitions and would allow the realization of the end application. Material deposition via a laser allowed such grading with the accuracy and control required to achieve the desired transition between layers. In this project functionally graded high strength/low weight and high-temperature oxidation resistant materials were used to potentially fabricate an FGM to be used in a space heat

exchanger. Ti6Al4V and Inconel 625 alloys are aerospace alloys and were considered to be the suitable candidates for the present study. Ni-Ti alloys are also used as functional materials for industrial and medical applications due to their high temperature oxidation resistance, shape memory property, and good biocompatibility [5].

The work reported in this dissertation aims to understand and explain the microstructure evolution in the functionally graded alloys Ti6Al4V and Inconel 625 alloys by LMD. Ti6Al4V/commercially pure-Ti with Inconel 718, Rene88DT, Inconel 625 has been previously functionally graded by a few researchers only with very limited success [6-10]. Previously functionally grading Ti6Al4V and Inconel 625 usually resulted in cracking, possibly due to large internal stresses from the multiple heat-cool cycles and formation of unwanted intermetallic phases (IMPs). In this work, effects of process parameters on the microstructural evolution in the functionally graded Ti6Al4V and Inconel 625 have been studied to a good extent. To minimize the occurrence of cracks in the fabricated structures different grading schemes were identified and also tested in this study.

1.2 PROJECT GOALS

The specific objectives of this research are summarized below:

- To investigate the effects of processing parameters and their interaction in the LMD process.
- To identify the feasibility of LMD of functionally graded materials Ti6Al4V and Inconel 625.

- To model, using finite element techniques the thermal and mechanical behavior of the multilayer LMD of more compatible systems such as SS316L and Inconel 625 on SS316L workpiece in order to understand the effect of processing parameters on cooling rates, residual strains, etc.,.
- To understand the microstructure evolution along the Ti6Al4V and Inconel 625 graded structure under different processing conditions.
- To attempt to solve the macroscopic cracking during functional grading of Ti6Al4V/Inconel 625.
- To try to explain scientifically the differences between cracked and un-cracked Ti6Al4V/Inconel 625 FGMs.

1.3 DISSERTATION LAYOUT

This thesis addresses in detail the microstructural evolution and (and possible reasons for cracking) of functionally graded Ti6Al4V and Inconel 625 alloys by laser metal deposition (LMD) process. Section 2 gives a general overview of the technology of LMD and its application in functionally grading different alloys. Section 3 describes the materials, equipment and processing conditions used throughout this project. The microstructure and consequent material properties are highly dependent on the temperature history of the material. Controlled microstructure development is essential when manufacturing high reliability components such as those used for aerospace applications. Modeling and simulation are widely used tools in manufacturing design as they reduce exhaustive research-experiments and costs. Section 4 presents an experimental study on functionally graded Ti6Al4V and Inconel 625 fabricated

structures. Results on microstructural evolution along the functionally graded Ti6Al4V and Inconel 625 are included in this Section. This section includes results on the finite element modeling to understand the effect of processing parameters on multilayer deposition of simplified systems such as SS316L and Inconel 625 on SS316L workpieces. Also presented in this section is a study on the microstructural evolution of the crack-free compositionally graded Ti6Al4V and Inconel 625 alloys. Section 5 is a discussion on functionally graded Ti6Al4V and Inconel 625 with supporting arguments from literature wherever deemed necessary. The section also covers results from thermodynamic modeling of the graded structures and the differences between the cracked and un-cracked FGMs. A general summary of the outcomes of the research work is then made in Section 6.

2. LITERATURE REVIEW

Functionally graded materials (FGMs) are a new generation of high performance materials-systems. In an ideal FGM, the properties of a component are spatially tailored to meet service requirements by controlling microstructural details during processing. A smooth transition between layers with varying compositions of the chosen alloys will result in a multi-functional material. Such multi-functional materials can fulfill more than one functional requirement separately. The functions can vary from mechanical to electrical to thermal. The concept of FGMs was first proposed around 1984-85 for use in aerospace applications [1]. The researchers devised a concept to fabricate a material by gradually changing (grading) the material composition, and in this way improve both thermal resistance and mechanical properties. Some potential applications for FGMs include electronic components, biomedical implants, thermal protective systems in spacecrafts and aerospace engines.

Most of the complex-multifunctional parts are composed of a "single material" with nominally uniform properties, but the tribological, fatigue and creep resistance and load bearing requirements vary widely throughout the part. Some of the requirements in general can be met by modifying the surface only through heat-treating for residual stress relief and enhancement of material properties using lasers. Bulk properties are difficult to modify or control using surface treatments. As a result the microstructure differs between surface and the bulk of material. High interfacial stresses in the transition zone between the surface and the bulk of the material can negatively impact the performance of the material over time. An alternative way is to make use of a combination of materials to meet the service requirements. Now, it is technically a challenge to produce any type of

component with variable microstructure and stress distribution within a single process using “different materials”. Conventional manufacturing methods use wasteful subtractive (i.e. machining) or forming processes to shape parts and then rely on welding and time-consuming heat-treatment processes to join different materials and improve bulk microstructures. Within turbine engines for example Waspalloy and Inconel superalloy microstructures deteriorate with time and crack due to thermal fatigue that originates at regions of discontinuous microstructure such as welded joints. Direct Metal Deposition by laser (DMD) is a single-stage layered manufacturing technique which has the ability to deposit any metal and many intermetallics into near-net shape parts in a single processing step [2]. This technique was developed from single-layer deposition, pioneered by the work of W.M. Steen [3], and allows the formation of fully-dense thin walled or bulky metallic parts through the pneumatic injection of powder into a moving, laser-induced melt pool. Heat transfer is extremely localized allowing accurate deposition, low dilution and a small heat affected zone. The final material properties are generally excellent due to rapid cooling induced by a self-quenching effect. The microstructure is very fine and thereby, an improvement in mechanical properties is observed. DMD also allows the manufacture of otherwise unrealizable parts (not related to material property changes), such as cooling dies with conformal cooling channels and original shapes. It was estimated that the DMD process can reduce the time of die production by 40% [11].

The successful use of this process in the *aerospace sector* also adds to its usefulness over conventional methods, as it eased the manufacturing of complex parts. But some of the challenges with DMD are dimensions and process control. Post process

machining and/or heat treatments have to be performed to improve the surface finish and reduce internal stresses in the part. This can be reduced by close control of dimension. Substantial cost reduction is possible, if desired properties can be achieved through process control and minimizing the post-process heat treatment. Microstructure manipulation can be achieved by controlling the cooling rates via meltpool size and solidification time control. To achieve this, a quantitative understanding of the relationship between independent process parameters (e.g., laser power, speed, powder deposition rate, etc.,), dimensions, cooling rates, microstructures, and properties is required [12].

2.1 PROCESSING OF FUNCTIONALLY GRADED MATERIALS (FGMs)

The ability to bring onto one platform a homogenized design method, heterogeneous solid modelling and DMD has been a revolutionary departure from traditional material selection methods [12]. The following section discusses two interesting types of FGMs- ceramic-metal grading, and metal-metal grading.

2.1.1. Ceramic-Metal (or CerMets) FGM Processing. CerMet such as SiC reinforced Ti6Al4V, TiC reinforced Ti by direct metal deposition (DMD) have been widely investigated for enhanced tribological performance [13, 14]. Casting methodology for many CerMets is not very effective as it can result in detrimental interfacial reactions because ceramic particles spend considerable time in contact with molten metal. Moreover, particle segregation can occur during casting and mold filling due to density differences between ceramic and metals. In contrast, powder metallurgical

methods can be used to attain elevated volume fractions of reinforcement, with limited or no interfacial reactions, since relatively lower temperatures can be maintained and exposure time controlled. The major disadvantage of powder metallurgical routes is that they are relatively complex and limited in terms of product geometry. Therefore, summing up the most important factors that need to be controlled to tailor a composite layer on to a surface of metallic substrate are: (a) ceramic particle dissolution and reaction with the melt at high temperatures; (b) distribution and volume fraction of the injected ceramic particles; and (c) thermal stresses built up in the composite layer during cooling of the melt pool. The Laser metal injection (LMI) process is one of the potential solutions for minimizing the reaction, with which no other process can compete in shortening the processing/reaction time. The ceramic particles need to be injected into the laser pool just behind the beam in such a way that the powder stream is positioned close to the beam, but without interfering it. This permits the particles to penetrate in the melt to certain depths and the method also avoids reaction of the particles with the melt at higher temperatures.

The strength and stability of the interfacial region between the ceramic reinforcement particles and the metal matrix governs the mechanical and physical response of CerMets [15]. Failure processes that are initiated by interfacial de-bonding are likely to occur when a composite material with a weak interface is subjected to an applied stress. The majority of CerMets are non-equilibrium systems due to the presence of a chemical potential gradient across the interface, which drives diffusion and/or chemical reactions to take place at the interface. Under controlled conditions such as temperature and exposure time, the formation of a limited reaction layer might be

desirable in order to obtain strong bonds. The limited dissolution of the particle results in stronger bonds and better mechanical performance. In the case of high levels of dissolution of the ceramic particles, which implies the presence of thick reaction layers, cracks are often initiated in the matrix.

Another problem that is associated with the majority of CerMets is a lack of wetting of the ceramic particles by metal systems. One of the approaches to mitigate the challenge of wetting was to encapsulate the ceramic materials in a metallic coating [16]. With metal coated ceramic particles a strong metallic bond can be formed between the coating material and the matrix metal. Segregation in the melt pool is another frequently observed phenomenon when materials have considerable difference in physico-chemical properties [17]. The heat generated from the center of the laser interaction zone lowers the density of heated powders. Cooler powders at the edge of the Heat Affected Zone (HAZ) will have higher densities. Therefore it will cause molten material at the edge of the HAZ to sink within the melt pool due to gravity (buoyancy force). Different material densities will cause variations in the movement of material within the melt. Movement of particles is also dependent on the viscosity of the melt [13] which again depends on the temperature field of the melt pool. Another factor that may contribute to material segregation in CerMets is surface tension. The surface tension of a material reduces with increasing temperature; cooler material at the edge of a HAZ will pull material from the center of the HAZ to the edge (Marangoni convection). There will therefore be a variation in movement of materials within melt due to surface tension forces.

Solidification cracking in CerMets is attributed to residual stresses as a result of the rapid cooling and the mismatches in thermal and mechanical properties between the

substrate and precursor powders [18]. At the beginning of solidification, the liquid phase is dominant in the microstructure, which can be deformed randomly and has good plasticity, and the dendrites can grow freely. With increasing percentages of the solid phase, a sealed skeleton is formed among solid phases and the residual liquid phase now cannot flow freely. At the period of solidification and shrinkage, a strain concentration will occur at the locations of non-continuous dendrite boundaries, which may result in local cracking. Because of the rapid cooling and solidification rate of this process, the initial cracks cannot be refilled by remaining liquid phase. Therefore, solidification cracks will be formed with the propagation of small cracks [19].

2.1.2. Metal-Metal FGM Processing. Metal-on-metal FGMs for aerospace applications are very sensitive to production methods. The large temperature gradients that occur during layered deposition process affect the meltpool size, which in turn affects the microstructure and impacts the mechanical properties significantly [4]. During layer by layer deposition, the melt-pool volume constantly changes. The fluid flow in the melt pool as a result of convection currents and surface tension driven flow can significantly affect the heat transfer, melt-pool penetration depths, segregation and porosity as already mentioned earlier [20]. This fluid flow results in mixing between the graded layers and ‘dilution’ from the substrate. The ‘dilution-D’ is dimensionless mathematical term and depends upon several factors such as the thermal conductivity of the material, initial temperature of the substrate, reflectivity of the material, powder flow rate, interaction time of the powder in the beam and laser power [21]. A relation for predicting dilution ‘D’ mathematically for Laser Engineered Net Shaping (LENS, which

includes DMD, selective laser sintering (SLS), etc.,) processes as a function of process parameters is given by the following equation:

$$D = \left(1 + \frac{\eta_d V_p \Delta H_s}{\eta_a \eta_m P - \eta_a V_p \Delta H_p} \right)^{-1} \quad [2.1]$$

where η_a, η_d, η_m are energy transfer, deposition and melting efficiencies and V_p, ΔH_s, ΔH_p and P are the volume of powder, melting enthalpy of substrate, melting enthalpy of powder and laser power, respectively. Laser energy transfer efficiency is a dimensionless parameter that is used to describe the ratio of energy that is absorbed by the workpiece over the energy generated by the heat source. The melting efficiency is used to describe the amount of energy that is used to create a molten pool from the energy delivered to and absorbed by the workpiece. The deposition efficiency is a parameter that is used to describe the ratio of actual deposition rate (i.e., powder that is fused into the melt pool) to the total mass flow rate of powder delivered by the system. The values of η_a, η_m do not change for single-pass deposits; however, in the case of multiple layers where more significant change in composition and geometry changes are produced η_a, η_m can change appreciably [22]. For example, complete construction of a thin wall of copper onto steel will eventually produce a local increase in thermal diffusivity and a change in heat-transfer condition from 3-D to 2-D. This localized increase in thermal diffusivity and shift from 3-D to 2-D can either increase or decrease the η_m.

The following is a simple model to determine the laser cladding processing window using statistical methods. This is obtained by correlating individual processing

parameters {P, S, F} with geometric features namely clad height, dilution factor, and α-angle related to track overlapping, and are given by following equations [17]:

$$\text{Clad Height, } \Phi_1 = \sqrt{\frac{PF}{S^2}} \quad [2.2]$$

$$\text{Dilution Factor, } \Phi_2 = \frac{PS}{F} \quad [2.3]$$

$$\alpha\text{- Angle } \Phi_3 = \frac{S}{F} \quad [2.4]$$

where P, S, F stands for laser power, travel speed and feed rate, respectively. In laser cladding some dilution between the coating and the substrate is required to ensure a metallurgical bond. However, to limit degradation of the coating properties, Felde et al. [23] suggested dilution between the workpiece and cladding to be contained between 3 and 5%. Optimization of the DMD process also requires the necessity to understand the powder feeding into the melt pool. Less mixing in the deposit is achieved when the powder was placed on the substrate ahead of the laser irradiation position. If there is a strong convective flow in the melt pool due to very high temperature gradient between the laser irradiated point and the fusion boundary, then it causes a mechanical mixing resulting in a heavily diluted clad layer. Again, a low powder feed rate also causes the clad layer to be heavily diluted due to the above phenomena [24].

The large temperature gradients in the meltpool are also responsible for internal stresses that occur during solidification. Solidification cracking is a function of solidification temperature range and the amount of terminal liquid, both of which are controlled by nominal compositions and solidification conditions [25]. If the temperature interval between the liquidus and solidus temperature is narrow, the dwell time of the

liquid weld metal becomes relatively short. In such cases, it is possible to minimize cracks and shrinkage porosity in the intermixing zone [26]. The residual internal stresses in the part are responsible for reduced performance as well as warpage, loss of edge tolerance and even delamination of layered deposited parts. One way to overcome the residual stresses in laser deposited parts is to use materials with a low coefficient of thermal expansion (CTE) over a wide temperature range, since internal stresses that occur during solidification and cool-down depend strongly on CTE [18]. For example, Invar is a 36% nickel–64% iron alloy with a very low coefficient of thermal expansion, near zero below temperature of 300°C. Above 300°C the yield strength decreases rapidly. This means that during solidification and cool-down of deposited Invar no elastic energy originating from thermal stresses can be stored in the material, because down to 300°C, the matrix is too soft to store a significant amount of elastic energy. Below this temperature, the thermal expansion coefficient is low enough to avoid the buildup of further residual stresses. Another method to reduce residual internal stresses is pre-heating the part prior to deposition. Kelbassa *et al.* [26] showed that a pre-heating temperature between 650-700 ^{o}C was required to obtain defect free single LMD tracks for a γ-TiAl deposit on Ti6Al4V and γ-TiAl substrates. A suitable pre-heating guaranteeing a defect free LMD result is still under investigation.

A fundamental understanding of how process variables relate to deposit characteristics determines the quality of the final part. As already mentioned, the most important process variables that affect the fabrication of a part and quality are laser input energy, travel speed, powder particle size, concentration distribution and powder flow rate [26-37]. As the laser power is increased the melt pool size increases up to a certain

level beyond which the energy of the laser only drives the melt pool temperature up without significant change in the depth of the molten zone. At the interface, the cooling rates are substantially higher at the lower power levels, when the molten zone is small. As the laser power is increased the quench rate at the interface settles at 1000-1500 K/s. At the highest laser power, the cooling rate is much lower, about 500 K/s, because more bulk heating of the sample occurs away from the molten zone. This results in a coarsened microstructure due to the grain growth. The process has been modeled using finite element techniques by Picasso *et al.* [38] and analytically modeled by Kaplan [39] amongst others [40-73]. Due to the additive layered nature of the LENS process the thermal cycles associated with the process can involve numerous reheating cycles. The complicated thermal cycling affects the material properties, residual stress and mechanical strength due to tempering and aging effects [6, 25].

Finite element modeling can be used as an effective tool to understand the multilayered deposition process. From the thermal model it is possible to capture information such as peak temperatures [45], melt pool size [46, 47], temperature gradients [48], etc from different locations in the thin wall structures. The fluid flow and solidification of material in the melt pool cannot be directly considered, as the coupled problem between solid and liquid is not included in the ABAQUS^{TM} software at present. If the effect of the fluid flow is neglected, the highest temperature in the melt pool predicted by a FEA thermal model can be very high - sometimes over 3273 K [49,50]. The computed values of cooling rates by Neela et al. [51] were greater than 15,000 K/s at locations that had experienced the laser beam. However the cooling rates decreased with increasing peak temperature. Hofmeister et al. [48] measured the temperature and cooling

rate around the melt pool by thermal imaging technology. The measured cooling rates ranged from 473 to 6273 K/s. These thermal models can be used to determine the locations of the thermal gradients with respect to part geometry. This information can be used to modify the processing parameters to reduce the distortion and thermal stress in part fabrication [48].

Other than processing parameters such as laser power and travel speed [49, 50], variables such as substrate size, number of clad layers and tool path direction also affected the temperature history and residual stresses in a part. Costa et al. [52] showed that decreasing substrate size caused the overall temperature to increase. As a result the microstructure in the top layers was affected causing a deviation of the process from non-equilibrium behavior. Hu et al. [53] showed that an increase in the number of clad layers or a higher laser power affected the clad height and caused more and more deposited layers to remelt. This was because the melt pool size remained constant throughout the cladding process. When the laser travels bi-directionally (start and end positions of the laser are different), tensile stresses increased progressively with subsequent layers as they were being deposited [54]. This is because the deposits made with a bi-directional tool path experienced slow cooling rates and the temperature of the clad steadily increased [55]. Zekovich et al. [56] showed that the *z*-direction stresses were more compressive in nature towards the inner regions of the wall for a uni-directional tool path than a bi-directional tool path. In a uni-directional tool path the start and end position for the laser during layered building is the same. The model was in agreement with the experimental values reported by Rangaswamy et al. [57, 58]. So far the residual stress distributions in the LENS^{TM} process have only been deduced from the measured strains (obtained

through X-ray diffraction or neutron diffraction) and then using elastic constants to calculate stresses. Moreover, to quantify these stresses within a clad layer has not always being straightforward [57-61] because of the requirement for a smaller specimen size. Hence, this requires further post-process machining prior to strain measurements using these techniques. Also, going from strain to stress using elastic constants is still not a reliable procedure since the elastic constants may not be known accurately.

2.2 THERMODYNAMIC MODELING TOOL IN LMD

In recent years, the application of phase-diagram information obtained from calculations to practical processes has increased significantly, as shown in Table 2.1. Software for calculation of phase diagrams and thermodynamic properties have been developed since the 1970's. A variety of software packages can be used for the calculation of phase diagrams. Frequently used software packages are ChemSage [75], Lukas programs [76, 77], MTDATA [74], Thermo-Calc. [78] and FactSage [79-82]. The computer databases that are available within FactSage are: SGTE, JANAF, FACT, MALT, IVTAN, HSC, etc. All of these software packages can be used for the calculation of phase equilibria. Several thermodynamic databases have been constructed from the assessments of binary, ternary, and quaternary systems. For the description of commercial alloys, it is quite likely that at least a dozen elements need to be considered. The modern developments in modeling and computational technology have made computer calculations of multicomponent phase equilibria easy.

Table 2.1 A selection of processes and materials for which thermodynamic calculations were being used to optimize production parameters [74].

Processes		
Leaching	Casting	Combustion
Roasting	Vapor Deposition	Waste Incin,
Sintering	Melting	Nitrate Control
Electrolysis	Refining	Recycling
	Precipitation	Etc.,
	Hardening	
Materials		
Steels	Semiconductors	Aqueous Solutions
Light Metal Alloys	Superconductors	Molten Salts
Superalloys	Coatings	Organic Mixtures
Solders,	Alloys	Slags
Ceramics	Hard Metal	Glasses
Cermets	Oxide	Etc.,

In the current work FactSage (v 6.1) was employed to perform thermodynamic calculations to study the complex Ti-Ni based multicomponent system because of the resource availability. The FactSage databases, which have been under development for 35 years, contain assessed model parameters for thousands of compounds and hundreds of solid and liquid solution phases of metallic, salt, oxide, etc. The FactSage thermodynamic computer system consists [79-82] of a suite of program modules and several large evaluated thermodynamic databases. The program modules access the databases to perform chemical equilibrium calculations by means of a general Gibbs energy minimization algorithm. The FactSage databases contain the thermodynamic properties as functions of temperature, pressure and composition for over 5000 pure

substances and hundreds of multicomponent solid and liquid solutions of metals, oxides, salts, etc.

The use of thermodynamic modeling to predict most stable phases, low melting compositions, etc., in a multicomponent systems [83-90] is not new. Experimental determination of these compositions can be very lengthy and expensive and hence this tool is very effective in cutting down the costs. Very limited work has been done in utilizing thermodynamic modeling to understand the microstructure evolution along the compositional gradient in a multicomponent systems produced by DMD. Lin et al. [6, 90] are the only ones who used Thermo-Calc with the aid of TTTi alloy database to calculate equilibrium liquidus T_l, solidus T_s and eutectic temperature T_e for the functionally graded Ti6Al4V- Rene88DT by laser metal deposition. The composition of Rene88DT is Ni (bal.), Cr (16%), Co (13%), Mo (4%), W (4%) and other minor elements. They showed that the equilibrium freezing range (ΔT_o) increased with increasing Rene88DT. The eutectic reaction initiated when the composition of the material measured by EDS showed about 10.4 pct Ni along the graded direction. In the present research work a similar attempt was made using measured EDS compositions at varying laser power to predict the equilibrium liquidus, solidus and eutectic temperatures by FactSage (v6.1). The calculations were performed using FACT and SGTE database. The software was also utilized to predict the equilibrium phases at room temperature when compositionally different layers were made to react at high temperatures. An X-ray diffraction technique was used to identify the presence of non-equilibrium and any equilibrium phases present along the graded structure.

2.3 RESEARCH SCOPE ON Ti- Ni BASED ALLOY BASED FGMs BY LMD

Most of the earlier research on direct metal deposition (DMD) concentrated on understanding the effect of process variables on thermal history of homogenous materials. Griffith et al. [91] correlated the build microstructure of H13 tool steel with the measured peak temperature thermal cycles, as shown in Fig. 2.1. The complicated thermal cycling affects the material properties including stress and mechanical strength due to tempering and aging affects. They used the H13 equilibrium phase diagram as a general guide to understand build microstructure. Region I composed of as-solidified H13 (last pass) and supercritically reheated material (fully re-austentized). Some amount of partitioning was observed as a result of solidification, except for C which was uniformly distributed due to the high diffusion rates. Region II of the build corresponded to the fifth layer from the top of the build. The region consisted of a mixture of carbides and martensite (formed from the austenite present at peak temperatures). Region III of the build not only underwent the above two cycles but also experienced subcritical thermal cycles. The microstructure consisted of martensite and carbides.

Kelly et al. [92] studied the microstructural evolution in Ti6Al4V build as shown in Fig.2.2. They deposited about 18 layers of Ti6Al4V on Ti6Al4V with each layer measuring 3 mm thick. The deposit exhibited layer bands which consisted of a colony of Widmanstätten alpha-Ti, while the nominal microstructure between layer bands exhibited basketweave morphology. Process parameters such as high power and low translational speeds resulted in slower cooling rates. Kobryn et al [93] observed a fine Widmanstätten two phase structure with discontinuous alpha at prior-beta grain boundaries at higher

cooling rates, in contrast to a coarse Widmanstätten structure with continuous alpha at prior-beta grains at slower cooling rates.

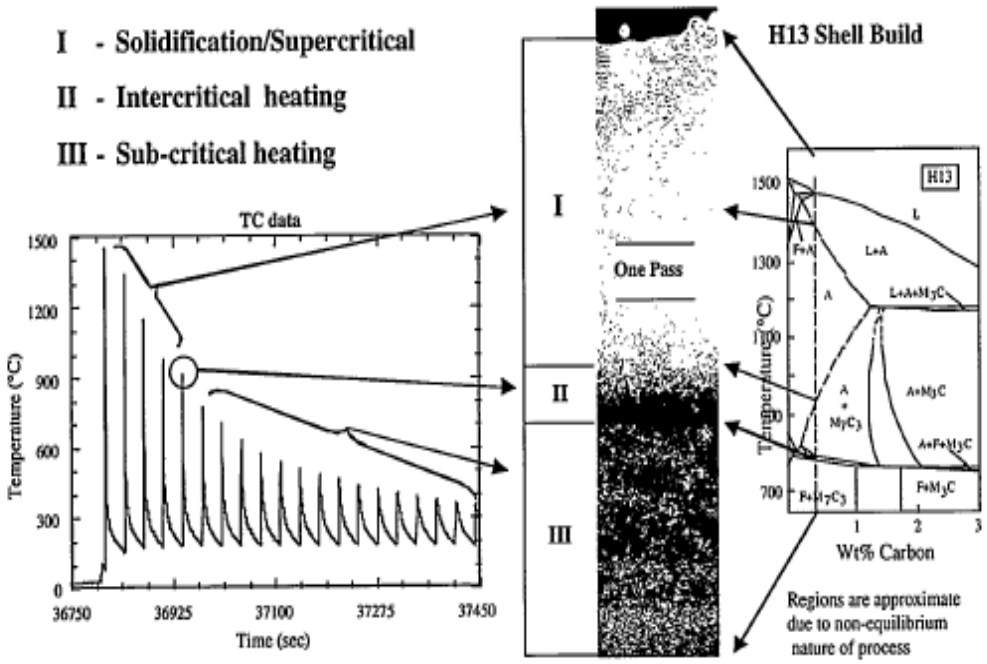

Figure 2.1 Correlation between measured thermal cycles, microstructure, and the phase diagram for H13 shell build [91].

They discussed that the banding essentially caused local changes in the number of fine, equiaxed alpha particles in the microstructure. An increase in the number of alpha particles was caused by the reheating of previously deposited material that occurred with subsequent deposition passes. Similarly Cottam et al. [94] studied the microstructure evolution in Ti6Al4V clads by holding the clad height and melt pool depth constant. This was achieved by varying the travel speed and adjusting the laser power to maintain constant conditions. The resulting microstructure in the clad zone showed a dendritic

microstructure whereas a refined Widmanstätten structure in the heat affected zone (HAZ) at slower cooling rates.

Over the period of years a lot of studies on Ti exploited the advantage of Laser Engineered Net Shaping (LENS^{TM}), which allowed the flexibility to deposit a blend of elemental powders and create an alloy in situ. Collins et al [95-98] observed a series of interesting microstructures along the graded Ti-xV and Ti-xMo, both being beta stabilizers. With the increasing V and Mo the volume fraction of retained beta-Ti was shown to increase. The morphology of alpha-Ti precipitates changed from Widmanstätten lath-like morphology (colony structure) to basketweave structure with change in V and Mo concentration. Further increasing the alloying content also resulted in formation of a biomodal distribution of alpha precipitates within the beta matrix for both Mo and V additions. The bimodal distribution was a result of longer alpha laths breaking up into shorter precipitates with relatively small aspect ratio. These larger laths precipitated during primary $\beta \rightarrow \alpha$ transformation during the deposition of a particular layer and subsequently break up occurred during the reheating of the same layer when new layers were deposited on top.

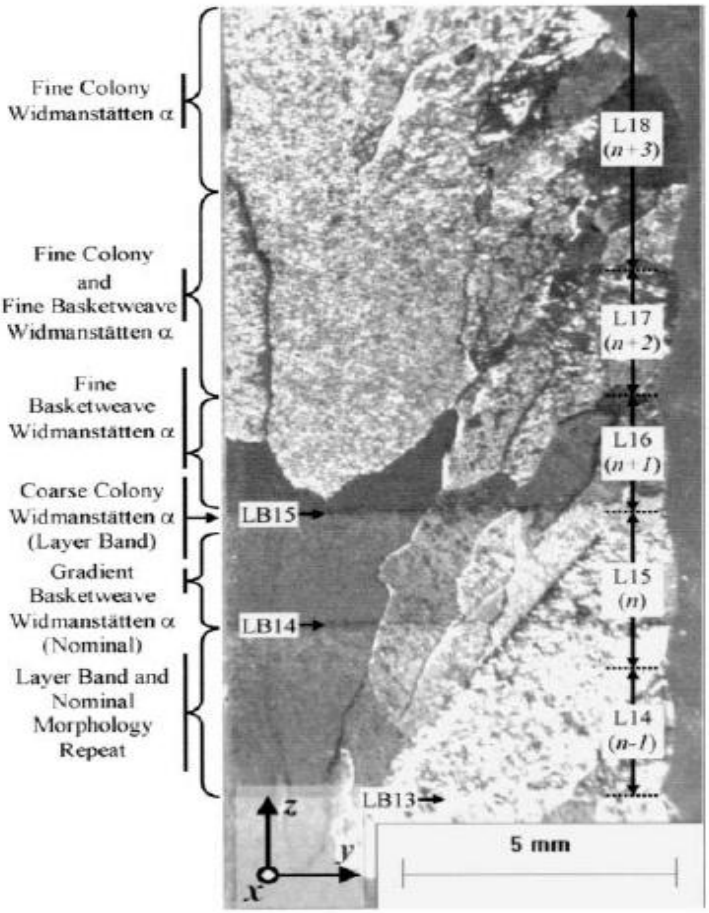

Figure 2.2 Microstructural evolution in Ti6Al4V builds [92].

Collins et al [96] observations on 90 at. % Ti- 10 at. % Cr graded layer to –V and –Mo was slightly different from their previous studies. Ti-Cr exhibit negative enthalpy of mixing and can exhibit rapidly solidified structures in the LENS deposition process. The microstructure primarily consisted of a partially decomposed β matrix with precipitates at the grain boundaries. In the Cr-depleted regions of the matrix equilibrium microstructure was observed; whereas Cr-rich regions showed metastable structures due to rapid solidification arising from high temperature gradients with the addition of extra heat to the meltpool. The inhomogeneity was observed either due to macrosegregation effects

during solidification or inhomogeneous mixing of powders in the LENS powder feeder. A further study to understand the effect of enthalpy of mixing in liquid on mixing process and consequently the homogeneity of the laser deposited alloys was carried out by Schwender et al. [98]. Ti-10 at. % Nb (positive enthalpy of mixing, endothermic) and Ti-10 at. % Cr (negative enthalpy of mixing, exothermic) were deposited under similar conditions by LENS^{TM} process. The microstructures of Ti-10 at. % Cr were fairly homogeneous whereas segregation of particles occurred at the layer interfaces in Ti-10 at.% Nb.

Most of the studies on FGMs in the literature were either investigated within the solid solubility range of the alloying element (ex. Ti-X=Mo, V, Cr, Nb, Co, etc., [92-97]) or systems (ex. Fe-Ni (stainless steel 316L-Rene88DT [6,8]) which showed reasonable compatibility in thermo-physical properties such as density, thermal diffusivity, coefficient of linear expansion, etc.,. There is limited literature available thus far on systems like Ni-Ti based alloys which have the tendency to form brittle IMPs beyond the solubility range. This is apparently because only partial success in producing this system by DMD has been reported due to a variety of metallurgical and mechanical reasons as mentioned above. Ni-Ti alloys have potential as functional materials for industrial and medical applications due to their high temperature and corrosion resistance, shape memory property, and good biocompatibility [8]. There have been a few reports on the laser welding of titanium and nickel alloys. Seretsky and Ryba [101] found that cracks occurred with the same frequency in welds made in single passes over one side only and multiple passes over both sides of the samples. It was not known if the cracking is due to the rapid quenching of the molten metal after irradiation, or to some chemical interaction

between titanium and nickel. Chatterjee et al. [102] butt welded Ti/Ni dissimilar materials using a CO2 laser to investigate the solidification microstructure. They found that macrosegregation, and brittle intermetallic compounds, Ti_2Ni and $TiNi_3$, were readily generated within the weld with macroscopic cracks. Chen et al [10] developed an analytical model from experimental results to understand the relationship between the formation of cracks and the melt pool behaviors including the melt pool area, the melt ration and cooling rate. When the laser beam is offset to the Inconel 718 side, there was significant reduction of the melt area in the Ti-6Al-4V side and the wider melt area in the Inconel 718 side. This resulted in a less vigorous convective flow in the molten zone around the keyhole, avoiding the formation of intermetallic phases in the weld. As most of the heat input was lost quickly on the Inconel 718 side before enough heat is transferred into the Ti-6Al-4V side to induce severe microsegregation. In contrast, Kamran [103] found that all the Inconel 718 clads on Ti6Al4V whether cracked or un-cracked indicated presence of Ti_2Ni, Ti and Ti_3Ni phases. They concluded that an appropriate selection of laser parameters may not be sufficient to avoid the production of such intermetallics. Similarly, Xu et al [8] found that increasing scanning velocity and decreasing laser power, as deposited microstructure exhibited an evolution from primary TiNi dendrite to two phase TiNi+B2 dendrite and finally to TiNi+$TiNi_2$ anomalous eutectic in Ti-50 wt% Ni clads.

There is very limited research available in literature on the functionally grading Ni-based superalloys and Ti6Al4V. Domack and Baughman [7] attempted to grade from 100 percent Ti6Al4V to 100 percent Inconel 718 at interval steps of 10 percent Inconel 718. Macroscopic cracks formed before the full transition from Ti6Al4V to Inconel 718

was achieved. The cracks developed when the target blend was about 40 percent Ti6Al4V and 60 percent Inconel 625. They determined that the cracks were not directly linked to metallurgical features, although the microstructures showed coarse dendrites and significant elemental segregation. They concluded that additional development of process parameters and powder feed control were necessary to ensure that target chemistry gradients are achieved without excessive material reactions. In another detailed study Lin et al. [6, 90] investigated the solidification behavior and phase evolution of Ti-6Al-4V, and Ti with Rene 88 DT. They presented a detailed microstructural evolution along the compositional gradient from 100 percent Ti-6Al-4V to Ti-6Al-4V with 38 percent Rene 88 DT and Ti with 60 percent Rene88DT. The microstructures consisted of anomalous eutectic structures formed as a result of rapid solidification. There was no mention of solidification cracking in their study.

Dong, et al. [104] functionally graded Ti6Al4V-316L using Inconel 625 as a transition layer. In their work the transition happened from 90% Inconel 625 to 90 Ti6Al4V, it was never 100%. The microstructure varied from TiNi + $TiNi_3$ eutectics at 20% Ti6Al4V + 80% Inconel 625 and 30% Ti6Al4V + 70% Inconel 625; and Ti+Ti_2Ni eutectics at 90% Ti6Al4V + 10% Inconel 625 and 70% Ti6Al4V + 30% Inconel 625. The authors claimed no visible cracks in the transition regions. But Figure 2.3 shows a transgranular micro-crack at the transition region of 10% SS316L + 90% Inconel 625 and 20% Ti6Al4V + 80% Inconel 625. This was further corroborated by the fracture of the tensile specimen at the transition of Inconel 625-Ti6Al4V interface. From the morphology of the fracture they concluded that cracks that initiated during deposition propagated along the interface among the intermetallics under the stress. The stresses can

also be generated by constrained elastic expansion or contraction due to transient temperature gradients, and thermal expansion coefficient mismatch, and changes in specific density due to solid phase transformations. The amount of heat input determines the cooling rate, which is inversely proportional to the square of the melt pool length. High thermal gradients results in a rapid cooling rate and increase the resistance to solidification cracking, alternately the presence of thermal strains caused by rapid cooling can also increase the crack initiation rate.

Although there have been some previous attempts to understand the microstructural evolution in these alloys and to transition from 100% Ti based alloy to 100% Ni based alloy, this objective has not been fully realized due to presence of cracks in the transition regions. In summary, this necessitates further research in order to establish a correlation between processing parameters and microstructures to attempt to obtain crack free compositionally graded Ti6Al4V/Inconel 625 FGMs.

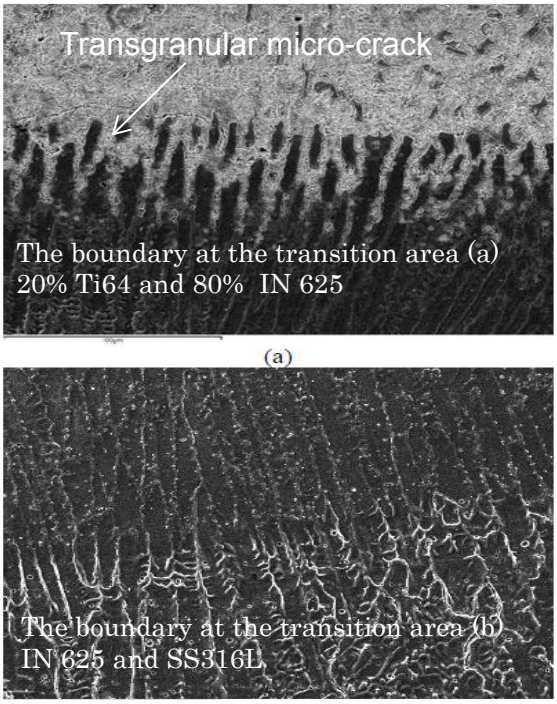

Figure 2.3 The boundary at the transition area (a) Ti6Al4V and Inconel 625 (b) Inconel 625 and SS316L [104].

3. EXPERIMENTAL METHODS

There are four types of experiments that were performed during the scope of this research: Materials Processing; Materials Testing and Characterization; Thermodynamic Modeling and Thermo-mechanical Modeling. The first section will cover the processing techniques used, including descriptions of starting pre-alloyed powders and laser deposition parameters for specific powders. The second section will cover the techniques used for microstructure and mechanical analysis for the thin wall structures produced by LMD. The final two sections will cover the thermodynamic modeling using FACTSAGE (v6.1) to evaluate phase-stability along the compositional gradient and thermo-mechanical modeling using ABAQUS^{TM} (v10.1) to determine the temperature history and residual strains in a fabricated structure.

3.1 MATERIALS PROCESSING

3.1.1. Laser Aided Manufacturing Process (LAMP). LAMP system was used to deposit the compositionally graded materials and clads in this thesis. The process utilized a 1 kW diode laser (Nuvonyx ISL-1000M, 808 nm, spot size 2.5 mm), a laser coaxial nozzle, a five-axis numerical control working table, and a powder feeder (as shown in Fig. 3.1). In a laser co-axial nozzle, powder and a gas stream can be fed at the same time. The functionally graded Ti6Al4V/Inconel 625 were built using argon as an assist gas. This was done to minimize any oxidation of the melt pool. The multilayers SS316L and Inconel 625 clads were built without using any assist gas. The argon gas was 99.99 percent pure. The flow rate of argon gas is 240 standard cubic centimeters per

minute (SCCM). The various compositional powders using Ti6Al4V and Inconel 625 for the functionally graded parts were prepared by wt% standard and argon was used to inject all the powders into the laser melt pool. Three types of deposition strategies were chosen for FGMs with powder compositions changing from nominal 100% (weight percent, wt.%) Ti6Al4V to nominal 100% (weight percent, wt.%) Inconel 625. Figure 3.2 shows the schematic of the deposition strategies for FGMs. Table 3.1 and 3.2 lists the process parameters that were used to build the thin wall structures. The 'thin wall' structures in the current research are single track multilayered 3D structure.

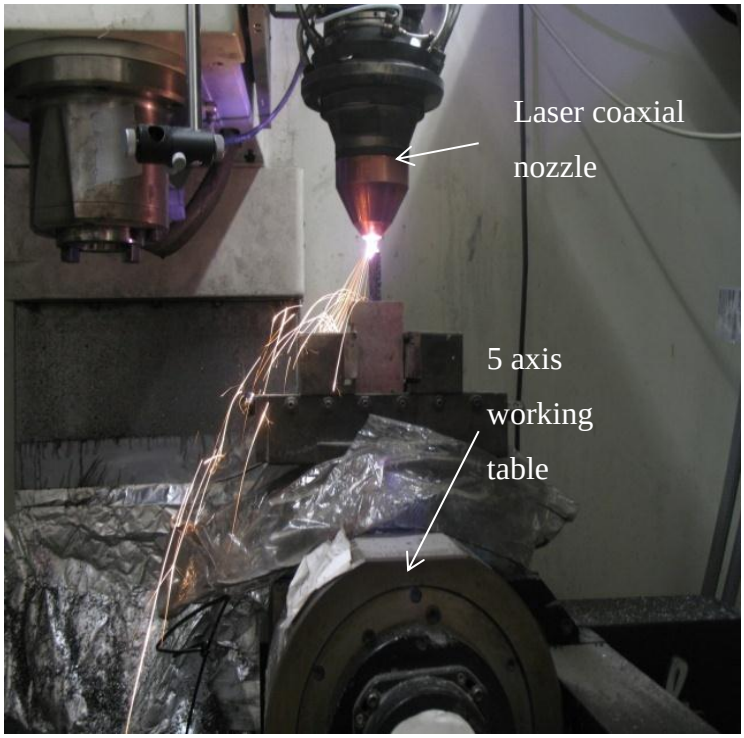

Figure 3.1 Laser Aided Manufacturing Process (LAMP) System. The powder and gas stream act as a single fluid and feed through the coaxial laser nozzle. The laser head is fixed and CNC moves in X-Y motion. Note: Powder feeder is not shown in the picture.

The thin wall structure can be made with or without compositional layers. Clads are built by laying down the same composition powder for each layer. And the FGM is

built by laying variety of compositional layers. For each composition 10 similar layers were put down. There was about a 1 minute delay while the powder compositions were changed after each compositional layer. This meant that the total process time for building an FGM was around 20 minutes, but it varied based on how many compositions were chosen. The composition in the FGM can only change as fast as the powder compositions are changed at the powder feeder. A gradient is defined as the highest jump in wt% over the deposit height. So there will be a "maximum gradient" in the graded structure dependent on both how the powder compositions are changed and on the powder yield. At high powder yield more of each composition will be deposited and so the gradient in [wt%/cm] will necessarily be less. Mixing in and between layers during deposition process is also another factor that will lead to a lower gradient than the "maximum gradient". The powder yield for clads was approximately 90%. For FGMs experiments in this study the yield was less than 10%. This was mainly attributed to the inefficiency of powder feeder, complexity involved in feeding the mixed powders, the powder capture at melt pool, in-ability to estimate the Z height (laser standoff distance) as the chemistry and density of the graded layers changed. As a result, the FGM samples were mostly under-built even though the mass per unit length for the layers was maintained constant.

In summary, the complexity involved in depositing mixed powders translated to poor process control of (i) powder yield for each powder (which may have been different for each powder composition and over time for each set of 10 layers), (ii) the laser absorption efficiency which may have varied with time (absorption can also be impacted by compositions of the layers), and (iii) the Z height from laser tool to the deposit.

Because of the above complexity involved in building FGMs therefore the scope of the current work was further constrained to (i) accept the deposits that were obtained and (ii) explain their microstructures in terms of the measured composition and process parameters.

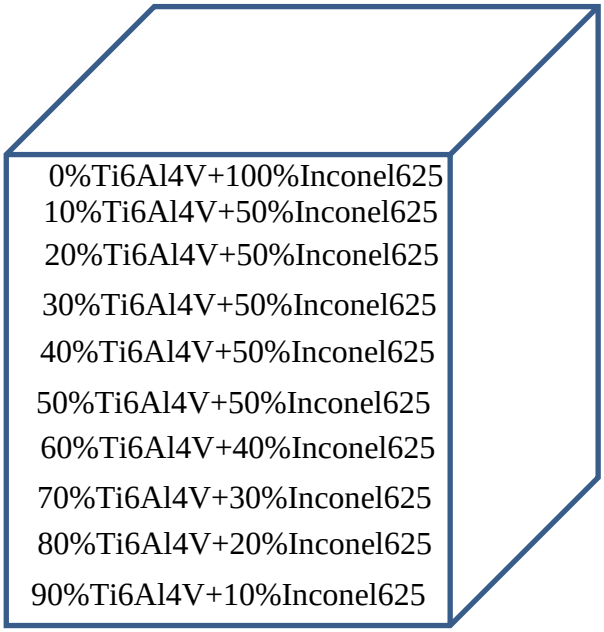

(a) Grading Chem I/Linear Grading

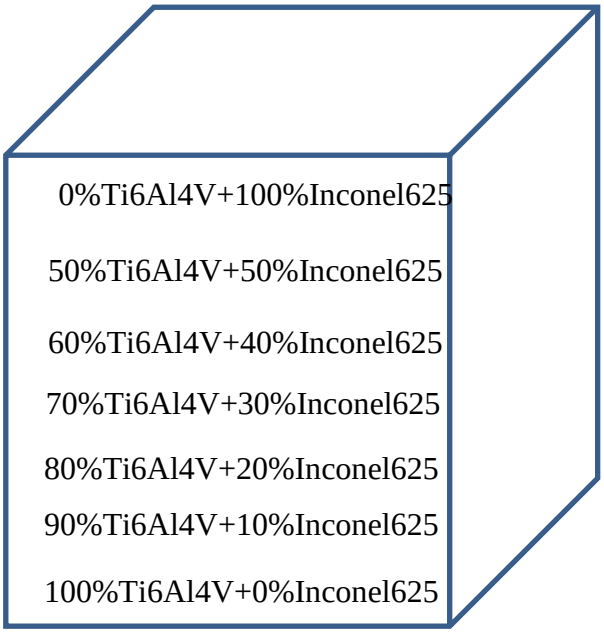

(b) Grading Chem II

Figure 3.2 Schematic of deposition strategy for Ti6Al4V/Inconel625 FGMs.

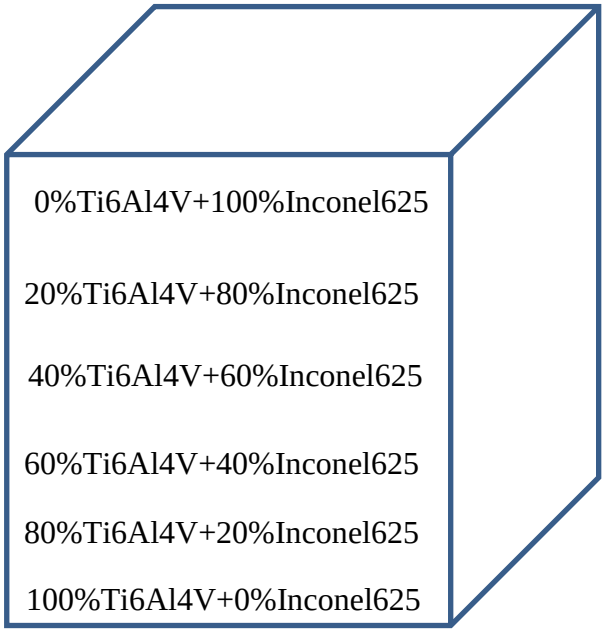

(c) Grading Chem III

Figure 3.2 Schematic of deposition strategy for Ti6Al4V/Inconel625 FGMs (Cont.).

Table 3.1 Deposition parameters for thermodynamic modeling part-1 and part-2 study.

Exp. No	**Grading Chemistry**	**Laser Power, W**	**Travel Speed, mm/s**	**Powder Feed Rate, g/min**	**Travel Dir.**	**No. of Layers**
1-Part 1	Chem-I	500	4.23	0.033	Bi-directional	10 ea. Per composition
2-Part 1	Chem-I	700	4.23	0.033	Bi-directional	10 ea. Per composition
3-Part 1	Chem-I	1000	4.23	0.033	Bi-directional	10 ea. Per composition
4-Part 2	Chem II	500	2.2,	0.133	Uni-directional, Bi-directional	10 ea. Per composition
5-Part 2	Chem II	500	8.46	0.033	Uni-directional, Bi-directional	10 ea. Per composition
6-Part 2	Chem II	500	4.23	0.133	Uni-directional, Bi-directional	10 ea. Per composition

Table 3.1 Deposition parameters for thermodynamic modeling part-1 and part-2 study (Cont.).

7-Part 2	Chem II	1000	4.23	0.133	Uni-directional, Bi-directional	10 ea. Per composition
8-Part 2	Chem II	1000	8.46	0.133	Uni-directional, Bi-directional	10 ea. Per composition
9-Part 2	Chem III	1000	4.23	0.033	Bi-directional	10 ea. Per composition

3.1.2. Pre-Alloyed Powders. The pre-alloyed Ti6Al4V, Inconel 625 and SS316L were supplied by Boeing Corporation. The label indicated powders with 45-100 μm sizes produced by gas atomization process and were spherical in shape. The nominal compositions of the as-received powders are given in Table 3.3.

Table 3.1 The Nominal Chemical Composition (wt%) of the powders[3.1].

Type of Powder	***Composition (wt%)***
Ti6Al4V	Ti(Bal.), Al(5.5-6.75), V(3.5-4.5), C (0.1), Fe (0.3), O (0.2)
Inconel 625	Ni (70), Cr (20-23), Mo (8-10), Nb+Co (3.15-4.15), Fe (5)
SS316L	Fe(bal), Cr(17-19), Ni(13-15), Mo (2.25-3.50) rest alloying elements

An EJ6100 scale with an accuracy of 0.1g was used to measure the weights of the pre-alloyed Ti6Al4V and Inconel 625 powders prior to making mixtures of varying compositions. In all the cases, the weighing was performed in ambient air. The powder blends was charged into 16 oz Fisher-Scientific Nalgene LDPE (low density polyethylene) plastic bottles. These bottles were placed into a Turbula® mechanical

powder mixer, and mixed for 1 hour. The premixed powder blends were subsequently fed into the powder hopper (powder feeder) to perform experimentation. In general, the denser Inconel 625 powder particles will tend to settle at the bottom of the container and hence some amount of powder segregation through settling cannot be ruled out during the experimentation. The output from the powder feeder was not measured experimentally, although it has been calibrated previously. One possible way to improve the homogeneity of the deposits is to deliver powders from different feeders. This will hopefully prevent any of the inhomogeneous distribution in the alloy powders that can result from segregation of powders in the powder feeder prior to deposition.

3.2 MATERIALS TESTING AND CHARACTERIZATION

3.2.1. Mechanical Testing. A Struers-Duramin -10 Microhardness Tester was used to measure the microhardness for the compositionally graded samples. The indents were imparted on the surface at 2N load and a holding time of 15 s. This technique was important in analyzing various composition gradients. The indents not only allowed an understanding of the trends in mechanical properties, but also acted as markers for subsequent SEM and standardless EDS analysis.

[3.1] http://www.cartech.com/products.aspx

3.2.2. Characterization Techniques. For the metallography studies the graded material was sectioned perpendicular to the laser scanning direction, mounted and polished by techniques described by Buehler[3.4] for Ti6Al4V. The final polishing was done using 0.05 μm alumina slurry. A variety of characterization tools such as scanning electron microscope (SEM), energy dispersive spectroscopy (EDS) and x-ray diffraction (XRD) were used to study the microstructures along the graded direction. The compositional layers were not easily distinguishable in SEM. Therefore, in all the clad and graded[3.2] samples a series of indents were imparted on the surface typically 0.1 mm apart. The indents in the graded regions were placed more closely than in the parent metal (0.15-0.3 mm) in order to obtain as much information as possible. But care was taken not to place them too close together such as to affect the values that were obtained. After the indents were made and the hardness measured, the samples were placed into the SEM. Compositions were measured from regions around the indent and the microhardness values were directly compared with the composition. The back scattered mode (BSE) in SEM was used to study the microstructural evolution in the samples.

Some of the regions in the compositionally graded samples were further evaluated by elemental mapping to better understand the distribution of various elements. There are some limitations with using the EDS tool for determining elemental compositions. For example, the short time for the EDS maps limits minimum detectability of the elements studies, and there may be at least ±5% error in measurements by standardless EDS technique.

[3.2] www.mybuehler.com.BUEHLER-SUM-MET™

[3.3] ASM Handbooks, Vol. 3

Identification of phases along the gradient direction was achieved using X-ray diffraction (Philips Xpert X-ray diffractometer, collimated beam spot size: 50-100 microns). The detection limit for XRD is about 1% . The phases in a compositional layer were identified by grinding the deposit to a certain depth for each layer. The depth of grinding for a specific compositional layer in the specimen was approximately identified by dividing the total deposit height by the number of compositional layers. In the current study every time 400-500 microns of material was removed an XRD was performed on the surface of that layer. The height of the deposit after removal of each layer was measured using Vernier calipers and digitally measured using Image J software. Because there was no clear delineation in the compositional layers the identification of phases for a given layer is only an approximation. And the various phases in the microstructure were determined with the help of both SEM images and XRD data.

3.3 THERMODYNAMIC MODELING

The thermodynamic database allows for the prediction of phase equilibrium, phase stability, phase transformations, and in turn can link the properties of the multi-phase materials to the alloy microstructure. In the present work the tool was utilized to predict the different phases that would form under equilibrium conditions during the various deposition strategies by using commercial software, Factsage (v 6.1). Two types of calculations were performed to understand the nature of complex reactions occurring in the multicomponent system. In one analysis, the elemental composition data from EDS was used as an input to calculate the liquidus temperature (T_L) and solidus temperature (T_S) and construct an equilibrium phase diagram. In a second analysis, the phases in the

final compositional layer for each composition were predicted based on the reactions between the graded layers at defined temperature conditions, an example of which is shown in Fig. 3.3. For the second analysis the nominal powder chemical constituents were entered for each of the graded composition layers.

The solution databases used for all the calculations were [FACT53] and [SGSL 1991]. The old versions of databases are not adequate enough to perform thermodynamic calculations and hence there is some discrepancy in data between the mathematical vs. experimental in the present work. The SGTE (2007) is an extensive new update of the previous SGTE (2004) and SGSL (1991) alloy database. There are some 300 completely assessed binary alloy systems (ca. 155 in the old SGSL database) together with about 120 ternary and higher-order systems (ca. 70 in the old SGSL database) for which assessed parameters are available for phases of practical relevance. The systems now incorporate 177 different solution phases (64 in SGSL) and 588 stoichiometric intermetallic compound phases (263 in SGSL).

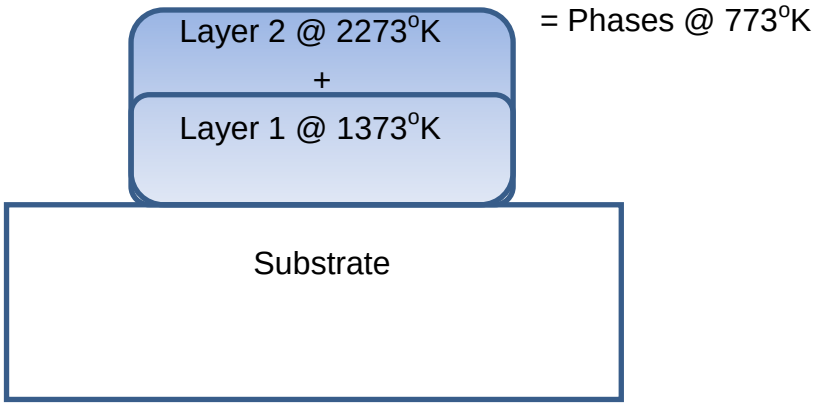

Figure 3.3 Schematic representation of the layers for Factsage calculations in the second part of thermodynamic modeling.

Ti6Al4V-Inconel 625 is a very complex multi-component system. For a phase to precipitate in an alloying system, the right thermodynamic and kinetic conditions have to be present. In general, the kinetic considerations when it comes to predicting what phases will form in an alloying system can be judged based on the driving energy for precipitation (DGP) of each phase and the temperature at which those phases are thermodynamically stable. In addition to the driving energy for precipitation (DGP), another good general predictor about the kinetics of precipitation is the temperature at which the phase starts to precipitate upon cooling. The lower the solvus temperature, the more sluggish the kinetics will be for the precipitation of that phase. Commercial kinetics-based software such as Thermocalc can predict phases based on the DGP and solvus-temperature calculations. In the present work whether a particular phase could precipitate or not was entirely based on thermodynamic calculations essentially because of the inability of Factsage to perform kinetics based calculations.

There are about 20 binary and 6 ternary systems known for the Ti6Al4V+Inconel 625 system. The major alloying elements (> 10 wt%) are Ti, Ni, Cr, Mo and the minor alloying elements (<10 wt%) are Fe, Al, V. Some of the major phase diagrams are shown in Fig. 3.4. In the systems like Cr-Ni; Cr-Ti, Cr-Mo, Ti-Mo and Ti-V there is a miscibility gap. This means there is a phase separation in solid or liquid. Also, in the Ti-Ni phase diagram there are two ordered phases present: (1) TiNi (ordered B2 type, CP_2) and (2) γ'TiNi3 (ordered L12 type, CP_4). In the first part of the thermodynamic modeling study, the compositions measured along the graded direction by standardless EDS analysis were used to obtain Solidus (Ts) and Liquidus (Tl) temperatures. The conditions assigned to the model included 1 atm and 2000 K. The temperature value selected for the

model was obtained from the FEA thermal model. The FEA thermal model predicted the temperatures of the molten layer to 2000 K. The inputs and boundary conditions for the FEA thermal model are discussed later in this Section. The 'Equilibrium' module was used to obtain Ts and Tl. When the phase has a miscibility gap (solid state or liquid state separation) the I-option provided in the module is selected to do more accurate calculations. Also, the I-option is required because the system has ordered solid solutions such as B2_BCC and L12_FCC, which are based on the BCC or FCC disordered state.

In the second part of the study the 'Reaction' module in Factsage was utilized to predict the phases that would form when two layers with different chemistries were made to react with each other. In the DMD process the layers not directly underneath the beam undergo solid state annealing as well as some amount of remelting; whereas the new layer that is being deposited starts in a totally molten state. This may result in the composition and microstructure of the final layer ending up being slightly different from the nominal composition. In the model, the remelting process is captured by reacting layer-1 with layer-2 as shown in Fig. 3.3. To simplify the model the entire volume of layer-1 is reacted with layer-2. In the calculations the pre-existing layer was assigned 1373 K whereas the new layer was assigned a temperature above its melting point based on the calculation from FEA thermal model. The possible product species for pure liquids and solids were selected for each of the graded layers and the outputs were saved as different streams under different temperatures. For the short times involved in the LMD process not much should happen in the way of microstructural evolution at any temperature below $0.4*T_m$ (K) (T_m, melting point), which is around 500^oC for Ni and Ti. The quantitative data of the phases for the final layer was tabulated at 100^oC. The

equilibrium products satisfied the mass balance and attained minimum Gibbs free energy state.

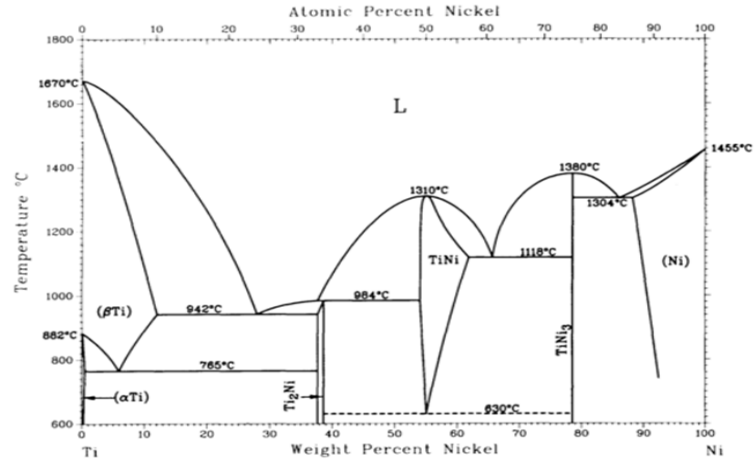

Ni-Ti crystallographic data

Phase	Composition, wt% Ni	Pearson symbol	Space group
(βTi)	0 to 12	*cI*2	$Im\bar{3}m$
(αTi)	0 to 0.3	*hP*2	$P6_3/mmc$
ω[a]	~10	*hP*3	$P6/mmm$ or $P\bar{3}m1$
Ti_2Ni	38.0	*cF*96	$Fd\bar{3}m$
TiNi[a]	~54 to 58	*mP*4	$P2_1/m$
TiNi	54.6 to 62	*cP*2	$Pm\bar{3}m$
γ″$TiNi_3$[a]	~77	*hR*21	$R\bar{3}m$
$TiNi_3$	79	*hP*16	$P6_3/mmc$
γ′$TiNi_3$[a]	~86 to 90	*cP*4	$Pm\bar{3}m$
(Ni)	88.4 to 100	*cF*4	$Fm\bar{3}m$

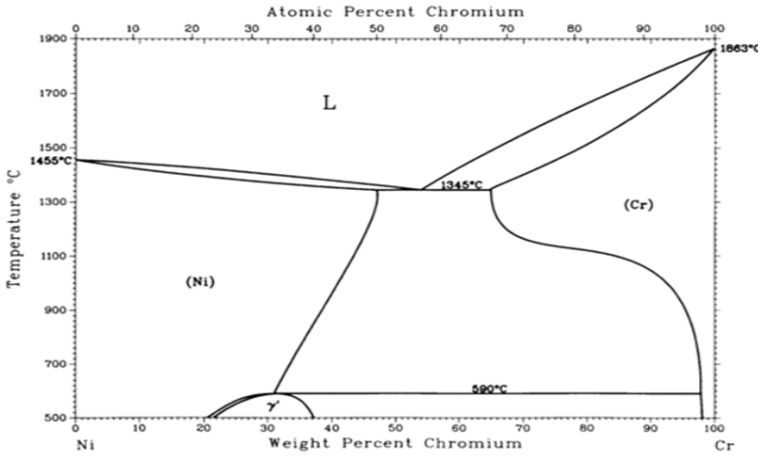

Cr-Ni crystallographic data

Phase	Composition, wt% Cr	Pearson symbol	Space group
(Ni)	0 to 47.0	*cF*4	$Fm\bar{3}m$
Ni_2Cr or γ′	21 to 37	*oI*6	*Immm*
(Cr)	65 to 100	*cI*2	$Im\bar{3}m$
Metastable phases			
σ	~28	*tP*30	$P4_2/mnm$
δ	100	*cP*8	$Pm\bar{3}m$

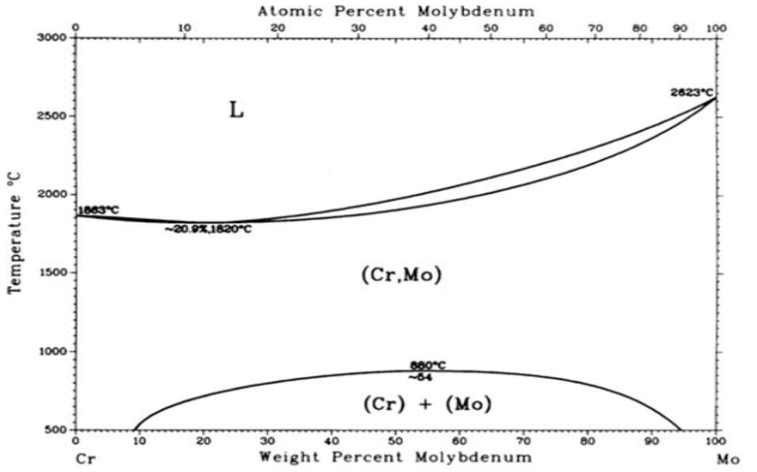

Cr-Mo crystallographic data

Phase	Composition, wt% Mo	Pearson symbol	Space group
(Cr,Mo)	0 to 100	*cI*2	$Im\bar{3}m$

Figure 3.4 Binary phase diagrams of major alloying elements[3.3].

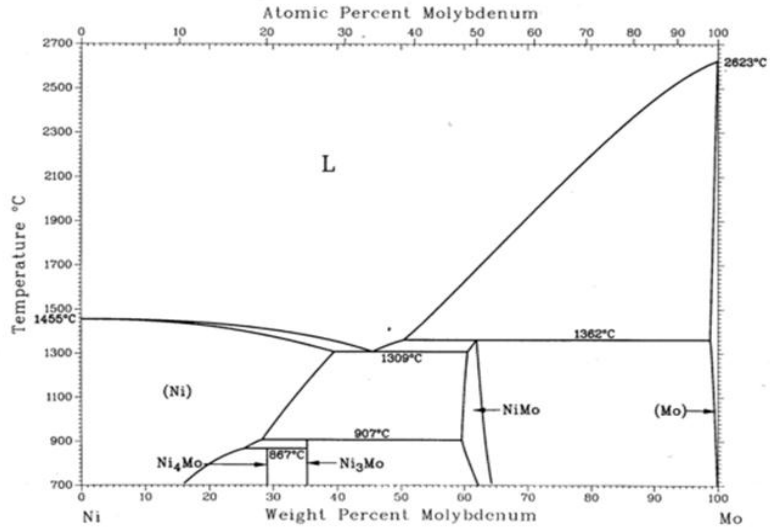

Mo-Ni crystallographic data

Phase	Composition, wt% Mo	Pearson symbol	Space group
(Ni)	0 to 38[(a)]	*cF*4	$Fm\overline{3}m$
Ni_4Mo	29.0	*tI*10	*I*4/*m*
Ni_3Mo	35.3	*oP*8	*Pmnn*
NiMo	63.9 to 65.7	*oP*112	$P2_12_12_1$
(Mo)	98.9 to 100[(b)]	*cI*2	$Im\overline{3}m$
Metastable phases			
Ni_2Mo	…	*oI*6	…
Ni_3Mo	…	*tI*8	*I*4/*mmm*
Ni_4Mo	…	*tI*10, *cF*4	…
$Ni_{17}Mo_5$	…	…	…

(a) At 1317 °C.
(b) At 1362 °C

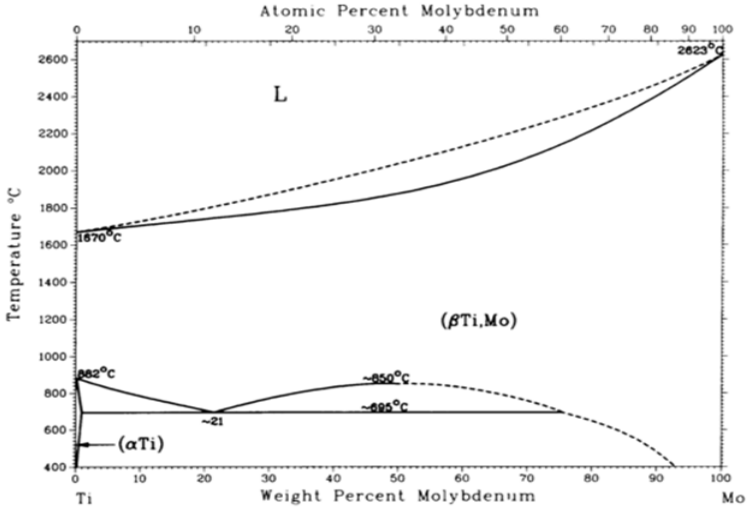

Mo-Ti crystallographic data

Phase	Composition, wt% Mo	Pearson symbol	Space group
(βTi,Mo)	0 to 100	*cI*2	$Im\overline{3}m$
(αTi)	0 to 0.8	*hP*2	$P6_3/mmc$
α′	[(a)]	*hP*2	$P6_3/mmc$
α″	[(a)]	*oC*4	*Cmcm*
ω	[(a)]	*hP*3	*P*6/*mmm*

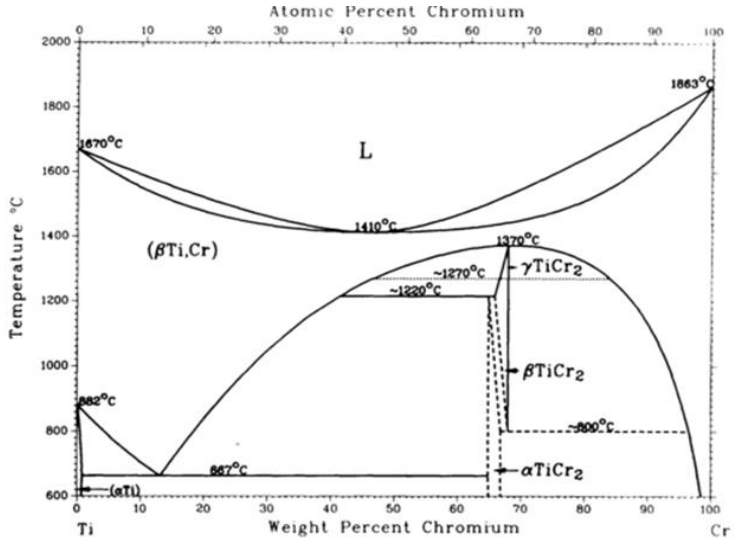

Cr-Ti crystallographic data

Phase	Composition wt% Cr	Pearson symbol	Space group
(βTi,Cr)	0 to 100	*cI*2	$Im\overline{3}m$
(αTi)	0 to 0.2	*hP*2	$P6_3/mmc$
$\alpha TiCr_2$	65 to 67	*cF*24	$Fd\overline{3}m$
$\beta TiCr_2$	66 to 68	*hP*12	$P6_3/mmc$
$\gamma TiCr_2$	66 to 68	*hP*24	$P6_3/mmc$
Metastable phase			
ω	…	*hP*3	$P\overline{3}m1$

Figure 3.4 Binary phase diagrams of major alloying elements[3.3] (Cont.).

3.3.1. Thermodynamic Modeling Tool Post Experimentation. For the first part of the study all the parameters were kept constant and only the laser power was changed, as shown in Table 3.1. The composition of the powder was changed every 10 layers in linear steps of 10% (Fig.2.2 (a)). The base metal was cold rolled Ti6Al4V (12.7 mm) and the first layer that was deposited on the top had a nominal composition of 90% Ti6Al4V+10% Inconel 625. The compositions were linearly changed from nominal 10 pct by weight of Inconel 625 to 100 pct by weight of Inconel 625. This study also made it possible to understand the effect of laser power on 'dilution' of Inconel 625 into the substrate. The phase diagram (Liquidus temperature, T_L and Solidus temperature, T_S) was constructed using the EDS compositional data along the gradient in fabricated structure. This data was acquired from measurements taken along a series of indentations along the composition gradient that were used to mark distance for the SEM. The indenter spacing in the original base material was varied non-linearly from 0.15 to 0.3 mm, but was made at intervals of 0.1 mm along the graded direction. The heights of the thin wall structures varied across all the experiments even when the mass per unit length of powder was held constant for each layer for each parameter. Some of the drawbacks in the experimental conditions in current research work have been discussed earlier in this Section.

For the second part of the thermodynamic modeling study the process parameters are shown in Table 3.2. After preparing the samples metallographically, the layers in the thin wall structure were not distinguishable in SEM. XRD was used to detect the phases in the thin wall structure along the graded direction. The procedure for sample preparation for XRD has already being discussed earlier in this Section. The results were

quantified and are presented later in Section-4. The microstructures along the graded structure can be well understood with the combination of SEM images and XRD data.

3.4 THERMO-MECHANICAL MODELING

During laser deposition process microstructure and residual strains in the fabricated part can be simultaneously affected by various process parameters such as laser power, travel speed, number of layers, etc. Residual strains are one of the most commonly studied factors in predictive models for multilayer deposition. Obtaining appropriate experimental data as input to calibrate the model is still an essential part of this implementation.

A nonlinear transient thermo-mechanical model was developed for the simulation of the multilayer laser deposition process, using ABAQUS™. In the model the thermal and mechanical fields were sequentially coupled. The FEA model was used to perform calculations for temperatures and strains for uni-directional and bi-directional tool paths under different processing conditions and verified experimentally. For the uni-directional tool path, the start point for each layer was the same, whereas in the bi-directional tool path the start and end point for each layer were different. The general approach in ABAQUS to the solution of nonlinear problems is to apply the loading (boundary conditions, heat fluxes, etc.,) in steps, with the load in each step being divided into increments. For a computationally efficient solution, the Newton-Raphson iterative method was adopted to solve equations after every load increment and the solution was checked for convergence. The transient thermal analysis was the first step during which the temperature field was calculated and saved for every step and these results were then

recorded as a thermal load for the mechanical analysis. The following phenomena were addressed within the FE model that was developed:

Heat Transfer: The laser beam was simulated as a moving heat source by means of an imposed flux on the surface of each new element. The units of surface flux are W/mm^2. Cooling of the thin wall structure was simulated by employing convection and radiation boundary conditions. Heat transfer into the bulk of the substrate was considered to take place by conduction only. Heat transfer along the thin wall occurs by conduction, convection and radiation. The effect of latent heat was also accounted for in the calculations. The thermal model was used to calculate cooling rates, peak temperature distribution and remelted layer depths for different processing conditions. In the LMD process the layers not directly underneath the beam undergo solid state annealing as well as some amount of remelting; whereas the new layer that is being deposited is in the molten state. The amount of the prior layer that remelts and mixes with the new layer can cause final layer to have a composition slightly different from the nominal composition.

Mechanical Analysis: The temperature fields from the thermal model were used as an input to perform stress calculations. During laser deposition there occur high temperature gradients in the thin walls. These temperature gradients are dependent on the process conditions, namely the direction of the tool path, laser power, laser travel velocity, and powder feed rate. In the stressed state, plastic strain develops at locations where the yield strength of the material has been realized. In the current model elastic-plastic behavior was assumed during deformation. Hooke's Law applies to the elastic strain, while nonlinear material behavior such as plasticity was simulated by using the following incremental plasticity models: (i) a yield condition, (ii) a yield law, and (iii) a hardening

law. The yield condition is based on Von Mises Distortion Energy hypothesis. The yield law states the plastic strain increment as coaxial and proportional to the deviatoric stress. The equation to predict yielding of materials under multiaxial loading conditions is given by:

$$\sigma_v = \sqrt{3J_2} \quad [3.1]$$

Where σ_v is Von Mises stress and $J_2$is second deviatoric stress invariant. In this case, yielding occurs when the equivalent stress,σ_v reaches the yield strength of the material in simple tension, σ_y. A rate independent isotropic hardening model was used because of the simplicity of the algebraic equations associated with integrating the model. This material model estimates yield stress changes uniformly in all directions as plastic straining occurs. The isotropic work-hardening law is shown below:

$$\sigma_y(\bar{\varepsilon}^p) = \sigma_o + h\bar{\varepsilon}^p \quad [3.2]$$

Where $\bar{\varepsilon}^p$ is plastic strain and h is hardening modulus. There was no external loading in the model calculations and constraints were applied to the workpiece so as to prevent rigid body motion.

3.4.1. Issues Not Addressed in Modeling. The FEA study was mainly conducted to reduce the experimental time and cost to understand the effect of process parameters on residual strains in the part. The model on temperatures and strains for multilayer cladding has already being reported in the literature and hence the current study undertaken is not original. The effort was mostly driven towards verifying these models experimentally by measuring the temperatures and strains using thermocouples and strain gages. The objective of the thesis was to successfully grade Ti6Al4V/Inconel 625 FGMs

which required some understanding of the process parameters. The FEA study was designed primarily around clads and not FGMs due to the complexity around material chemistry, nature of grading process, lack of thermo-mechanical data, and computing time to name a few. Even within the multilayer cladding via LMD the following aspects were not within the purview of this work for the reasons described below:

Kinetics: Phenomena such as grain growth, precipitate coarsening, recrystallization or decomposition of metastable phases are all thermally activated and eventually affect the stress/strain fields. These issues were not addressed as meaningful information could be established from the current 3D FEA models for various processing conditions without the necessity for such details. This approach not only reduced the computation time but also reduced the complexity to perform the extensive thermo-mechanical calculations.

Cracking/Failure: When a part is subjected to a series of thermally activated processes, there is the possibility of the occurrence of failure at the deposit/substrate interface by cracking and/or de-lamination. However, cracking and/or failure were not accounted for in 3D modeling. The model was studied solely to understand the effect of processing parameters on stresses in thin wall structures.

Powder Injection: During laser aided powder deposition, the powder particles are injected continuously into the melt even as they interact with the focused laser beam. The current model does not account for the characteristics of the powder during deposition due to computational constraints. The time event for the model begins immediately after a set of particles are deposited. The addition of powder particles required continuous updates in the solution geometry and was achieved by successive discrete addition of new set of

elements into the computational domain using an element activation feature. The distance traveled by the laser beam for each layer along the substrate was calculated by dividing the total time into a number of small time steps. This time dependent thermal problem was solved sequentially by introducing (or activating) a new set of elements at the beginning of each time step. This stepwise approach has been schematically presented in Fig. 3.5.

Fluid Mechanics: During laser metal deposition temperatures typically exceed the melting point of the material. The current research focused on the estimation of stress fields and ignored the effects of fluid flow and melt-pool dynamics. The newly activated elements in the computational domain were added "strain free" at their melting point.

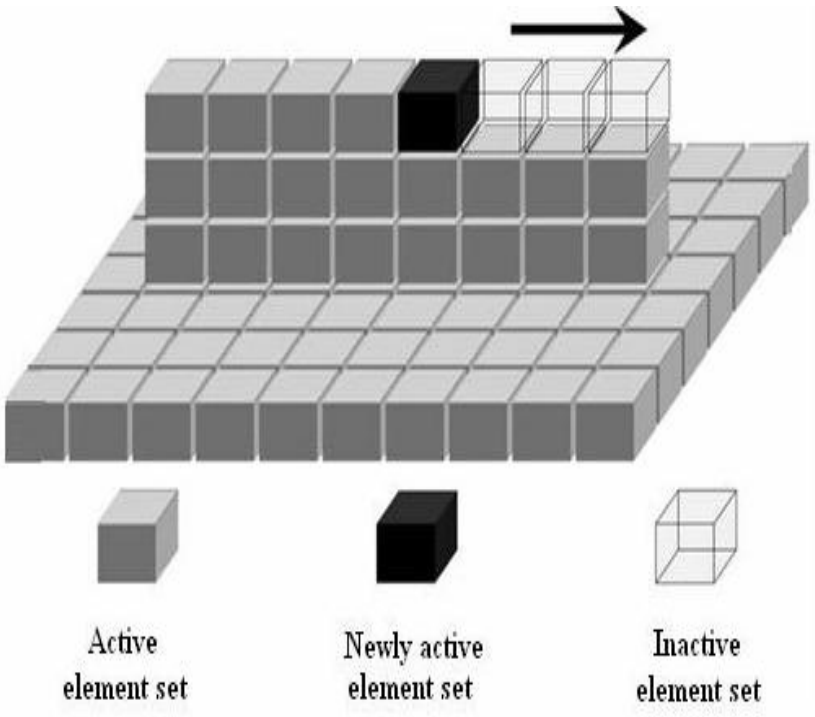

Figure 3.5 Material addition modeled by activating new sets of element [51].

3.4.2. Experimental Validation of FEA Modeling. A model is useful only if it can be experimentally validated. In the current research, in-situ real time strains were measured using high temperature strain gages which have been used only in jet engines and power plant applications thus far. These high temperature strain gages (HFH-series, HITEC PRODUCTS Inc. (USA)) have an operating range of 1375^{o}C and were spot welded to the part at the "reference position" shown in Fig. 3.6. The experimental set-up with the thermocouples, High Temperature Strain Gage (HTG) and Room Temperature Strain Gage (RTG) to validate the FEA model is presented in Fig. 3.6. The gages were located 6 mm away from the centerline of the clad. By doing some thermal calculations it was found that the temperatures in that location were safe to place the thermocouple and the strain gages. The temperature data were collected from a K-type thermocouple at a rate of 1000 samples per second at the "reference position". In a similar manner the HTG and RTG (post processing) were placed at the reference position and the data was also acquired at a rate of 1000 samples per second. The comparison of experimental with simulated results allowed the estimation of the relative importance and role of the complex physical interactions that govern the direct laser metal powder deposition process.

Table 3.2 Detailed analyses performed under different processing conditions. Sets 1-3 the substrate material was SS316L, P= power, TS= laser travel speed, FR= powder feed rate.

Set No.	Process Parameters	Experimental	FEA	Post Process Machining	HT Strain Gage & Thermocouple
1	P: 1000 W TS: 4.23 mm/s FR.: 12 g/min 15 Layers **Uni.**	Powder: SS316L	Thermal and stress model	Machining using LT strain gages	Confirmed FEA thermal and stress model
2	P: 1000 W TS: 4.23 mm/s FR.: 12 g/min 15 Layers **Bi.**	Powder: SS316L	Thermal and stress model		Confirmed FEA thermal and stress model
3	P: 1000 W TS: 8.46 mm/s FR: 12 g/min 15 Layers **Uni.**	Powder: SS316L		Machining using LT strain gages	

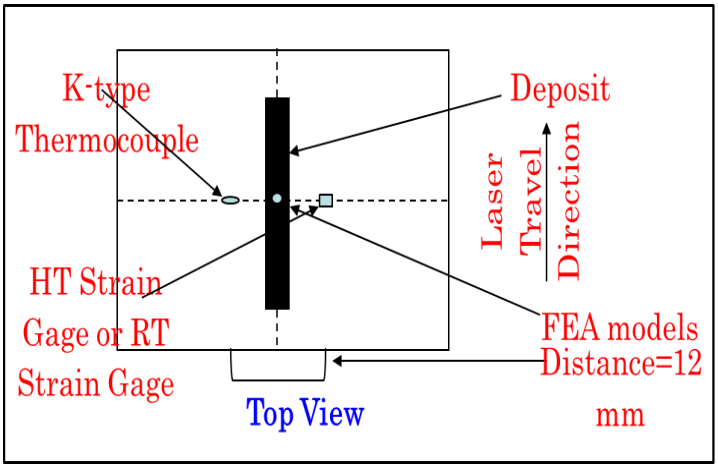

Figure 3.6 Experimental set-up for the thin wall deposition process to validate the thermal and stress models. The strain gages were placed on the substrate 6 mm away from the centerline of clads (reference position). Note: not drawn to the scale.

Table 3.3 Modeled and experimental deposit heights.

Set no.	Experimental Conditions	Materials	Clad Ht. assumed in FEA model	Clad Ht. measured
1	P: 1000 W. FR: 12 g/min TS: 4.23 mm/s No. of Layers: 15 TD: uni-directional	SS 316L on SS 316L	15 mm for 15 layers	10 mm for 15 layers
2	P: 1000 W. FR: 12 g/min TS: 4.23 mm/s No. of Layers: 15 TD: Bi-directional	SS 316L on SS 316L	15 mm for 15 layers	9 mm for 15 layers

The data from thermal and stress models presented in the thesis were obtained at the centerline of the clad, as shown in Fig. 3.6. Similarly, the data obtained from thermocouple and strain gages were recorded at 6 mm away from the centerline of the clad. Both the thermal and stress models were validated experimentally under similar deposition conditions, as shown in Table 3.4. The SS316L and Inconel 625 clads were built with no cover gas. The powder yield was close to 100% for these clads. In the uni-directional tool path the start and end position of the laser is the same and in bi-directional tool path they are different for each pass. All the samples were fabricated with a powder mesh size of -100/+325 (particle sizes between 45 and 150 μm) and compositions of powder are listed in Table 3.2. The dimensions of the substrate are 50.8x50.8x12.7 mm. Table 3.5 shows that the measured clad heights are smaller than the heights assumed in the model. In the model shrinkage or distortion of the thin wall was

not taken into account which is commonly seen when performing experiments. Hence, there are variations in the clad heights between model and experiments.

4. RESULTS

Some of the early experimentation involved multilayer deposition (cladding) of 100% Inconel 625 onto a Ti6Al4V workpiece under different process conditions. All deposits showed severe cracking that originated at the top of the deposit with crack lengths corresponding to the entire clad height, an example shown in Fig. 4.1. The crack openings became smaller at the interface between the deposit and workpiece. The presence of these cracks showed a need for compositionally grading the two alloys to minimize the cracking in the layers and also the interfacial stresses. The compositional grading of two or more alloys can be easily attempted using laser processes. Some of the key parameters that play an important role in deposition processes are laser power, travel speed, powder feed rate, Z- height control, etc. And in order to understand the effect of laser process parameters, finite element modeling (FEA) was performed in the current research work to understand the thermal and mechanical stress fields that originate during a multilayer deposition. The FEA modelling was performed on simple materials systems that would not show any solid-state phase transformations during or after laser processing. 100% Inconel 625 on SS316L and 100% SS316L on SS316L were chosen for this reason, as well as the easy availability of thermo-mechanical data for these systems.

Based on the results of the FEA, the parameters that were chosen to be used were the ones that would result in lower stresses during deposition; and hence, enable Ti6Al4V/Inconel 625 compositionally grading from 100% of one system to 100% of other. The research mainly focused on understanding the effect of grading (and process

parameters) on microstructures and how to minimize cracks in a graded structure. Only partial success was achieved because of various experimental challenges encountered during the course of this (as discussed in Section 3) research work. But in this thesis some insightful information on the phase transformations is provided. There are four sections in this Section. Section 4.1 covers results on cladding 100% Inconel 625 on Ti6Al4V workpiece. Section 4.2 covers the results on thermo-mechanical modeling using ABAQUS^{TM} and the validation of the FEA results by experiments conducted on simple material systems. Sections 4.3 and 4.4 include results on functionally graded Ti6Al4V/Inconel 625 thin wall structures and thermodynamic modeling using FACTSAGE (v6.1). In these sections a detailed study on the effect of laser process parameters on the composition and microstructure of graded Ti6Al4V/Inconel 625 with different grading schemes is provided. The section also covers the use of thermodynamic modeling on predicting equilibrium microstructure evolution along the graded direction.

4.1 EFFECT OF PROCESS PARAMETERS ON INCONEL 625 CLADS

4.1.1. Microstructure and Composition. Figure 4.1 on the left shows the optical images of Inconel 625 clads deposited on Ti6Al4V workpieces. It is typical to see stress induced cracks near the interface between the workpiece and clad or in clads for dissimilar systems when cooled down to room temperature. In Figure 4.1, the crack lengths correspond to the entire clad height. The macroscopic cracking observed in all the deposits can be attributed to certain factors such as hot tearing during solidification, thermo-physical properties mismatch between workpiece and clad, intermetallic phases (IMPs) formation at the interface and in the clad zone due to mixing of Ti and Ni, and

residual stresses in the final part. The coefficient of thermal expansion (CTE) at room temperature of Inconel 625 is higher than Ti6Al4V. Initially thermal strains during the melting process are low or zero, but the strains begin to increase as the solidification progresses. Because of the differences in CTE, the opposing stresses in the clad (tensile stresses) and bulk of workpiece (compressive stresses) could have led to macroscopic cracks upon cooling, as shown in the figure 4.1 (a). When preheating temperatures of 540oC were used during the LMD process fewer cracks with smaller crack openings were observed, as shown in the Figure 4.1 (b).

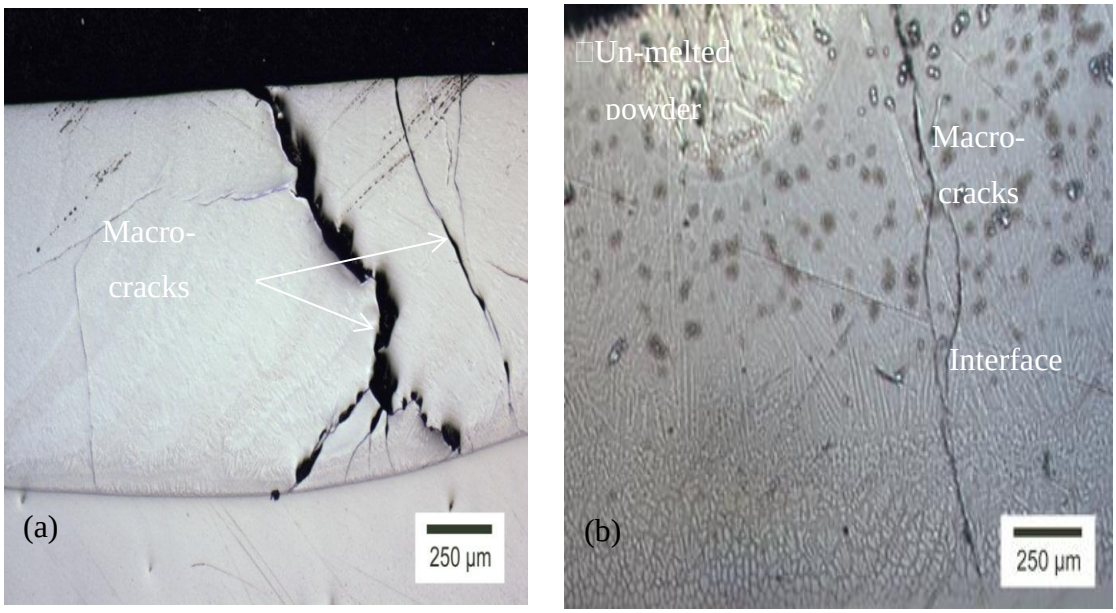

Figure 4.1 Inconel 625 clad deposited on to Ti6Al4V workpiece at 1000 W (a) un-etched sample with cracks, and (b) Deposit showing cracks using preheating of 540^{o}C during LMD process.

While determining a suitable preheating temperature to minimize the cracks in a clad, it is necessary to know what kind of solid-state phase transformations might occur during cooling process. The Ti-Ni has two types of melting reactions: congruent (TiNi, $TiNi_3$) and incongruent (Ti_2Ni). These three compounds form directly from the melt and

are stable at room temperature. But the liquid must have these specific alloy compositions to cause their formation. For the Ti-Ni system higher preheat temperatures (> 540^{o}C) may not stop the precipitation of Ti_2Ni, TiNi or Ti_3Ni phases. But it may help minimize the sudden change in stress levels and hence reduce the occurrence of cracks in clads. Limited by the equipment's operating temperature (only 540^{o}C) the pre-heating experiments at higher temperatures were not carried out. The existing process also required longer preheating times to achieve equilibrium in the Ti6Al4V workpiece before the start of LMD process.

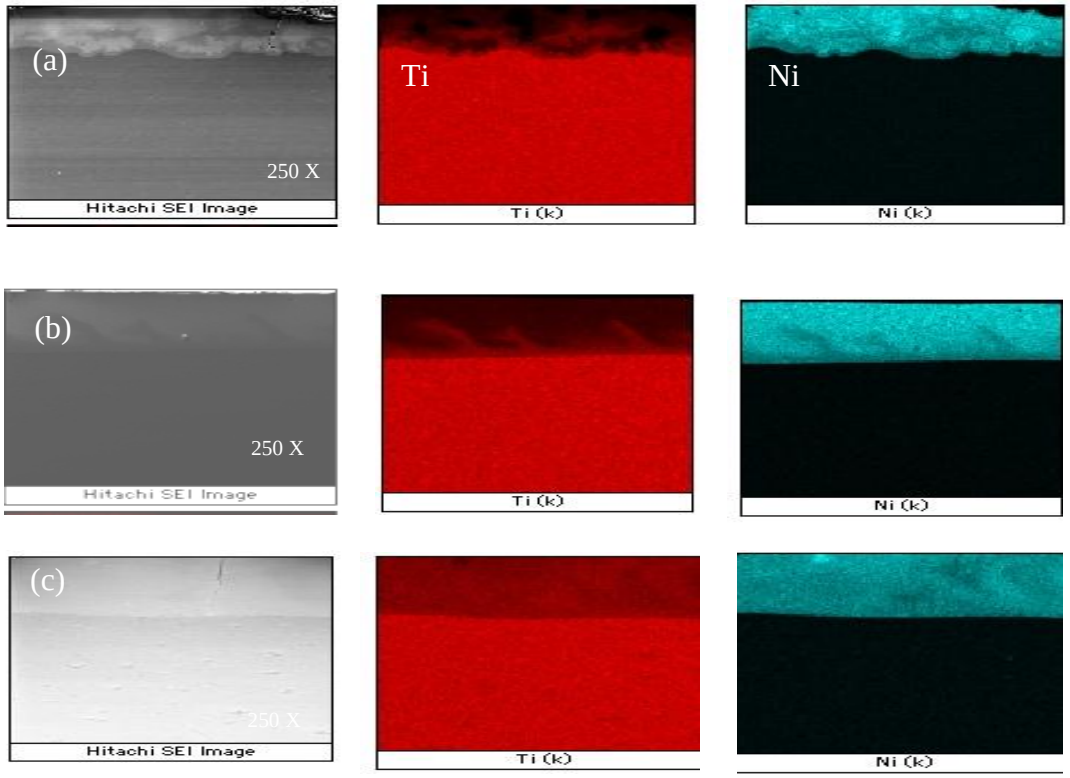

Figure 4.2 EDS Compositional maps of Inconel 625 clad on Ti6Al4V under different process parameters showing the segregation in the clad zone: (a) 300 W, 4.23 mm/s, (b) 600 W, 4.23 mm/s, and (c) 1000 W, 4.23 mm/s.

Table 4.1 EDS Compositional data of clads processed under different laser conditions.

No.	Power, W	Trvl. Speed, mm/s	Fe	Al	Mo	V	Cr	Ni	Ti
1	300	4.23	1.06	0.80	3.06	0.67	13.02	57.19	24.47
2	600	4.23	1.80	0.56	2.62	1.48	11.34	51.59	30.62
3	600	8.47	2.63	1.52	1.92	2.35	6.49	30.42	54.69
4	1000	4.23	1.29	1.17	2.28	1.97	8.54	36.67	48.07
5	1000	8.47	2.03	1.52	1.92	2.35	6.49	30.42	54.68
6	1000	12.7	1.61	2.06	1.84	2.46	5.84	26.66	59.51
7	1000	16.9	1.29	1.55	2.08	2.26	7.06	32.99	52.76

Figure 4.2 shows the compositional maps of the deposits cross-sectioned along the laser travel direction. Table 4.1 shows the average compositional data of clads under various processing conditions. The segregation in the clad layer shows that though 'mixing' was initiated, it remained incomplete during the deposition process at lower laser power levels. From the compositional data, at higher powers more dilution of the clad occurred with the migration of Ti from the workpiece into the clad. But more Ti in the clad with increasing travel speed was apparent only at low power. The 'Geometric dilution' *D*- is similar to 'mathematical dilution' described in Equation [2.1] and [2.3] in Section 2. The 'Geometric dilution' *D* is defined as the ratio between the melted workpiece and deposited powder which is given by the equation

$$D = \frac{A_s}{(A_s + A_p)} \qquad [4.1]$$

Where A_s is the cross-sectional area of melted workpiece and A_p is the cross-sectional area of deposited powder. The amount of dilution of Ti in Inconel 625 clads is examined at different processing conditions. At constant power and powder feed rate dilution increased with the increasing travel speed and saturates at higher travel speed, as shown

in Fig. 4.3 (a). This trend was most apparent at 600 W. Also, at a constant travel speed and powder feed rate the dilution increased with the increasing laser power as shown in Figure 4.2 and 4.3 (a). The experimental data presented here agrees to the relationship identified between Dilution and laser power, travel speed using a statistical model described in Equation [2.3].

There are three dimensionless process efficiencies that can affect the heat flow and solidification behavior in the Laser Engineered Net Shaping (LENS)^{TM} process. They are the laser energy transfer efficiency, melting efficiency and deposition efficiency already described in Section 2. The experimental and mathematical modeling studies conducted by Dupont et al [22] showed that average energy transfer efficiency is only 40 pct. For the laser deposition process to be efficient, the total energy transferred from the laser source to the workpiece must possess enough energy to melt the underlying workpiece and the incoming powder flux. More than half of the laser beam energy is never transferred to the workpiece but is reflected by the meltpool and powder particles. The research also showed that the powder mass flow rate and the type of powder delivered to the pool have only a small effect on energy transfer efficiency. They observed that the type of workpiece material and to some extent the surface quality contributed most to laser beam absorption.

The melting efficiency is defined as the ratio of energy required for melting ($A_p \Delta H_m$, per unit length) to actual absorbed energy ($h_a \frac{P}{S}$, per unit length) [22].

$$h_m = \frac{Ch}{Ry} = \frac{SA_p \Delta H_m}{h_a P} \qquad [4.2]$$

$$ch = \frac{S^2 A_p}{\alpha^2} \quad [4.3]$$

$$Ry = \frac{h_a PS}{\alpha^2 \Delta H_m} \quad [4.4]$$

where S is the heat-source travel speed, A_p is the total deposit cross-section, ΔH_m is the melting enthalpy, h_a is the laser energy efficiency (40 pct; which is suggested from literature [22], α is the thermal diffusivity of the workpiece, and P is the laser power. The melting efficiency is strongly affected by processing parameters and the material thermo-physical properties. The equations in the literature were primarily derived for single pass clads; except for the Inconel 625 cladding which is a single pass all of the experiments in this thesis are on multilayer deposition process. For materials with dissimilar thermo-physical properties [Inconel 625 (2.67 J/mm^3) onto Ti6Al4V (13 J/mm^3) workpiece], an average value of melting enthalpy between the two was used, 7.8 J/mm^3. Using the equation [4.2] the melting efficiency was calculated for various process parameters. A plot of Ch versus Ry as shown in Fig. 4.3 (b) gave the following relation.

$$Ch = 0.16Ry - 0.8524 \quad [4.5]$$

Since the ratio of Ch/Ry yields the melting efficiency, Equation [4.5] can be manipulated to yield the following:

$$h_m = 0.16 - \frac{0.8524}{R_y} \quad [4.6]$$

The following equation for melting efficiency is reported in the literature [22] and is used with current data from thesis to compare to Equation [4.5].

$$h_m = 0.31 - \frac{0.47}{R_y} \quad [4.7]$$

Equation 4.6 or 4.7 can be used to estimate melting efficiency when processing parameters and material thermophysical data are known. In theory, the melting efficiency increases with the increasing rate of energy (i.e. laser input power) delivered to the workpiece [22]. When energy is distributed to a localized region at a much faster rate (i.e. higher laser power and/or travel speed), there is effectively less time available for the energy to be transported away from the molten region by thermal conduction to the surrounding material. Therefore, more total energy is used to create and maintain the molten weld pool. Therefore, melting efficiency increases as well. In Figure 4.3(c) melting efficiency is plotted as a function of laser input power at a constant powder mass flow rate (0.083 g/s). The results show that the calculated melting efficiency using Equation [4.6] tends to stay constant at 1000 W but shows a drop at 600 W for higher travel speeds. At a combination of higher travel speeds and higher laser power, a larger fraction of the total energy is retained to melt the underlying workpiece. If the travel speed becomes too high, eventually there is less time available for transferring energy to the workpiece and hence melting efficiency will decrease. The melting efficiency computed from Equation [4.7] derived from literature shows to saturate with increasing travel speeds at 600 W. Overall a combination of higher power (1000 W) and higher travel speed (15 mm/s) showed higher melting efficiency.

As already described earlier in Equation [2.1] the dilution is also affected by melting efficiency. The process parameters that affect dilution and melting efficiency are laser power and travel speed. For example, at a constant powder feed rate, more of the incoming laser power is available for melting the underlying substrate and increasing dilution. One of the differences between single and multipass will be that dilution in clads

by workpiece and in/between layers will increase with increasing number of passes. There are no models available thus far in the literature to calculate dilution with increasing number of passes.

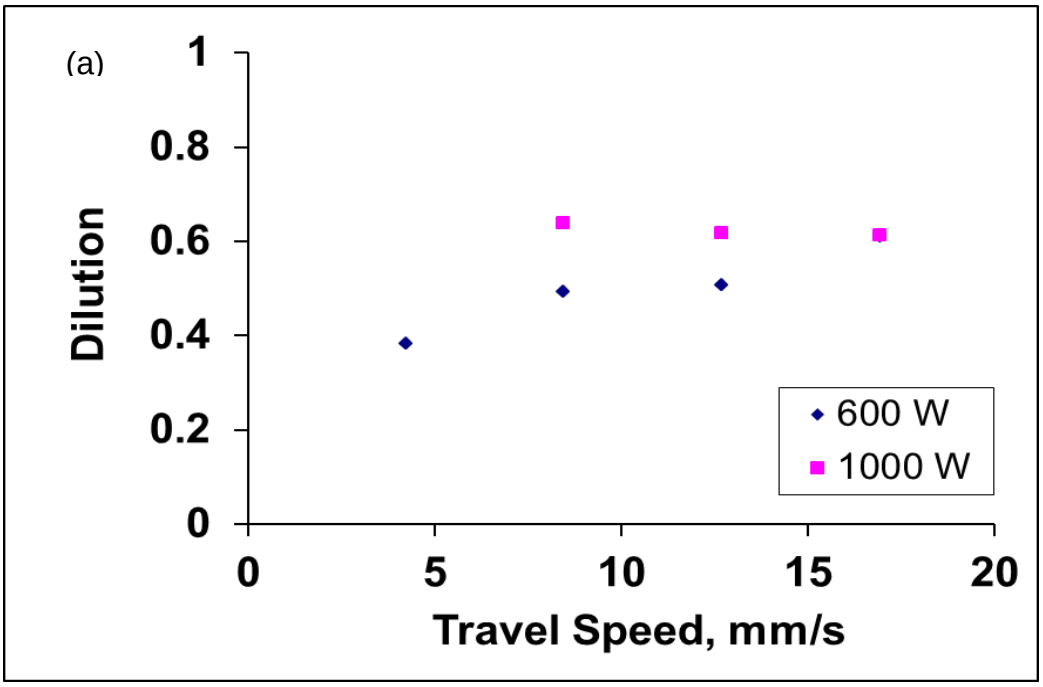

Figure 4.3 (a) Effect of dilution of workpiece and clad on laser process parameters, (b) Plot of Ch versus Ry, (c) melting efficiency of the workpiece and incoming flux at varying laser speed.

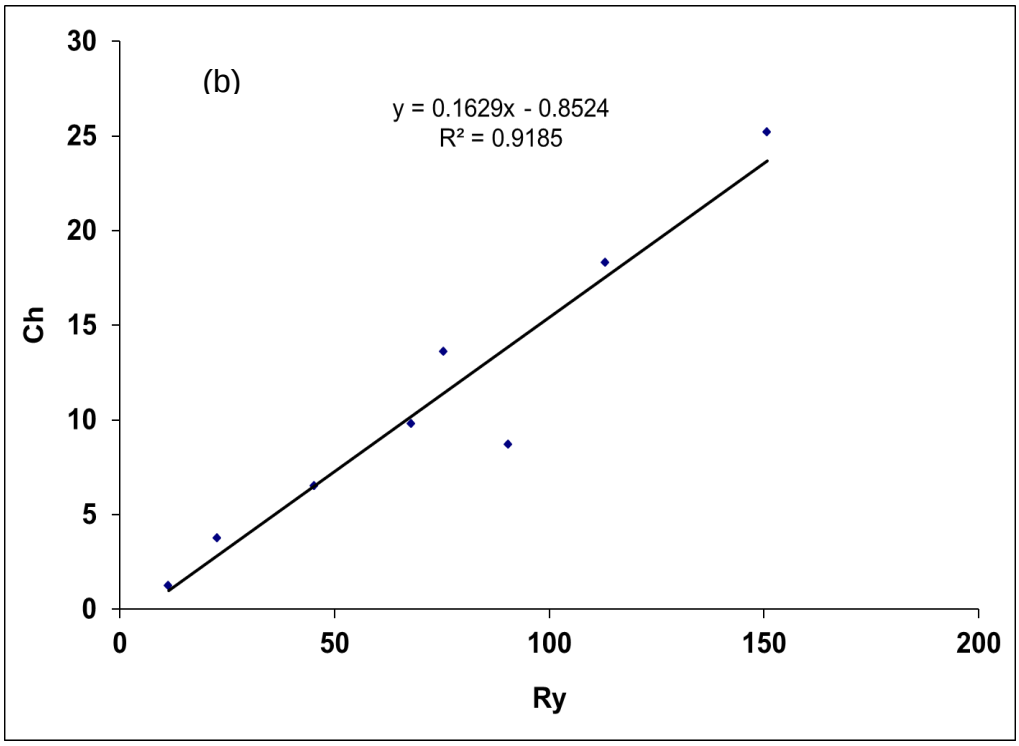

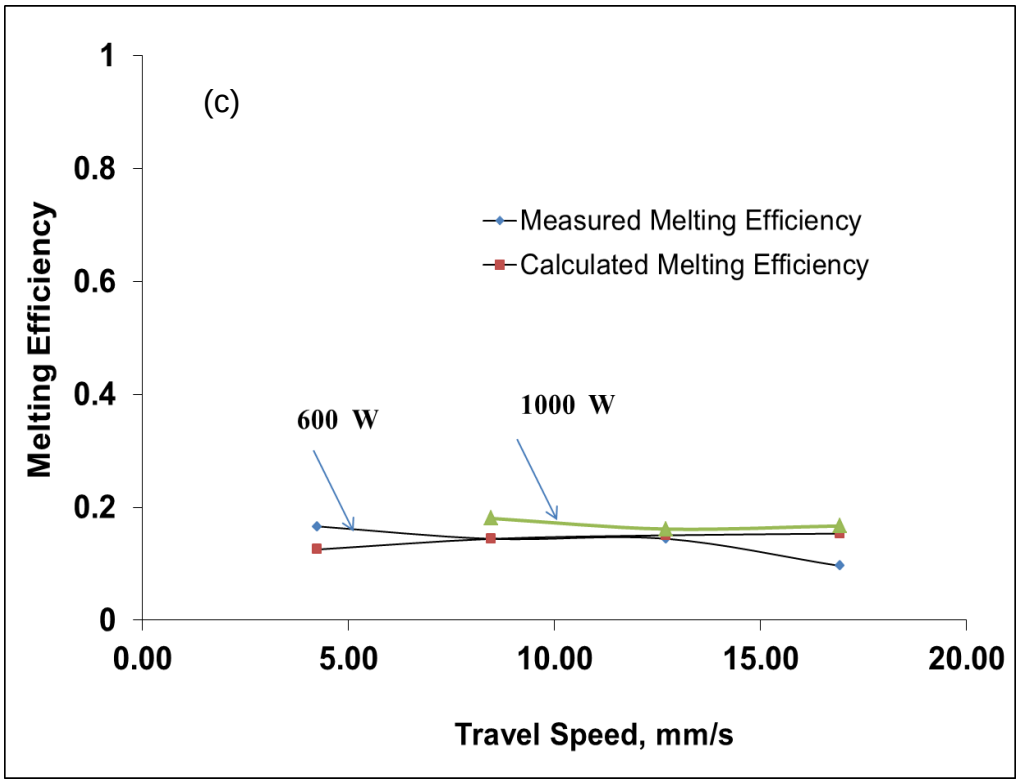

Figure 4.3 (a) Effect of dilution of workpiece and clad on laser process parameters, (b) Plot of melting efficiency versus Ry, (c) melting efficiency of the workpiece and incoming flux at varying laser speed (Cont.).

4.1.2. Mechanical-Microhardness. Figure 4.4 shows a plot of hardness as a function of depth for Inconel-625 clad on a Ti6Al4V workpiece. The hardness line profile can be divided into three distinct regions: the clad-region, and the dilution and the workpiece region. The hardness of the clad is 11 GPa and is 3 times more than the workpiece. The cracks shown in Fig. 4.1 are a result of the sharp transition in both the metallurgical (dilution by Ti, possible formation intermetallic phases (IMPs) at the interface and clad) and mechanical properties across the interface.

In summary the data on clads shows a lack in understanding of the effect of process parameters on both metallurgical and mechanical (i.e. residual strains) properties in this complex structure. A significant amount of cracking was seen in all clads under different processing conditions. The Inconel 625 clads were diluted with high amounts of Ti. This shows a need for grading Ti6Al4V and Inconel 625 together in order to minimize the cracking in clads, and sharp transition of compositional and mechanical properties at the interface; and also minimize dilution in Inconel 625 layers by Ti. The following items have been identified as a pathway to gain understanding and achieve the objective of successfully grading Ti6Al4V and Inconel 625 together:

(1) Perform Finite Element Analysis (FEA) on clads to understand the effect of process parameters on thermal and mechanical strains. (2) Understanding and tailoring the microstructure of compositionally graded Inconel 625 to Ti6A4V by performing a series of experiments. 3D thermo-mechanical models can help understand the effect of process parameters such as laser power, travel speed, tool path direction on peak temperatures, cooling rates, remelted layer depths and residual strains for the LMD process. For the thermo-mechanical models the multilayer deposition of SS316L and Inconel 625 on

SS316L workpiece will be studied. The above material-systems are simple to handle in ABAQUS™ as "liquid" and "solid" are the only two phases that are formed during melting and cooling. This thesis will not cover the topic of modeling on functional grading of Ti6Al4V and Inconel 625 mainly because of unavailability of thermo-mechanical data for this complex system. The rule of mixtures has been applied to generate thermal and mechanical inputs for the two material systems used by Borjesson and Lindgren[18], viz.$n = n_1\ v_1\ +\ n_2\ v_2$; $v_1\ +\ v_2$=1; where v_1, v_2 were volume fractions and n_1, n_2 were thermal properties of the two materials at the given temperature. But the model is not very reliable as it will not take into account the effect of phase transformations in the liquid and solid state on the instantaneous strains and final residual strains that will develop in a part. As we already know, Ti6A4V and Inconel 625 when mixed together in different proportions form a multitude of metallurgical compounds and will also contribute to stresses. ABAQUS™ (V 10.1) modeling software is not designed to handle or incorporate microstructural phase transformations of this level of complexity. Performing thermo-mechanical modeling without incorporating the metallurgical transformations will not provide any useful information.

As mentioned above in the second bullet, the microstructures can be tailored very well by using different compositions and/or process parameters. In this thesis both routes were investigated. Each route showed certain degree of feasibility, but the process parameters to obtain a crack-free Inconel 625 deposit on Ti6Al4V were not optimized in the research work. This is because of certain experimental challenges that were encountered during this research and have been discussed in Section 2.

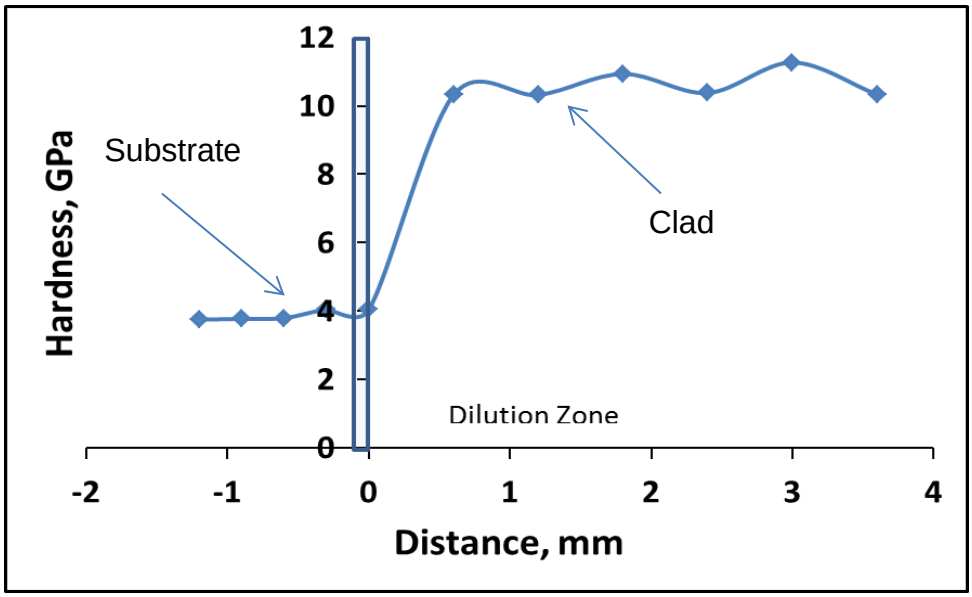

Figure 4.4 Hardness plotted as a function of depth of Inconel 625 clad on Ti6Al4V workpiece.

4.2 FEA MODELING AND EXPERIMENTAL VALIDATION ON CLADS

An experimental and numerical investigation of the effects of the laser process parameters on the residual strain distribution has been performed previously, but residual stress distributions in the Laser Engineered Net Shaping (LENS^{TM}) process have only been deduced from the measured strains (obtained through X-ray diffraction or neutron diffraction) and then using elastic constants to calculate stresses. Moreover, to quantify these stresses within a clad layer has not always being straightforward [45, 49, 51, 52, 106]. Also, going from strain to stress using elastic constants is not a reliable procedure since the elastic constants may not be known accurately.

In this research work, a 3D thermo-mechanical finite element model was developed to simulate multilayer deposition of SS316L and Inconel 625 clads on stainless steel workpieces. The development of the model was carried out using the ABAQUS^{TM}

(V 10.1) software package. The model has been used to estimate the temperature distribution, peak temperatures, cooling rates and remelted layer depths as a function of process parameters, such as laser power and traverse velocity during actual fabrication. The thermal behavior during the deposition process was experimentally measured in-situ using K-type thermocouples. The results from the model heat transfer analysis were used as inputs to compute residual strains in multilayer clads and workpiece. Some of the stress models were qualitatively compared with experiments using High Temperature Fe-Cr-Al strain gages. The data from numerical modeling was used to understand the microstructure, phase and composition in clads.

4.2.1. Governing Equations and Boundary Conditions. A nonlinear transient thermo-mechanical model was developed for the simulation of the laser deposition process, using ABAQUS^{TM} (V 10.1). In the model, the thermal and mechanical fields were sequentially coupled. The transient thermal analysis was the first step during which the temperature field was calculated and saved for every step and these results were then used as thermal inputs for the mechanical analysis. The addition of powder particles in the LMD process required continuous updates in the solution geometry and was achieved by successive discrete addition of a new set of elements into the computational domain using an element activation feature. The generic 3D heat conduction governing equation Eq. (4.7) was solved to obtain the transient thermal distribution within the part:

$$\frac{\partial}{\partial x}\left(k\frac{\partial T}{\partial x}\right)+\frac{\partial}{\partial y}\left(k\frac{\partial T}{\partial y}\right)+\frac{\partial}{\partial z}\left(k\frac{\partial T}{\partial z}\right)=pc_p\left(\frac{\partial T}{\partial t}\right) \qquad [4.7]$$

where ρ, C_p and *k* refer respectively to density, specific heat and thermal conductivity; T and t refer to temperature and time variables respectively. The term on the right side of

Eq. [3.6] depicts the thermal energy at a point in the clad while the first three terms on the left side of the equation refer to the conductive heat transfer in the x, y and z directions respectively. To model the deposition process the following assumptions were made:

- An initial temperature of 300 K was assumed for the entire work piece. Both the work piece and the coordinate mesh were fixed. The laser moved in positive and negative x- direction with a constant speed v; and for every new layer that got deposited the laser moved in positive z- direction.
- The displacements of the bottom edge nodes in X-; Y-; and Z- directions of the workpiece were all restricted to zero to prevent rigid body motion.
- The model takes into account the effects of conduction, convection and radiation during LMD processing.
- The following boundary conditions were applied to the deposit wall and top of the workpiece:

$$q = -h(T-T_0) \quad [4.8]$$

$$q = \sigma \in (T^4 - T_0^4) \quad [4.9]$$

Where q is heat flux per unit area, h is the convective heat transfer coefficient, $\in$ is emissivity, σ is the Stephan-Boltzmann constant and T_0 is ambient temperature.

- All thermo-physical properties for Inconel 625, and SS316L were considered to be temperature-dependent and found in the literature [64].
- No phase transformation phenomena were considered in the current model. The model does not take into account thermal shrinkage, distortion and poor powder yield that were observed while conducting experiments.

The structure for clads in the modeling was built by cladding 15 single layer tracks on top of each other with a length of 25.4 mm, a thickness of 1 mm, and a width of 2.5 mm. The layer thickness in the FEA model as mentioned was fixed to 1 mm and the powder feed rate in the experimental conditions was adjusted to attain a 1mm thick layer during each pass. This made a deposit wall nominally of 15-mm tall in the FEA model. The wall was fabricated on the surface of a workpiece that was 12.7-mm thick, 50.8-mm wide, and 50.8-mm long. To simulate mass addition (powder deposition), the "Birth and Death" feature in ABAQUS^{TM} (V 10.1) was used per pass. Initially all elements in the track were "killed", a process which multiplies the heat capacity matrix or the stiffness matrix of these elements by a very small value, usually on the order of 10^{-6}, so they virtually disappear from the simulation. The first born sets of element were positioned onto the workpiece with a set of initial boundary conditions. Of the subsequent elements, the model used the results from the previous step as the initial condition for the birth of each new set of elements. In the modeling each clad layer was divided into 8 small slices containing a set of elements of 3.175 mm long.

Finally the moving heat source was simulated by applying a concentrated surface heat flux on the model for a time equal to the distance between model nodes of the slice divided by the laser velocity. The laser power efficiency used in the deposition model was 40 per cent which was derived from studies conducted by Dupont [22]. The powder deposition efficiency was assumed to be 100%. A convective heat transfer coefficient was applied to the external surfaces of the deposit wall with a value of 30 $Wm^{-2}\ K^{-1}$ and a fluid temperature of 300 K, whereas for the end faces of the workpiece-plate a coefficient of 300 $Wm^{-2}\ K^{-1}$ was assumed to account for faster cooling by the fixture-

vice. During the laser cladding experiments a fixture-vice was used to hold the workpieces in place. A radiation boundary condition was applied to the entire deposit wall and the emissivity was assigned a value of 0.4 referred from literature [22]. The workpiece for the entire thermo-mechanical model was meshed using a quadratic reduced-integration hexahedral element. The mechanical analysis was a simple static analysis. In the model the bottom edge nodes of the workpiece were fixed to prevent rigid body motion. The total strain ε is composed of elastic strain ε_e, conventional plastic strain ε_p, plastic strain from transformation plasticity ε_{tp}, and thermal strain ε_t:

$$\varepsilon=\varepsilon_e+\varepsilon_p+\varepsilon_{tp}+\varepsilon_t \qquad [4.10]$$

Plastic strain from transformation induced plasticity was not considered in the current model as there are no known phase transformations to occur in SS316L or Inconel 625 in solid state. Hooke's Law applies to the elastic strain while the combination of yield condition, yield law and hardening law applies to the plastic strain. The yield condition used was von Mises distortion energy hypothesis. A rate independent isotropic hardening model was used because of the simplicity of the algebraic equations associated with integrating the model. All the equations for above theories are presented earlier in Section 3. In the above analyses, the failure criterion was not implemented. As a result the analyses do not predict the cracking tendency, but only the stress magnitudes.

4.2.2 Thermal and Stress Models and Experimental Validation. Figure 4.5 shows a simulated temperature distribution along the clad towards the end of deposition and with the conditions specified in the caption. The temperature of each nodal point within the solid was calculated as a function of time. There are significant temperature

gradients along the height of the clad. The model predicts high temperatures in the top most layers. The temperatures shown here have exceeded the melting point of SS316L (1600 K). The upper layers retain the heat from the laser for a longer time as they are not in good thermal contact with the workpiece, which acts as a heat sink [105]. And the bottom of the clad always cooled faster due to conduction of heat to the workpiece. The fluid flow and solidification of material in the melt pool cannot be directly considered as the coupled problem between solid and liquid is not included in the ABAQUS^{TM} (V 10.1) software at present. If the effect of the fluid flow is neglected, the highest temperature in the melt pool predicted by FEA thermal model can be very high - sometimes it is over 3273 K [49, 105]. Fig.4.6 shows result from the simulation of the peak temperature distribution calculated at the centerline of the clad for the conditions given in the captions. More figures can be found in Appendix A. During multi-layer cladding, initially the workpiece serves as the main heat sink. As the clad height increases its cooling occurs through the deposit layers resulting in a decrease in cooling rate. After certain number of passes a quasi-steady state condition can exist between the clad and the surroundings and the layers will eventually take much longer to cool down. The models showed peak temperatures reaching as high as 3500-4000 K, which is 1000-1500 K more than the melting point of the stainless steel. In the model, by the end of deposition of 15th layer all the layer remelted for the conditions described in the caption.

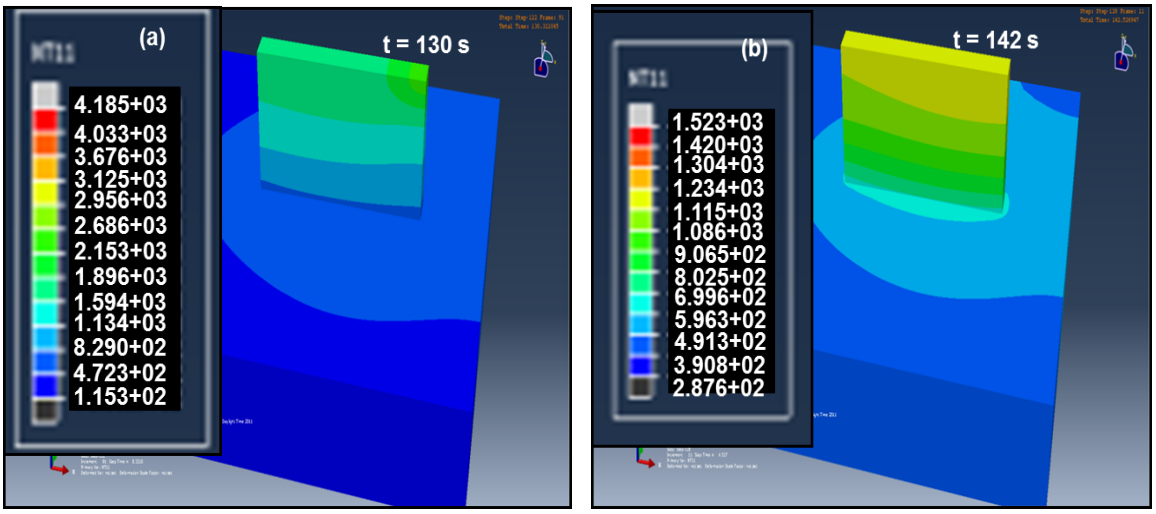

Figure 4.5 Transient temperature history of thin wall at the end of deposition @ 1000 W, 4.23 mm/s, tool path= Bi-directional; Materials: SS316L on SS316L workpiece: (a) t = 130 s, (b) t = 142 s.

Interestingly, the peak temperatures predicted in the layers were lower at a combination of low temperature and higher travel speeds or for uni-directional laser tool path. Wang et.al [45] from their thermal model predicted a similar behavior and showed that the peak temperatures calculated during thin wall deposition were dependent on laser travel velocity and laser power. The addition of more layers and subsequent laser passes alters the peak temperature distribution in the preceding layers, resulting in secondary peaks in the temperature histories which can again go beyond the melting point of the material. For example the layer-1 in Fig 4.6 at the end of deposition cool down to 500 K, but as layer-2 is deposited on the top the layer-1 again reheats to temperatures slightly above the melting point of the material. As more and more layers are deposited on the top, even if most of the layers do not remelt the temperatures in the layers can still be above 800 K. For the upper layers, the effect of substrate is reduced and the accumulation of thermal energy at the end of each cycle causes the primary and secondary peak

temperatures to be somewhat higher than that at the end of its previous cycle. These thermal models are useful in situations where it is very hard to monitor the peak temperatures attained by each layer during deposition. This is because even the high-end thermocouples or temperature sensors that are currently available in the market are not designed to withstand such a high temperatures during the thermal processes.

The temperature history of the workpiece during the multilayered deposition was measured both experimentally and recorded numerically at the "reference" position. A more detailed description of the location of the reference position on the workpiece, different tool path directions, etc., is already described previously in Section 2. In short the reference position is 6 mm away from the centerline of clad. Figure 4.7 shows a typical example of a temperature profile predicted by the FEA model on the workpiece using the conditions defined in the caption. There is an initial10 second delay in the simulation model due to the user defined input condition and has no impact on the thermal output from FEA. The model predicts that the workpiece retains more heat with increasing the laser power or number of clad layers represented by the number of peaks in the Figs. 4.7a, b and c. The simulation and experimental results agree very well with each other. Interestingly, the workpiece size is initially a determining factor in effective heat extraction. A faster heat extraction from, and more effective cooling of the deposited material, can be achieved by using larger workpiece. Conversely, a small workpiece will heat up rapidly, reducing its heat extraction capability. Costa et al.[52] predicted from their FEA model that decreasing the workpiece size caused the average temperature to increase in the deposit. As a result, the material in the upper layers of their part could not cool down below the M_s temperature and the microstructure remained fully austenitic in

their study. As the amount of residual heat increases it can potentially initiate solid-state transformations to occur in the workpiece and within the deposit which can be detrimental to the overall structure.

The thermal model has also been used to understand the effect of laser tool path on temperature distribution in the workpiece at the reference position, as shown in Fig. 4.7 (b and c). The experimental results show a dependency of the tool path direction on the heat transfer rate ($\frac{\partial T}{\partial t}$) and the fluctuations in temperature keep increasing with layers; whereas the simulation reaches a steady state by the end of deposition of the 7^{th} clad layer. In other words, the amount of heat extraction in thermal model is the same whether we add 10 layers or 20 layers, as it is happening through a narrow region of thin wall structure than the bulk of substrate. The model showed smaller temperature gradients in the workpiece for uni-directional laser tool path. In the uni-directional tool path the start and end position of the laser beam does not change. The low temperature gradients in the uni-directional tool path are primarily because the workpiece had sufficient time to cool between the layers when compared to the bi-directional tool path where the laser is rastering back and forth. There is a good agreement between the experiments and FEA model for uni-directional tool path; whereas small temperature gradients continued to exist in the workpiece for the bi-directional tool path. Overall, in both the cases the heat accumulation in the workpiece increased with increasing number of clad layers.

The output from the thermal model was only peak temperatures at each node. Cooling rates of each layer in the current FEA model were computed from the time difference when the nodes in the center region of the clad were seen at the last liquidus temperature and next solidus temperature. Calculations for nodes in the center of the thin

wall were computed using the following expression after the laser beam has moved away from that node:

$$\frac{\partial T}{\partial t} = \frac{|T_l - T_s|}{|t_i - t_s|} \quad [4.11]$$

Where $\frac{\partial T}{\partial t}$ is the cooling rate, (T_l -T_s) is the difference between the liquidus and solidus temperatures and *(t_l-t_s)* is the time interval between recording T_l and T_s. The calculated results of the FEA model are shown in Fig. 4.8. The thermal model further reinstates the earlier discussion that cooling rates in the thin wall are affected by the number of clad layers, laser tool path direction, processing parameters and thermo-physical properties of the materials. The predicted cooling rates ranged anywhere from 473 to 6000 K/s. In the case of Inconel 625 clad on an SS316L workpiece (Fig. 4.8(b)) the cooling rate was initially high in the first 1 or 2 layers and decreased thereafter. This is because the thermal conductivity of the stainless steel 316L workpiece is slightly higher than Inconel 625.

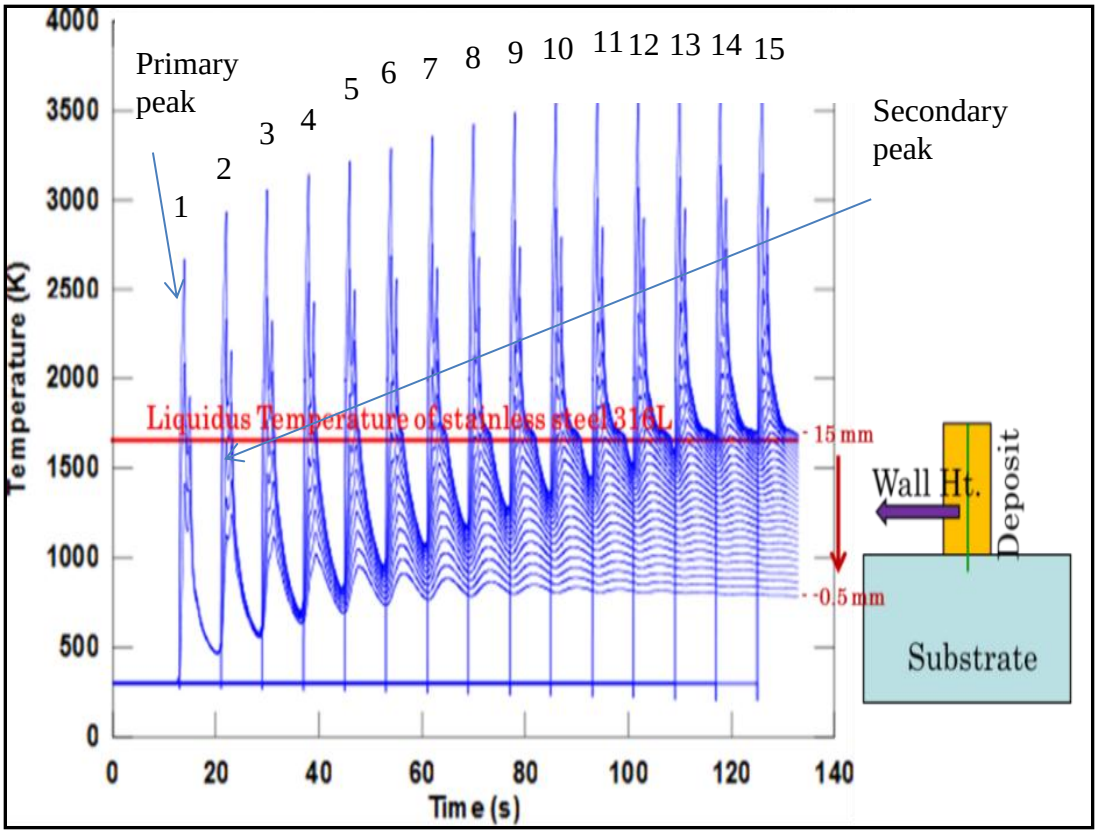

Figure 4.6 Peak temperature history predicted for each layer of thin wall at the end of deposition at the reference position @ 1000 W, 4.23 mm/s, tool path= Bi-directional; Materials: SS316L on SS316L workpiece.

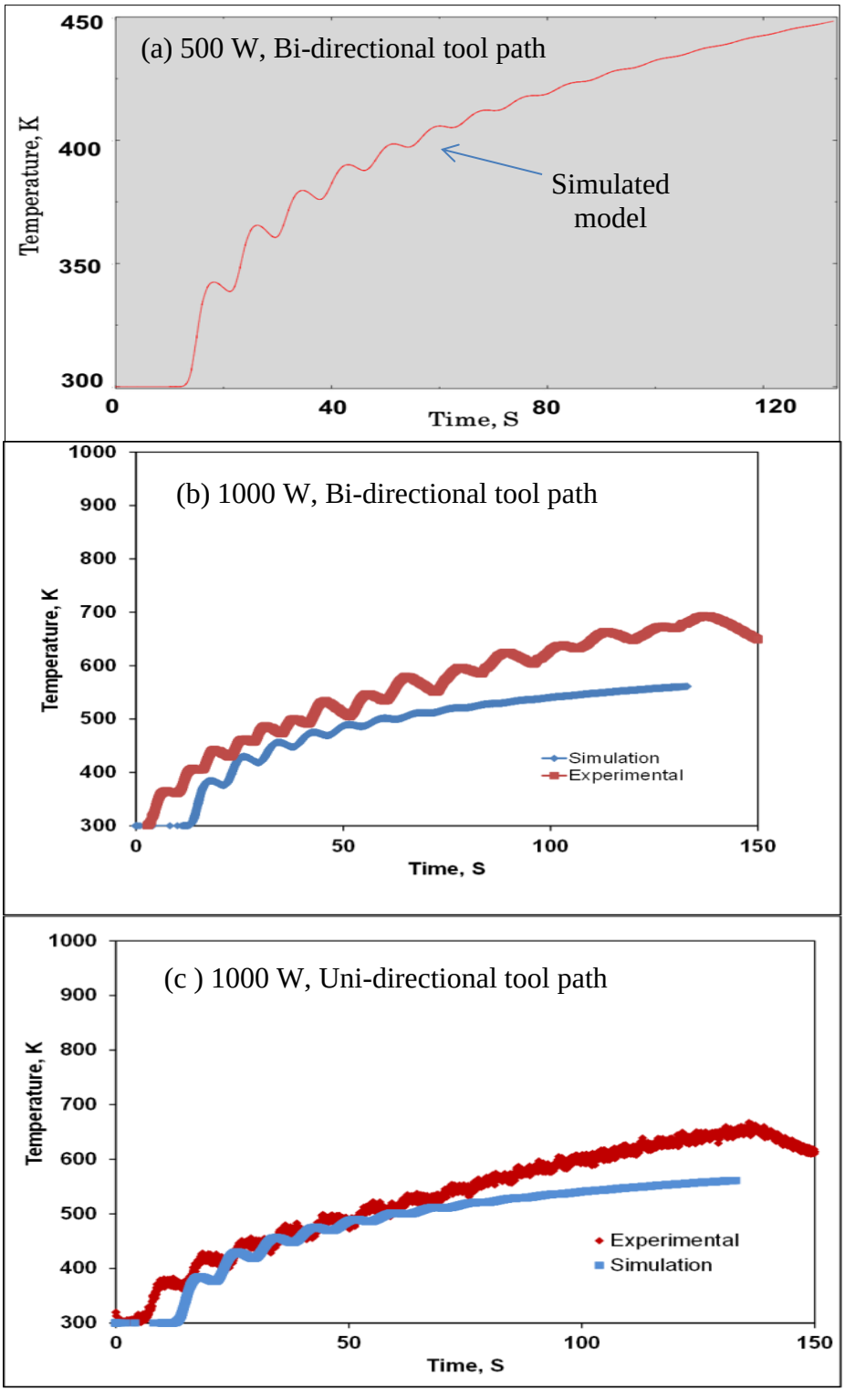

Figure 4.7 Predicted at the reference position which is 6 mm away from centerline of clads (a) FEA thermal model 500 W, 4.23 mm/s (b) & (c) Simulation and experimental comparison1000 W, 4.23 mm/s, 12 g/min; 15 layers Materials: SS316L on SS316L workpiece.

In literature [51] the computed values of cooling rates were greater than 15,000 K/s at locations that had experienced the laser beam. However the cooling rates decreased with the increasing peak temperature. Another research group [48] experimentally measured the temperature and cooling rate around the melt pool by thermal imaging technology. The measured cooling rates ranged anywhere from 473 to 6273 K/s [48] and agrees very well with FEA predictions made in the current research work.

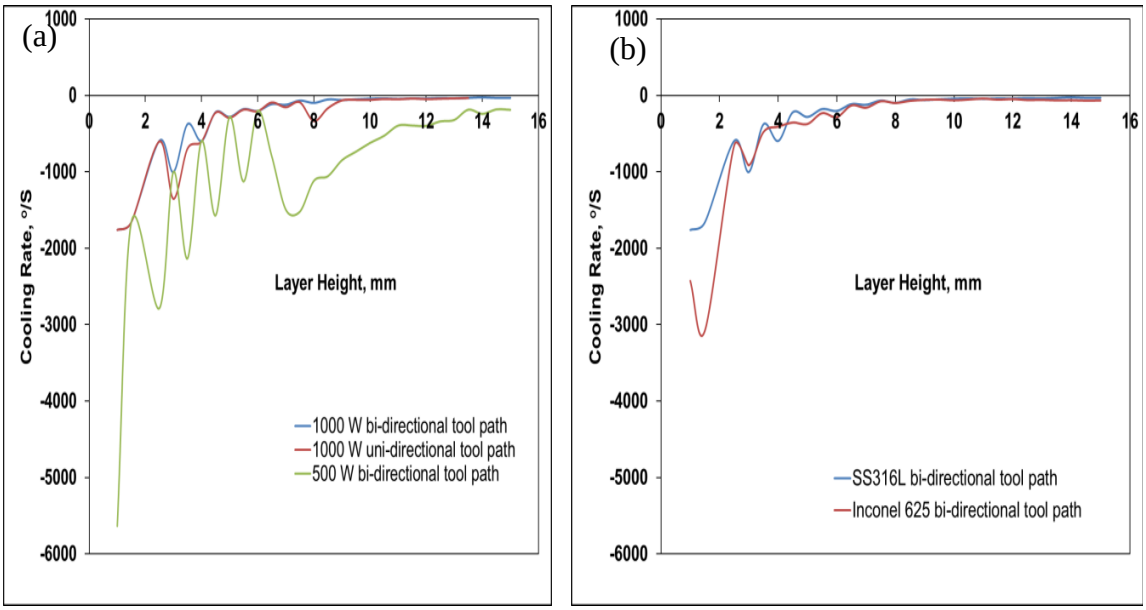

Figure 4.8 Cooling rates of each layer computed for thin wall deposits at the reference position at a laser scan speed of 4.23 mm/s for (a) SS316L on SS316L (b) SS316L on SS316L and Inconel 625 on SS316L.

The thermal model was also used to predict the remelting depth of the already deposited layer when a new layer is being added. The remelted layer depth is a very important output from the model and requires some understanding as it greatly influences the microstructure and chemistry of the deposited structure. Frequent remelting of prior layers not only increases mixing between layers but may homogenize the composition of

a functionally graded structure, negatively effecting the grading. Also remelting can lead to unwanted precipitation of solute phases which can make the structure prone to brittle failures.

Figure 4.9 shows the remelted layer depths computed from the thermal model for different clads. The output from the thermal model was only peak temperatures at each node. The remelted depths were calculated from the model whenever the solidified node re-melts ($T \geq T_m$) every time the laser passes over the nodes at the centerline of clad. The remelted layer depths were generally high except in the first layer that was being deposited. This is because of its proximity to the workpiece which acts as a large heat sink [105]. The remelted layer depth and 'Geometric Dilution' described in a previous section show some similarity. This is because the factors that control the two outputs are the same: laser power, travel speed, number of clad layers, powder feed rate, etc. A research [53] group showed that an increase in the number of clad layers or higher laser power affected the clad height and caused more and more deposited layers to remelt. This was because they observed that the melt pool size remained constant throughout the cladding process. Another research group [105] predicted that faster laser scanning speeds produce an insignificant remelted layer depth which can cause a failed metallurgical bond between the clad and workpiece. This is because [53] with the increasing travel speeds the molten pool depth became shallower and unstable as the heat input was insufficient to maintain the melt.

As the first deposit layer was laid down a portion of the workpiece remelted. Based on the computational results the meltpool depth in the workpiece is smaller at higher cooling rates for lower laser power. In the current model the remelted layer depth

was not predicted for a combination of lower laser power and uni-directional tool path. The amount of remelting in the previous layer steadily increased as more and more layers were deposited on top of each other. There is some fluctuation in the data, but overall continuously increasing trends in the amount of remelted layer depth with increasing number of passes was observed. In one of the FEA models [55], it was shown that not only did hot-clads (bi-directional deposits) experience slow cooling rates, but also the ambient temperature of the clad steadily increased. In the current model study, initially the remelted layer depth was slightly lower for the uni-directional tool path when compared to the bi-directional tool path. As the number of passes increase, the depths look more or less the same for the two tool paths.

Figure 4.9 also shows the Inconel 625 deposition on SS316L workpiece to initially have lower values for the remelted depths, eventually exceeding that of the SS316L deposition on SS316L workpiece. This may be because the SS316L workpiece conducts heat faster and better from the initial few layers; whereas conductivity slows down as more and more layers of Inconel 625 are laid on top of each other. There is a big limitation of the current thermal model as the nodes for computing the cooling rates and remelted layer depth were pre-determined. Further refinement in the mesh could have captured the subtle details more efficiently, but this could only be achieved at the expense of computing time and was not considered in the current research work.

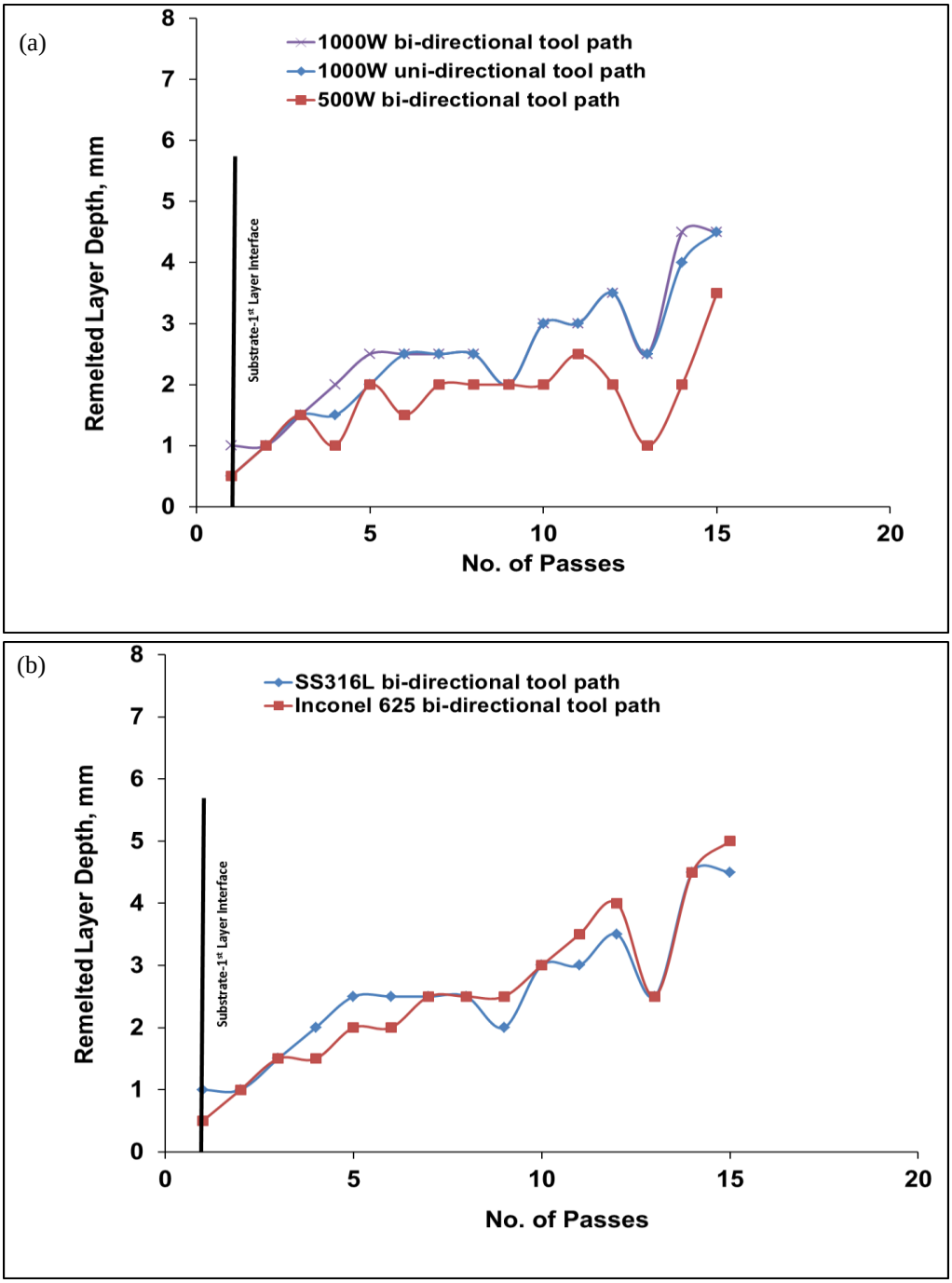

Figure 4.9 Computed remelted layer depth for thin wall deposits at the reference position (a) 4.23 mm/s, 15 layers; SS316L on SS316L (b) 4.23 mm/s, 15 layers; SS316L on SS316L and Inconel 625 on SS316L.

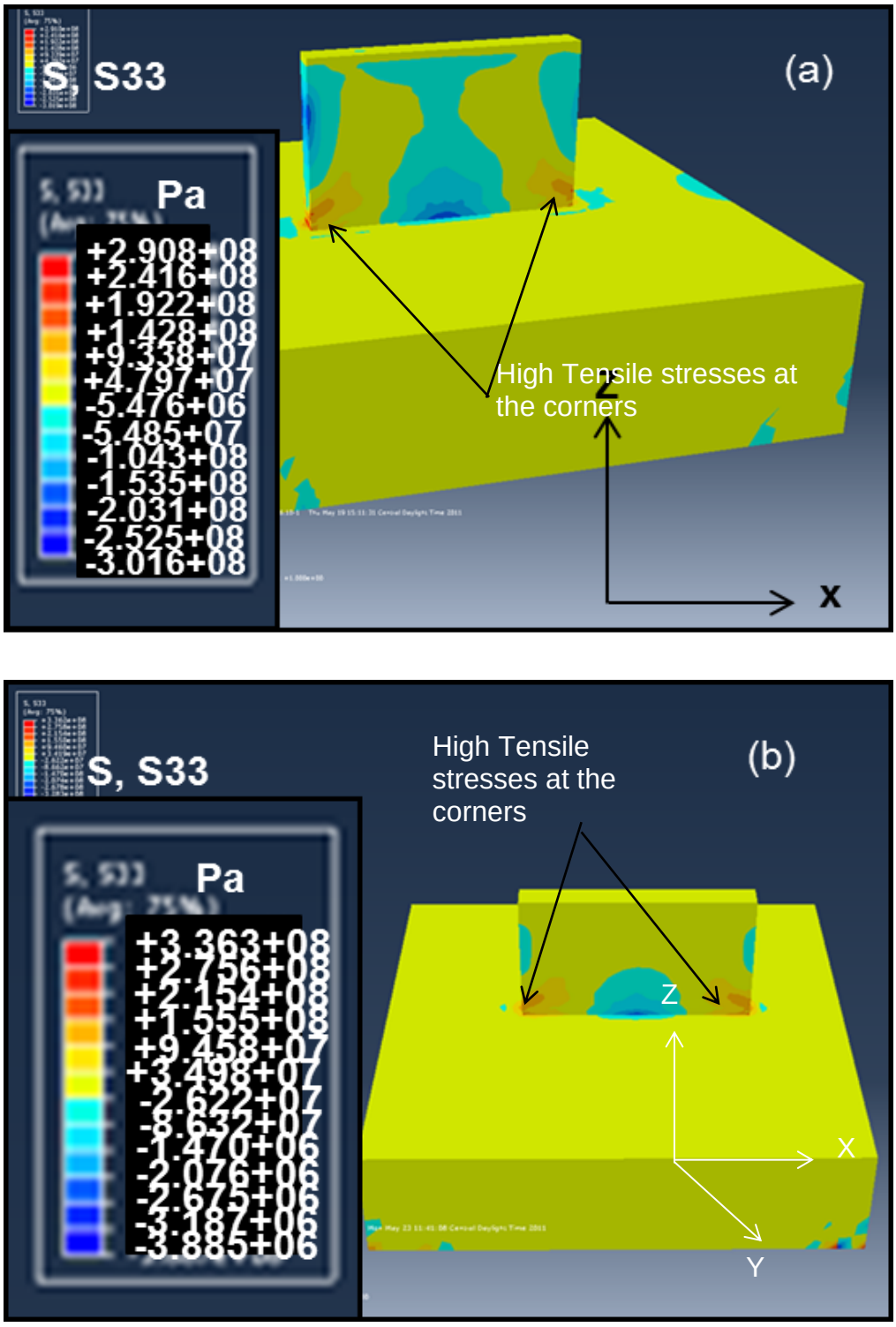

Figure 4.10 Stress σz in thin wall (a) bi-directional tool path (b) uni-directional tool path; SS316L on SS316L, 15 layers, 1000W and 4.23 mm/s.

During 3D fabrication by laser processing, a complex thermal and strain history is experienced in different regions of the build depending upon the process parameters. This is because the molten metal will not support a load, therefore the stresses underneath the laser beam is zero. As a consequence of the thermal expansion during heating, a plastic compressive zone occurs ahead of the beam, and as a result of thermal contraction during cooling, a plastic tensile zone occurs behind the molten pool. After the deposition and cooling sequences, the inhomogeneous temperatures disappear and so does the elastic thermal stress. The stress that remains is residual stress. The instantaneous strain and residual strain accumulation in the structure is the main cause of cracking during and after fabrication. The management of residual stress and the resulting distortion is a critical factor for the success of a process.

Figure 4.10 shows the distribution of stresses obtained by finite element modeling under the conditions described in the caption. The instantaneous thermal strains in a part are zero at melting but tend to increase as the part begins to solidify. In the current model the instantaneous strains during the solidification were not monitored and only final stresses in the part are reported. Localized high tensile stress values were observed at the corners of the thin wall as shown in Fig. 4.10 and are comparable for both the tool paths. According to the Von Mises yield criterion, a material is said to start yielding when its Von Mises stress reaches a critical value known as the yield strength σ_y. The Von Mises stress is used to predict yielding of materials under multiaxial loading condition from results of simple uniaxial tensile tests. Figure 4.11 (a) and 4.12 (a) shows that Von Mises stresses were lower than yield strength of SS316L which is ~300 MPa. Therefore, no yielding occurred in the model and no cracks were observed in the fabricated parts at the

end of deposition. Figure 4.11 and 4.12 show the three stress components (σ_x, σ_y,, and σ_z) for the left, right, and center-region of the thin wall along the entire length of the deposit with respect to the scanning direction. The stress distribution in the vertical-center line (Fig 4.11 (d) and 4.12 (d)) show that the compressive stress σ_z is increasing towards the substrate while the stress σ_y is almost zero (Fig. 4.11 (c) and 4.12 (c)) which is in good agreement with the stress distribution shown in the literature [56-58]. The distribution of stress in the σ_x direction appears to be very complex at the vertical center line for the two tool paths. The σ_x stresses for the uni-directional tool path is uniaxial in the x-direction at the center of the wall; whereas the stresses are biaxial in the x- and z-direction at the center of the wall for the bi-directional tool path. In general, the uni-directional tool path created stress values slightly lower than the bi-directional tool path which is expected according to the lower temperature differences during deposition (Fig. 4.7). There may be a possibility of greater remelt at the ends for the bi-directional tool path, although this was not evaluated in the current model. At the side walls a complex triaxial stress state is present close to the workpiece while the stresses close to the free end away from the workpiece converge to zero.

The instantaneous stresses developed in the workpiece during laser deposition were recorded using high temperature (HT) strain gages placed at the reference position- as shown in Fig.4.13. The gages were placed at 6 mm away from the centerline of clad. More details on the location of gages are presented earlier in Section 3. The strain gages recorded a progressive increase in instantaneous tensile stress in the workpiece for the bi-directional tool path as the layers were being deposited (Fig. 4.13(a)). A research group [54] showed in their FEA model that there was a progressive increase in the level of

tensile stress as subsequent layers (10 layered models) were deposited for the bi-directional tool path. In the model, stresses in the layers reached as high as 700 MPa and in the workpiece about 200 MPa during the deposition processes.

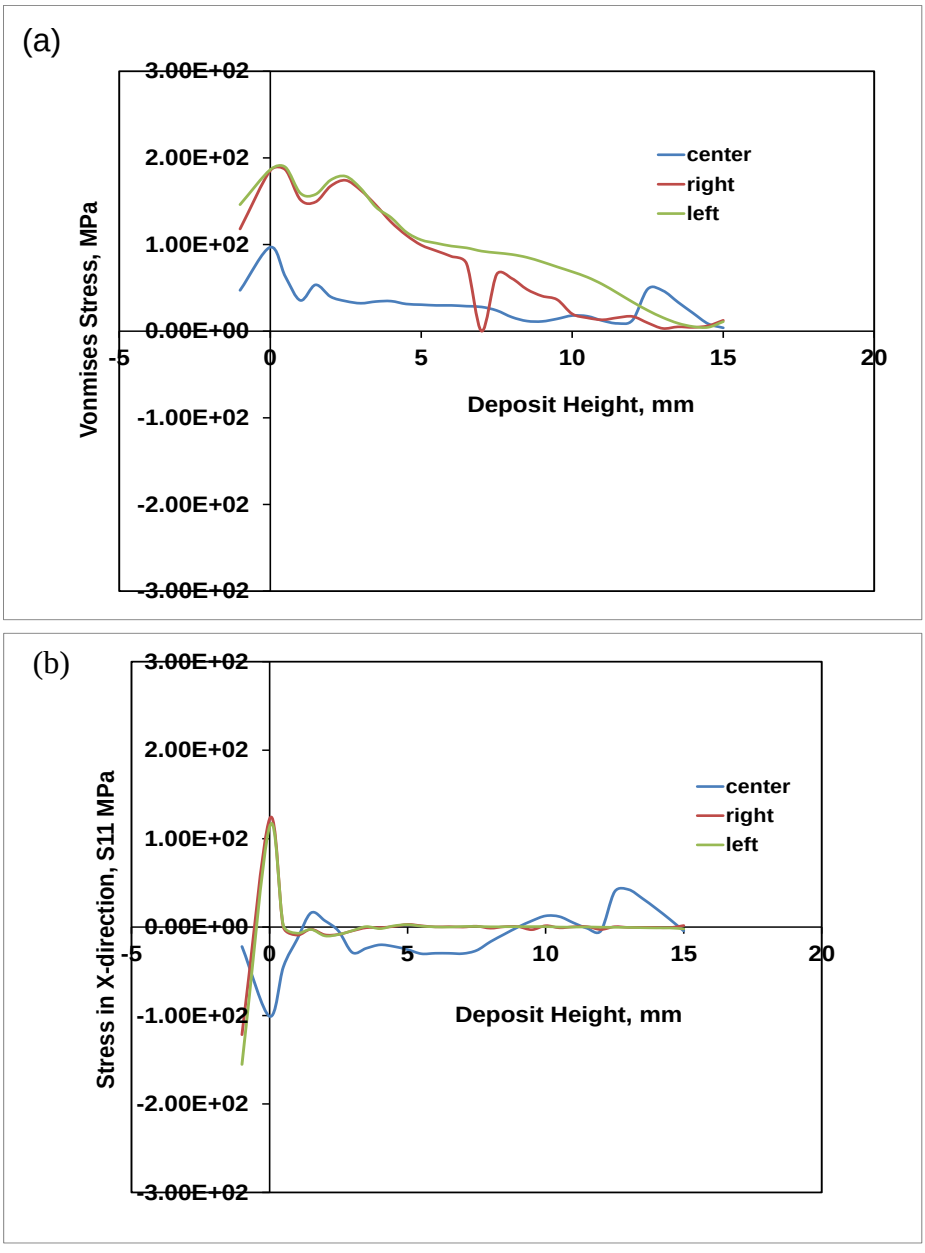

Figure 4.11(a-d) Stress in thin wall for bi-directional tool path; SS316L on SS316L, 15 layers, 1000W and 4.23 mm/s.

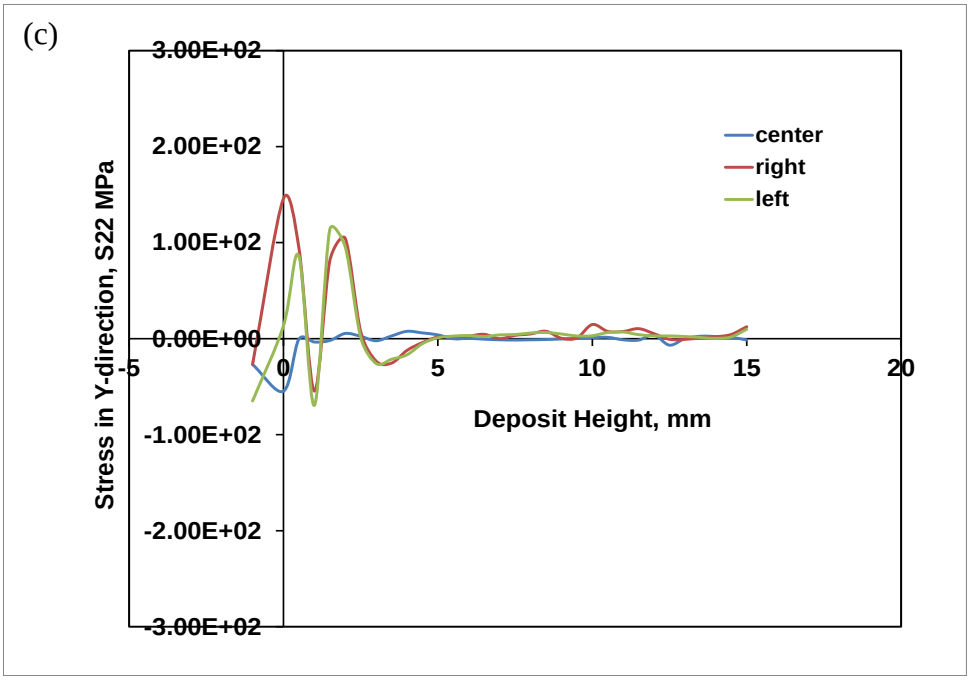

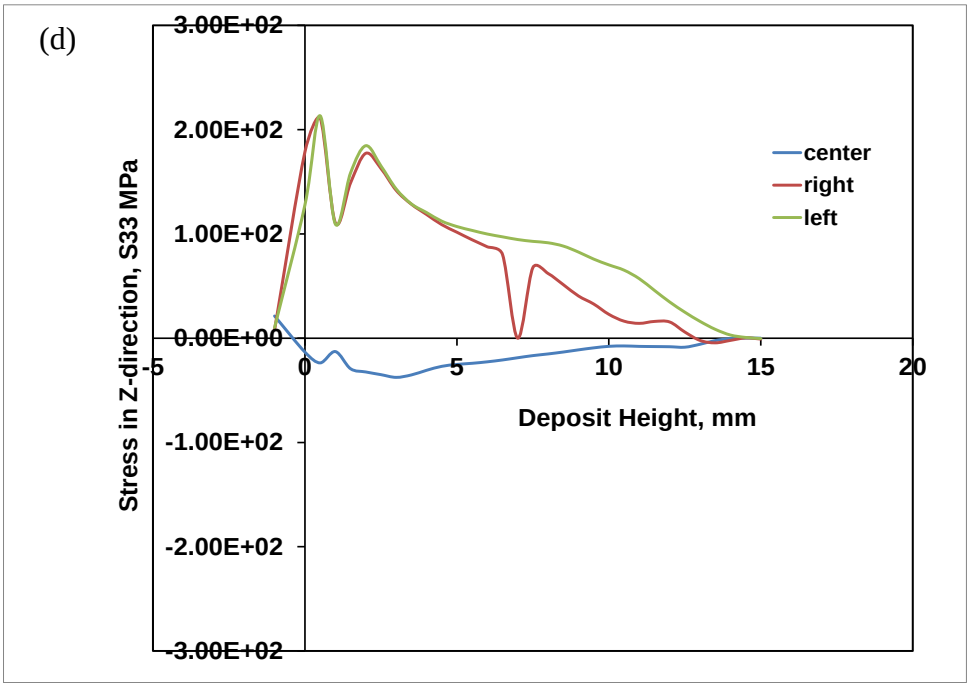

Figure 4.11 (a-d) Stress in thin wall for bi-directional tool path; SS316L on SS316L, 15 layers, 1000W and 4.23 mm/s (Cont.).

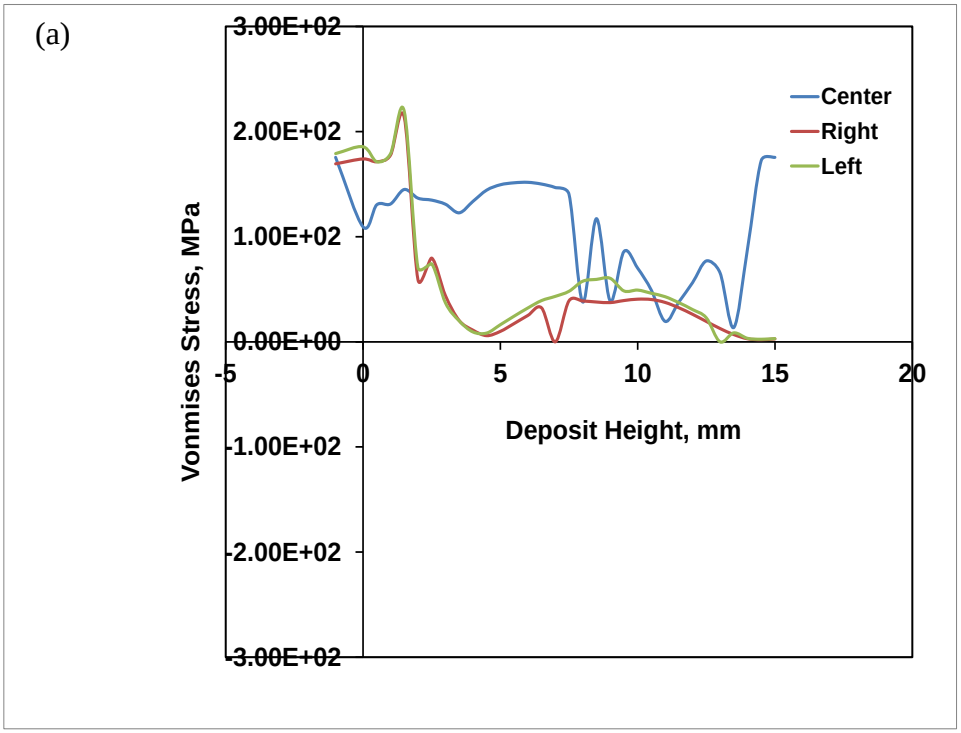

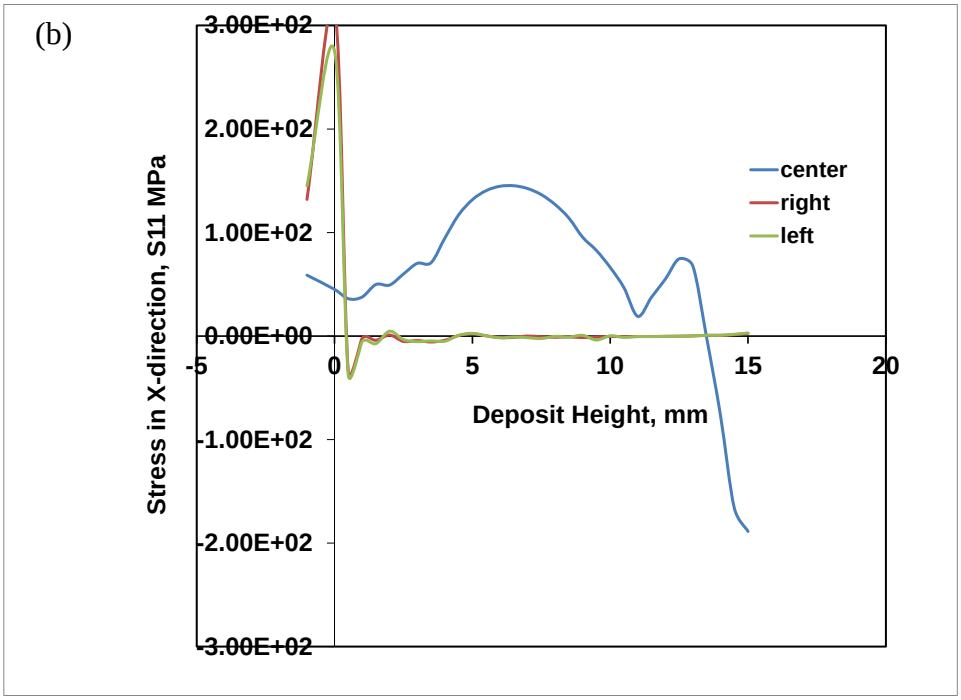

Figure 4.12 (a-d) Stress in thin wall for uni-directional tool path; SS316L on SS316L, 15 layers, 1000W and 4.23 mm/s.

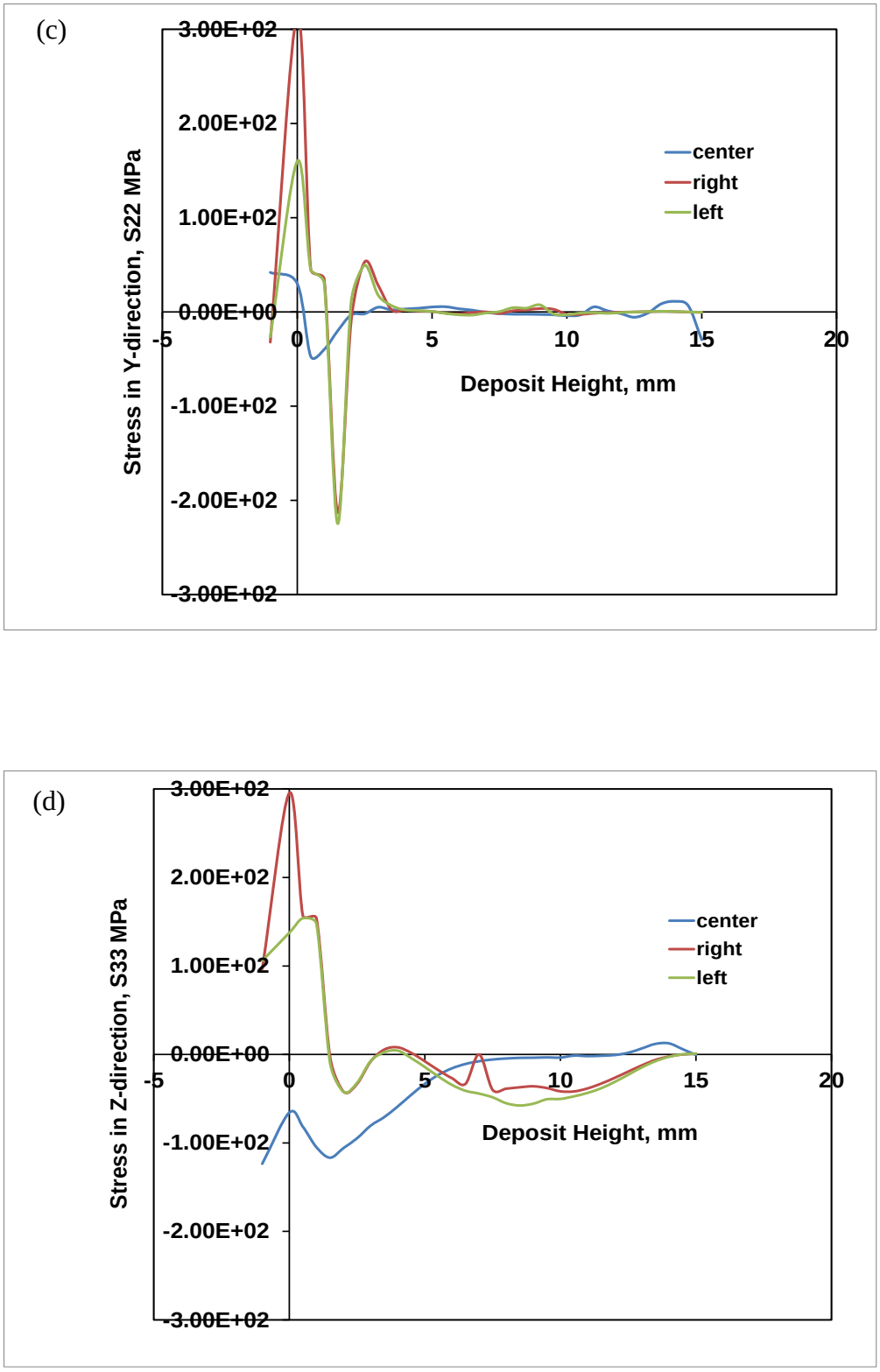

Figure 4.12 (a-d) Stress in thin wall for uni-directional tool path; SS316L on SS316L, 15 layers, 1000W and 4.23 mm/s (Cont.).

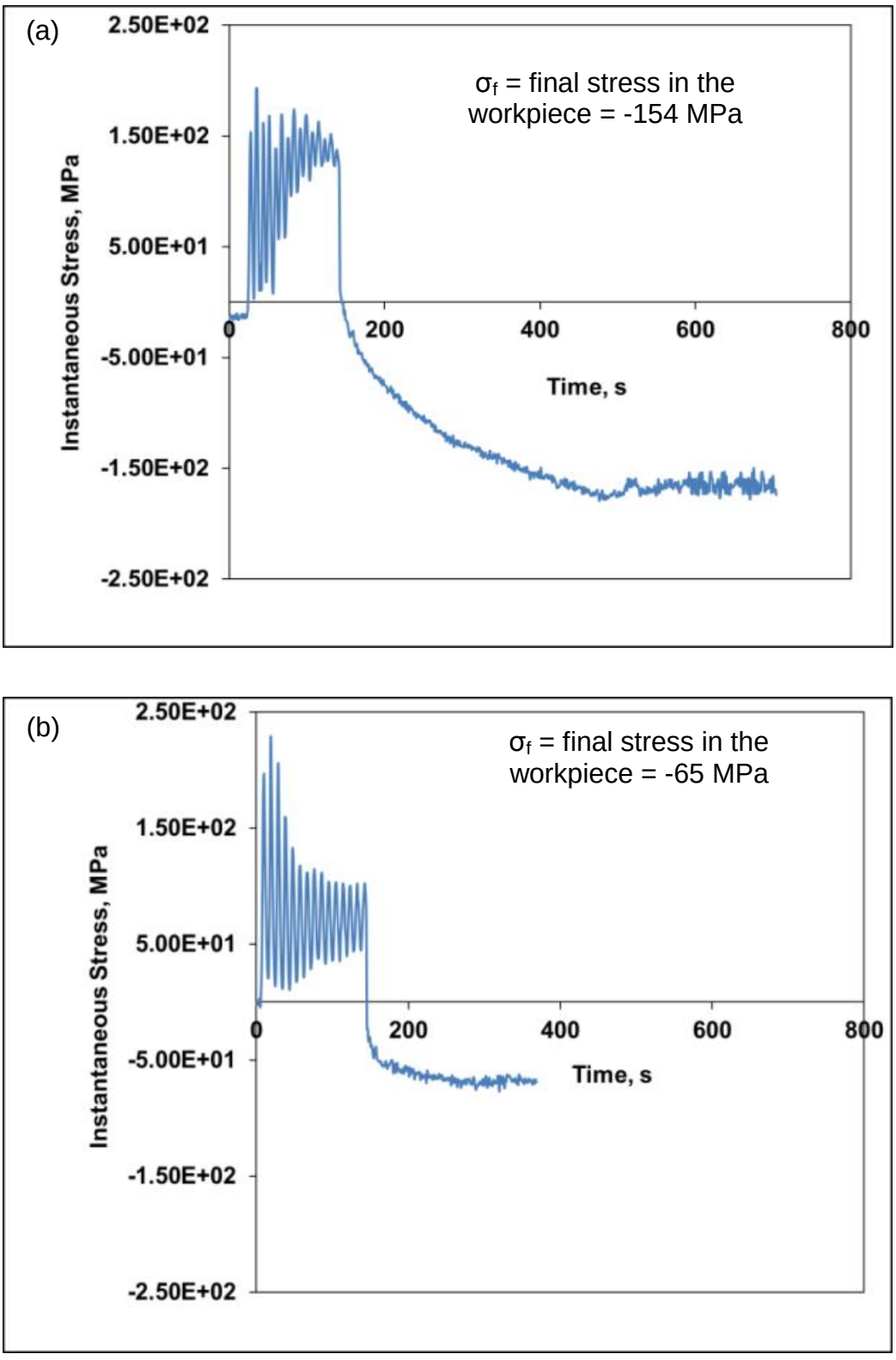

Figure 4.13 Instantaneous stress recorded at reference position by HT strain gages in thin wall for (a) bi-directional and (b) uni-directional tool path, (c) FEA model ; SS316L clad, 15 layers, 1000W, 4.23 mm/s; 12g/min, strain gages aligned in laser travel direction.

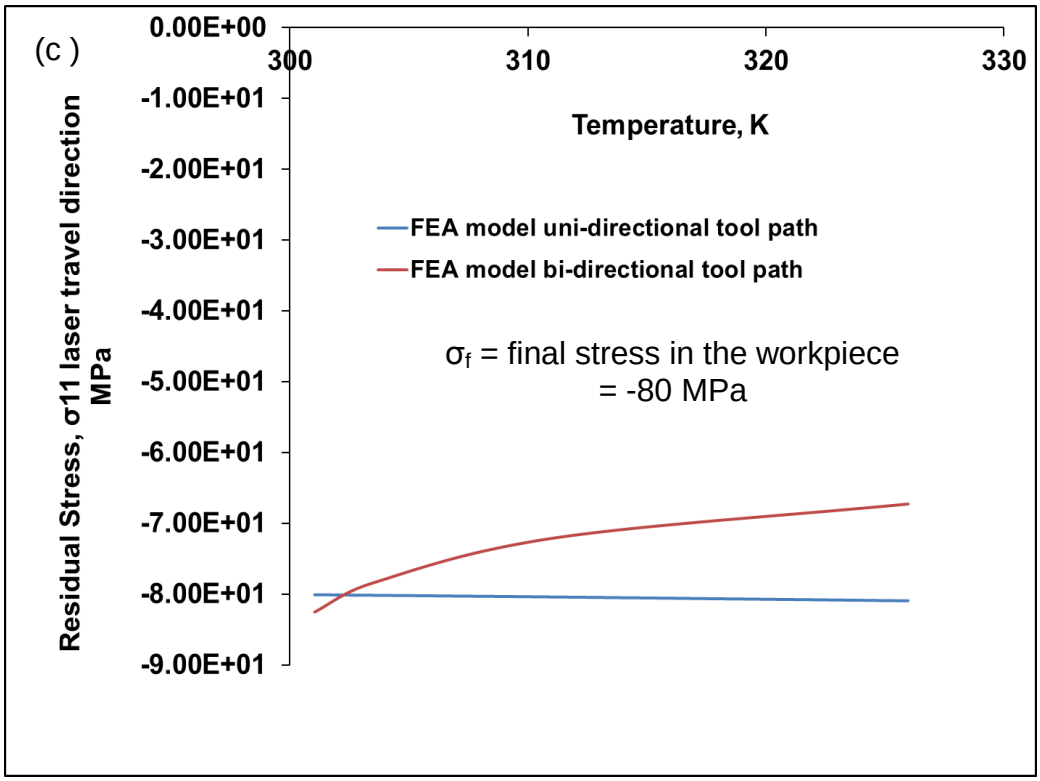

Figure 4.13 Instantaneous stress recorded at reference position by HT strain gages in thin wall for (a) bi-directional and (b) uni-directional tool path, (c) FEA model ; SS316L clad, 15 layers, 1000W, 4.23 mm/s; 12g/min, strain gages aligned in laser travel direction (Cont.).

In the case of the uni-directional tool path, because of lower temperature gradients in the deposited layers, the instantaneous stresses were progressively compressive in the workpiece as more and more layers were added to the wall (Fig. 4.13(b)). The FEA model at the reference position computed a final compressive residual stress of -80 MPa for the uni-directional tool path and -82 MPa for the bi-directional tool path (Fig. 4.13(c)); whereas the HT strain gages recorded -65 MPa for the uni-directional tool path and -154 MPa for the bi-directional tool path. The FEA results at the reference position did not show significant difference between the two tool paths. Also, the trends were

similar between FEA and the experimental values recorded by the HT strain gages at the reference position.

Typically the residual stresses in clads [69, 106] have been experimentally measured using hole-drilling techniques by a placing a strain-gage on the clad surface at a distance from the hole. In the current study post-clad machining operations were performed on clads and the stresses relieved from the workpiece were recorded using low temperature strain gages placed at the reference position. Figure 4.14 shows the stresses measured in the workpiece as the layers were machined away one by one. A clear relationship between the stress relieved due to machining of each layer and the deposition conditions could not be established. The only takeaway was that as the layers were machined one after the other, the final stresses that remained in SS316L workpiece were more or less compressive at all the deposition parameters.

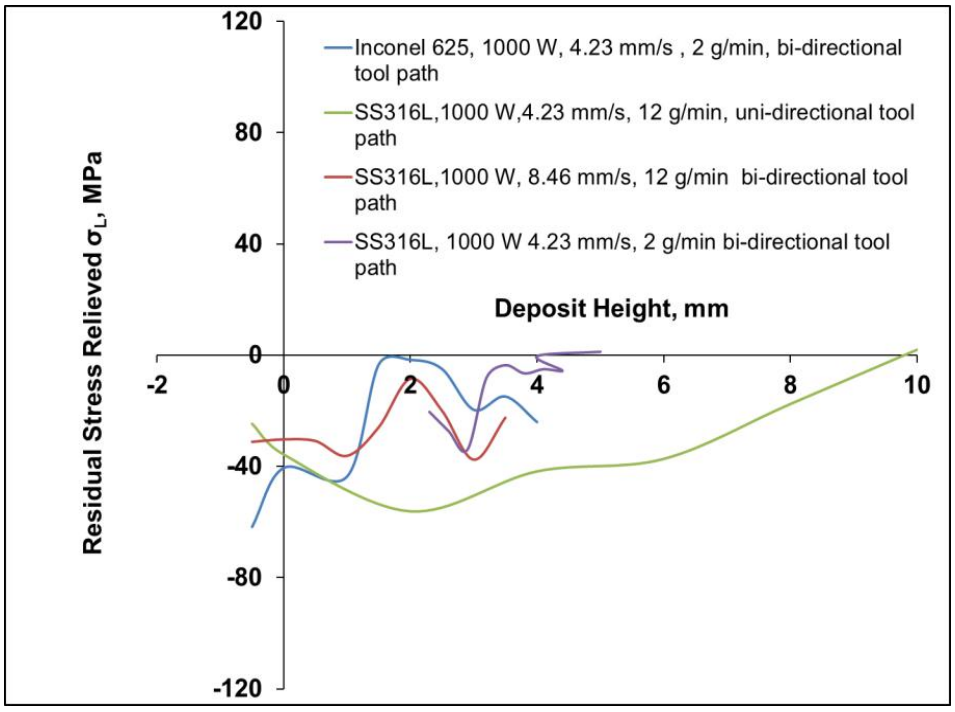

Figure 4.14 Post clad machining operation on the 15 clad layers under different processing conditions (along the laser travel direction).

4.2.3. Microstructure, Phase and Composition of SS316L and Inconel 625 Clads.

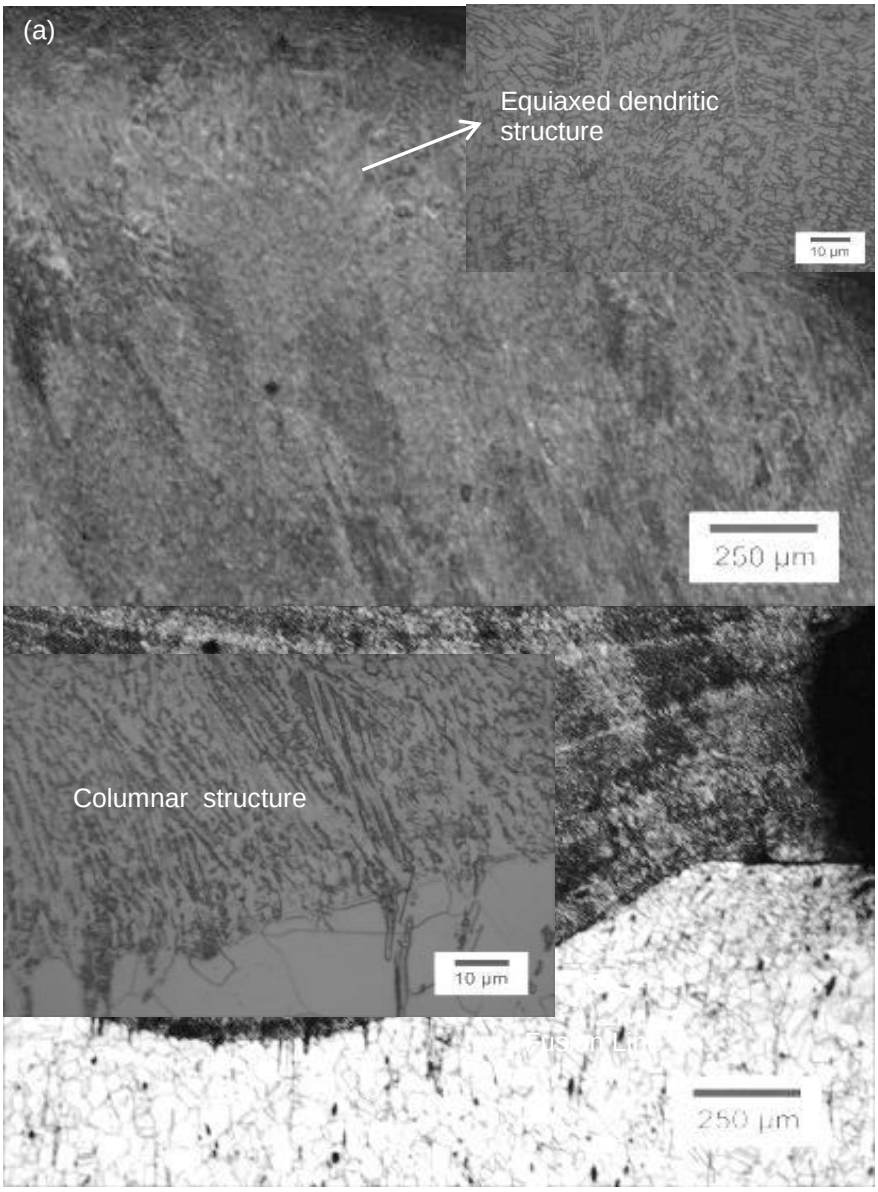

Figure 4.15 Transverse section microstructure at 1000W, 12 g/min, 4.23 mm/s and 15 layers, (a) SS316L on SS316L workpiece, uni-directional tool path; and (b) Inconel 625 on SS316L workpiece, bi-directional tool path.

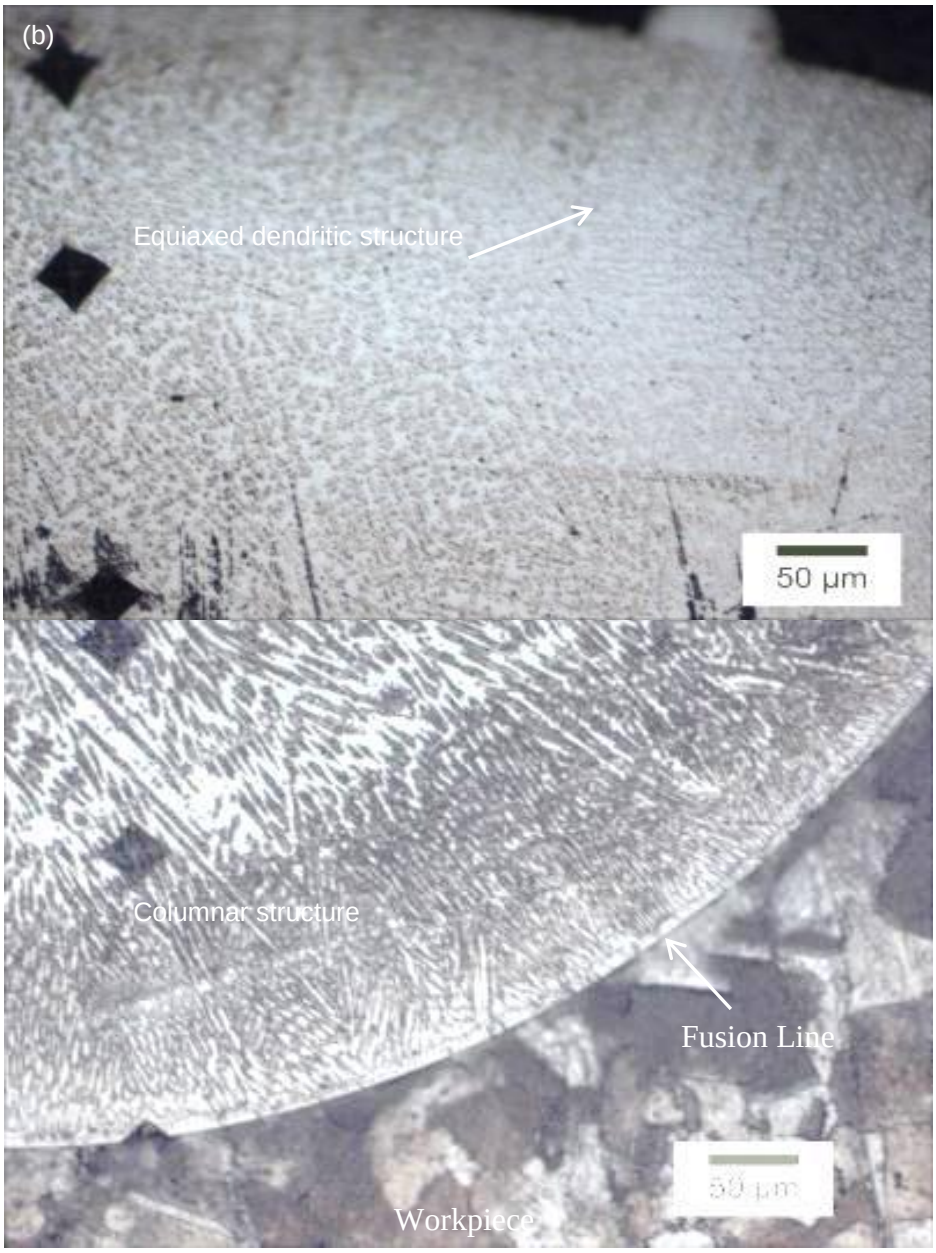

Figure 4.15 Transverse section microstructure at 1000W, 12 g/min, 4.23 mm/s and 15 layers, (a) SS316L on SS316L workpiece, uni-directional tool path; and (b) Inconel 625 on SS316L workpiece, bi-directional tool path (Cont.).

Laser cladding could present a heterogeneous microstructure that can differ from point to point. Figure 4.15 describes the macrostructure of 316 SS and Inconel 625 clads. Planar, columnar and equiaxed dendritic structures were visible at various locations. In all the deposits, the macrostructures were columnar in nature, with the axis of the columnar grains parallel to the build direction of the deposit. The columnar grain morphology indicates that the heat flow is parallel to the build direction and that the thermal gradient was likely very high. All the macrostructures exhibited columnar morphology in the bottom-most regions of the clad. The columnar grains grew epitaxially from the planar interface between clad and the workpiece, and the growth directions of the columnar grains were tied to the laser scanning direction. In the laser deposition process very rapid solidification rates are attained and therefore the layers in proximity to the workpiece would cool faster [70]. Because of such high temperature gradients the interface is usually planar. The upper part of the deposit cooled more slowly compared to the bottom. The top most layers of the clad showed a fine dendritic structure with classical secondary dendrite arms. Due to the very high solidification velocity in the bottom layers the secondary dendrites could not grow. The microstructure transitioned from fully columnar to equiaxed dendritic from bottom to the top of clad layers.

The effect of laser tool path on the grain orientation was determined by {111} pole analysis, as shown in Fig. 4.16. For the analysis the sample orientation is shown in Fig. 4.16. When we measure the {111} pole figure, what we actually measure is the distribution of directions normal to the {111} plane in each grain. This direction is also called {111} pole. There was no significant texture in the specimens as no special pattern can be seen in the pole figures. Figure 4.17 shows the standardless EDS compositional

analysis along the length of the clad. The distribution of elements such as Fe, Cr and Ni is uniform in the SS316L clad and workpiece; whereas a gradual transition in composition from the workpiece to the clad can be seen in the Inconel 625 clad which is to be expected.

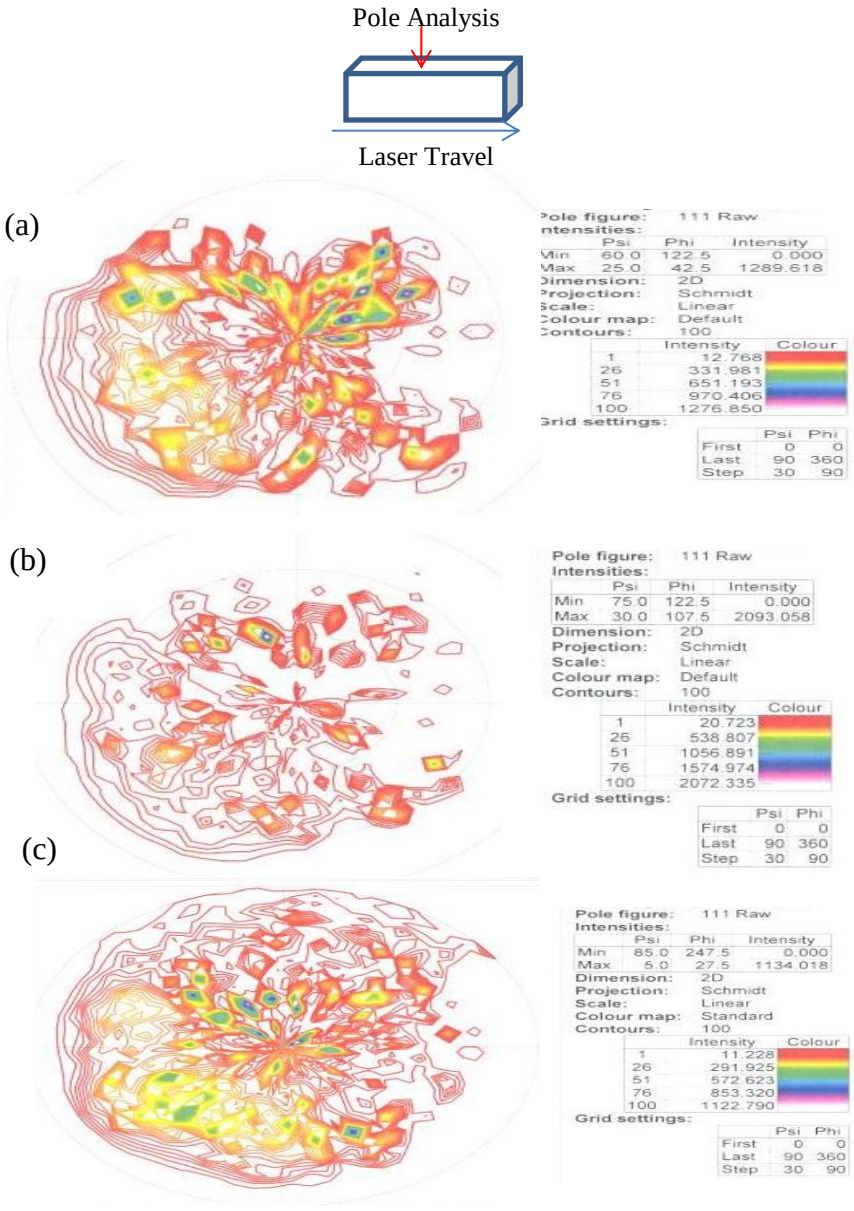

Figure 4.16 Pole figure analysis of (111) plane, 1000W, 12 g/min, 4.23 mm/s, 15 layers, Materials SS316L on SS316L workpiece (a) bi-directional,
(b) uni-directional; Materials: 2 g/min, Inconel 625 on SS316L workpiece (c) bi-directional, (d) uni-directional.

(d)

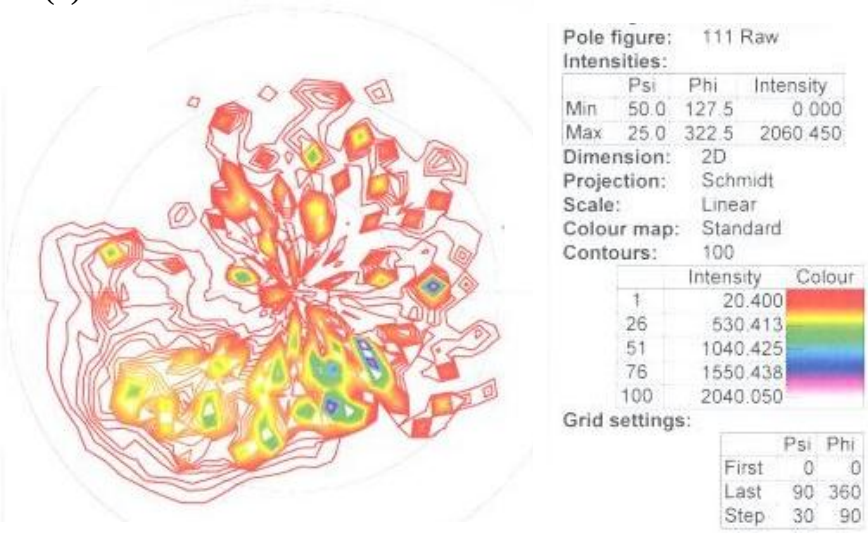

Figure 4.16 Pole figure analysis of (111) plane, 1000W, 12 g/min, 4.23 mm/s, 15 layers, Materials SS316L on SS316L workpiece (a) bi-directional,
(b) uni-directional; Materials: 2 g/min, Inconel 625 on SS316L workpiece (c) bi-directional, (d) uni-directional (Cont.).

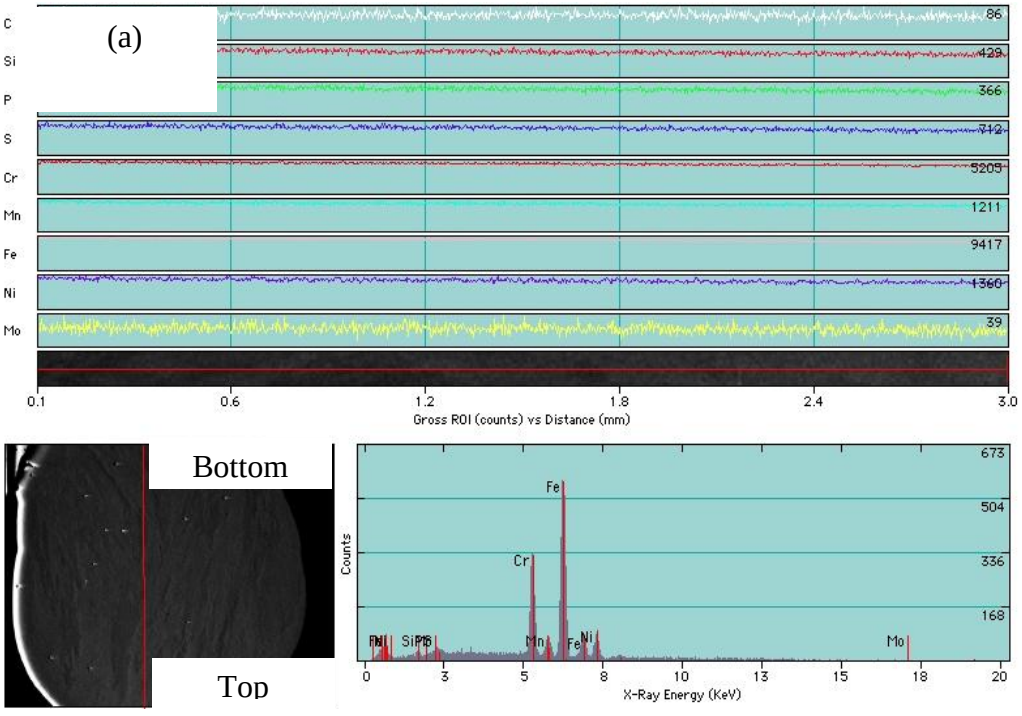

Figure 4.17 Composition line scans, bi-directional tool path (a) Materials SS316L clad, 1000W, 12g/min, 4.23 mm/s, 5 layers, bi-directional, (b) Materials: Inconel 625 clad, 1000 W, 4.23 mm/s, 15 layers, 2 g/min.

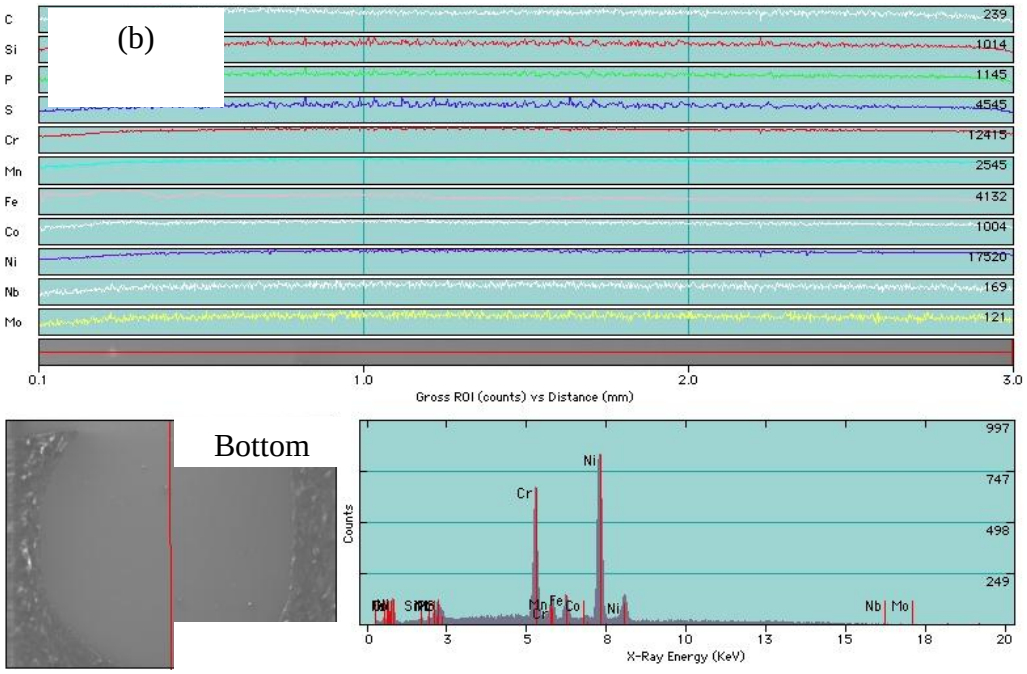

Figure 4.17 Composition line scans, bi-directional tool path (a) Materials SS316L clad, 1000W, 12g/min, 4.23 mm/s, 5 layers, bi-directional, (b) Materials: Inconel 625 clad, 1000 W, 4.23 mm/s, 15 layers, 2 g/min (Cont.).

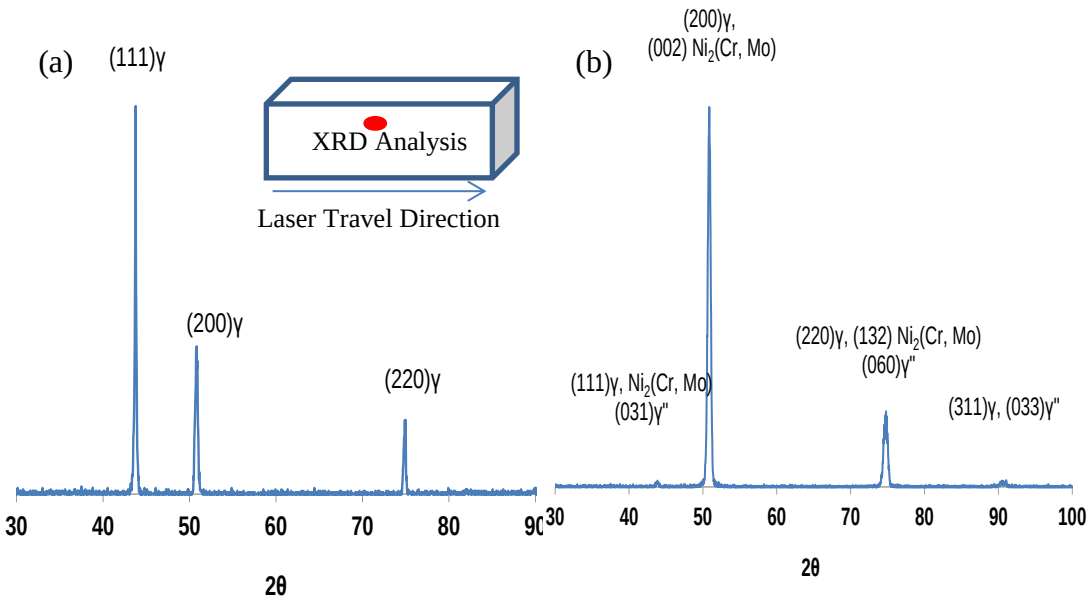

Figure 4.18 X-ray diffraction pattern for (a) SS316L clad, (b) Inconel 625 clad.

Figure 4.18 shows the XRD patterns for SS316L and Inconel 625 clads deposited on stainless steel 316L workpiece. For the analysis the sample orientation is shown in Fig. 4.18. The texture effects were found in the XRD patterns, but were not found in the pole figures for the processing conditions described above. Because of directional solidification arising due to high temperature gradients and rapid cooling rates it is possible to achieve a more uniform microstructure in laser cladding. The XRD patterns show mono phase γ for SS316L clad, whereas the γ, γ", and Ni_2(Cr, Mo) phases were observed in Inconel 625 clad [70]. The peaks of γ" (BCT DO_{22} structure), and Ni_2(Cr, Mo; Orthorhombic Pt_2Mo structure) overlapped with the peaks of the γ matrix.

4.3 EFFECT OF PROCESS PARAMETERS ON FUNCTIONALLY GRADED TI6AL4V/INCONEL 625

The Ti6Al4V and Inconel 625 systems were functionally graded in order to minimize the interfacial stresses due to the sharp transitions at the interface. The microstructural transitions were studied as a function of grading with different compositions and laser process parameters such as laser power, travel speed, tool path direction, powder feed rate, etc. The deposition conditions were never optimal because the powder yield was only 6.5 percent; more details on the experimental conditions were already presented earlier in Section 2.

4.3.1. Microstructure, Composition and Phase. The microstructure, composition and phase for various processing conditions are discussed in this section.

4.3.1.1 Linear grading chem-I under varying laser power. All the samples showed macrocracks; Fig.4.19 is an example of cross-section perpendicular to the laser scanning direction showing macrocracks half- way through the deposit. A 2 mm banding can be seen near the region where cracks terminated. The banding was seen in all the deposits. Further discussion of the cracks in the deposits is presented in a later section of the results.

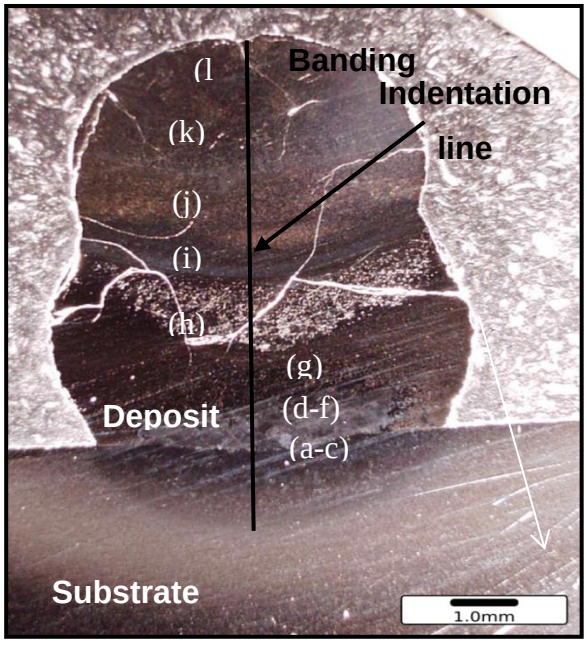

Figure 4.19 Example cross-section of Ti6Al4V/Inconel 625 graded deposit at 700 W. Note the presence of macro-cracks. The composition of the deposit was recorded along the indentation line. The (a)-(l) correspond to the locations where the data were acquired in SEM as presented in the Fig.4.24.

Figure 4.20 (a -c) shows the results obtained from standardless EDS compositional analysis of the various elements along the graded direction as a function of laser power. The final deposit heights varied between the processing conditions partly due to poor powder capture efficiency (<10%) even when the mass per unit length for

each layer was held constant. Also, the measured composition changed linearly over a certain distance and thereafter remained constant through the remainder of the graded layers. The compositional layers at higher laser powers appeared to be completely mixed during the deposition process.

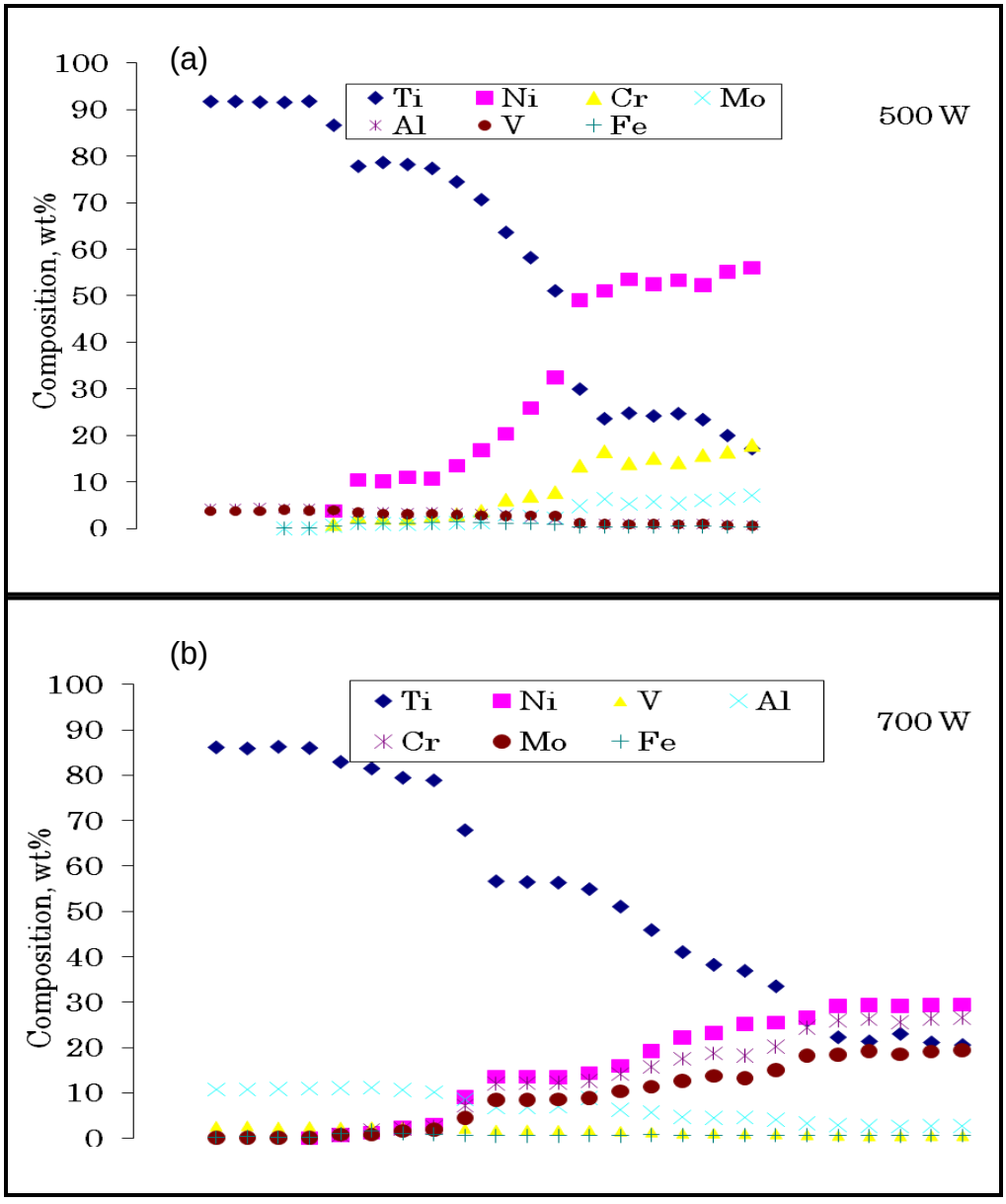

Figure 4.20 (a-c) Compositional gradient of the LMD Ti6Al4V/Inconel 625 functionally graded deposit as a function of laser power, distance measured from the initial substrate-deposit interface (0 mm).

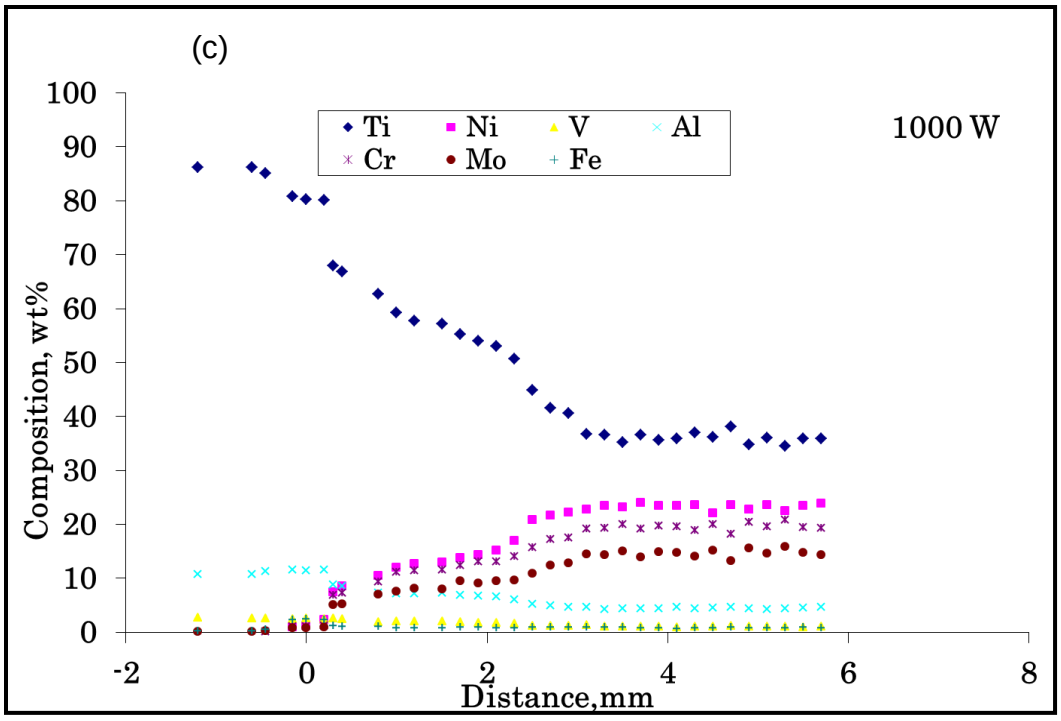

Figure 4.20 (a-c) Compositional gradient of the LMD Ti6Al4V/Inconel 625 functionally graded deposit as a function of laser power, distance measured from the initial substrate-deposit interface (0 mm) (Cont.).

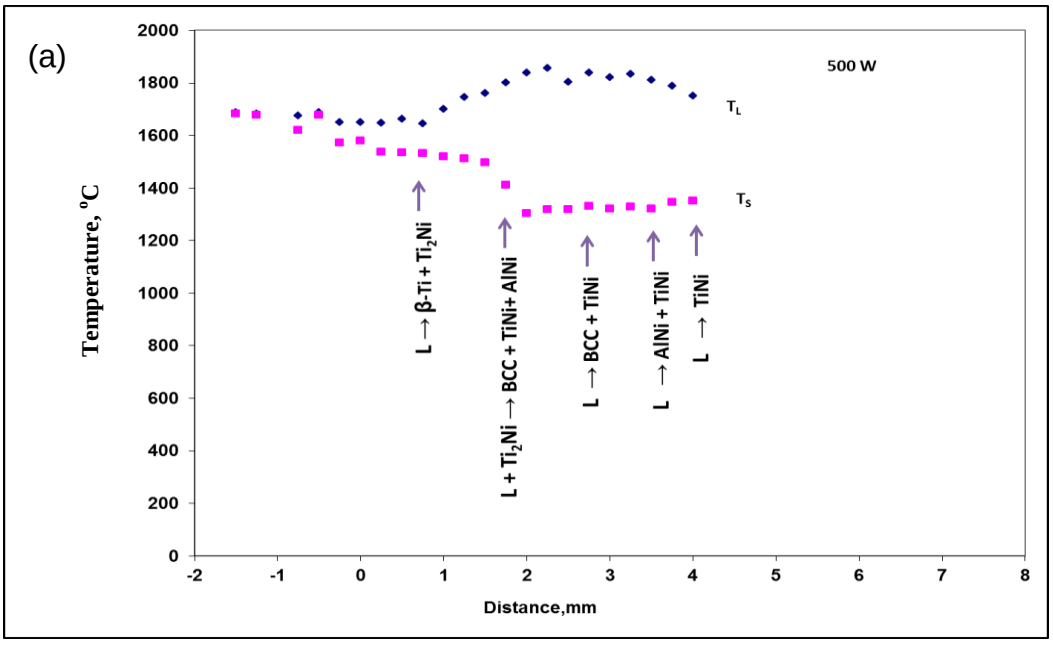

Figure 4.21 (a-c) FactSage calculation of equilibrium liquids, T_L, and solidus temperature, T_S, as function of laser power, distance measured from the initial substrate-deposit interface (0 mm). Note: Bold arrow indicates location along the gradient; BCC is Cr and Mo rich beta Ti based compounds, i.e. β-Ti or TiNi.

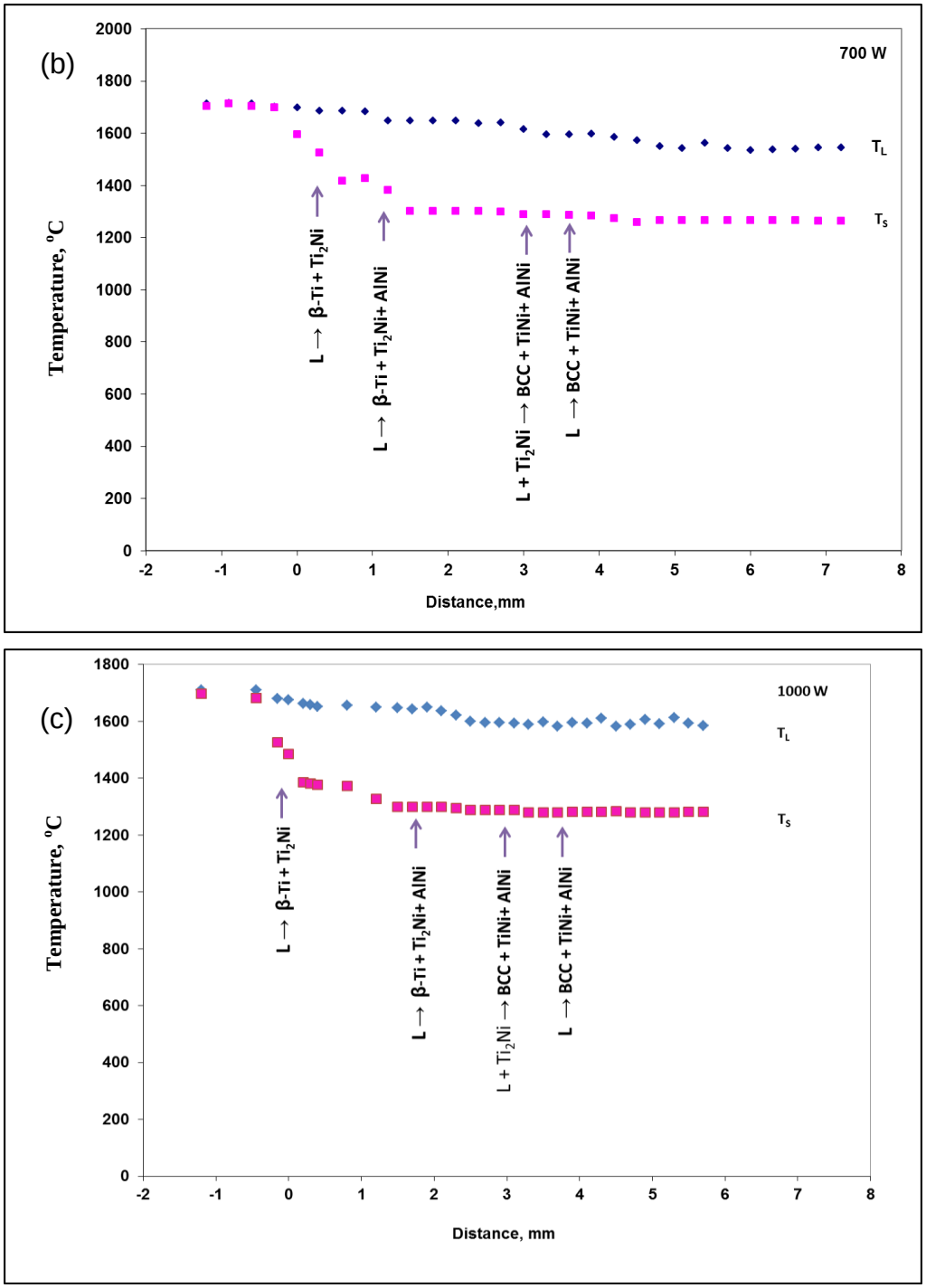

Figure 4.21 (a-c) FactSage calculation of equilibrium liquids, T_L, and solidus temperature, T_S, as function of laser power, distance measured from the initial substrate-deposit interface (0 mm). Note: Bold arrow indicates location along the gradient; BCC is Cr and Mo rich beta Ti based compounds, i.e. β-Ti or TiNi (Cont.).

In general the compositional data showed that decreasing laser power significantly reduced the amount of mixing in/between the layers. The thermal models showed that the degree of remelting of prior layers decreased with decreasing laser power. Therefore, it becomes more imperative to explore a process window with higher cooling rates so as to result in lesser mixing for functional grading.

The elemental composition data from EDS was used as an input to calculate the liquidus temperature (T_L) and solidus temperature (T_S) under equilibrium conditions using the commercial software, FactSage, as shown in Fig. 4.21. The data can also be used to interpret the equilibrium freezing ranges ($\Delta T^{S\rightarrow L}$) in the graded alloy. The results showed that the $\Delta T^{S\rightarrow L}$ increased rapidly when the amount of Inconel 625 increased; at the initial stage $\Delta T^{S\rightarrow L}$ of Ti6Al4V was only about 5 K, while after the addition of Inconel 625, at a distance of ~0.6 mm from the substrate, $\Delta T^{S\rightarrow L}$ reached 200 K. Moreover, the results of equilibrium thermodynamic predictions obtained from using the Factsage software showed that the eutectic reaction of $L \rightarrow \beta + Ti_2Ni$ is initiated at that location. The $\Delta T^{S\rightarrow L}$ slightly varied as a function of the laser power from anywhere between150 to 200 K. The composition of the graded material at this position measured by the EDS analysis was also found to vary between Ti-2.36Ni-X (remaining elements) at 700 & 1000 W to Ti-10.43Ni-X at 500 W. Further increasing the amount of Inconel 625 would result in an increase in $\Delta T^{S\rightarrow L}$ by 300 K. This corresponds to a distance of 3 mm from the substrate. The composition at this position measured by the EDS analysis was found to vary between Ti-20 to 24.8 Ni-X. Such high freezing ranges can potentially result in hot cracking or tearing or solidification cracking during solidification. Solidification cracking is generally a function of composition and the resulting

temperature range, where compositions that exhibit large solidification temperature range are generally crack susceptible. In hot tearing, lliquid cannot reach the regions where it is needed due to blockage or narrow channels between solidifying grains. According to the thermodynamic calculations for 500, 700 and 1000 W, one of the primary phases changed from Ti_2Ni to TiNi at a composition of 30.79 pct Inconel 625. Further increase in nominal Inconel 625 content beyond this point resulted in no significant change in $\Delta T^{S \to L}$. This flat response may be mainly due to mixing in/between layers. Other experimental factors that could have contributed to this lack of grading can be poor powder capture efficiency, lack of control over Z-height, etc. More details have been described earlier in Section 3.

The thermodynamic calculations also predicted the formation of other compounds such as a BCC Cr and Mo phase and AlNi. With further increase in nominal Inconel 625 content in the layers, the thermodynamic calculations predicted three different types of solidification reactions occurring in the final layers:

$L \to BCC + AlNi + NiTi$, at 1000 W and 3.6 mm from interface

$L \to BCC + AlNi + NiTi$, at 700 W and 3.75 mm from interface

$L \to NiTi$, at 500 W and 4 mm from interface

The composition in the layers did not change for 700 W and 1000 W from a distance of 3 mm from substrate and may be due to mixing in/between graded layers. The composition at this location is Ti-23Ni-X at 700 & 1000 W whereas it was Ti-56Ni-X at 500 W. This significant difference in composition can also be due to more mixing occurring in the layers at high heat input. At a nominal concentration of 100 percent by weight Inconel 625, under equilibrium conditions Factsage predicted the following

reaction: $L \rightarrow FCC$ (gamma Ni) which is rich in Ni, Cr and Mo. The primary phase predicted by thermodynamic calculations at different laser powers in the final layer was only TiNi due to the presence of significant amount of Ti in the matrix.

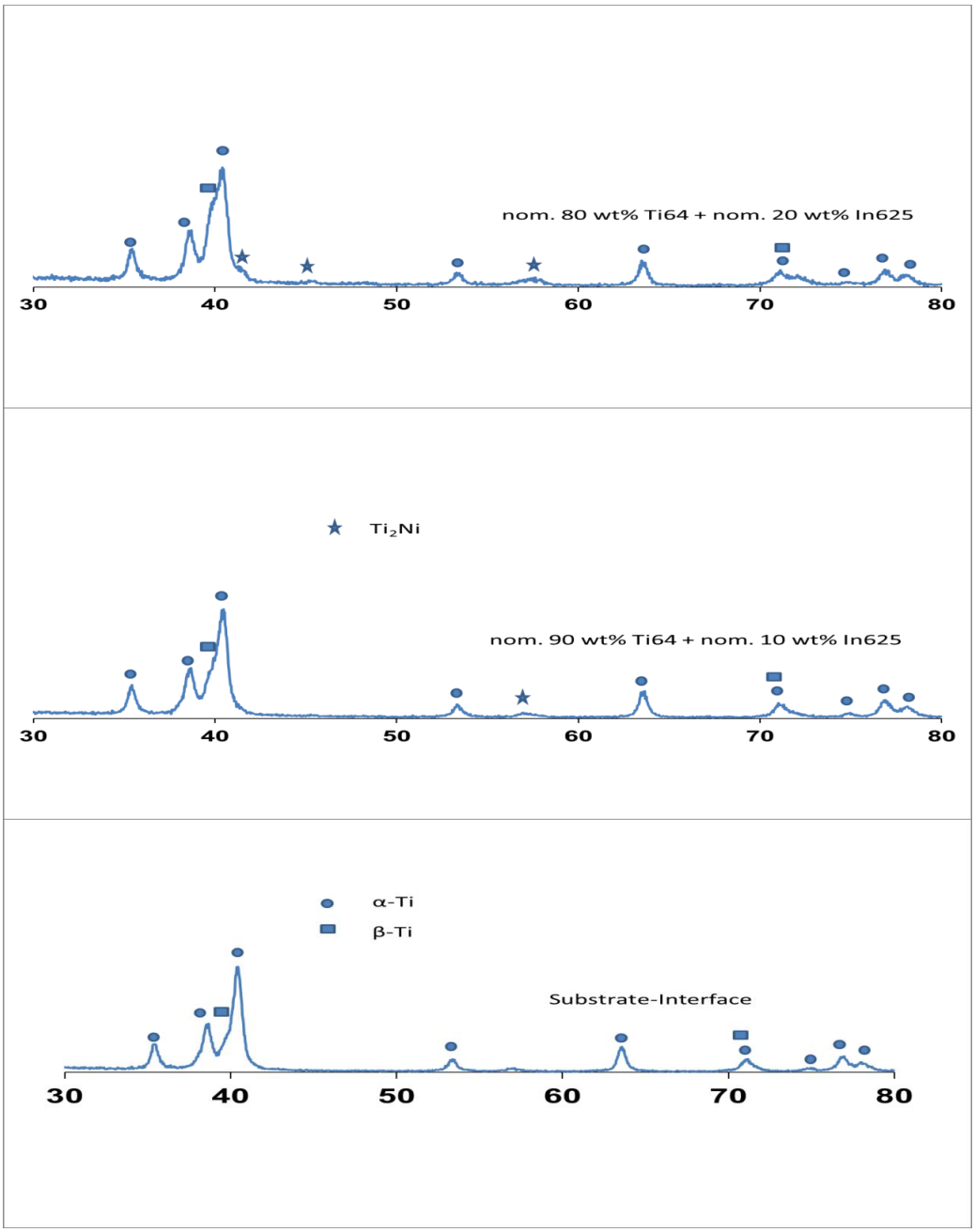

Figure 4.22 X-ray diffraction patterns at 500 W along the composition gradient measured perpendicular to the laser scanning direction.

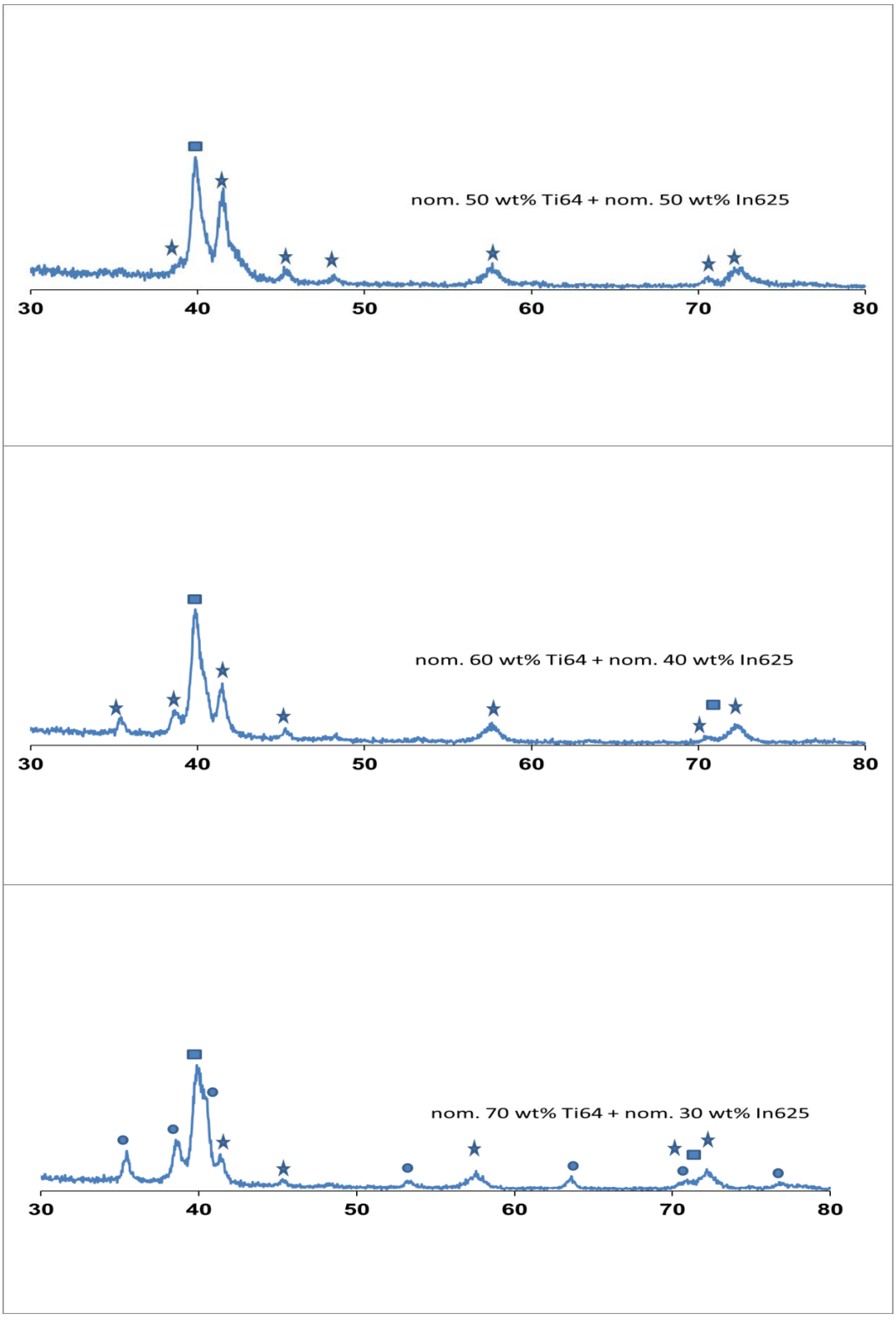

Figure 4.22 X-ray diffraction patterns at 500 W along the composition gradient measured perpendicular to the laser scanning direction (Cont.).

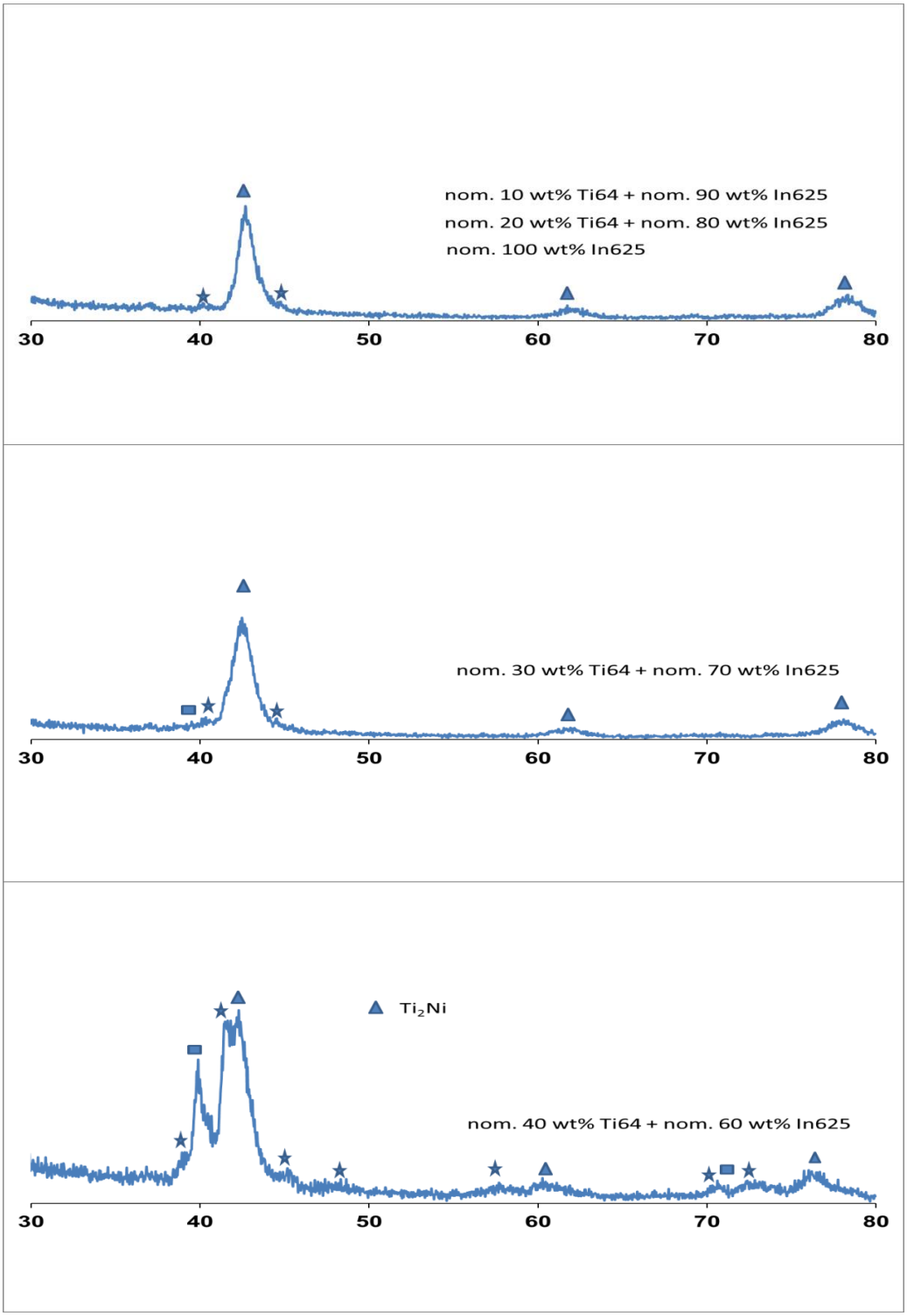

Figure 4.22 X-ray diffraction patterns at 500 W along the composition gradient measured perpendicular to the laser scanning direction (Cont.).

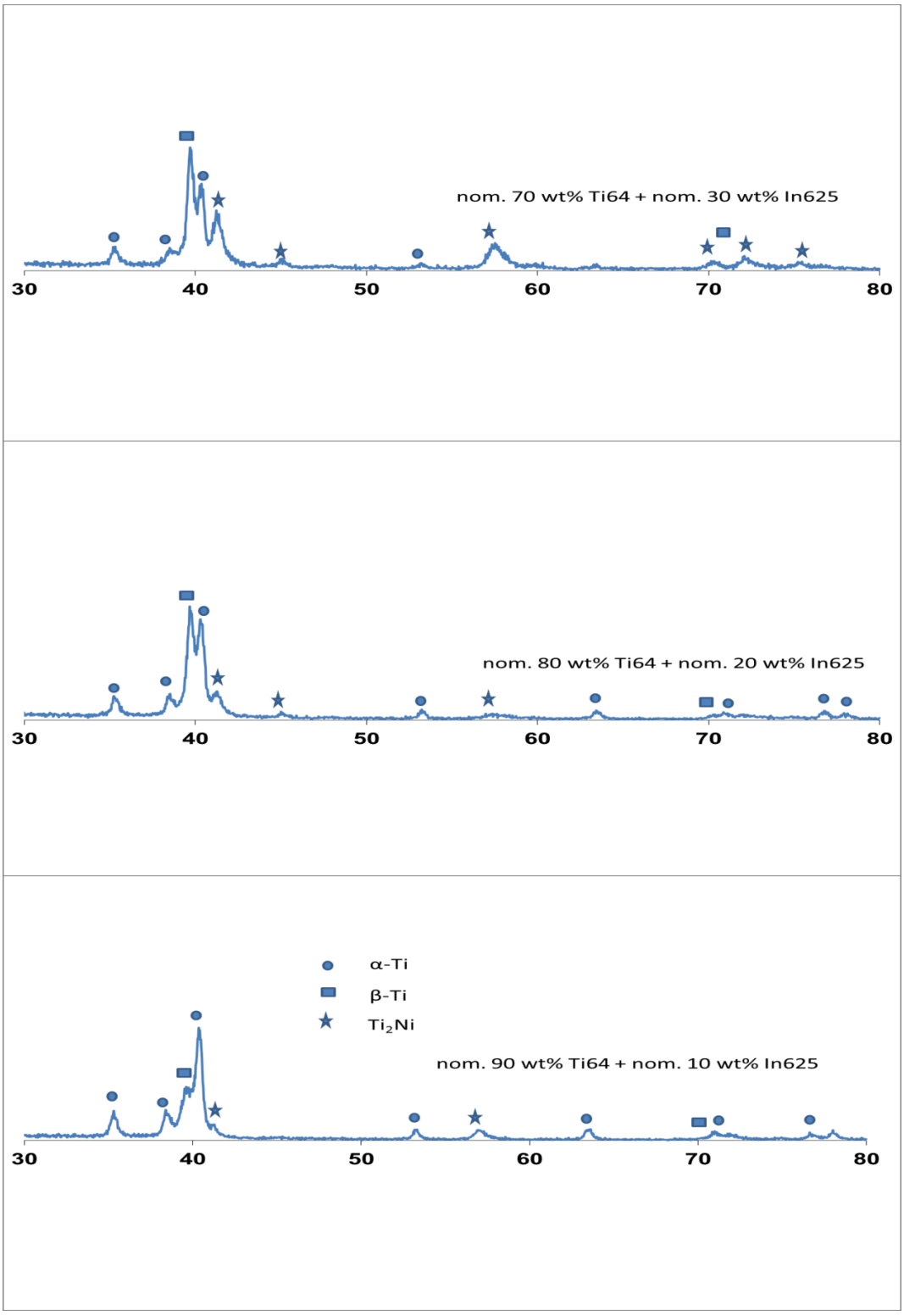

Figure 4.23 X-ray diffraction patterns at 1000 W along the composition gradient measured perpendicular to the laser scanning direction.

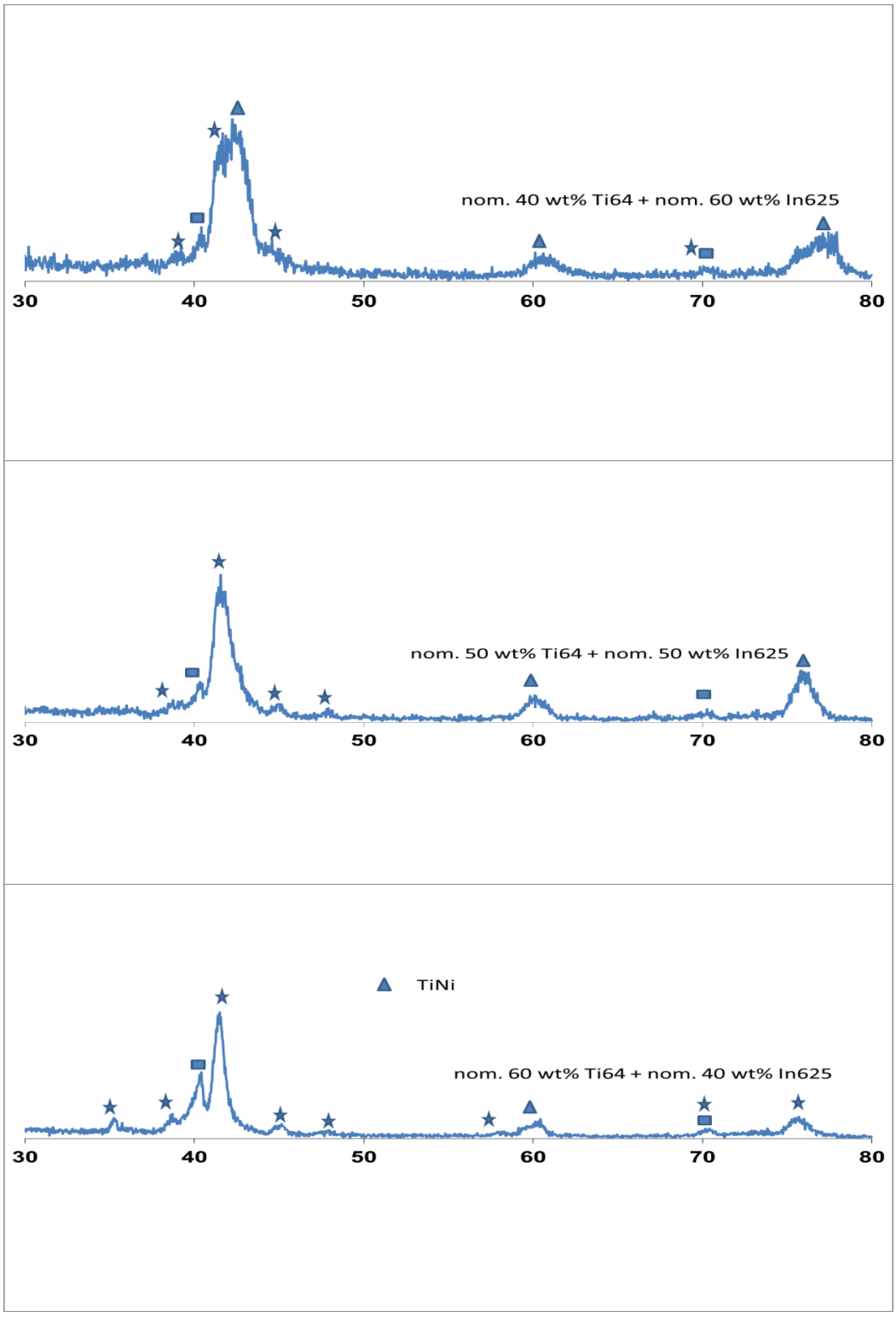

Figure 4.23 X-ray diffraction patterns at 1000 W along the composition gradient measured perpendicular to the laser scanning direction (Cont.).

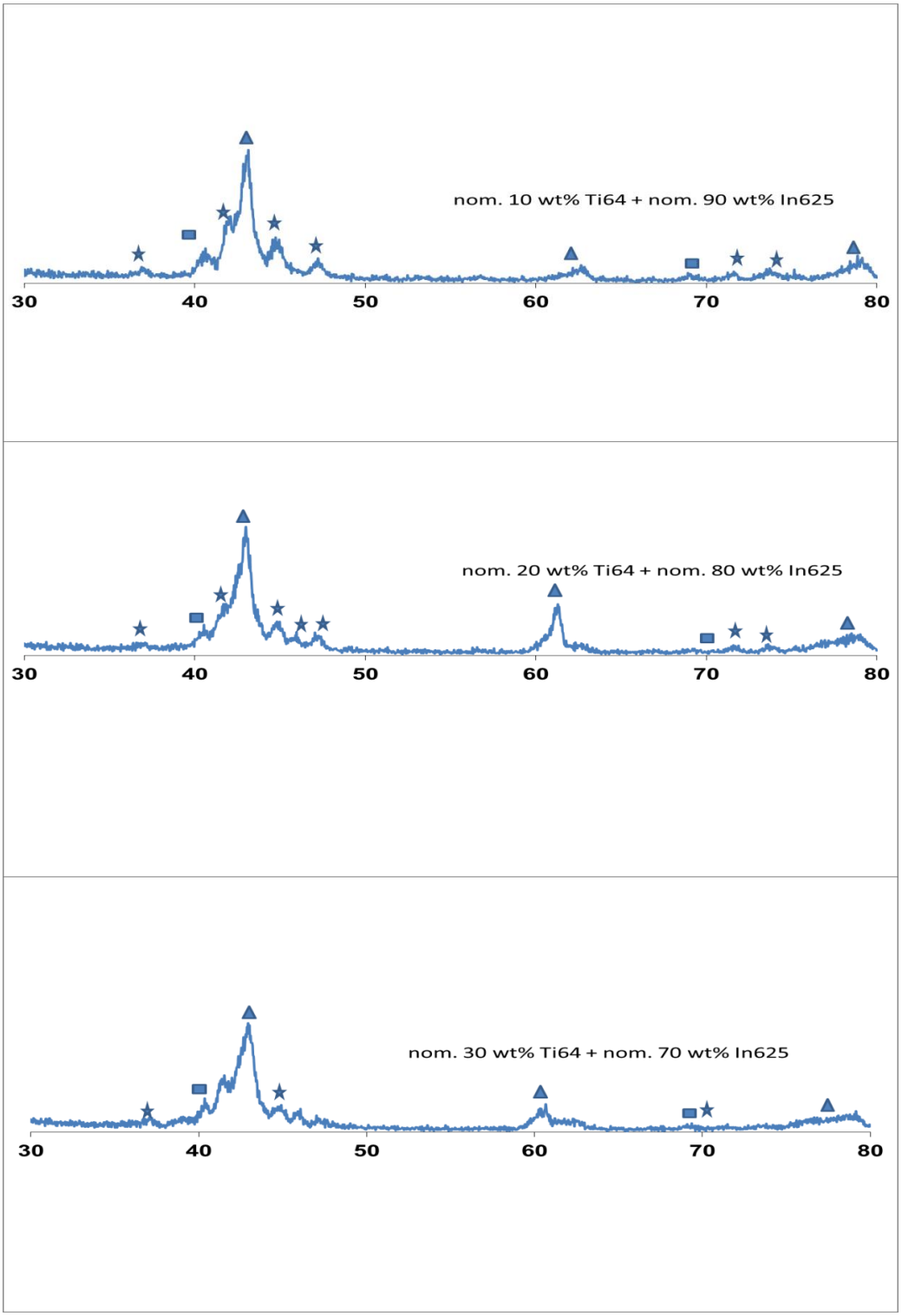

Figure 4.23 X-ray diffraction patterns at 1000 W along the composition gradient measured perpendicular to the laser scanning direction (Cont.).

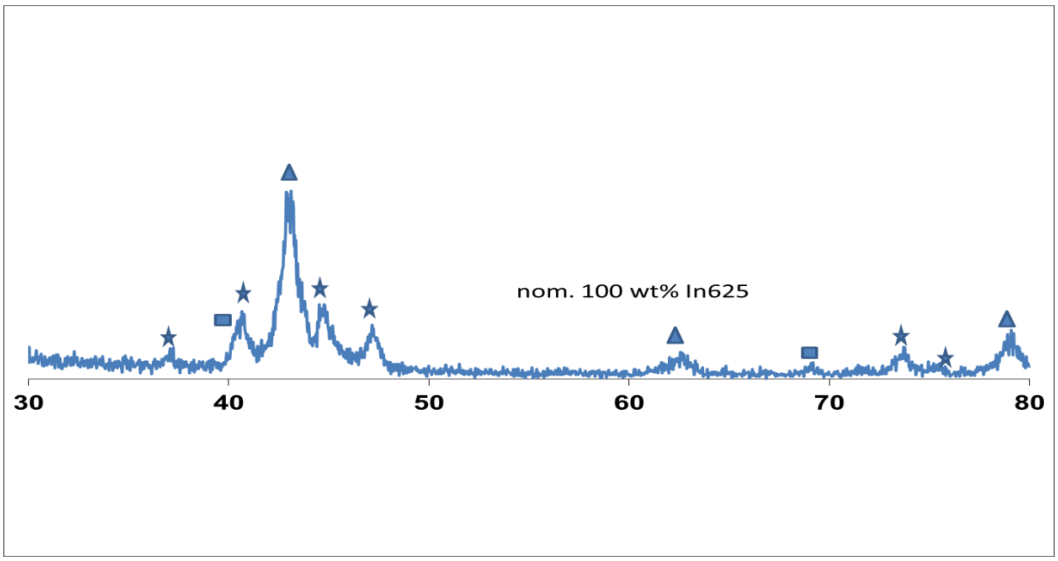

Figure 4.23 X-ray diffraction patterns at 1000 W along the composition gradient measured perpendicular to the laser scanning direction (Cont.).

Figure 4.22 and 4.23 show the XRD patterns of locations along the compositional gradient at 500 and 1000 W. The analyses were performed on cross sections perpendicular to the laser scanning direction. These results indicate that a series of phase evolutions occurred at 500 W:

- α+β to α+β+Ti_2Ni (minor phase)
- α+β+Ti_2Ni (minor phase) to β+Ti_2Ni (major phase)
- β+Ti_2Ni+TiNi (major phase) to Ti_2Ni+TiNi (major phase)

And at 1000 W the evolution along the composition gradient was:

- α+β+Ti_2Ni (minor phase) to α+β+Ti_2Ni (major phase)
- α+β+Ti_2Ni (major phase) to α+β+Ti_2Ni + TiNi (major phase)

At 1000 W no compositional grading was observed at approximately 3 mm away from the workpiece-deposit interface, similarly XRD analysis showed no apparent change in

phase evolution from nominal 40 pct Ti6Al4V + 60 pct Inconel 625 to nominal 100 pct Inconel 625.

More detailed investigation of phase transformations in the Ti6Al4V-Inconel 625 graded material was studied by evaluating the microstructural changes along the compositional gradient using scanning electron microscopy. Figure 4.24(a through m) shows back scattered electron (BSE) micrographs of the microstructures at 500 W at various locations as the nominal powder composition was varied from 10 to 100 pct by weight of Inconel 625. The microstructure of the workpiece shows typical Widmanstätten α-Ti laths in prior β grains. The Ti6Al4V has both the α-stabilizers such as Al and β-stabilizers such as V. The Widmanstätten α-Ti laths (from transformed prior β) lay at different orientations in the matrix with β-Ti found at the interfaces between α-Ti laths. The phase of light contrast in between the α-laths is the β-phase. The width of α-Ti laths on average is about 1 μm. With the addition of Inconel 625, the volume fraction of β-Ti increased, as shown in Fig. 4.24(b). Also, the $\Delta T^{S\rightarrow L}$ increased with the addition of Inconel 625 in the layers, as shown in Figure 4.21. This also resulted in a substantial decrease in the average aspect ratio of α-laths. The microstructure consists of a duplex mixture of coarser α-precipitates and a substantially refined distribution of α-laths.

There is a noticeable change in microstructure in Figure 4.24 (a) and (b). During multilayer deposition process, the solid state annealing of existing layers occurs because of the deposition of subsequent layers on top of the existing layers. This could result in secondary precipitation within the retained β matrix. Thus, the coarser α-precipitates are possibly a result of solid state primary precipitation of α within β that formed initially during the deposition process. The finer scale α-laths are possibly a result of secondary

decomposition of the β matrix during post-deposition annealing. The aspect ratio of primary α precipitates is smaller when compared to secondary α laths. The secondary precipitation can also be due to an incomplete martensitic transformation from β to α'. This phenomenon could be caused by the relatively high martensitic transformation temperature (M_s) due to enrichment of the alloying element in the interlath β regions. In contrast to the bimodal structure in Fig. 4.24(b), there is a substantial decrease in the volume fraction of α phase. The microstructure primarily consists of β phase with small volume fraction of α precipitates dispersed uniformly within the matrix.

Figure 4.24 d, e, f and g shows the microstructure corresponding to a nominal composition of 90 pct Ti6Al4V-10 pct Inconel 625. The microstructure consisted of a mixture of refined α-Ti precipitates in the β phase and discrete Ti_2Ni laths and particles all over. It is possible that α-Ti + Ti_2Ni eutectoid transformation has begun at grain boundaries of β phase. The grain boundary Ti_2Ni particles are nicely shown in the elemental maps in Fig. 4.25(a). The EDS analysis measured the composition of the graded material at this level of Inconel 625 to be Ti-10.17 pct Ni-2.32Cr- 1.02Mo-3.48Al-3.24V.

The volume fraction of Ti_2Ni phase was found to increase gradually when alloy Inconel 625 was increased (Fig. 4.24(e). Apart from being at the boundaries, more Ti_2Ni precipitates were developed within the matrix. Further increase in Inconel 625 powder from nominal 20 to 40 pct by weight resulted in a significant change in the microstructure: the β cellular growth changed to β dendritic. The cellular to dendrite transition (CDT) occurs at some critical conditions relating to thermal gradient (G), the growth rate (V), and alloy composition (Co). The change from cells to dendrites is

probably associated with supercooling arising from compositional effects, i.e. constitutional supercooling in the liquid between the cells causing interface instabilities in the transverse direction. The microstructure consists of β dendrites with β+Ti_2Ni divorced eutectic in the inter-dendritic regions. The elemental maps indicate the β-Ti to be enriched in Cr and Mo, as shown in Fig. 4.25(b). The volume fraction of Ti_2Ni further increased as the nominal Inconel 625 powder composition was increased to 40 and 50 pct. The microstructure also shows presence of β Ti dendrites.

As the nominal content reached to 60 pct by weight of Inconel 625, the microstructure consisted of some β Ti dendrites and discontinuous TiNi particles in theTi_2Ni matrix. At a nominal content of 70 pct by weight of Inconel 625 (Figure 4.24(h)), the microstructure consisted of a mix of two phase TiNi + β-Ti dendrites and anomalous eutectic of TiNi + Ti_2Ni. The anomalous structures are formed as a result of rapid solidification and are discussed in more detail in Section 5. The results of the EDS analysis shows the TiNi phases to be enriched in Cr and Mo (white color); and the β- Ti phase is rich in Ni. The size of the dendrite arms appears to be dependent upon the cooling rate of the thin wall structure. Figure 4.25 (c, d, e, f) shows the elemental map of the microstructure shown in Fig. 4.24(j). As the nominal powder composition changed from 80 to 100 pct the microstructure consisted of a mix of two phase equiaxed TiNi + β-Ti dendrites in an anomalous eutectic structure of Ti_2Ni+TiNi (continuous major phase).

Figure 4.26 shows the microstructural changes along the graded material at 700 W. The microstructures from a through i are comparable to 500 W. The microstructure at a nominal 60 pct by weight of Inconel 625 (Fig. 4.26(h) shows a two phase mix of TiNi + β-Ti particles in an anomalous eutectic structure of TiNi+Ti_2Ni. As the nominal

composition of Inconel 625 reached 70 pct by weight the microstructure consists of TiNi rod and plate like particles in a continuous matrix of Ti_2Ni. When the nominal composition reached 80 wt% (Fig.4.26 (j) the matrix showed a two phase structure of Ti_2Ni + TiNi with TiNi particles in the Ti_2Ni phase. As the composition changed from 90 to 100 pct by weight a fine lamellar eutectic structure of Ti_2Ni+TiNi can be seen in the matrix. Some transgranular cracks can be seen along the TiNi particles. Figure 4.27 shows the microstructural changes along the graded material at 1000 W. The microstructures from a through d in Fig. 4.27 are again comparable to 500 and 700 W. At a nominal composition of 60 and 70 pct by weight of Inconel 625 (Fig. 4.27 e and f) the microstructure consisted of a mixture of TiNi and β-Ti particles in a Ti_2Ni matrix. When the nominal composition changed from 80 to 100 pct by weight (Fig. 4.27 g to i) the microstructure consisted of a two phase mix of TiNi and β-Ti dendrites and an anomalous eutectic of TiNi + Ti_2Ni. The matrix transformed from a non-lamellar to a lamellar structure consisting of Ti_2Ni + TiNi, which looks like a "Chinese-script". There is some influence of laser power on the microstructure along the graded structure. The elemental analysis at 500 W showed lower concentrations of Ti, Al, and V in the top most layers of the graded structure when compared to 700 and 1000 W (Fig.4.20). Despite its higher melting point, Ti melts more than Ni due to its lower thermal diffusivity, making the average composition of each deposited layer richer in Ti. Therefore, in order to reduce mixing between layers and successfully transition to100 pct by weight to Inconel 625 it is necessary to control the heat input to layers by optimizing laser process parameters.

The change in hardness along the gradient direction as a measure of distance from the interface (0 mm means initial substrate-deposit interface) is shown in Fig. 4.28. When

Inconel 625 was introduced into the graded layers, a noticeable increase in hardness was observed, but the hardness was virtually unchanged with the change in laser power. When the nominal composition of Inconel 625 reached 10 pct by weight the hardness reached a local maximum value at 1 mm from the substrate and stayed constant. It is considered that the initial increase in the hardness curve with increasing Inconel 625 was a result of (i) increase in of the amount of β phase and Ti_2Ni precipitates (ii) decrease in volume fraction and refinement of α-Ti laths, and (iii) the increase in content of Inconel 625 resulted in solid solution hardening with β phase being enriched with Cr, Mo and Ni. Beyond this, the hardness increased sharply with the formation of β-Ti + Ti_2Ni anomalous eutectic and precipitation of TiNi particles. When the nominal composition of Inconel 625 changed from 70 to 100 pct by weight the formation of anomalous eutectic of TiNi + Ti_2Ni and a two phase mix of TiNi + β-Ti dendrites resulted in only a very slight change in the hardness values.

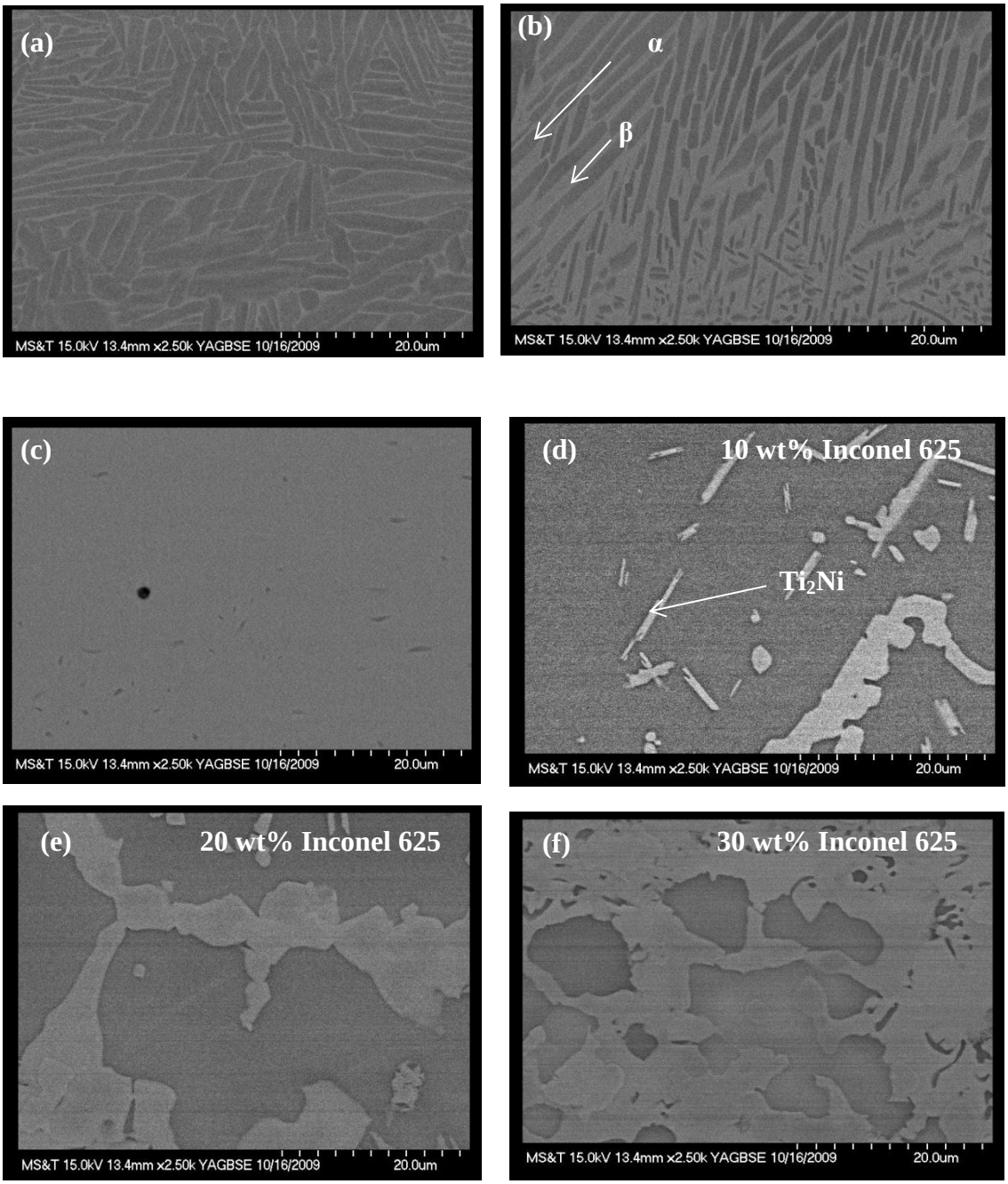

Figure 4.24 Back Scattered Electron images (b through e) of Chem I showing microstructure along the composition gradient at 500 W (a-c) Widmanstätten structure in melt zone of base plate. Note: all the compositions are nominal and calculated from measured data.

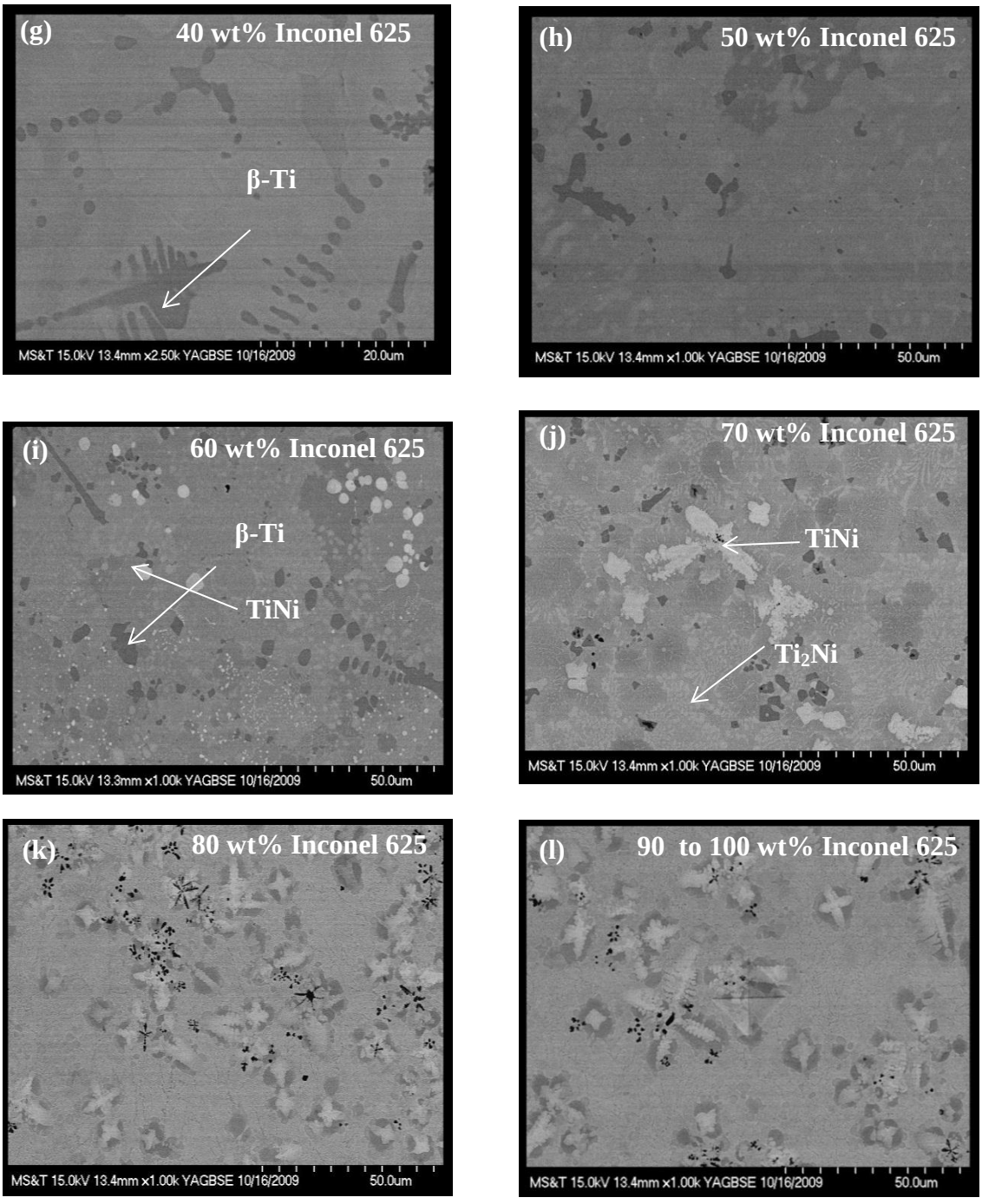

Figure 4.24 Back Scattered Electron images (b through e) of Chem I showing microstructure along the composition gradient at 500 W (a-c) Widmanstätten structure in melt zone of base plate. Note: all the compositions are nominal and calculated from measured data (Cont.).

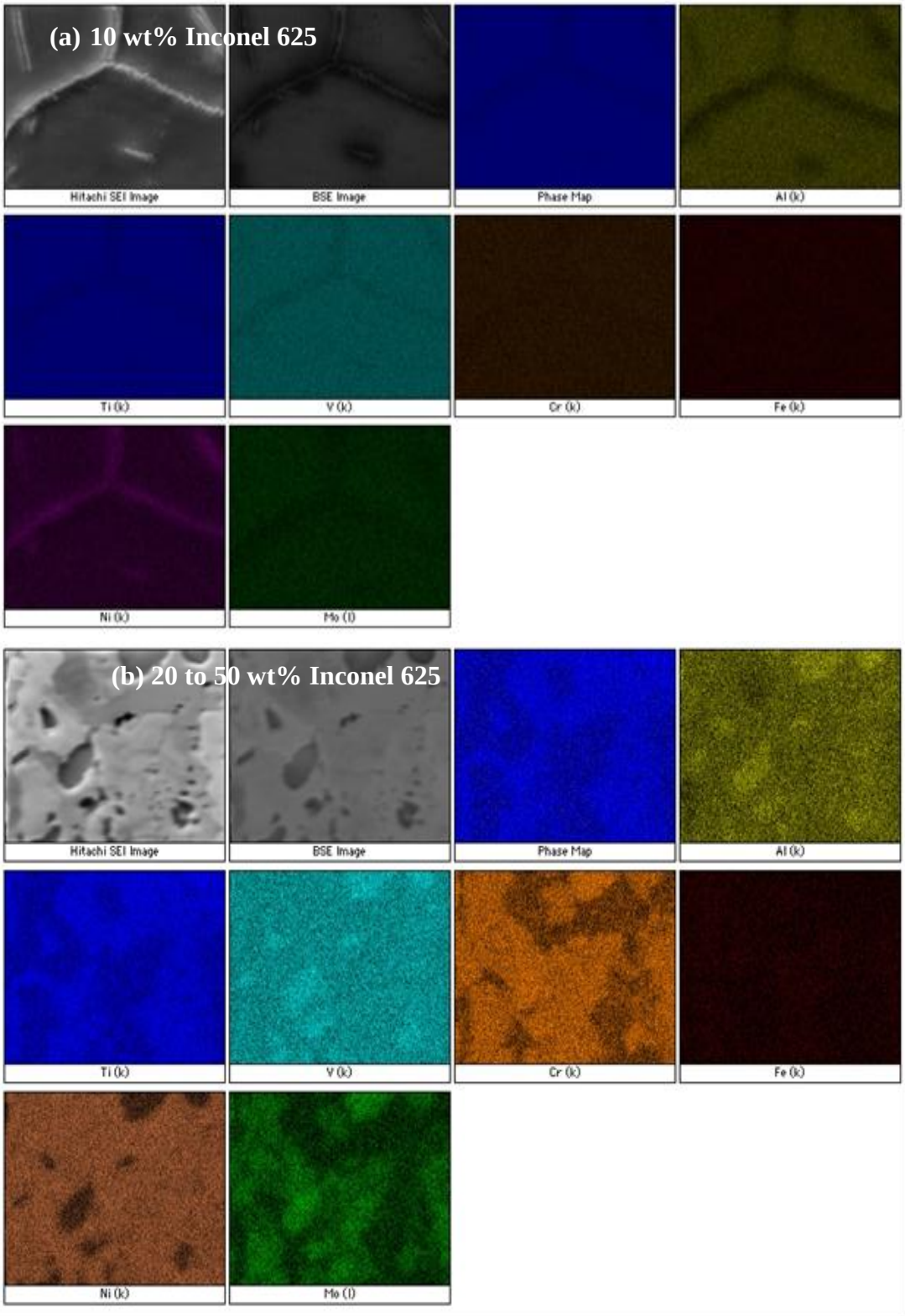

Figure 4.25 X-ray elemental maps showing the elemental distribution in the various phases along the composition gradient for different laser processing conditions. Note: all the compositions are nominal and calculated from measured data.

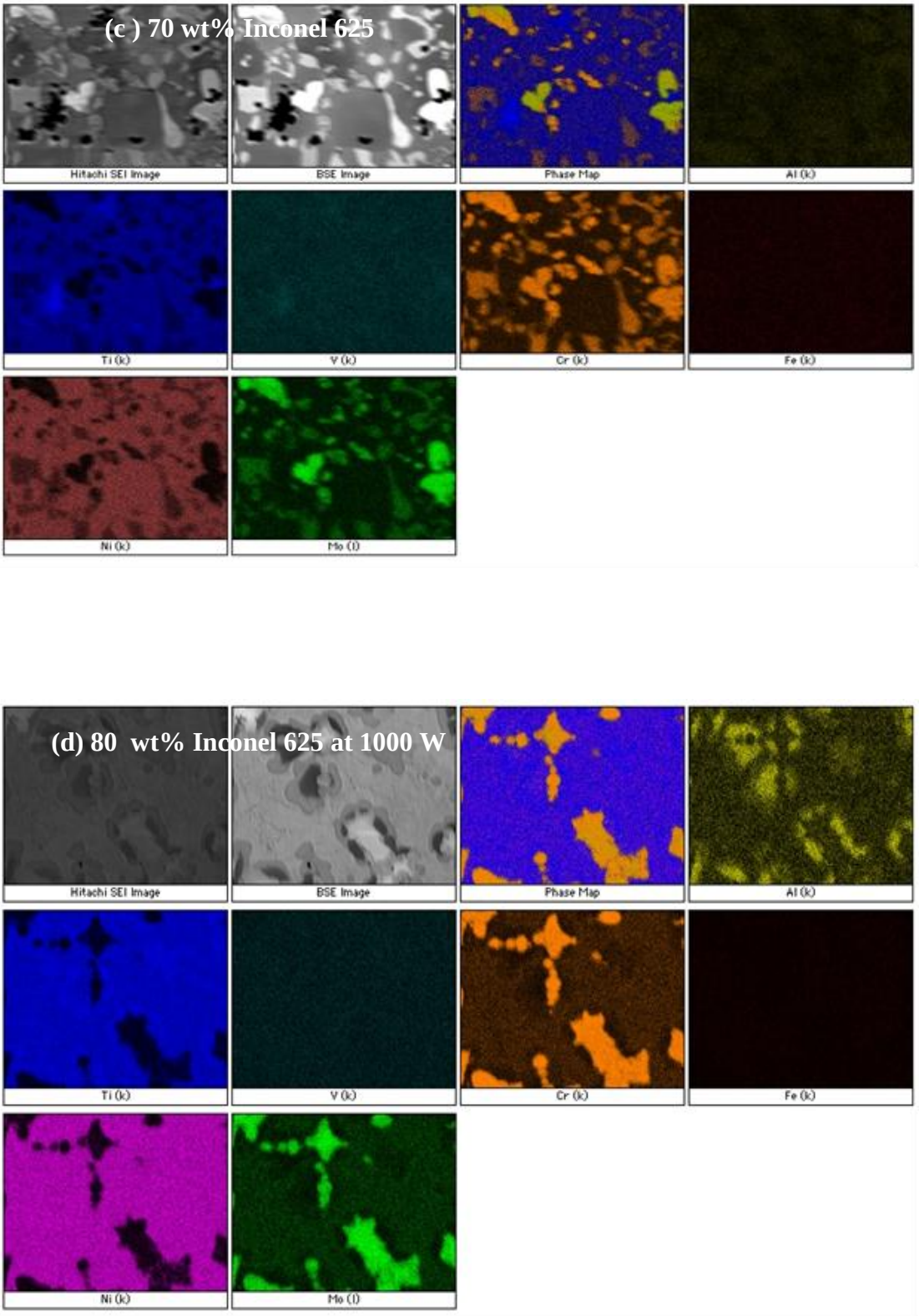

Figure 4.25 X-ray elemental maps showing the elemental distribution in the various phases along the composition gradient for different laser processing conditions. Note: all the compositions are nominal and calculated from measured data (Cont.).

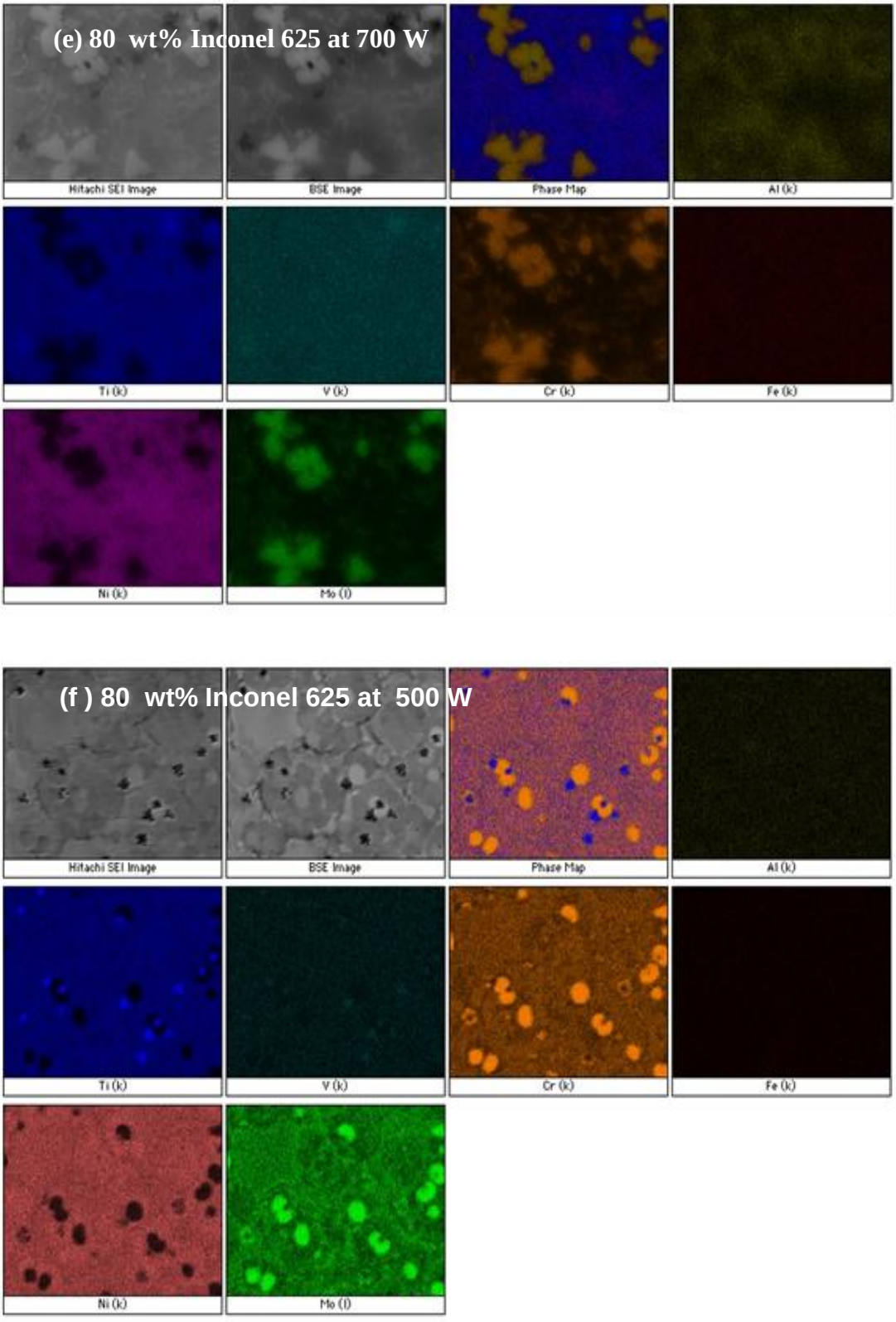

Figure 4.25 X-ray elemental maps showing the elemental distribution in the various phases along the composition gradient for different laser processing conditions. Note: all the compositions are nominal and calculated from measured data (Cont.).

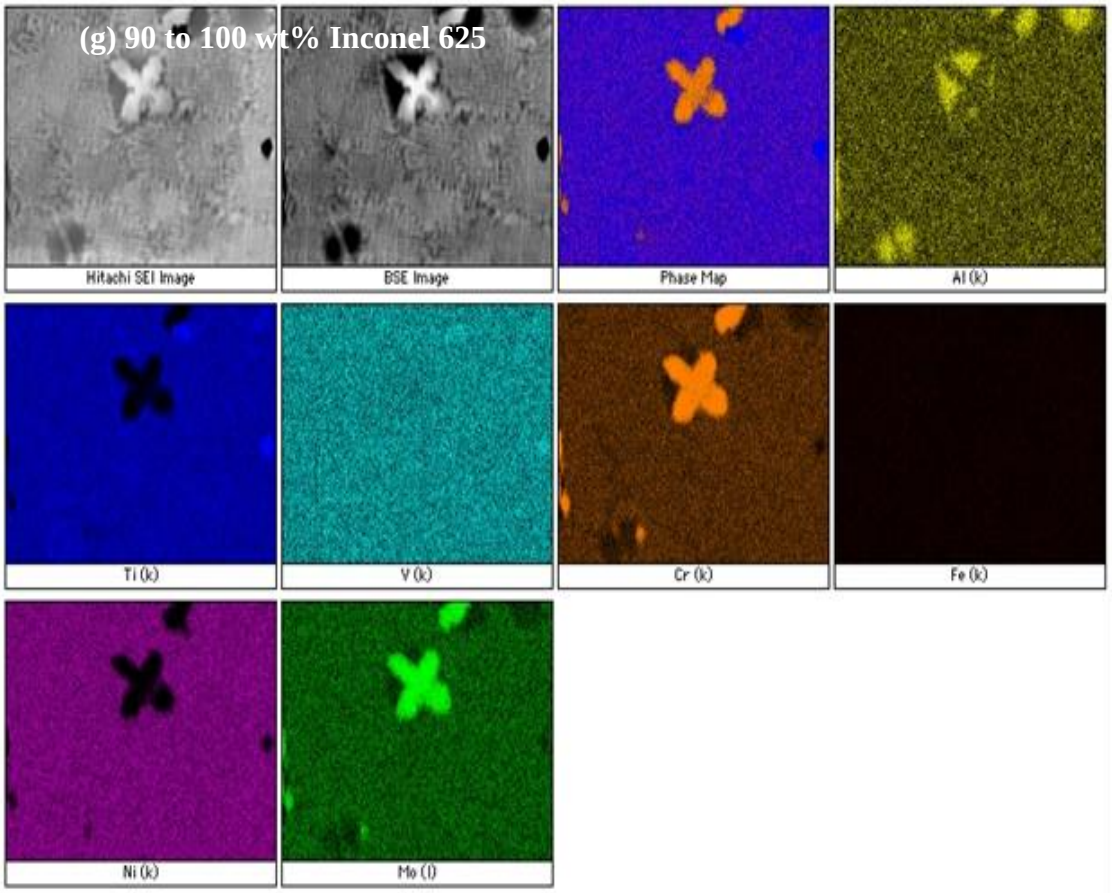

Figure 4.25 X-ray elemental maps showing the elemental distribution in the various phases along the composition gradient for different laser processing conditions. Note: all the compositions are nominal and calculated from measured data (Cont.).

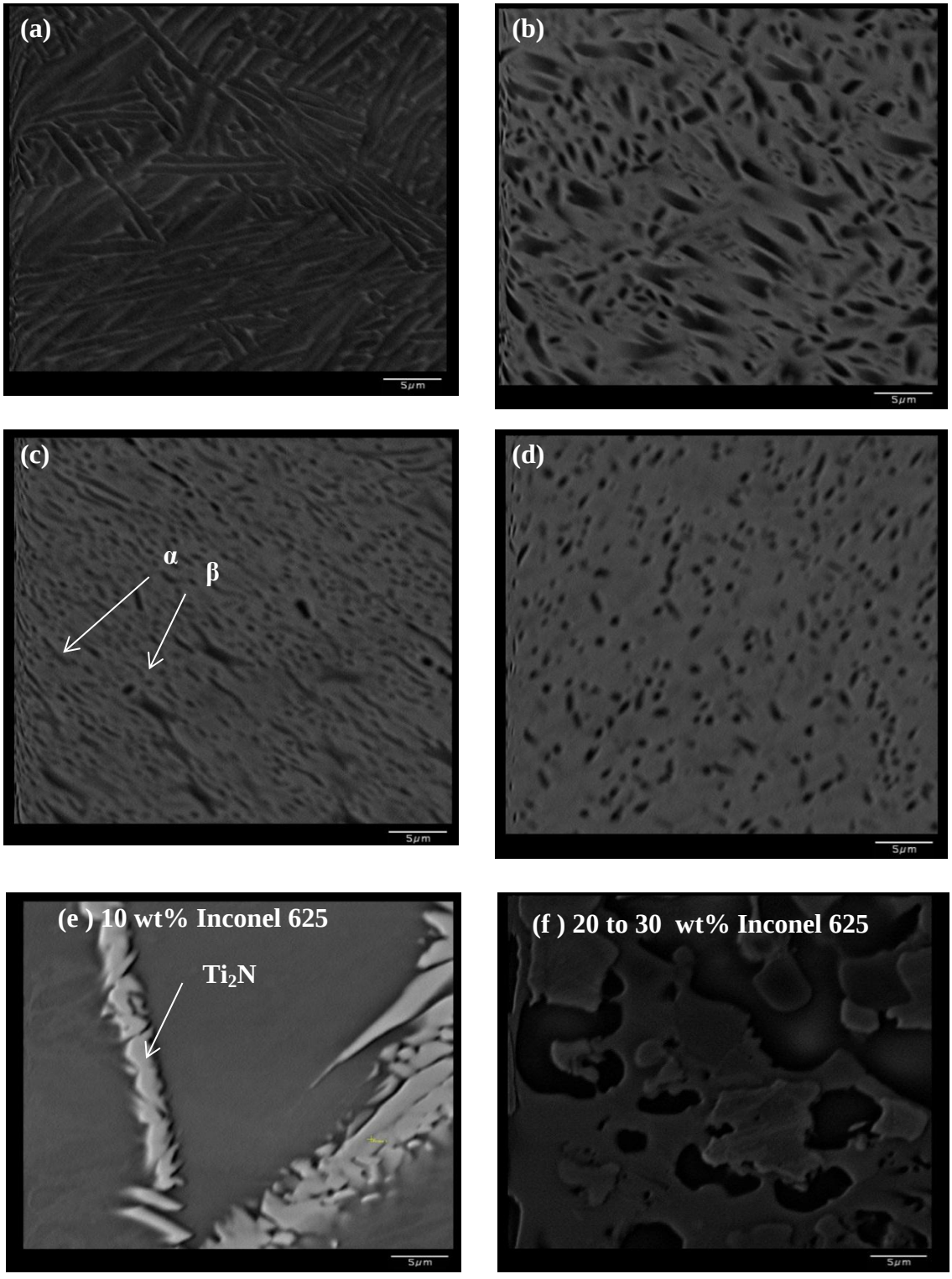

Figure 4.26 Back Scattered Electron images (b through e) of Chem I showing microstructure along the composition gradient at 700 W (a-d) Widmanstätten structure in melt zone of base plate. Note: all the compositions are nominal and calculated from measured data.

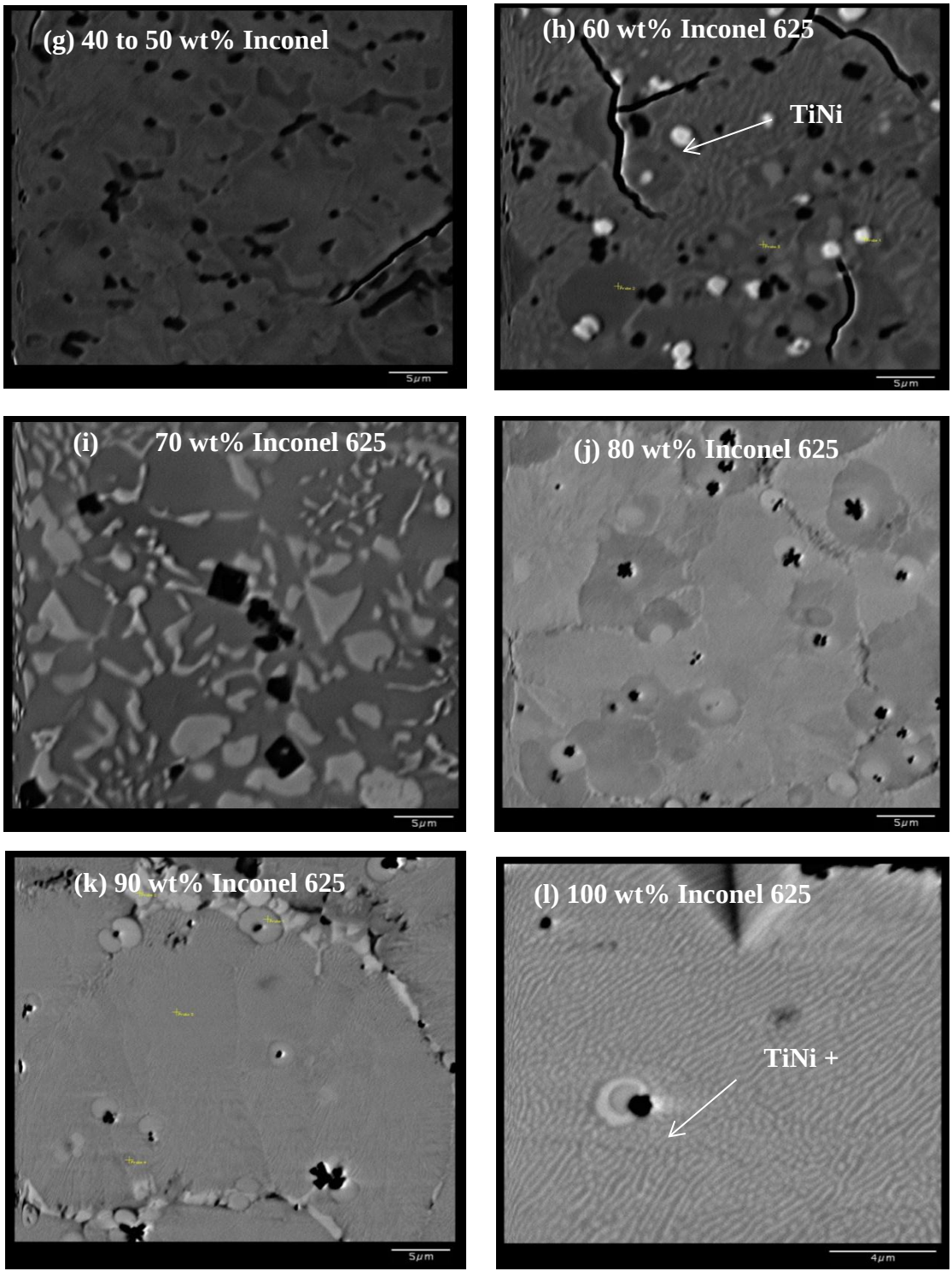

Figure 4.26 Back Scattered Electron images (b through e) of Chem I showing microstructure along the composition gradient at 700 W (a-d) Widmanstätten structure in melt zone of base plate. Note: all the compositions are nominal and calculated from measured data (Cont.).

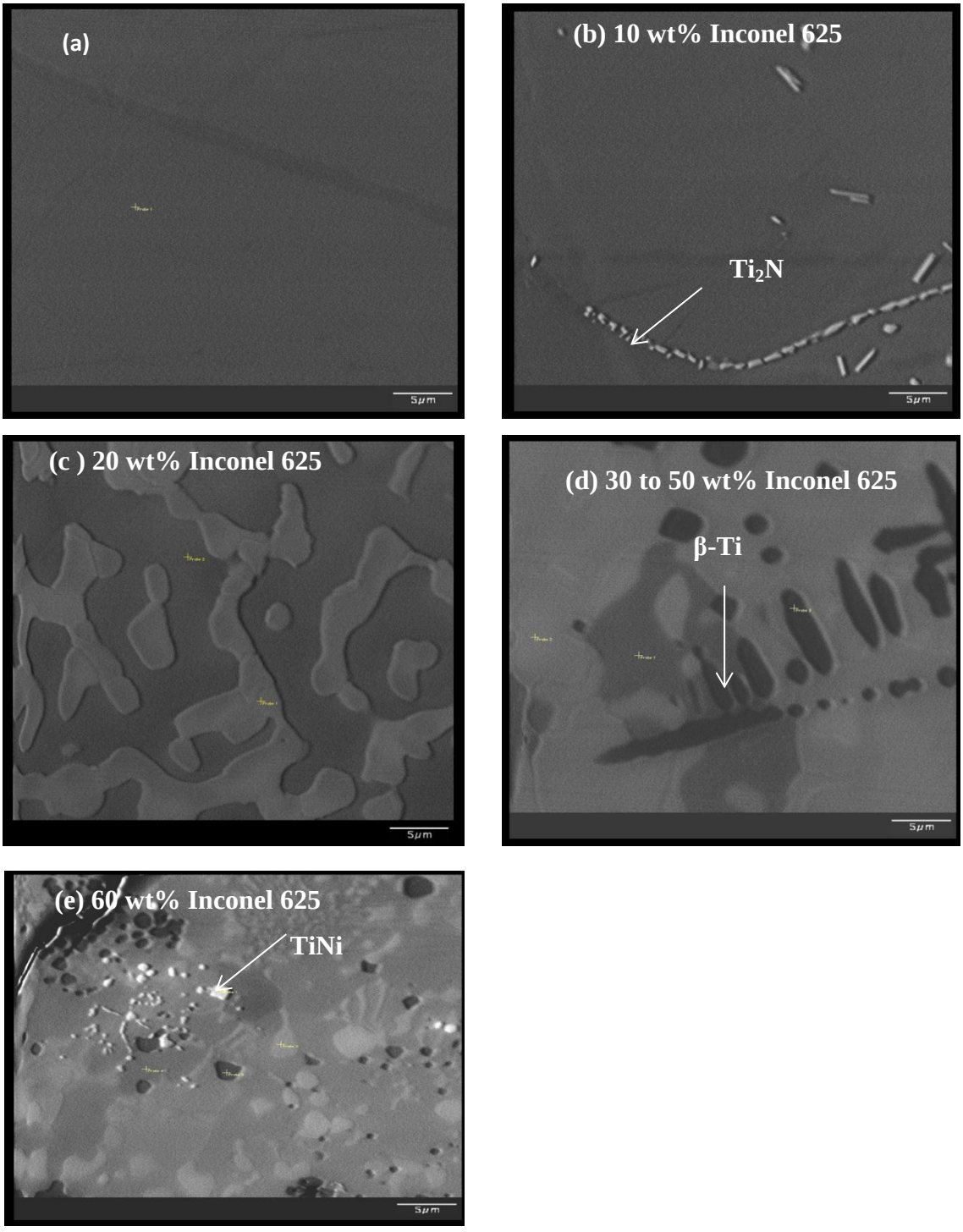

Figure 4.27 Back Scattered Electron images (b through e) of Chem I showing microstructure along the composition gradient at 1000 W (a) Widmanstätten structure in melt zone of base plate. Note: all the compositions are nominal and calculated from measured data.

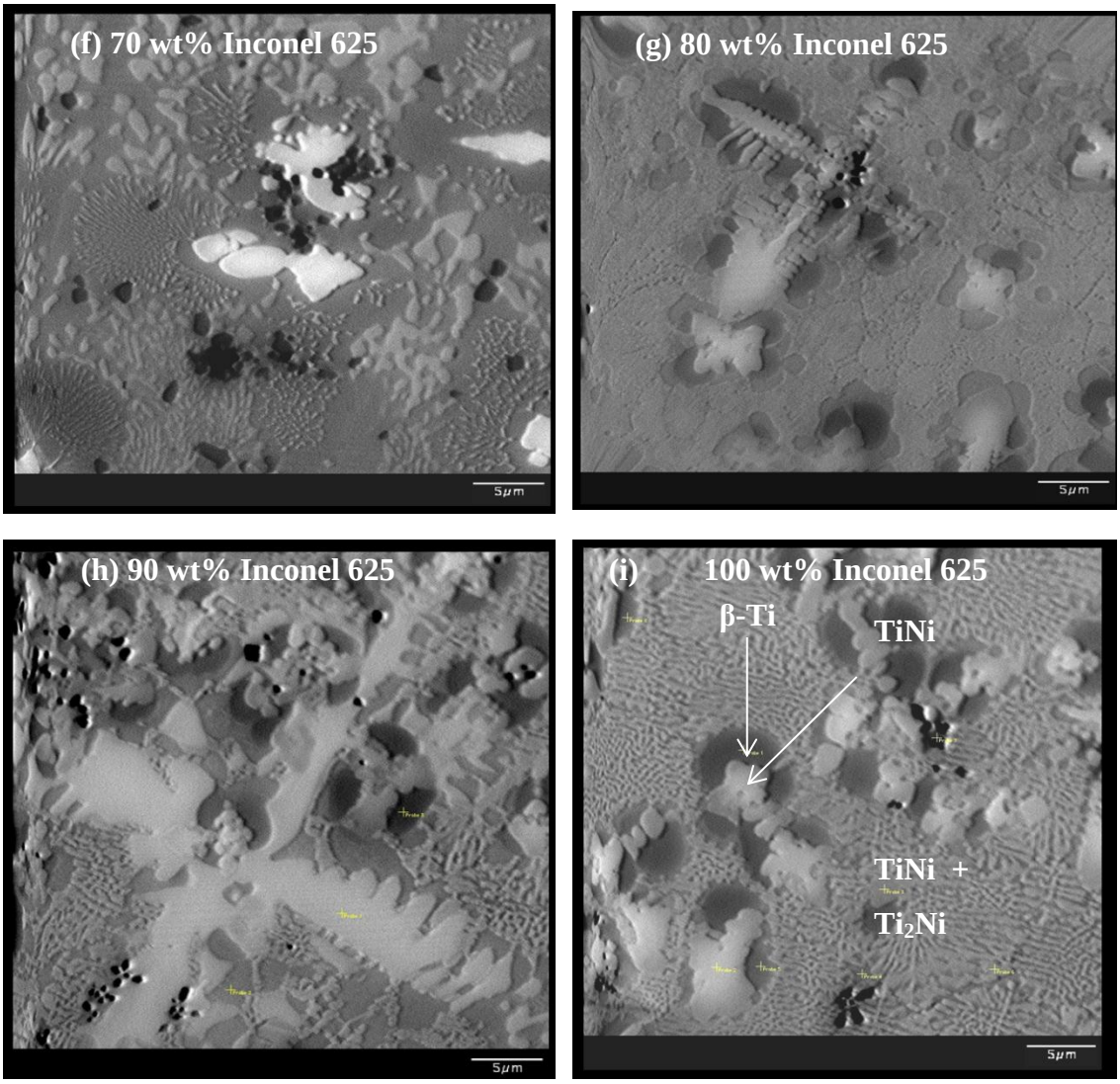

Figure 4.27 Back Scattered Electron images (b through e) of Chem I showing microstructure along the composition gradient at 1000 W (a) Widmanstätten structure in melt zone of base plate. Note: all the compositions are nominal and calculated from measured data (Cont.).

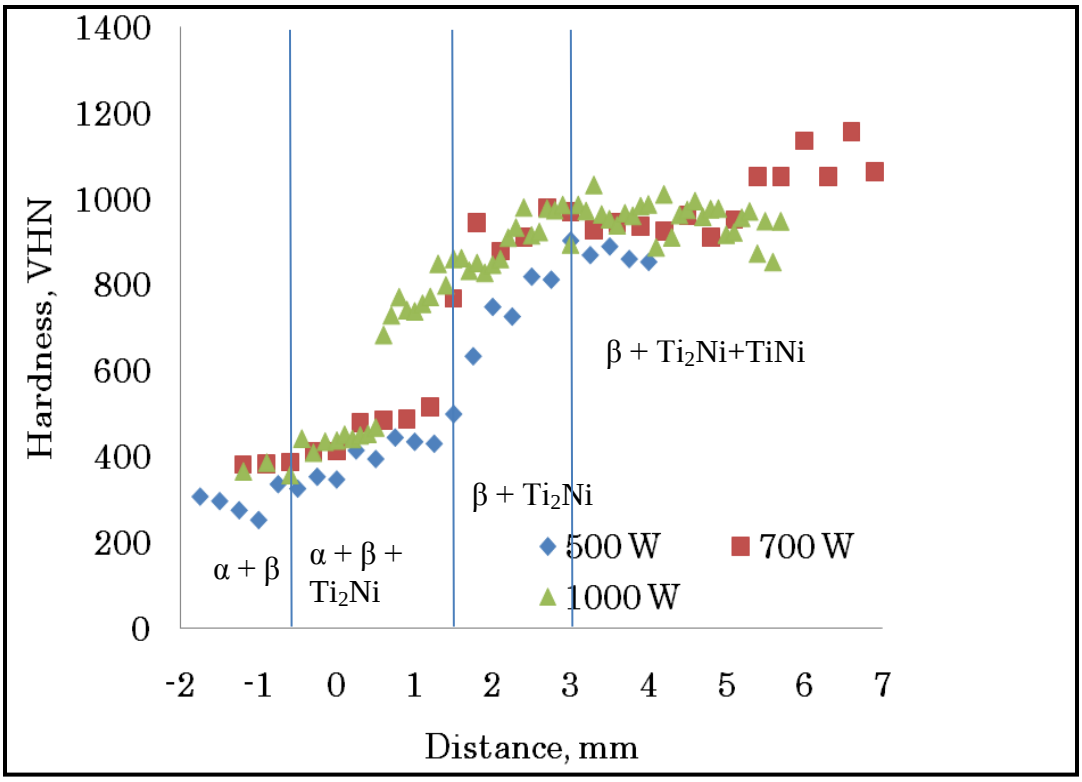

Figure 4.28 Hardness values of the functionally graded material measured along the composition gradient for Chem I, *0 mm = means initial substrate-deposit interface.

4.3.1.2 Non –linear grading under different processing conditions. The non-linear grading in this section refers to Chem II and Chem III. Figure 4.29 (a -i) shows composition profiles of the measured data obtained from standardless EDS analysis of elemental Ni (other elements not shown) along the graded direction compared against the nominal value under different processing conditions. The nominal value here is the wt% of Ni that was experimentally added during the grading process. From the EDS results for all the process parameters shown in Fig. 4.29, we observed that it was not possible to achieve the 'staircase-level' type of transition because of remelting and mixing of previous layers. To achieve a more 'staircase-level' grading it is necessary to minimize

the ‘Delta’. The difference between nominal and experimental wt% Ni is defined as ‘Delta’. And the ‘Delta’ was assigned as the response or output in the factorial design. In order to understand mixing in layers the process parameters like laser power, travel speed, and feed rate were used to construct a 2 level 3-factorial design using Minitab 16.

For all the process settings the value for ‘Delta’ was obtained from the difference in nominal and experimental wt% Ni from the top-most layer of the deposit. Because no further layers will be added to the top-most layer hence the chances of mixing will be minimized. In the design we assumed that the speed 2.12 mm/s for one of the process setting was comparable to 4.23 mm/s and hence assigned a value of 4.23 mm/s; and similarly we assumed 6.75 mm/s for one of the process setting to be comparable to 8.46 mm/s and assigned a value of 8.46 mm/s. When the factorial design was analyzed the ‘Pareto’ chart showed that none of the parameters had any statistical significance i.e. $p > 0.05$ in minimizing the ‘Delta’, as shown in Fig. A.1 (a) attached in the appendix A. In the chart we see that factor-A which is the power (W) has the least influence on the design. Hence the factor-A along with interaction terms AC and AB were removed from the design. This generated a ‘Pareto’ chart with p-values although slightly > 0.05, but gave an R-sq of 89.09 % as shown in Fig. A.1 (b). This means that this DOE has a statistical significance of 89.09 % and not 100 %. The factorial plots in Fig. A.2 show a very flat response for power, but the increasing speed and powder feed rate decreases the ‘Delta’. The contour plots provide an operating window for laser processing to minimize the mixing between layers. In Fig. A.3 with increasing speed and feed rate the ‘Delta’ decreases. And at constant speed the ‘Delta’ decreases with increasing power and feed rate; while no clear relation could be established between power and speed. In summary,

the ideal “stair-case” level grading was attained at only high power and faster travel speeds as shown in Fig. 4.29 (d). But the “delta” was lowest at low power and faster travel speeds (Fig. 4.29 (h)). The compositional data shown in Fig. 4.29 h agrees well with peak temperatures in the thermal model, as shown in Appendix A. At higher powers and faster travel speed the peak temperatures predicted in the layers decreased, the lowest recorded was for low power and faster travel speed.

In reality composition in the FGM can only change as fast as the powder compositions are changed. A gradient is defined as the highest jump in wt% over a certain distance. So there is a “maximum gradient” dependent on both how fast the powder compositions are changed and on the powder yield. At high powder yield more of each composition will be deposited and so the gradient in [wt%/cm] will necessarily be less. Mixing will lead to a lower gradient than the “maximum gradient”. Total mixing prevents any grading, but once the ability to achieve some composition gradient is achieved then there are many factors to consider. If the mixing is “moderate” it will require more material to be deposited to get from say pure A to almost pure B. But the gradient will be less steep and that may lead to lower stresses. If the mixing is “low” then the gradient will be steeper leading to less material being deposited to get from composition A to composition B. In terms of compositions that cause problems because they are favorable for the formation of brittle phases, moderate and low mixing seem to be no different. In the case of Ti6Al4V/Inconel 625 FGMs, close to the same Ti/Ni ratios will occur somewhere in the deposit whether the mixing is moderate or low. But composition gradients and thermal history will be different in the case of different mixing levels. The grading strategy was primarily changed from linear to non-linear to see if the

microstructure could be tailored to minimize the precipitation of Cr and Mo enriched TiNi phase in the graded layers.

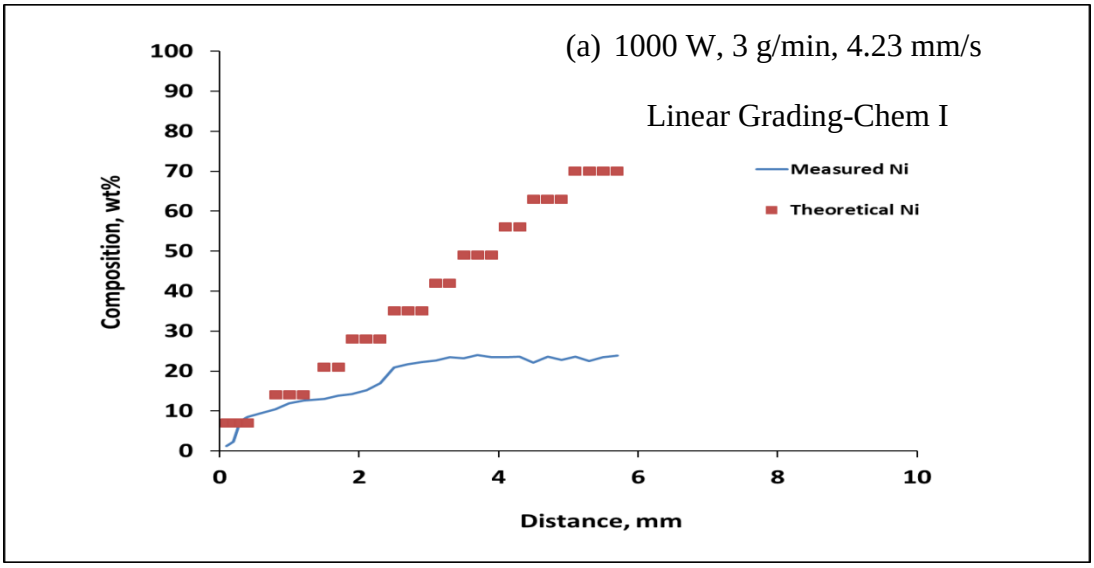

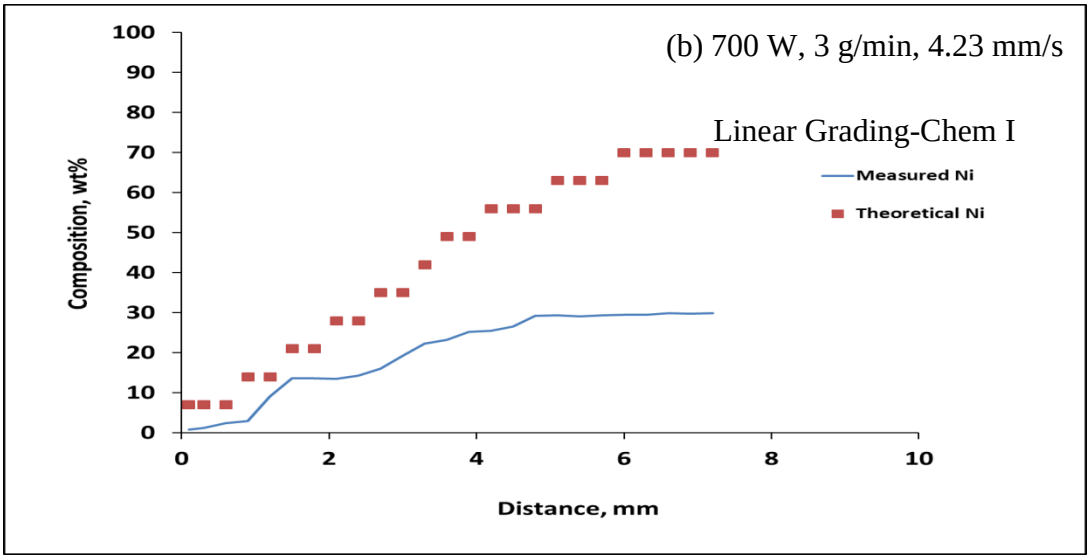

Figure 4.29 Plot against nominal composition vs. measured elemental Ni obtained from EDS of Ti6Al4V-Inconel 625 FGM for various processing parameters and grading styles.

"Fig. A.X" refers to figures attached in the appendix

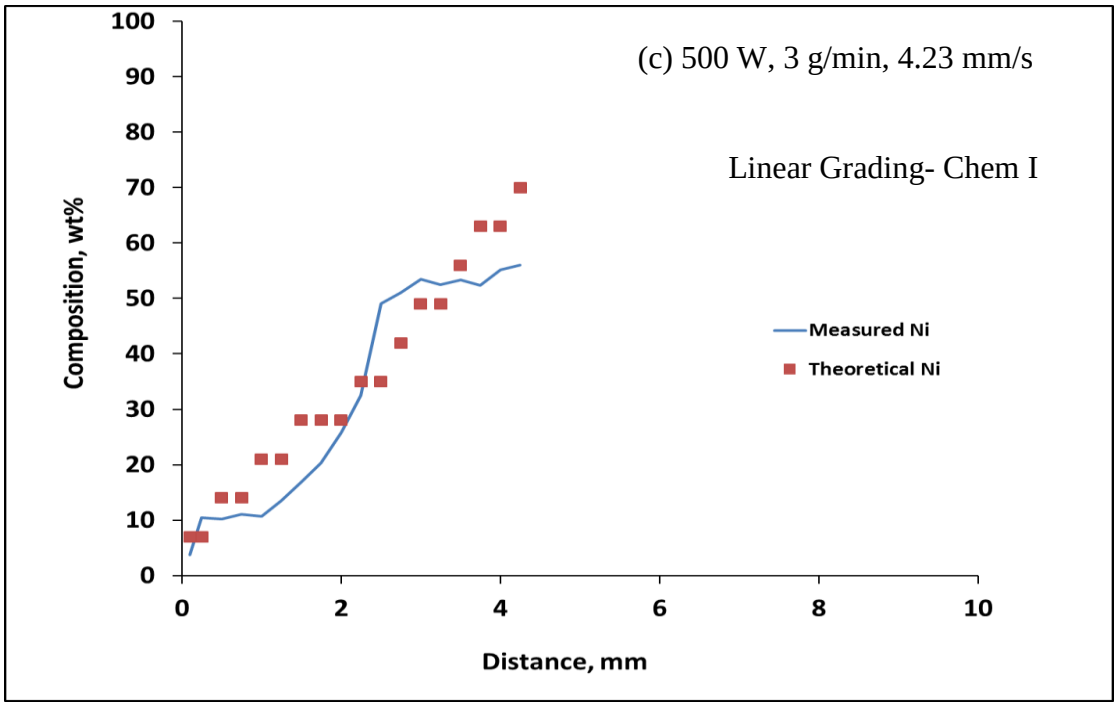

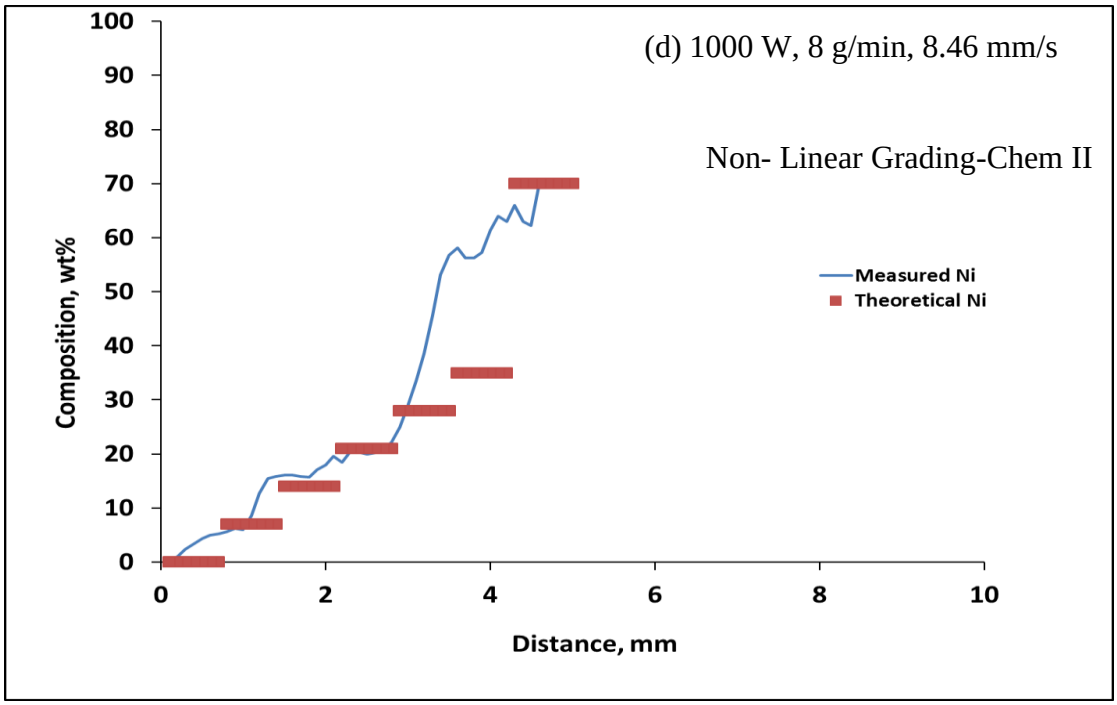

Figure 4.29 Plot against nominal composition vs. measured elemental Ni obtained from EDS of Ti6Al4V-Inconel 625 FGM for various processing parameters and grading styles (Cont.).

.

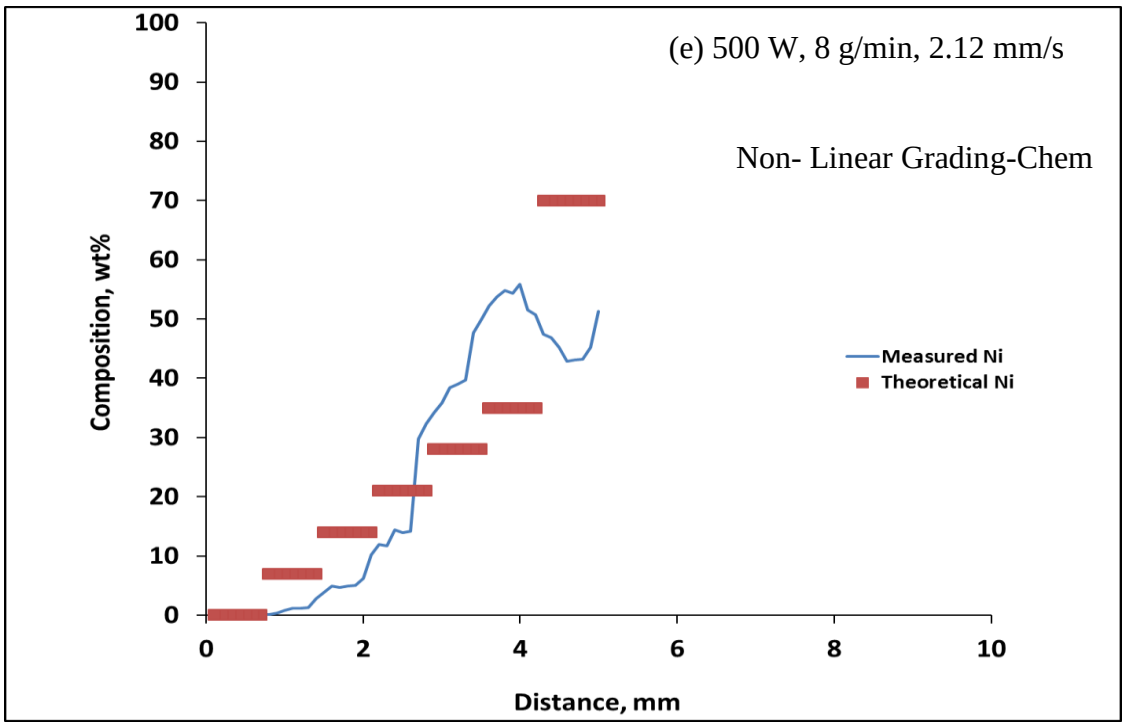

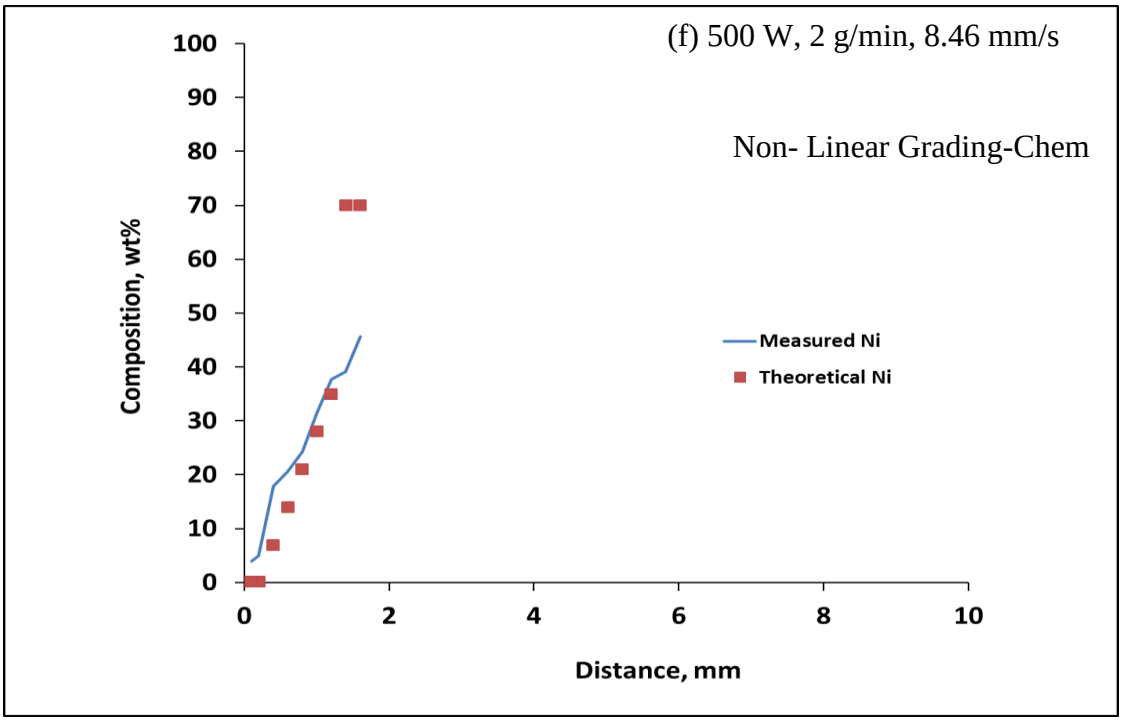

Figure 4.29 Plot against nominal composition vs. measured elemental Ni obtained from EDS of Ti6Al4V-Inconel 625 FGM for various processing parameters and grading styles (Cont.).

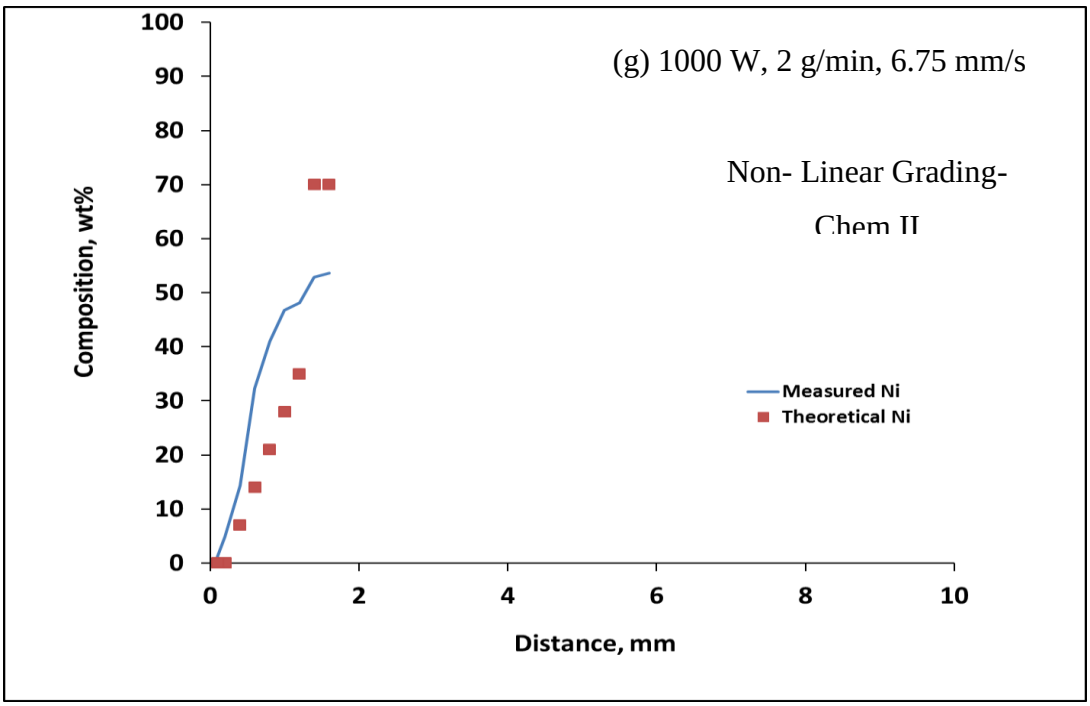

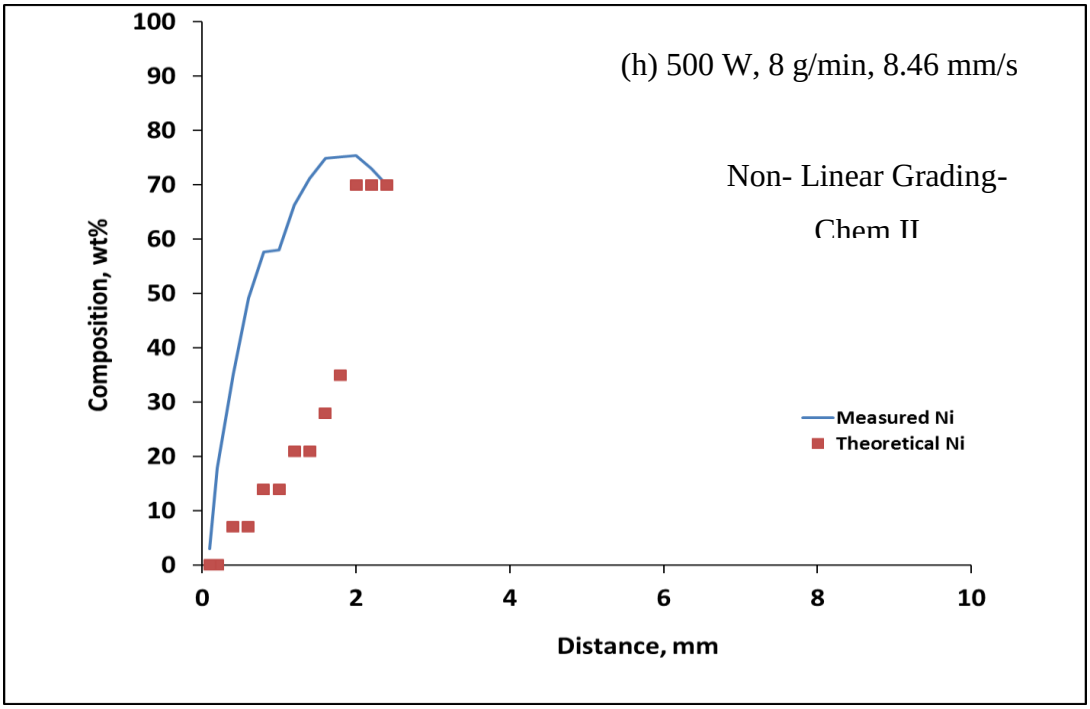

Figure 4.29 Plot against nominal composition vs. measured elemental Ni obtained from EDS of Ti6Al4V-Inconel 625 FGM for various processing parameters and grading styles (Cont.).

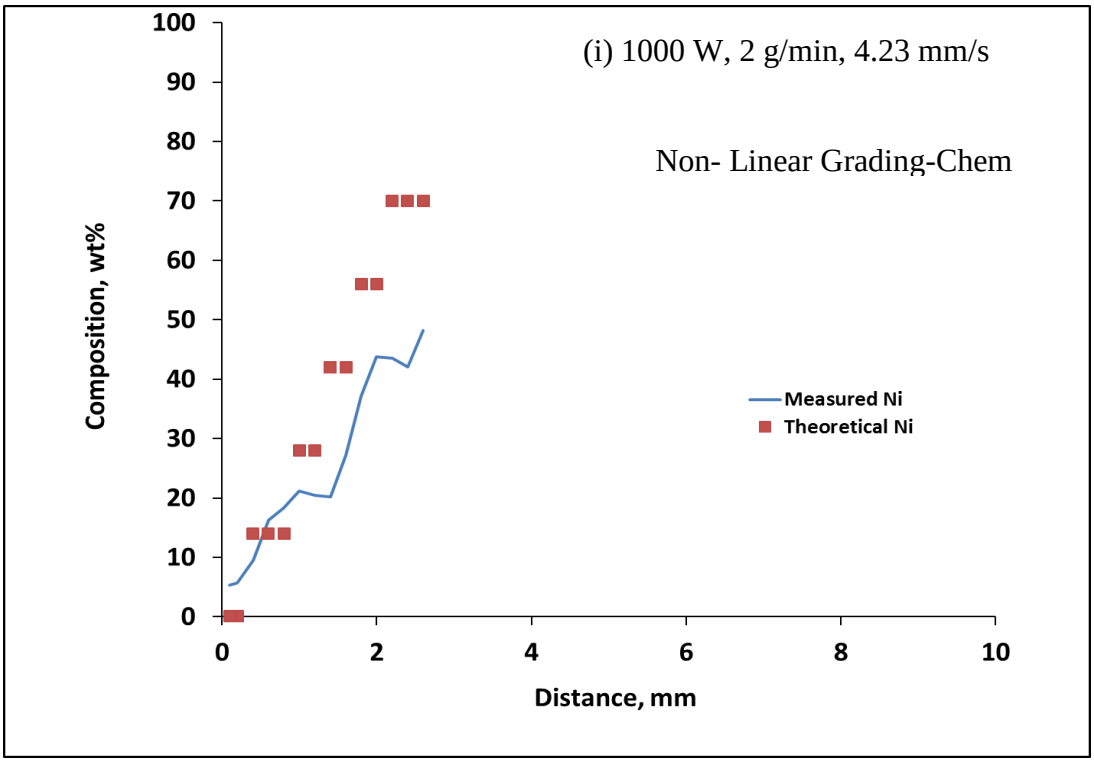

Figure 4.29 Plot against nominal composition vs. measured elemental Ni obtained from EDS of Ti6Al4V-Inconel 625 FGM for various processing parameters and grading styles (Cont.).

.

Figure A.4, A.5 & A.6 shows the XRD patterns of locations along the compositional gradient for Chem II and Chem III. The analyses were performed on cross sections parallel to the laser scanning direction. This means that the layers were ground to a certain depth prior to performing XRD analysis. The experimental data was compared to the thermodynamic modeling results achieved using FactSage V 6.0. The calculations were performed to predict the phases that would precipitate if two layers with different compositions reacted under equilibrium conditions. More details on the model are discussed in Section 2. The solution databases used for the calculations were [FACT] and [SGSL]. In the modeling only the nominal chemical constituents were entered for each of the graded composition layers. The pressure was fixed at 1 atm. The possible product

species for pure liquids and solids were selected for the graded layer and the outputs were saved as different streams. For the short times involved in the LMD process not much would happen in the way of microstructural evolution at any temperature below $0.4*T_m$ (K) (T_m, melting point), which is around 500^oC for Ni and Ti. The quantitative data of the phases was tabulated at 100^oC. The equilibrium products satisfied the mass balance and attained minimum Gibbs free energy state.

The quantitative data obtained from Factsage was experimentally verified with the XRD. Tables A.1 and A.2 show the quantitative data for the two deposition strategies. Factsage predicted a lot of minor and major phases that would form under equilibrium conditions. The Factsage prediction for Chem II showed the following major phases along the graded structure:

- α-Ti (major phase) + Ti_2Ni
- to α-Ti + Ti_2Ni
- to α-Ti + Ti_2Ni (major phase)
- to Ti_2Ni (major phase) + TiNi
- to $TiNi_3$.

The Chem III showed phase evolution from

- α-Ti (major phase) + Ti_2Ni
- to Ti_2Ni (major phase) + α-Ti
- to Ti_2Ni (major phase) + TiNi
- to TiNi (major phase) + $TiNi_3$
- to $TiNi_3$ finally at the top most region of the graded structure.

Apart from the above major phases the modeling also predicted Ti_3Al, V, Cr, Mo, Fe_2Ti, $NbCr_2$, Cr_3Mn_5, AlNi, CoAl, $Ni_{24}Cr_{20}Mo_{12}$, Ni, $MoNi_4$, $NbFe_2$, Ni_3Al and Fe. Most of the phases predicted by the model were present in the minority except for Ti_3Al, V, Cr and Mo. The XRD quantitative analysis was performed for the above to confirm the data predicted by the thermodynamic modeling. Tables A.1 and A.2 also show the quantitative representation of the XRD data. The deposition strategy Chem II at 1000 W laser power showed phase evolution from:

- α-Ti + β-Ti
- to α-Ti + β-Ti "*" + Ti_2Ni to (minor)
- to α-Ti (major phase) + β-Ti"*" + Ti_2Ni + TiNi (< <)
- to β-Ti"*" + Ti_2Ni + TiNi
- to Ti_2Ni + TiNi + Ti_3Ni (major phase).

In case of deposition strategy Chem II at 500 W the phases evolved from:

- α-Ti + β-Ti
- to α-Ti + β-Ti"*" + Ti_2Ni to (minor)
- to β-Ti"*" + Ti_2Ni
- to β-Ti"*" + Ti_2Ni + TiNi
- to Ti_2Ni + TiNi + Ti_3Ni (major phase).

In case of deposition strategy Chem III the phases evolved from:

- α-Ti + β-Ti

"*"β-Ti was not quantifiable by XRD software. The equilibrium predictions by Factsage did not indicate the presence of β-Ti either. The only evidence found is presence of β-Ti in microstructures and supported by literature.

- to α-Ti (major phase) + β-Ti"*" + Ti_2Ni
- to β-Ti β-Ti"*" + Ti_2Ni
- to β-Ti"*" + Ti_2Ni (major phase) + TiNi.

Unlike Factsage the XRD showed 2θ peaks for Cr_5Al_8, V_5Al_8, $AlNbTi_2$; and FeTi and $Mo_{0.84}Ni_{0.16}$ instead of Fe_2Ti and $MoNi_4$. Some of the major 2θ peaks of Ti_3Al overlapped with Ti_2Ni; and V and FeTi overlapped with TiNi and hence could not be quantified. Therefore, their presence in the graded layers cannot be ruled out. Also, β-Ti could not be very well quantified by the software. Gamma prime (γ', Ni_3 (Ti,Al)), and gamma (γ, Ni) phase were detected by the XRD in the top-most layer of the graded structure for deposition strategy Chem II at 500 and 1000 W. Since mixing occurs in the melt pool it is impossible to restrict the movement of various alloying elements across the graded layers in the laser metal deposition process. Therefore, only a 95 percent grading to Inconel 625 was achieved in the top-most region.

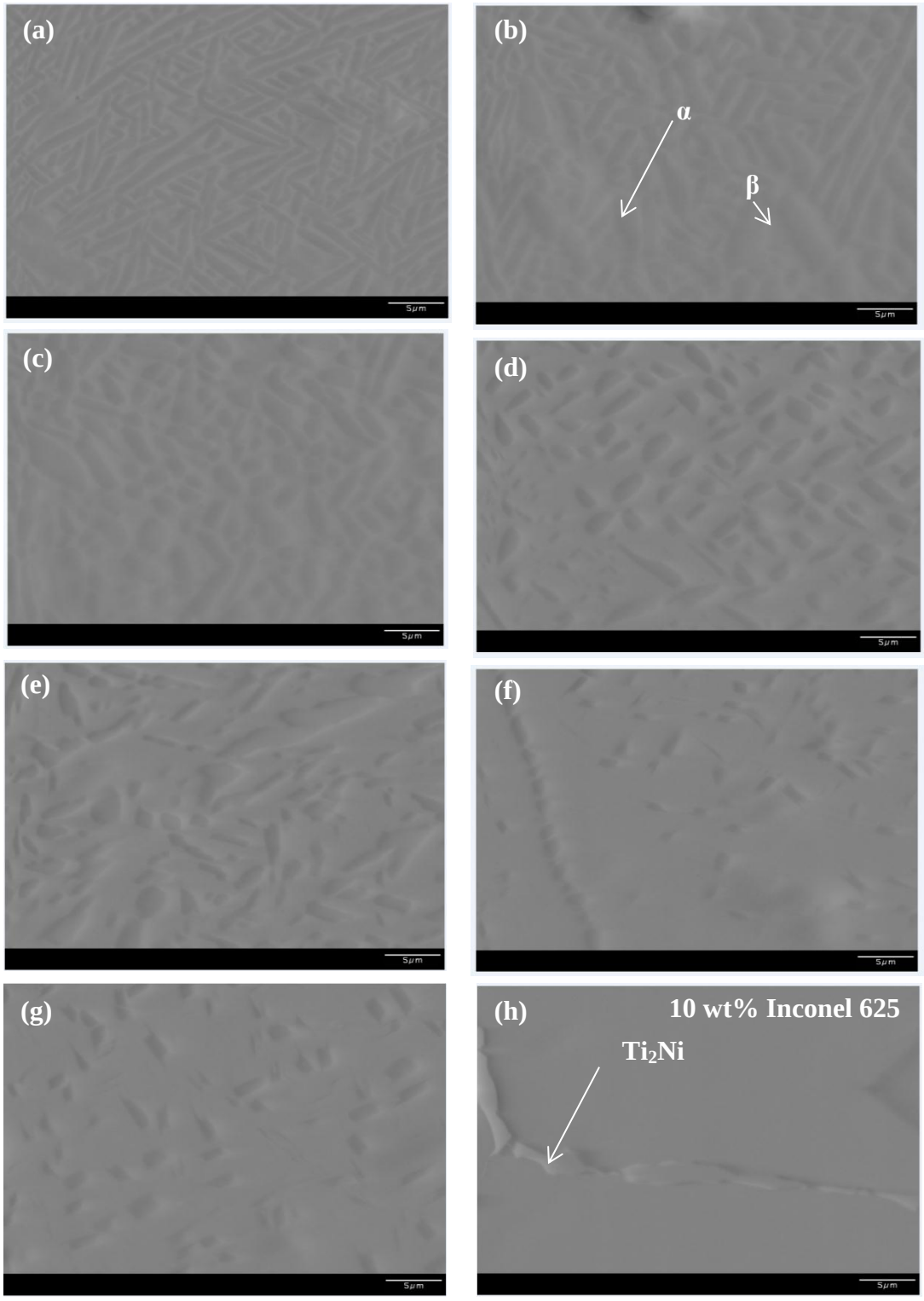

Figure 4.30 Back Scattered Electron images of chem II (a through k) showing microstructure along the composition gradient at 500 W; (a-g) microstructure in melt zone of base plate. Note: all the compositions are nominal and calculated from measured data.

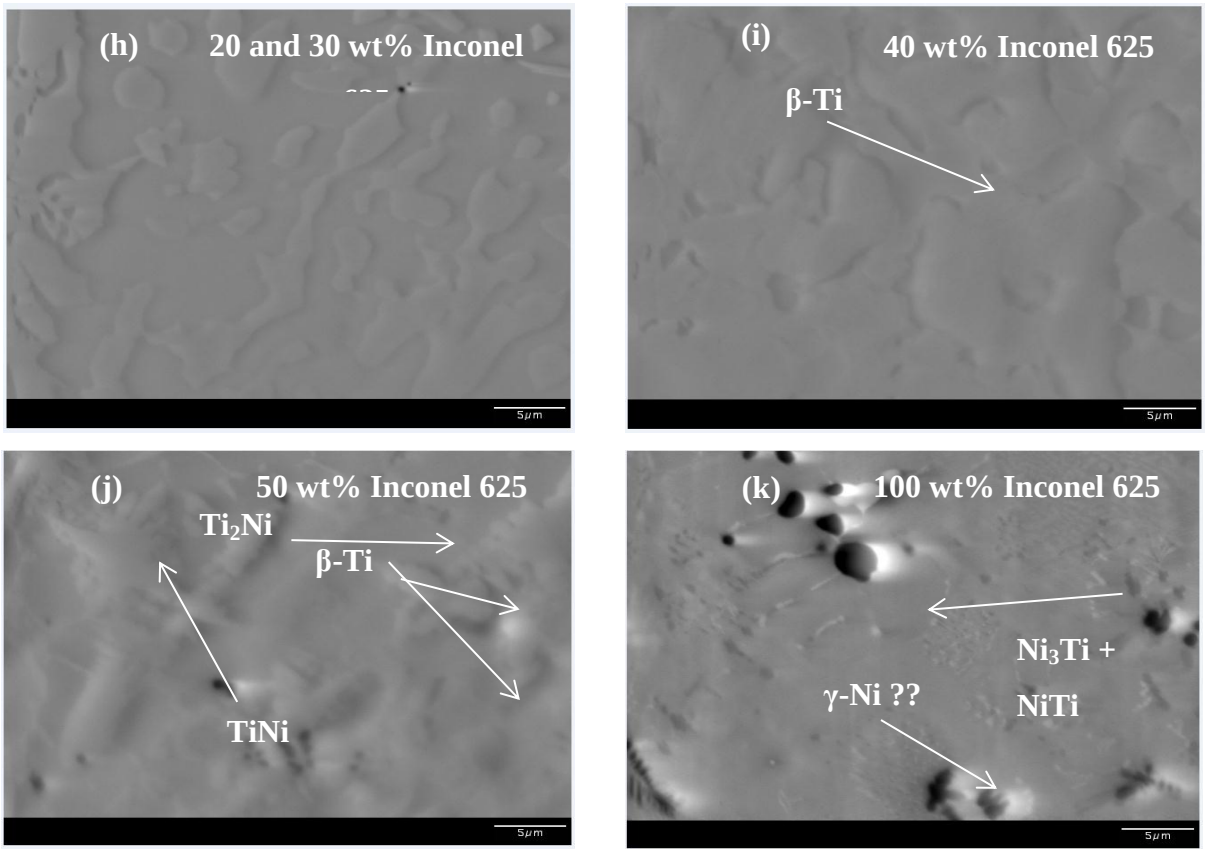

Figure 4.30 Back Scattered Electron images of chem II (a through k) showing microstructure along the composition gradient at 500 W; (a-g) microstructure in melt zone of base plate. Note: all the compositions are nominal and calculated from measured data (Cont.).

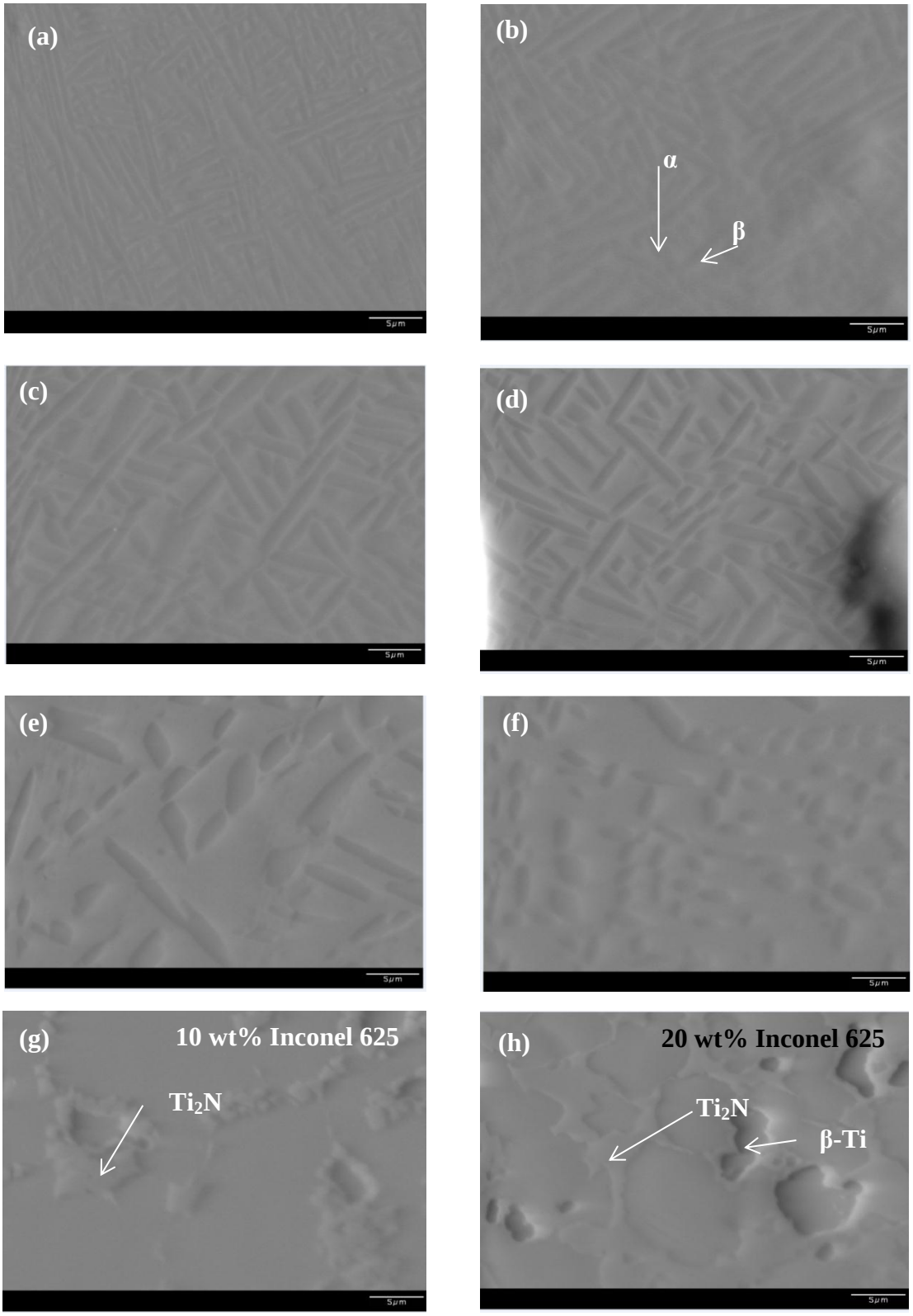

Figure 4.31 Back Scattered Electron images of Chem II (a through l) showing microstructure along the composition gradient at 1000 W; (a-f) microstructure in melt zone of base plate. Note: all the compositions are nominal and calculated from measured data.

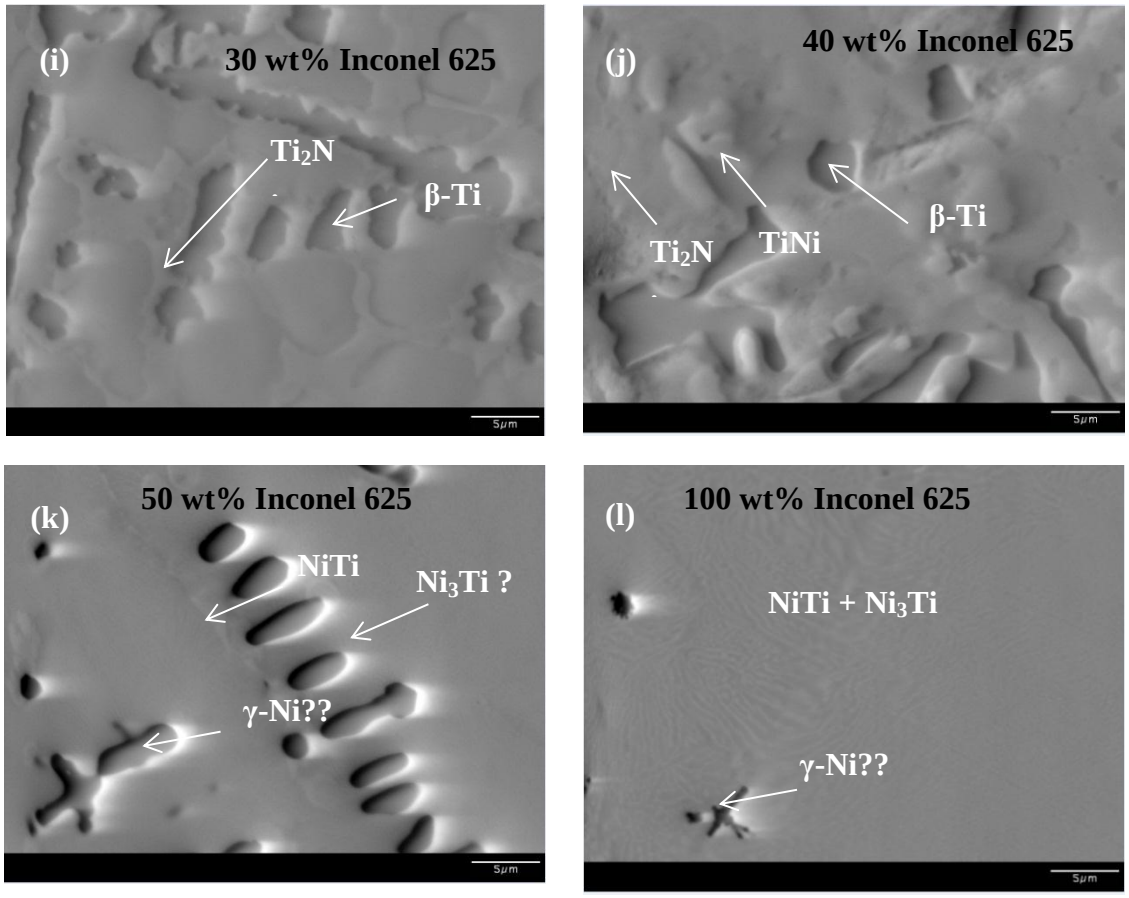

Figure 4.31 Back Scattered Electron images of Chem II (a through l) showing microstructure along the composition gradient at 1000 W; (a-f) microstructure in melt zone of base plate. Note: all the compositions are nominal and calculated from measured data (Cont.).

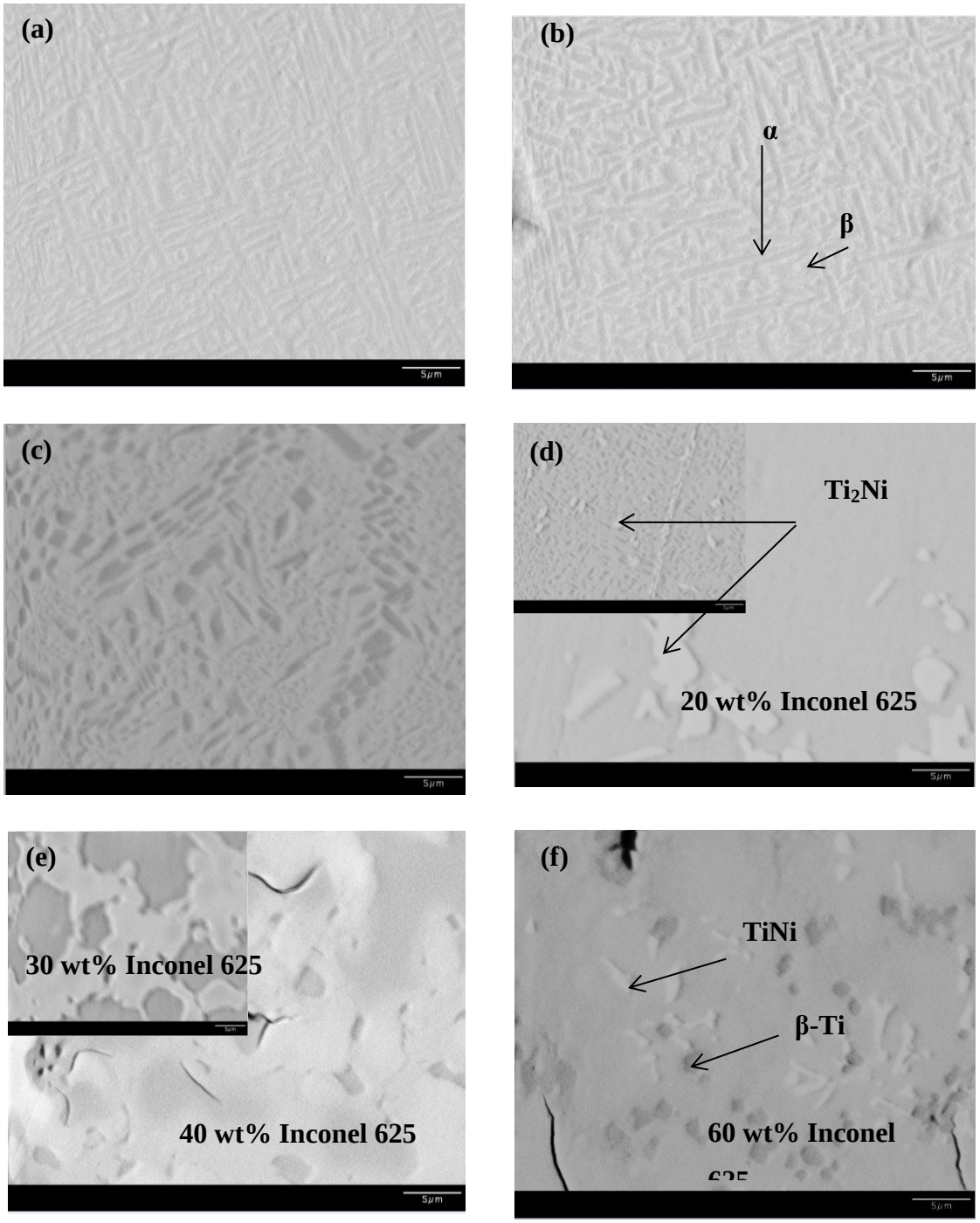

Figure 4.32 Back Scattered Electron images of Chem III (a through h) showing microstructure along the composition gradient at 1000 W; (a-c) microstructure in melt zone of base plate. Note: all the compositions are nominal and calculated from measured data.

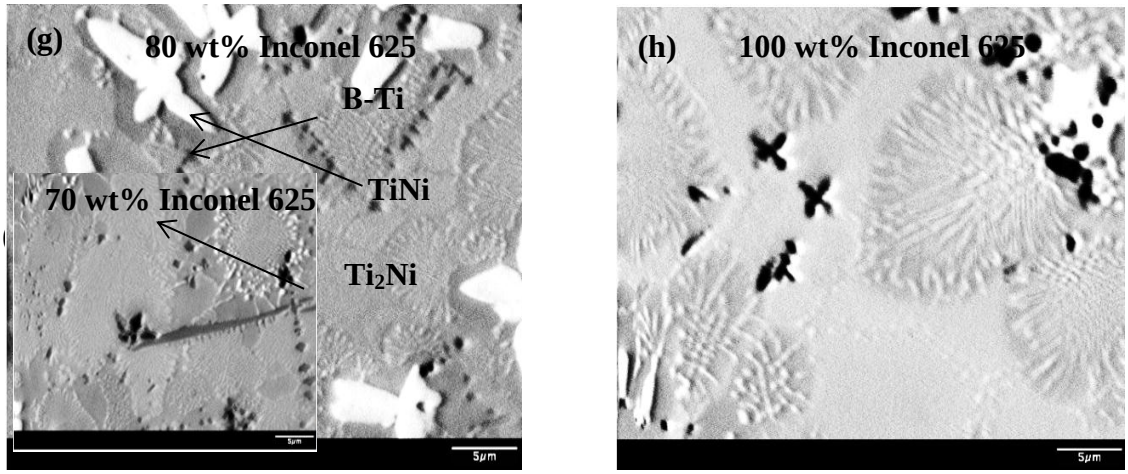

Figure 4.32 Back Scattered Electron images of Chem III (a through h) showing microstructure along the composition gradient at 1000 W; (a-c) microstructure in melt zone of base plate. Note: all the compositions are nominal and calculated from measured data (Cont.).

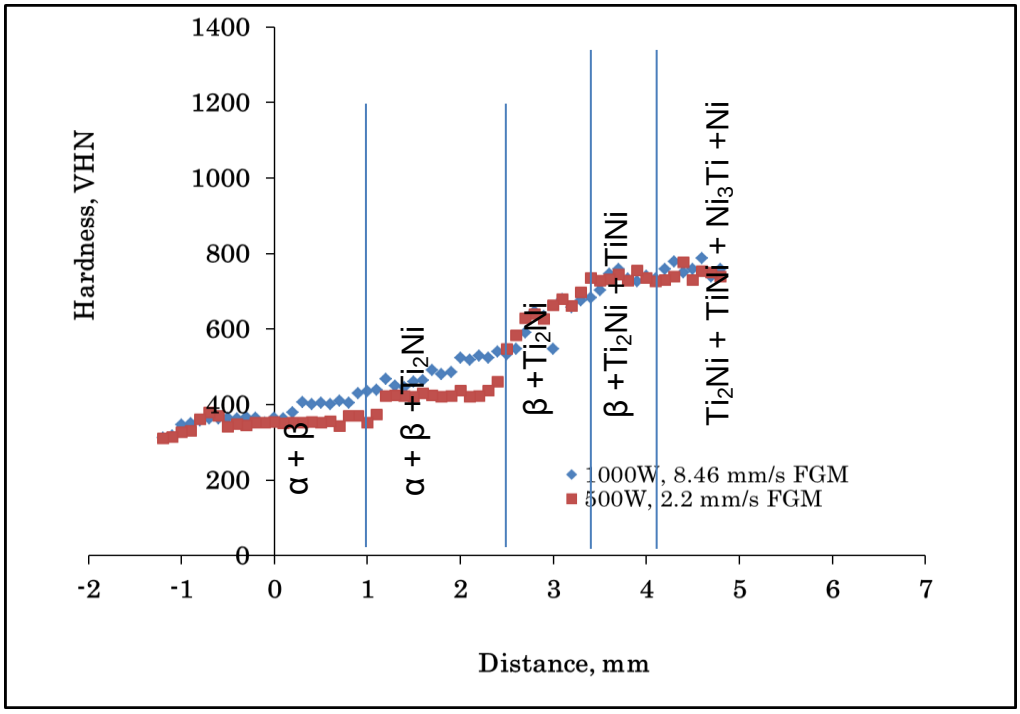

Figure 4.33 Hardness values of the functionally graded material measured along the composition gradient for Chem II, *0 mm = means initial substrate-deposit interface.

.

A more detailed analysis of the phase transformations in the Ti6Al4V-Inconel 625 non-linearly graded-Chem II material was performed by evaluating the microstructural changes along the compositional gradient using scanning electron microscopy. Figure 4.30 (a through l) and 4.31 (a through l) shows micrographs of the microstructures at 500 W and 1000 W at various locations as the nominal powder composition was varied from 10 to 50 wt. % and 100 wt. % Inconel 625. The mass per unit length for the builds were kept the same and the travel speed was adjusted to attain the same build height. The microstructure in Fig. 4.30 (a) and 4.31 (a) shows typical Widmanstätten α-Ti laths in prior β grains. The Widmanstätten α-Ti laths (dark phase) lay at different orientations with respect to each other in the matrix with β-Ti (light phase). The width of α-Ti laths on an average is about 1 μm. With the addition of Inconel 625, the microstructure consists of a duplex mixture of coarser α-precipitates and a substantially refined distribution of α-laths, as shown in Fig. 4.30 (b through g) and Fig. 4.31 (b through f). The volume fraction of β-Ti increased and there is a decrease in the average aspect ratio of α-laths. These microstructures are comparable to the linearly graded Ti6Al4V-Inconel 625 structures discussed in previous section.

Figure 4.30 (h) and 4.31 (g) shows the microstructure corresponding to a nominal composition of 90 pct Ti6Al4V-10 pct Inconel 625. The microstructure consists of Ti_2Ni phase present at the grain boundaries of β phase. The corresponding elemental map is shown in Fig. A.7 (b). The presence of Ti_2Ni shows that α-Ti + Ti_2Ni eutectoid transformation occurred at grain boundaries of β phase, although, the α-Ti precipitates in the β phase were difficult to resolve in SEM micrographs. The EDS analysis measured

the composition of the graded material at this level of Inconel 625 to be Ti-10.64 pct Ni-2.3Cr- 1.6Mo-2.7Al-1.9V.

Further increase in Inconel 625 powder from nominal 20 to 30 pct by weight resulted in a significant change in the microstructure: the β cellular growth changed to β dendritic. The microstructure consists of β dendrites with β+Ti_2Ni divorced eutectic in the inter-dendritic regions. In case of 1000 W the XRD detected a possibility of presence of small amounts of α-Ti, but this phase was not seen under SEM. The elemental maps indicate the β-Ti to contain Cr and V, as shown in Fig. A.7 (c). The volume fraction of eutectic-Ti_2Ni increased slightly as the nominal Inconel 625 powder composition was increased to 40 pct. The size of eutectic-β-Ti remained unchanged. When the nominal content reached 50 pct the microstructure of the 500 W deposition consists of a mix of two phase TiNi + β-Ti dendrites and anomalous/abnormal eutectic of TiNi + Ti_2Ni. The results of the EDS analysis shows the TiNi phases to be enriched in Cr and V (white color); and the β- Ti phase is rich in Ni as shown in the elemental map in Fig A.7 (e). The microstructure of 500 W and 100 pct by weight of Inconel 625 is comparable to 1000 W and 50, 100 pct by weight of Inconel 625 (Fig. 4.30 (k) and Fig. 4.31 (k) and (l)). The microstructure consists of a matrix phase of Ni_3Ti+TiNi eutectic. The XRD detected small amounts of Ti_2Ni and Ni-(Cr, Mo) (γ) peaks. Ti_2Ni was difficult to differentiate in the microstructure. A hard face such as Ni_3Ti, TiNi will abrade differently versus a soft phase such as Ni-(Cr, Mo) (γ). Deducing from XRD Ni-(Cr, Mo) (γ) being a softer phase is seen showing recessed features in Fig. 4.30 (k) and Fig. 4.31 (k) and (l). The corresponding elemental map is shown in Fig A.7 (f).

Figure 4.32 shows the microstructure of the Chem III deposit at 1000 W as a function of depth along the graded material. The microstructures shown in the micrographs from a through c are comparable to the prior ones showing the decreasing volume fraction and size of the α-Ti laths. The composition in the graded layers in Chem III was changed each time by a step of 20 pct of Inconel 625 by weight. But similar to Chem I and Chem II, the α-Ti + Ti_2Ni eutectoid transformation in Chem III occurred at the grain boundaries of the β phase as shown in the insert of Fig. 4.32 (d) around 10 pct of Inconel 625. The microstructure consists of a mix of coarse α-Ti precipitates with refined α-Ti precipitates in the remaining β and discrete Ti_2Ni laths and particles. The corresponding elemental map is shown in Fig A.8 (a). The microstructure at a nominal 20 pct of Inconel 625 (Fig. 4.32 (d) shows some continuous and discrete Ti_2Ni phase delineating the boundaries of prior β grains. Fig. 4.32 (e) shows β dendrites with β+Ti_2Ni divorced eutectic in the inter-dendritic regions. As the nominal composition of Inconel 625 reached 60 pct the microstructure consists of mix of β-Ti and TiNi rod and plate like particles in a continuous matrix of Ti_2Ni. The corresponding elemental maps are shown in Fig A.8 (c). Both intergranular and transgranular cracks can be seen in the matrix. When the nominal composition changed from 60 to 100 pct of Inconel 625 (Fig. 4.32 (f-h), the microstructure consists of a two phase mixture of β-Ti and TiNi dendrites in the Ti_2Ni matrix. The corresponding elemental map is shown in Fig A.8 (d).

The change in hardness along the gradient direction as a measure of distance from the interface (0 mm means initial substrate-deposit interface) is shown in Fig. 4.33. The behavior is similar to the data already reported in the previous section. When Inconel 625 was introduced into the graded layers, a noticeable increase in hardness was observed,

but the hardness virtually remained unchanged with any change in the process parameters. When the nominal composition of Inconel 625 reached 10 pct the hardness reached a local maximum value at 1 mm from the substrate and stayed flat. A gradual increase in hardness with increasing Inconel 625 is likely the result of (i) an increase in the amount of β phase and Ti_2Ni precipitates (ii) a decrease in the volume fraction and concomitant refinement of the α-Ti laths, and (iii) the increase in the content of Inconel 625 resulting in solid solution hardening of the β phase by the enrichment with Cr, Mo and Ni. A sharp increase in the slope of hardness curve is due to the formation of β-Ti + Ti_2Ni anomalous eutectic and precipitation of TiNi particles. No further increase in hardness occurred as the nominal composition of Inconel 625 changed from 50 to 100 pct. This showed that the formation of the anomalous eutectic of TiNi + Ni_3Ti phase contributed to only a slight change in the hardness values. Appendix A shows similar hardness values along the graded direction for some of the process parameters not discussed here.

5. DISCUSSION

This Section includes discussion on the results from Ti6Al4V/Inconel 625 FGMs fabricated under different laser processing conditions and grading chemistries. The section covers in more detail about the phase transformations that occurred along the compositional gradient and provides supporting arguments from the literature that have attempted to do a similar work. Also to be discussed are the microstructures fabricated from 'successful' FGM experiments where no observable cracks were detected in the parts. However, because of the complexity involved in building FGMs and some of challenges encountered during the experimentation, the scope of current work is constrained to (i) accept the deposits that were obtained and (ii) recognize that the process was uncontrolled and hence the resulting microstructure studies reported here are centered primarily around observing compositional changes.

Before going into detail further on the functionally graded Ti6Al4V/Inconel 625, we summarize here the relevant features of the Ti/Ni system. The thermo-physical properties are listed in Table 5.1. An important property pertaining to the transport of heat in the melt zone is thermal diffusivity (α) of the material. From the table 5.1 we can see that the thermal diffusivity Ni $\approx$ 2 Ti, and also the density of liquid nickel is higher than liquid titanium ($\approx$ twice). Both these factors will influence the fluid flow in the melt pool and may govern mixing and segregation in the melt pool, as shown in Fig. 4.2 in the previous Section. Figure 5.1 summarizes the relative stability of different phases in the Ti–Ni system as a function of composition and temperature. There are three intermediate phases in the system which can form directly from the liquid: Ti_2Ni, NiTi, and Ni_3Ti. The

phases NiTi and Ni_3Ti are congruently solidifying, whereas Ti_2Ni forms via a peritectic reaction involving the liquid and the NiTi phase.

Table 5.1 Thermo-physical properties of titanium and nickel [107]

Properties	**Titanium**	**Nickel**
Melting Temperature, ^{o}C	1668	1445
Thermal Diffusivity, $\mu m^{-2} \cdot S^{-1}$	8.85	20.11
Thermal Coefficient of Expansion, $\mu m \cdot m^{-1} \cdot K^{-1}$	8.6	13.4
Liquid Density, g/cm^3	4.11	7.81

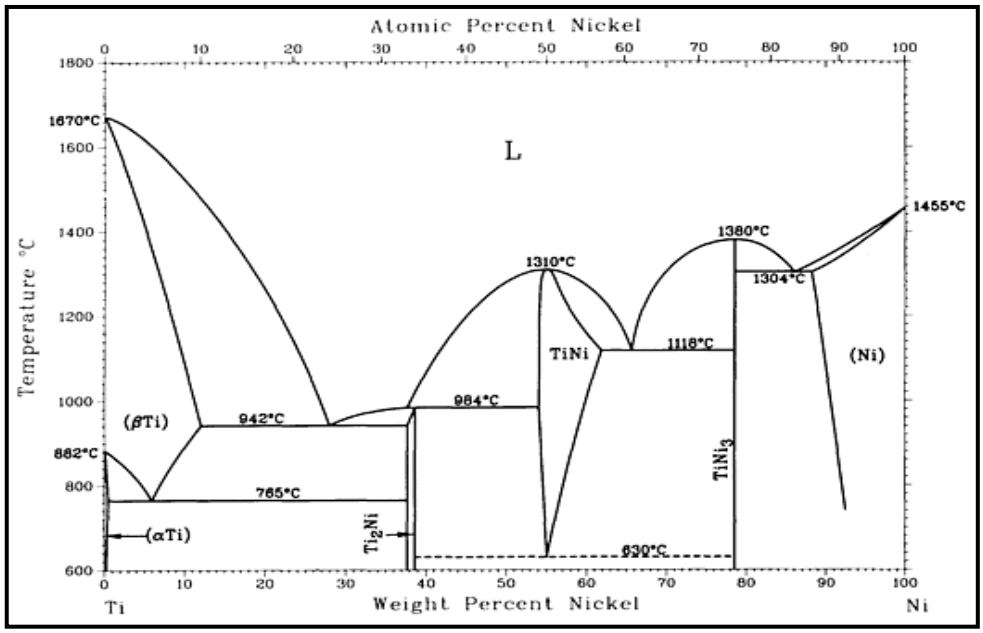

Figure 5.1 Equilibrium phase diagram of Ni-Ti. Note the intermetallics Ti_2Ni, TiNi, $TiNi_3$, Source : ASM handbooks Vol 3[3.3].

5.1 PHASE DIAGRAM

Graded Ti6Al4V-Inconel 625 is a complex system and the microstructure evolution along the composition gradient should be considered in terms of multi-composition phase equilibria. There is no available quaternary system with Ti, Ni, Cr, and Mo for describing the phase equilibria in the Ti6Al4V-Inconel 625 graded material. When considering the Ti-Ni, Ti-Cr, Ti-Mo, Ti-Ni-Cr and Ti-Ni-Mo, it is found that only Ti-Mo and Ti-Cr have slightly similar phase equilibria characteristics at the Ti-rich corner. Nevertheless, in the Ti-Ni-Cr[3.3] and Ti-Ni-Mo[3.3] materials, as well as the Ti6Al4V-Inconel 625 graded material, the main phases present are the Ti-rich solid solution and (Ti, Ni) compounds, but there is a multitude of other minor phases that could also form from the multi-component system: Ti-Al-V-Ni-Cr-Mo-Fe-Nb-Co. The thermodynamic modeling software predicted about 23 intermetallic phases that could form under equilibrium conditions; whereas XRD identified only a small number of these phases that formed under the non-equilibrium conditions of laser deposition. Solvus temperature is a good predictor to distinguish between the phases that are likely to form and those that are rather unlikely to form. In general, the lower this solvus temperature, the more sluggish the kinetics will be for precipitation of a phase.

In order to determine the precipitation of a phase from liquid or solid it is imperative to know the liquidus temperature, T_L, and solidus temperature, T_s. If the solvus temperature of a particular phase is lower than the solidus temperature it will not precipitate from liquid phase directly.

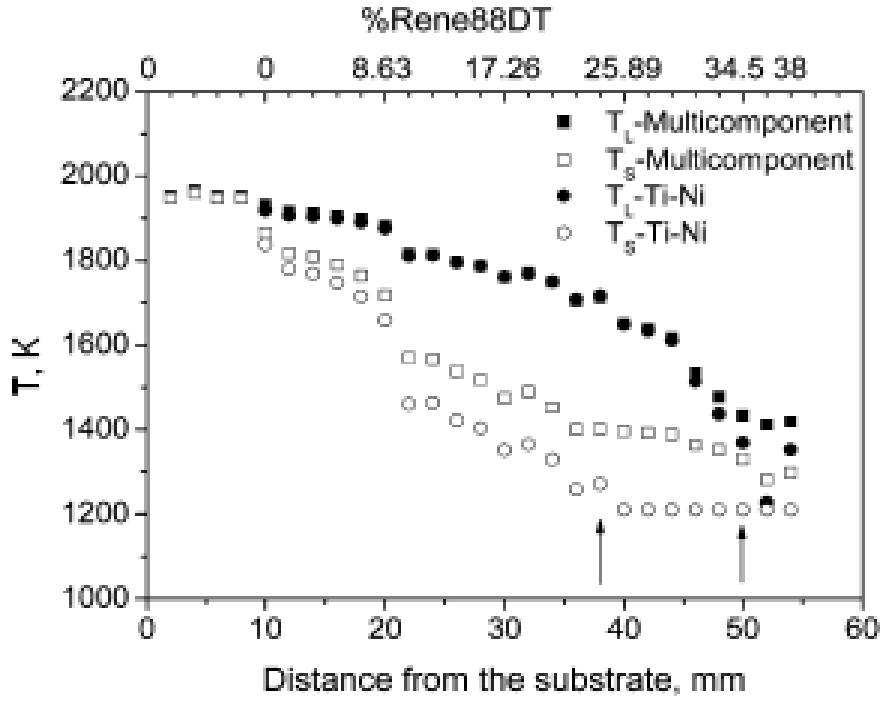

Figure 5.2 Calculated equilibrium liquidus, T_L, and solidus, T_S, as a function of percentage of Rene88DT. The first arrow indicates the eutectic reaction, while the second arrow indicates the beginning of hypereutectic region [90].

Because the kinetics are slow for solid-state transformations the phase may not precipitate at all. In two of the linearly graded structures at 700 W and 1000 W the maximum measured Inconel 625 in the "linearly" graded structure did not exceed beyond 35 pct by nominal weight even when the nominal composition in the layer was deposited to yield 100 pct by weight. This was attributed to mixing in/between layers. And hence in general, the computed values of T_L and T_s in Fig. 4.21 (a to c) using Factsage from measured elemental Ni along the compositional gradient and the microstructures were comparable to Lin, et al. [90] The only caveat here was that at 500 W the composition along the graded layer reached 80 pct by nominal weight, but the microstructures were still very much comparable to 700 and 1000 W up to a nominal weight of 100%. The

complexity involved in depositing mixed powders translated to poor process control as discussed in more detail in earlier Sections.

XRD was performed to identify and quantify the phases along the graded structure. This is done by analysis software which tries to match all the major 2-θ peaks in the diffraction patterns found in Joint Committee on Powder Diffraction Standards (JCPDS) to the measured data. A limitation of the quantification tool in XRD is the inability of the software to quantify the data if there is a shift in 2-θ peaks either due to expansion or contraction of the lattice in the presence of other alloying elements. In the study, during the quantification analysis some of the phases had to be manually eliminated due to the shift in 2-θ peaks in order to allow the software to compute the data. Because of this severe limitation there is some discrepancy between the quantified data shown in Table 5.2 and 5.3 and Figures A.4-A.6. Therefore, the data presented in Tables 5.2 and 5.3 should be taken with a lot of caution by the reader. Powder diffraction patterns shifted by ± 0.5-1.0^{o} from the original position along the compositionally graded structure. Given below is some discussion on various phases that were presented in Table 5.2 and 5.3.

Table 5.2 Phases predicted along the compositionally graded direction.

Phase	**Solvus Temperature, ^{o}C**	**Phase Formation**	**Comments**
Ti_3Al (*hp8*):	1150	Sluggish, not likely to form	➢ May only precipitate from the solid solution ➢ size distribution may be fine
V, Cr, Mo, Nb, Co and Fe			➢ Both Ni and Ti have very high solubility for these elements at higher temperatures. These elements would probably exist as solid solutions.

Table 5.2 Phases predicted along the compositionally graded direction (Cont.).

Fe_2Ti (*hp12*)	1427	Likely to form from liquid	➢ size distribution may be coarse ➢ The amount of Fe is less than < 5 wt%. May likely remain in the solid solution of Ni and Ti.
$NbCr_2$ (*hp12*)	1770	Likely to form from liquid	➢ size distribution may be coarse ➢ The amount of Nb is less than < 3 wt%. May likely remain in the solid solution of Ni and Ti.
$NbCo_2$ (*hp12*)	1480	Likely to form from liquid	➢ size distribution may be coarse ➢ The amount of Nb and Co is less than < 3 wt%. May likely remain in the solid solution of Ni and Ti.
$NbCo_3$ (*hp24*)	1247	Likely to form from liquid	➢ size distribution may be coarse ➢ The amount of Nb and Co is less than < 3 wt%. May likely remain in the solid solution of Ni and Ti.
Co_2Ti (*hP24*)	1235	Sluggish, not likely to form	➢ May only precipitate from the solid solution ➢ size distribution may be fine ➢ Amount of Co is less than < 1 wt%. Most likely it will remain in the solid solution of Ni and Ti.
NiCrMo (fcc)		Will form	➢ A nickel-based austenitic phase that usually contains a high percentage of solid solution elements such as Co, Cr, and Mo. The phase has a face centered cubic structure.
Cr_3Mn_5	ND	ND	ND
AlNi (*cP2*)	1638	Likely to form from liquid	➢ size distribution may be coarse ➢ Amount of available Al is a limiting factor for how much of AlNi will precipitate.
CoAl	ND	ND	ND
$MoNi_4$ (*tI10, cF4*)	867	Sluggish, not likely to form	➢ Llikelihood of $MoNi_4$ intermetallic phase is low. ➢ size distribution may be fine ➢ May remain in the solid solution of Ni and Ti.
$NbFe_2$ (*hp12*)	1627	Likely to form from liquid	➢ size distribution may be coarse ➢ The amount of Nb and Fe is less than < 5 wt%. ➢ May likely remain in the solid solution of Ni and Ti.
Ni_3Al	1350	Likely to form	➢ size distribution may be coarse

Table 5.2 Phases predicted along the compositionally graded direction (Cont.).

(*cP4*)		from liquid	➢ The amount of available Al is a limiting factor for how much of Ni_3Al will precipitate.
$AlNbTi_2$	ND	ND	ND
FeTi (*cp2*)	1315	Sluggish, not likely to form	➢ Likelihood of FeTi intermetallic phase is low. ➢ size distribution may be fine ➢ The amount of available Al is a limiting factor for how much of FeTi will precipitate.
Cr_5Al_8 (*hR26*)	1350	Likely to form from liquid	➢ size distribution may be coarse ➢ The amount of available Al and Cr is a limiting factor for how much of Cr_5Al_8 will precipitate.
V_5Al_8 (*cI52*)	1670	Likely to form from liquid	➢ size distribution may be coarse ➢ The amount of available Al and V is a limiting factor for how much of V_5Al_8will precipitate.

Apart from the major Ni-Ti phases, most of the minor phases that are discussed above were not identified by XRD. This is not a surprise because of the non-equilibrium nature of the LMD process. However, there were still few equilibrium minor phases that were predicted by thermodynamic modeling and were present in extremely small amounts and also identified by XRD in the graded layers. These equilibrium phases are $NbCr_2$, $NbCo_2$, Mo_xNi_y, CoAl, Fe_xTi, Ni_xAl and $NbFe_2$. Interestingly it was found that some of these equilibrium phases began to appear when the nominal composition in the graded layer exceeded 20 pct by weight of Inconel 625 and almost all were present when the composition reached 100 pct by weight of Inconel 625, as shown in the Tables 5.2 and 5.3. Apart from increasing volume fraction of Inconel 625 in the graded layers one of

the factors that can influence *'the equilibrium'* behavior is the high temperature gradients in the graded structure.

The FEA modeling on multilayer clads (Fig. 4.8) showed that the cooling rates decreased by an order of magnitude as each new layer was deposited on the pre-existing layer. The predicted cooling rate for the very first few layers was as high 6000 K/s and became as low as 473 K/s for the top layer in the clad. Initially, the workpiece serves as the main heat sink and effectively extracts the heat from the very first few layers. This rapid cooling can enable us to achieve non-equilibrium phases in the very early phase of deposition process. The microstructure is extremely refined in such cases, i.e. the second phases and the matrix have a fine structure. As more layers are added the cooling rate decreases rapidly, and the behavior can be more equilibrium in nature. Also, there is more time available for solid state transformations to occur in the graded layers. Therefore the microstructures from the "non-equilibrium" process are more or less comparable to as-cast microstructures. However, the amounts of each element present will be a limiting factor in determining how much of a certain phase will precipitate in the graded layers.

5.2 MICROSTRUCTURE EVOLUTION ALONG THE GRADED DIRECTION

5.2.1. Early Phase Transformations. Based on the experimental observations from Fig. 4.24 (a to c), 4.26 (a-d), 4.27 a, 4.30 (a to g), 4.31 (a to f) and 4.32 (a to c), it is possible to propose a sequence of transformations leading to microstructural development in these graded layers. The observations are similar to prior research work conducted by Collins, et al. [95-97] on Ti-X (X = Mo, V, and Cr) systems. For convenience to the reader the discussion will be limited to Fig. 4.31 (a to f) because all the graded layer microstructures can be discussed by this particular one. There will be occasional references to other figures wherever it is necessary during the discussion.

In the initial stages of deposition with relatively low alloying content of Inconel 625, the microstructure primarily consisted of a large volume fraction of α in the form of Widmanstätten laths (Fig. 4.31 (a). Increase in the alloying content results in an increase in the volume fraction of β. The α-laths are unable to thicken to the same extent and are forced to retain larger volume fractions of inter-lath β phase (Fig. 4.31 (b) [95-97]. A further increase in alloying content led to a larger volume fraction of β, this is microstructurally manifested with a reduction in the density of large primary α laths (Fig. 4.31 (c and d). A few primary laths grow and thicken significantly during the solidification of the same layer, still retaining a large volume fraction of β.

Reheating of existing layers occurs when more layers are being deposited. Subsequently, during re-heating of the same layer, two secondary solid state transformation processes occur. First, there is the precipitation of secondary α laths within the regions of retained β phase. Second, there is a re-precipitation of β at the primary α lath/β matrix interface that grows into the laths eventually breaking up laths

into more equiaxed-like α precipitates [95-97]. Collins et al. [95-97] observed as a result of above processes that the primary α laths were supersaturated with alloying elements and the β phase being under-saturated at room temperature. As a result biomodal distribution of α precipitates were observed in the microstructures.

Similar results were obtained in this work and the resulting microstructure consisted of a bimodal distribution of α precipitates as shown in Fig. 4.31 (c-f). The volume fraction of β phase is relatively large, and only a small fraction of α, distributed as fine precipitates is visible in the microstructure. Also interesting to note was a thick continuous layer of α was observed along the grain boundary (Fig. 4.30 a) at relatively low alloying concentrations, similar to observations made by Collins, et al. [95-97]. As the concentrations of Inconel 625 alloying elements in the layer increased, discrete α precipitates which are substantially smaller in size, are formed along the grain boundary (Fig. 4.30 f). Similar observations were made in the microstructures as well by Lin, et al. [90].

5.2.2. Decomposition of β-TI. Figure 5.3 presents a reproduced schematic diagram [90] showing the possible metastable phase boundaries that may be present under non-equilibrium conditions resulting from rapid cooling. The discussion below is in line with that suggested by Lin et al. [90]. For relatively pure Ti, the martensitic transformation temperature (M_s) will be comparatively high. On fast cooling the microstructure would transform from β to martensitic structure at point A in Fig. 5.3. With the increase in alloying elements the M_s temperature will decrease, represented by points B to D.

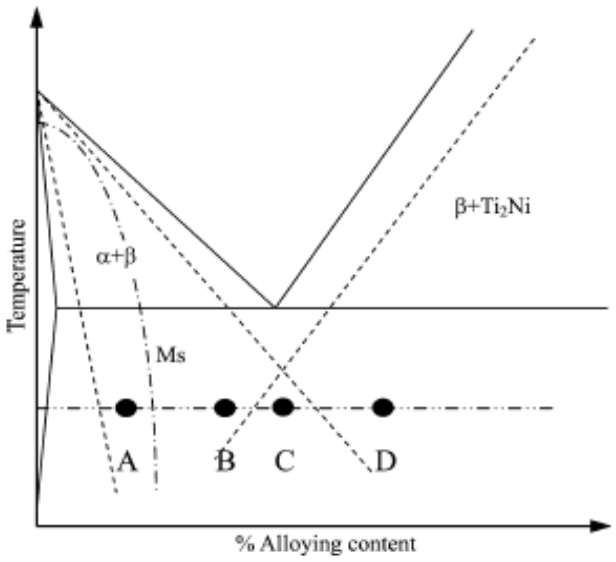

Figure 5.3 Schematic diagram showing the possible metastable phase boundaries arising from rapid cooling, which indicates both the equilibrium phase boundaries (solid lines) and the non-equilibrium ones (dash lines). Superimposed on these phase boundaries is the M_s curve (dash-dotted line) for martensitic transformation of the β phase [90].

At point A and B, α phase is supersaturated with the alloying elements whereas the Ti_2Ni phase remains unsaturated relative to β. Therefore, the decomposition of β

phase by the eutectoid reaction will not occur. At point C, both the phases are supersaturated with the alloying elements and hence the decomposition of $\beta \rightarrow \alpha + Ti_2Ni$ will occur. At point D the Ti_2Ni phase is supersaturated with the alloying elements and α phase does not occur. Also, increasing the alloying elements further stabilizes the β phase in the microstructure.

In the current work Point A and B shows the diffusional transformation of $\beta \rightarrow \beta + \alpha$ and this is represented in Figure 4.24 (a to b), 4.26 (a to b), 4.27 a, 4.30 (a to b), 4.31 (a to b) and 4.32 (a to b). Point C is very well captured in the Figure 4.31 d (insert). Point D is again very well captured by Figures 4.24 (e), 4.26 (e), 4.27 ©, 4.29 (h), 4.31 (g), and 4.32 (d).

5.2.3. Lamellar/Non-Lamellar Microstructure from Eutectoid Reaction. The products of eutectoid decomposition of β phase may decompose in to [108-110]: bainite mode and pearlite mode. Bainite is a non-lamellar product of eutectoid decomposition wherein the two low temperature phases precipitate sequentially, rather than synchronously, and do so in a manner which results in the development of non-lamellar particles of the minority phase amongst crystals of the majority phase formed. The microstructure would usually consist of a non-lamellar dispersion of Ti_2Ni intermetallic compound particles amongst proeutectoid α [108]. The eutectoid decomposition in pearlite mode occurs as a lamellar, cooperative transformation. The transformation into either lamellar or non-lamellar mode in a number of Ti-X alloys was studied by Franti et al. [109], and was found essentially to be independent of reaction temperatures. This is quite different from analogous ones in Fe-C alloys, where pearlite is the principal eutectoid structure formed at high temperatures and bainite plays this role at low temperatures. Figure 5.4 and 5.5 shows the TTT-curves for the initiation of the proeutectoid and the bainite reactions in the hypoeutectoid alloys and near eutectoid Ti-Ni alloys. In the hypoeutectoid Ti-X alloys, much smaller undercoolings below the β transus were normally sufficient to make Widmanstätten α the dominant morphology in hypoeutectoid alloys. Hence the formation of pearlite is usually prevented whereas the precipitation of isolated compound particles at α plate to form bainite can still occur at reasonable rates; as shown in Fig. 5.6. In Ti-Ni near-eutectoid alloys, the proeutectoid α reaction is so very fast that sideplate formation will begin to appear prior to the nucleation of Ti_2Ni intermetallic compound; hence bainite forms instead of pearlite.

In the present study, below a nominal composition of 10 pct by weight of Inconel 625 the decomposition of β phase resulted in the formation of Widmanstätten α dominant morphology, as shown clearly in Fig. 4.32 (d, insert). In this hypoeutectoid alloy there is the precipitation of isolated Ti_2Ni compound particles at the α plate in the form of bainite. When the measured composition was above Ti-10.17 pct Ni-2.32Cr- 1.02Mo-3.48Al-4.24V in Fig. 4.31 (g) and 4.32 (d), there was no evidence of decomposition of product phase into either bainite or pearlite mode. These results are in good agreement with Lin, et al. [90].

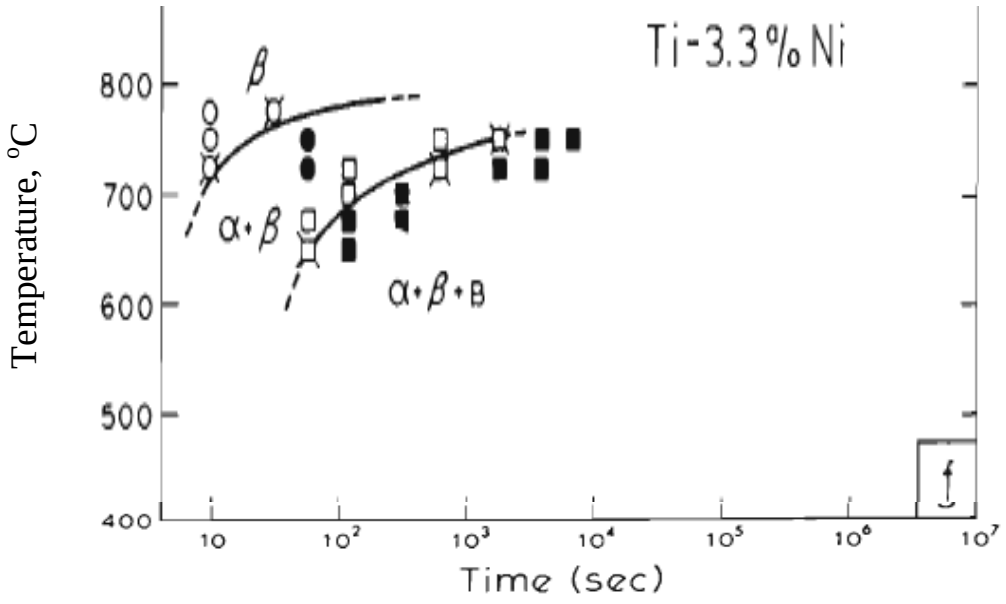

Figure 5.4 TTT-diagram for the initiation of the proeutectoid α reaction and the beginning of the bainite and/or pearlite reaction in the hypoeutectoid alloys. B = bainite. Hollow, sputniked and filled data points indicate reaction times prior to, at the beginning of, and subsequent to initiation of the proeutectoid α reaction (circles), and compound precipitation in either the bainitic or pearlitic modes (squares) [109].

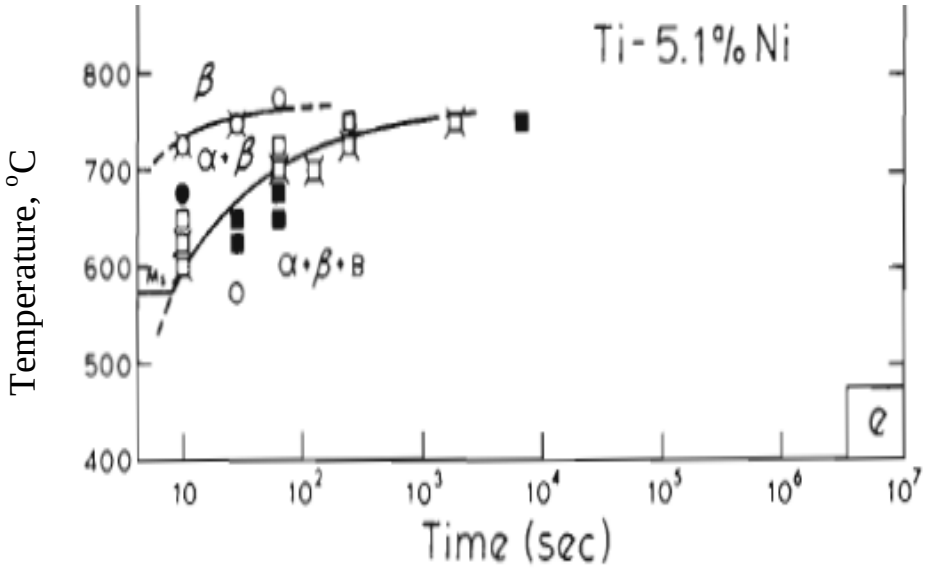

Figure 5.5 TTT-diagram for the initiation of the proeutectoid α reaction or proeutectoid compound reaction and the beginning of the bainite and/or pearlite reaction in the neareutectoid alloys. B = bainite. Hollow, sputniked and filled data points indicate reaction times prior to, at the beginning of, and subsequent to initiation of the proeutectoid α reaction (circles), and compound precipitation in either the bainitic or pearlitic modes (squares) [109].

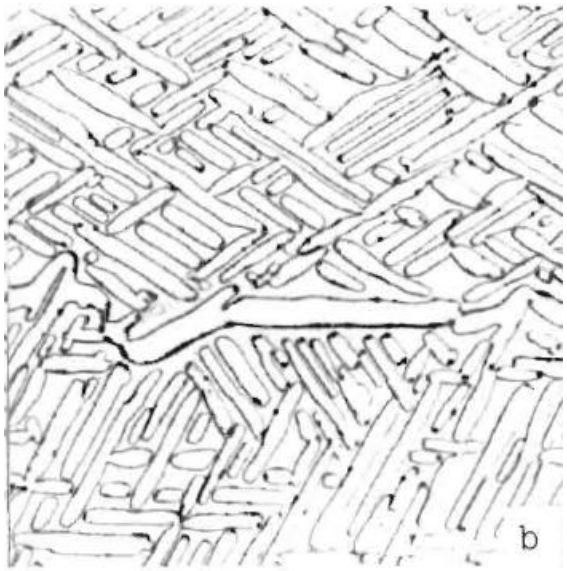

Figure 5.6 Start of bainite reaction in Ti-3.3 at. pct Ni with compound particles nucleated at intragranular α plates and at αallotriomorphs [109].

5.2.4. Formation of Anomalous/Abnormal Eutectic Structures from Rapid Solidfication. When the nominal composition in the graded layers was increased beyond 50 pct by weight of Inconel 625, the Ni in the graded layers reached more than 30 pct (max being 50 pct in Chem II and III) by weight in grading Chem I when measured by standardless EDS analysis. The microstructure showed presence of a mixture of two phase TiNi + β-Ti dendrites and anomalous Ti_2Ni + TiNi eutectics, as shown in Fig. 4.24 (j to l), 4.27 (g to i), and 4.32 (g to h). The Ti-Ni binary phase diagram in Fig. 5.7 shows that a composition greater than 40 pct by weight of Ni would likely initiate an equilibrium peritectic reaction. The calculated equilibrium phase diagram in the current study shown in Fig. 4.20 predicts a peritectic reaction at around 22 pct by weight of measured elemental Ni. In an equilibrium peritectic reaction one solid phase reacts with a liquid phase on cooling to produce a second solid phase. The usual product of peritectic solidification is a primary phase surrounded by peritectic/secondary phase and remaining liquid, due to the difficulty of diffusion in the solid primary phase. The possibility of coupled growth in peritectic systems has been reported by several researchers [111-114]. There is a possibility of coupled growth of primary and peritectic phase also called as a 'metastable eutectic reaction' in peritectic alloys if the growth of primary phase can be slowed down by a high temperature gradient. The slowdown of primary phase is possible with rapid solidification.

These metastable reactions as a result of rapid solidification can be predicted from an equilibrium data. Perepezko and Boettinger [115] showed a simple way of finding the T_o curve is to draw the T_o curve connecting the midpoints between the liquidus and solidus lines at a given temperature. The minimum degree of undercooling which is

thermodynamically necessary for the diffusionless transformation of a liquid alloy to a solid solution, for a given alloy composition, is expressed by the T_o curves in the phase diagram. Such a condition is shown in Fig. 5.7, where the metastable liquidus of Ti_2Ni and TiNi intersect with contrary slopes [90]. As the Ni is rejected in front of the Ti_2Ni interface and Ti rejected in the front of TiNi interface, this will result in an evolution of Ti_2Ni-TiNi eutectic (cooperative growth) structures. Lin et al. [90] stated that the liquidus of Ti_2Ni and TiNI will be further shifted to a lower temperature region as a result of a strong kinetic undercooling and the capillary effect.

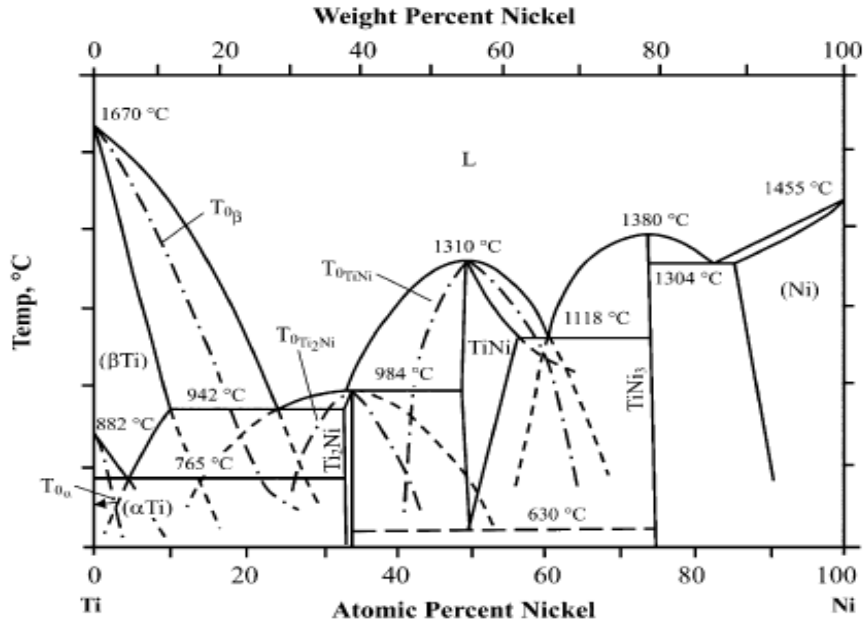

Figure 5.7 A phase diagram of the Ti-Ni system, the figure also shows the extension of possible phase fields and the T_o curves of the phases [90].

Now, whether the growth would be metastable lamellar eutectic or anomalous eutectic will depend on the growth velocity in the melt pool. Lin et al. [90] saw very high growth velocities in their melt pool for Ti6Al4V-Rene88DT multicomponent system. The conditions for anomalous eutectic to become the unique microstructure were [113, 114]

large undercooling's such that the phases are capable of nucleating independently with sufficiently large growth velocities. Because of this large undercooling the eutectic takes on a mode of divorced growth as compared with the normal cooperative lamellar growth. Large undercooling's are most commonly observed in LMD process. And the laser process parameters greatly influence the solidification process and microstructures. Xu, et al. [8] studied the influence of v_s and P on microstructure in Ti-50 wt% Ni, as shown in Fig. 5.8. The laser energy density (D_e) was defined as the following:

$$D_e = \frac{P}{dMv_s} \quad [4.1]$$

where d is the laser spot area that can be calculated by the laser beam diameter, M is the deposition amount of powders, and D_e is a dimensionless parameter, which expresses the energy to melt the unit powder in unit time and area. They found that the dendrite arm spacing decreased with increasing the scanning velocity and decreasing the laser power. Divorced eutectic structures were obtained in the resulting microstructure.

Similar metastable eutectic byproducts were observed in the microstructures in the current research work. Both the metastable lamellar eutectic or anomalous eutectic structures were observed based on the processing conditions. The representative figures are shown in Fig. 4.24 (l), 4.26 (l) and 4.27 (i). In the current work, with the increase in nominal composition of Inconel 625 beyond 50 wt% dendritic structures were observed in the microstructure. From the mathematical equation described above if the beam spot size and mass per unit length of powder deposited in each layer were to be the same, with the change in energy density for grading chem I (with increasing power at constant velocity) the microstructure showed two phase TiNi + β-Ti eutectic dendrites at both 500 W and 1000 W, as shown in Fig. 4.24 and 4.27, although Figure 4.26 (i) at 700 W does

not show presence of any two phase TiNi + β-Ti eutectics dendrites but only divorced TiNi eutectics. The secondary dendrite arm spacing appears to remain unaltered with the processing parameters, as shown in Fig. 4.24 (i, taken at lower magnification) and Fig. 4.27 (i, taken at higher magnification). Interestingly the microstructure in Chem I changed from divorced to pseudo-normal cooperative mode at 500 W and 1000 W along the graded layers in Fig 4.24 and 4.26. In summary, except for the differences in composition between 500 W and 700 W, 1000 W the effect of laser power on microstructure evolution is very inconclusive. The microstructures along the graded direction were initially similar for all the three laser powers, and varied towards the end of deposition process. This could have occurred due to lack of a better control over the process as discussed in earlier Sections. As a result of it there may have been some variations in solidification times or cooling rates along the deposit height during and after deposition process. From the FEA thermal model (Fig. 3.8) we know that the rate of cooling in the layers is initially driven by the proximity to the workpiece. Also, the ability of the clad to cool down dropped by an order of magnitude with increasing number of layers.

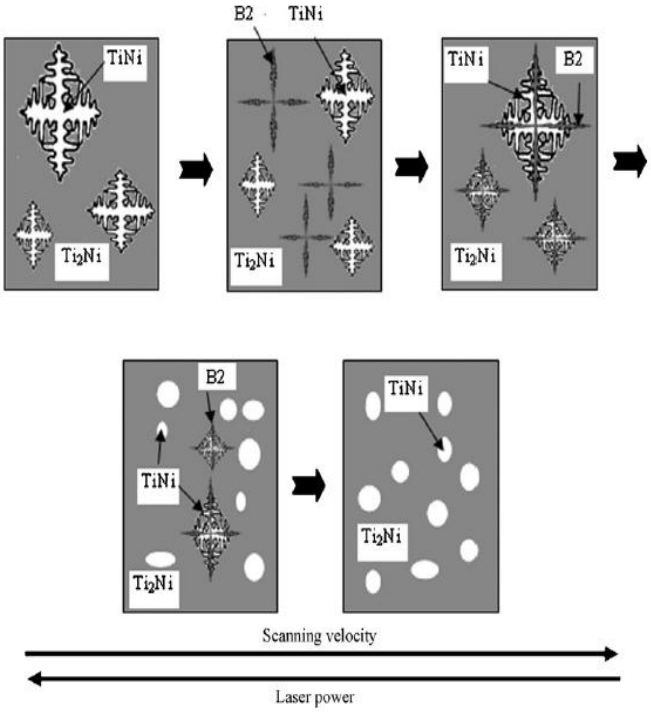

Figure 5.8 Schematic diagram showing the solidification processes and the forming mechanisms of as-deposited microstructures which vary with the processing parameters [8].

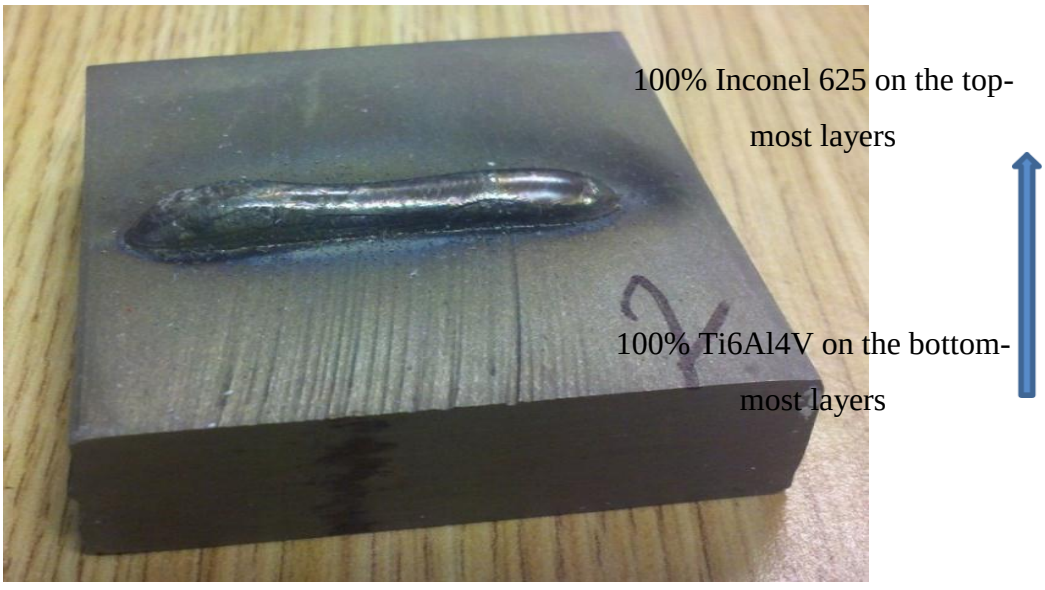

Figure 5.9 Image of a defect-free functionally graded Inconel 625/Ti64 fabricated using Chemistry I (70 layers) composition by LMD @ 1000 W, tool path=Bi-directional, 8 g/min, and 8.46 mm/s.

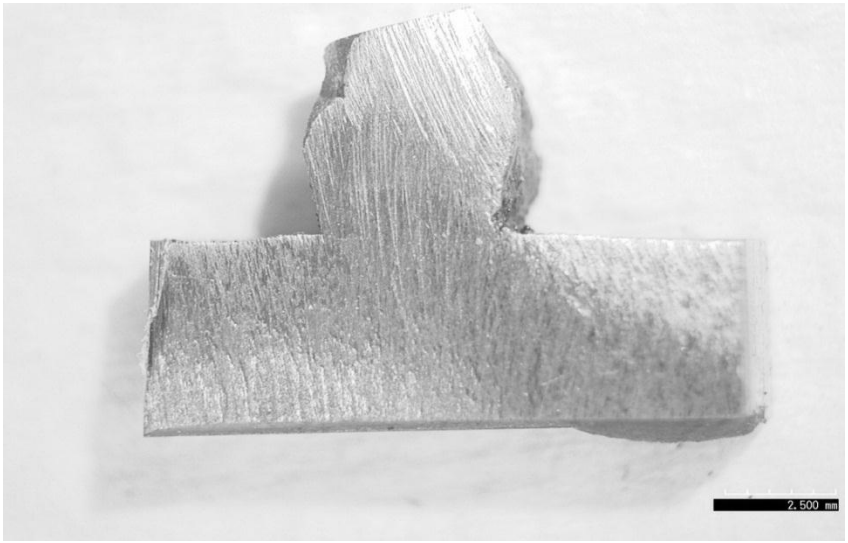

Figure 5.10 Image showing a machined cross-section of the non-linearly graded Chem I (1000 W, 8 g/min, and 8.46 mm/s). Note: no cracks can be seen in the deposit.

5.3 DIFFERENCES BETWEEN LINEAR AND NON-LINEAR GRADING

The main difference between graded chem I, II and III is the absence of macro and micro-cracks in Chem II. Figure 5.9 and 5.10 shows a macrostructure of a crack-free graded Chem II thin wall structure. As the nominal composition reached beyond ~50 pct by weight of Inconel 625 cracks were observed in the graded Chem I and Chem III thin wall structures. Figure 4.19 shows macro-cracks in the linearly graded structure; whereas Figure 4.26 h and k and Figure 4.32 f shows micro-cracks along the TiNi precipitate phase in the microstructure. The microstructures in the graded Chem III structures (Fig. 4.32 (a to h) are comparable to the linearly graded structures and were discussed already in the above section. However the microstructures in the Chem II were only comparable up to 50 pct by weight with the Chem I and Chem III.

Domack and Baughman [7] also observed macro-cracks when the target blend was about 40 percent Ti6Al4V and 60 percent Inconel 625. They determined that the cracks were not directly linked to metallurgical features. But the microstructures showed coarse dendrites and significant elemental segregation. They concluded that additional development of process parameters and powder feed control were necessary to ensure that target chemistry gradients are achieved without excessive material reactions. A Similar research work by Dong et al. [104] showed micro-cracks at the transition region of 10% SS316L + 90% Inconel 625 and 20% Ti6Al4V + 80% Inconel 625. They saw fracture of the tensile specimen at the transition of Inconel 625-Ti6Al4V interface. From the morphology of the fracture they concluded that cracks that initiated during deposition propagated along the interface among the intermetallics under the stress. In both these studies little attempt was made to understand the reason behind the solidification cracks and the resulting microstructures.

In the present study we observed that the microstructures for the graded Chem II structures (Fig. 4.30 and 31) are slightly different as the composition changed from 50 to 100 pct by weight of nominal 625. In Chem I at 500 W the composition of Ni in the final layers was ~15-20 percent lower than that at 1000 W, and hence the microstructures are slightly different. But in general the microstructures transformed from anomalous eutectic structures of Ti_2Ni + TiNi to Ti_3Ni + TiNi two phase structures and possibly presence of γ phase based on the XRD. The measured Ni in the Chem I and Chem III at nominal of 50 to 100 pct by weight of Inconel 625 was in the range of 30 to 50 pct as compared to 30 to 70 pct Ni for Chem II. In other words, no cracks were present in all the grading's of Chem II but a transition to almost 100 pct by weight of nominal Inconel 625

was achieved only at a combination of high laser power, high travel speed and high powder feed rate, as shown in Fig. 4.29 (d). But the conditions that "worked" involved a very low powder efficiency, a very long manufacturing time (~20 minutes), and a very "low" deposit height (~6mm). Chen et al. [10] from their analytical and experimental work on Ti6Al4V/Inconel 718 laser welding also showed that a combination of high laser power and welding speed and offsetting the laser beam approximately from the interface to the Inconel 718 side minimized cracking in the welds.

One thing to note when grading Chem II is compared to Chem I and Chem III is that between 50 to 100 pct by weight of nominal Inconel 625 the number of compositional steps decreased from 4 to 1. This probably minimized the formation of coarse equiaxed dendrites or faceted structures of TiNi phase resulting from an increase of thermal gradient due to accumulation of heat as the deposit grew thicker. Figure 4.26 h and k, and Figure 4.32 f show microcracks present near the semi-coherent structures in the graded Chem I and Chem III. Although circular precipitates minimizes the interfacial energy but the coherency strains increases. The elemental mapping in general showed the dendritic and faceted TiNi phase to be rich in Cr. Lin et al. [90] considered the Cr-enriched TiNi phase to be a pre-martensitic rhombohedral phase (R-phase). This phase was found at the interdendritc regions of Co enriched TiNi dendrites, at which lower cooling rate was experienced. The Cr-enriched TiNi phase formed at the interdendritic regions resembled the form of a block or lath. In the current work, whether the TiNi phase is R-phase has not been confirmed by TEM, but is deduced from the above author's study.

R-phase is a martensitic phase, but is not "the" martensite(soft, ductile B19') that is responsible for the shape memory and superelastic behavior. Commercially available 50:50:: Ti:Ni alloy is responsible for the shape memory (in which recovery to original shape can happen by heating) and superelastic effect (exhibit enormous elasticity when worked at temperatures slightly above transformation temperature). Partial substitution of Ni with some other alloying elements such as Fe, Co, and Cr in TiNi or annealing in the range of 350-500°C can decrease the M_s temperature more strongly than the "premartensitic" R phase start temperature (R_s). When austenite (B2, cubic structure) transforms to the R-phase (rhombohderal distortion of cubic structure, equivalent d-spacing) its energy is reduced and its propensity to transform to martensite (soft, ductile B19') is lessened. Brachet et al. [116] showed that the addition of 2%Fe on a TiNi alloy induced formation of R-phase that resulted in brittle failure during charpy tests conducted in the temperature ranging from -25 to 0°C.

In summary it is possible to achieve a 100% grading of Ti6Al4V and Inconel 625 at higher laser powers, faster travel speeds and higher powder feed rate. The cracks in the fabricated structure can be minimized by controlling the formation of R-phase in the microstructure.

6. CONCLUSIONS AND FUTURE WORK

6.1 CONCLUSIONS

This thesis has tried to cover a broad range of topics such as finite element modeling, thermodynamic modeling of multicomponent system, microstructure evolution in the functionally graded Ti6Al4V and Inconel 625 alloys, etc. Brief summary of the findings are as follows:

- Current literature available on Titanium based and Nickel based alloy FGMs is very limited and the potential of these alloys has not been fully utilized. It has been shown in the present work that LMD is capable of producing functionally graded multi-component systems for a wide range of applications. However, because of the complexity involved in building FGMs and some of challenges encountered during experimentation, the scope of the current work was constrained to (i) accept the deposits that were obtained in this research work and (ii) recognize that the process was uncontrolled and hence the resulting microstructure studies reported here are centered primarily around observing compositional changes and identifying the phases by XRD.

- *In Domack et al. [7] words "A refined experimental program is needed to resolve technical issues like macroscopic cracking, elemental segregation etc.," in multi-component Ti-Ni FGMs.* In this research work an attempt was made to understand the effect of process parameters on achieving 100 pct nominal Inconel 625 grading in the thin wall structures. A combination of high laser power, faster

travel speed and high powder feed rate was found to be beneficial in achieving the goal.

- 3D thermo-mechanical models were built to understand the effect of process parameters such as laser power, travel speed, tool path direction, etc., on peak temperatures, cooling rate and remelted layer depths, residual strains, etc., for the LMD process. The models were constructed on the multilayer deposition of SS316L and Inconel 625 on SS316L workpiece. The above material-systems are simple to handle in ABAQUS^{TM} as "liquid" and "solid" are the only two phases that are formed during melting and cooling. These models were experimentally verified in-situ using K-type thermocouples and high temperature strain gages. The results from these models were used in this thesis to interpret the structure-property relationships in the functionally graded Ti6Al4V and Inconel 625 FGMs. The thermal profiles and strain measurements of the FEA models were in agreement with the experiments. The thermal profiles showed very high initial cooling rates and as the number of layers increased in the thin wall structure the cooling efficiency dropped by an order of magnitude. This kind of behavior resulted in a deviation from non-equilibrium conditions, not typical for LMD process. Some of the minor phases predicted from thermodynamic modeling under equilibrium conditions were detected in the functionally graded Ti6Al4V and Inconel 625 structures because of equilibrium behavior. The mechanical models were in agreement with experiments within 5-10% of each other. Not much information could be gained from modeling as to why solidification cracking occurred in the functionally graded Ti6Al4V and Inconel 625 FGMs.

- The microstructure evolution in the functionally graded Ti6Al4V and Inconel 625 FGMs agreed very well with the data provided in literature. Also, some process parameters were identified in this research work that could achieve transition from 100 % nominal Ti6Al4V to 95-100% nominal Inconel 625. Further repetitions at these parameters were impeded by process stability and experimental setup. The cracks in the FGMs were believed to be a result of precipitation of coarse circular and dendritic precipitates of pre-martensitic R-phase TiNi in the anomalous eutectic of TiNi + Ti_2Ni matrix. This usually occurred as the nominal composition of Inconel 625 exceeded 50 pct by weight in the graded layers during deposition. In the non-linear grading Chem II, precipitation of R-phase was minimized. Thus, no observable cracks were identified and a transition to 95-100% nominal Inconel 625 was achieved.

6.2 RECOMMENDATIONS FOR FUTURE WORK

In the research work presented in this dissertation a lot of problems were encountered during functional grading of Ti6Al4V and Inconel 625 and warrants further investigation. The results of this dissertation point to several interesting directions for future work:

- The probability of success in obtaining a defect free Ti6Al4V and Inconel 625 FGM is dependent on choosing optimal process parameters, process stability and reproducibility. Even in conditions that “worked” a very low powder efficiency and long manufacturing time (~20 minutes), and “low” deposit heights (~6mm) were issues. In summary, the complexity involved in depositing mixed powders

translated to poor process control of (i) powder yield for each powder (which may have been different for each powder composition and over time for each set of 10 layers), (ii) the laser absorption efficiency which may have varied with time (absorption can also be impacted by compositions of the layers), and (iii) the Z height from laser tool to the deposit. These factors need to be a considered in future research work on the production of Ti-Ni based alloys FGMs.

- The possibility of using Inconel 625 workpiece for grading from 100 pct nominal Inconel 625 to Ti6Al4V should be explored. The hypothesis is that with lower melting point and higher thermal conductivity of Inconel 625 over Ti6Al4V the heat will dissipate faster. This may result in lower thermal gradients and a wider fusion zone and minimize the likelihood of formation of Ti-Ni intermetallics.

APPENDIX

THIS IS AN APPENDIX CONTAINING ADDITIONAL FIGURES FROM RESULTS SECTION

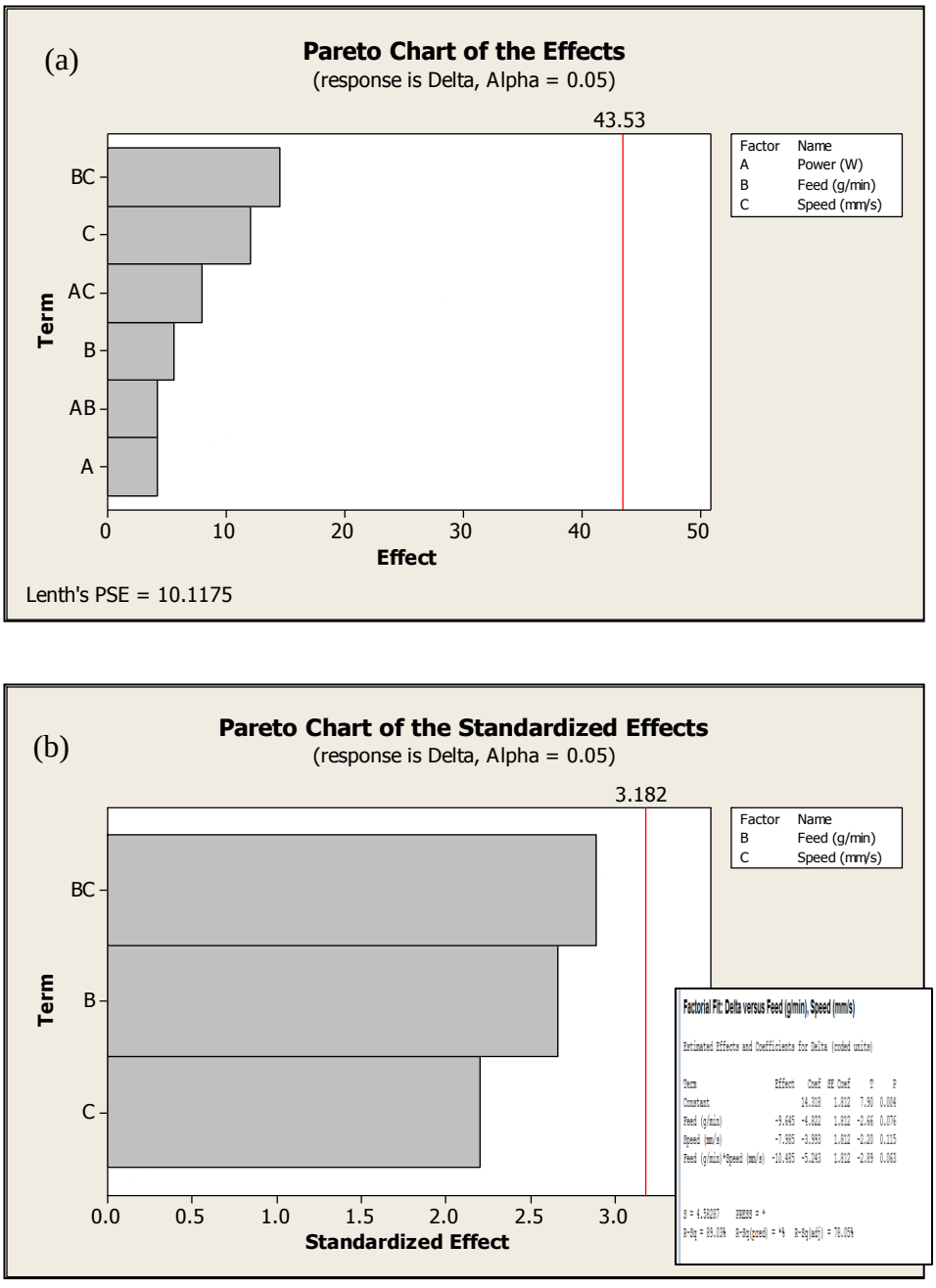

Figure A.1 Pareto chart showing the effect of processing parameters in minimizing mixing in the layers.

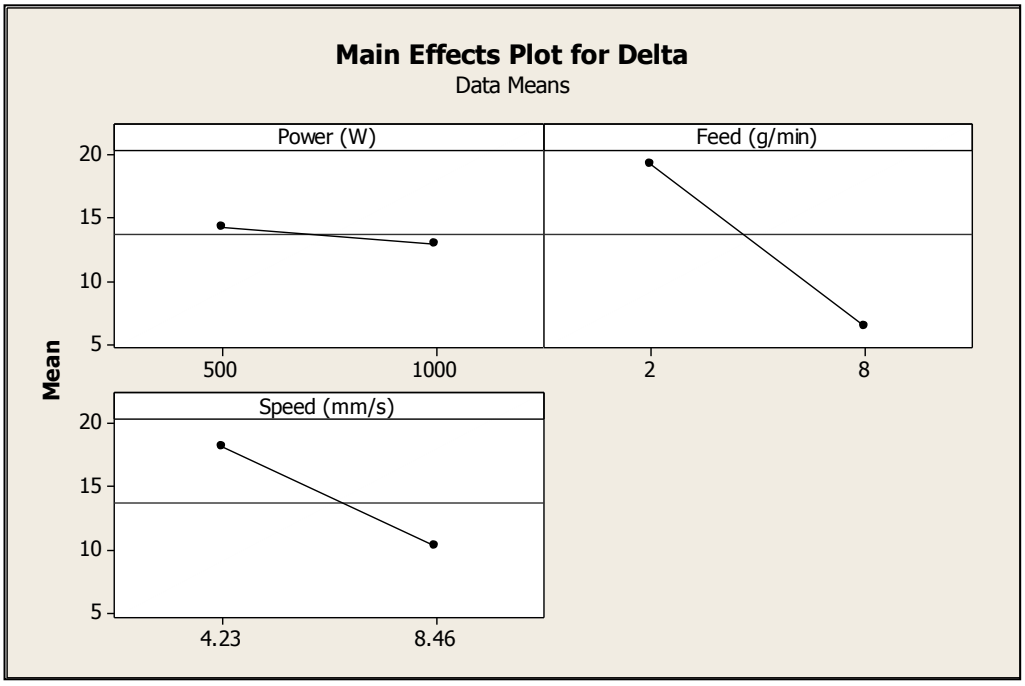

Figure A.2 Plot shows the effect of processing parameters in minimizing mixing in thelayers.

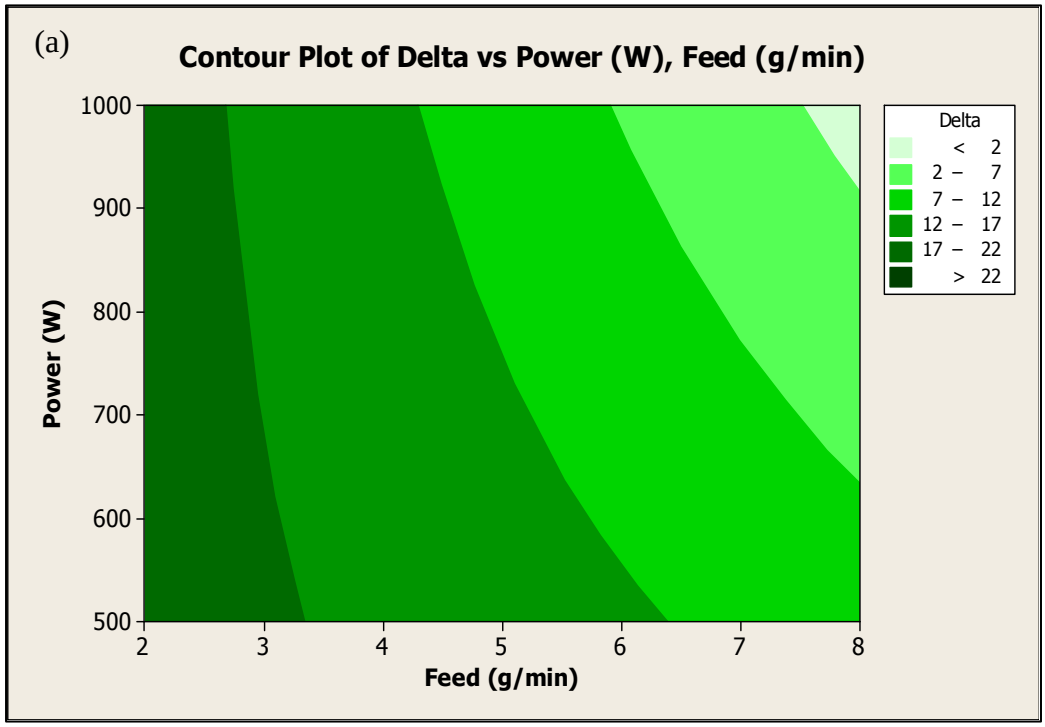

Figure A.3 Contour plot shows the effect of processing parameters in minimizing mixing in the layers.

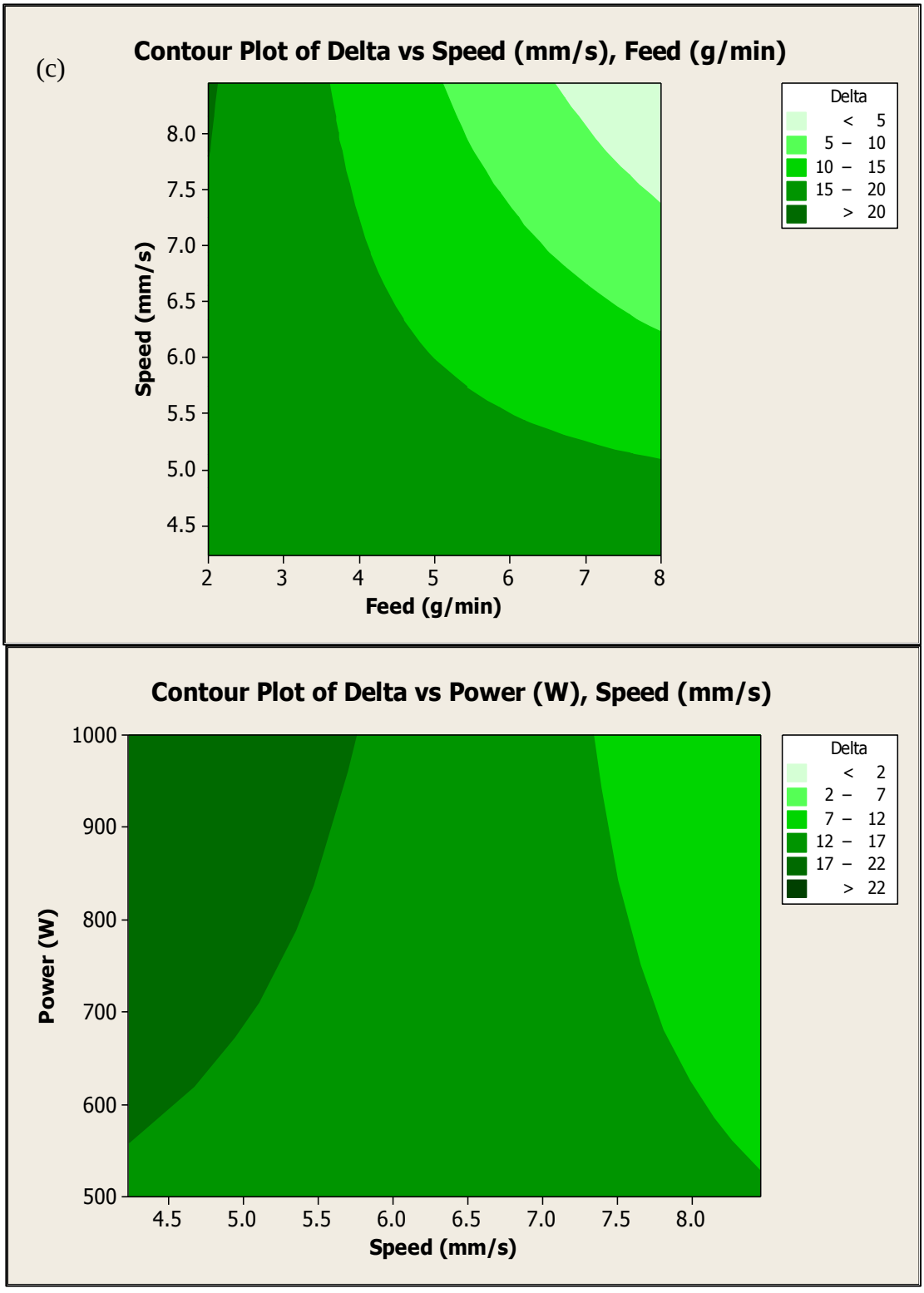

Figure A.3 Contour plot shows the effect of processing parameters in minimizing mixing in the layers (Cont.).

Table A.1 Factsage Modeling and XRD Verification for deposition Strategy Chem II at 1000 W, ND=not detected, *= overlap with Ti_2N/ not resolved, **=overlap with NiTi/not resolved, No database= no peak patterns at room temperature. 100 represents 100 wt.% Ti6Al4V-0 wt% Inconel 625, 80 represents 80 wt.% Ti6Al4V-20 wt.% Inconel 625.

Chem I	Ti_3Al	Ti-α	$NiTi_2$	V	Cr	Mo	Fe_2Ti	$NbCr_2$	$NbCo_2$	Cr_3Mn_5	AlNi	CoAl	NiTi	Ni
Factsage [90]+ [10]	34.85	51.97	9.09	4.8	0.7	0.10		0.26	0.01					
XRD		<hcp-82%, c-<1%	<4%	**	ND	<7%	ND	ND	ND	ND	ND	ND	ND	ND
Factsage [80]+ [20]	32.91	28.63	28.78	5.4	3.0	0.81		0.78	0.02	0.04				
XRD	*	<50.5	<24.8	**	ND	<6.9%	ND	<5%	ND	ND	ND	ND	<1%	ND
Factsage [70]+ [30]	32.00	9.90	49.46	3.0	2.0	0.5	0.05	2.31	0.04	0.42				
XRD	*	<14%	<19%	**	<2%	<4%	ND	<12%	<3%	ND	ND	<3%	<10%	ND
Factsage [60]+ [40]	18.71		61.99	1.20	4.7	4.4	2.43	2.84	0.55	1.16	1.13	0.29		
XRD	*	ND	<14.9%	**	<2%	<2%	ND	<7.9%	<3%	ND	ND	<2%	<4%	ND
Factsage [50]+ [50]	2.17		80.40	1.00	4.1	2.0	3.29	1.67	0.06	0.19	4.07	0.36		
XRD	*	ND	<5%	**	<2%	<3%	ND	<13%	<4%	ND	ND	<45	<13%	ND
Factsage [0]+ [100]				1.0	4.17			6.14	0.12	1.18				6.7
XRD	*		<9.2%	**	<1%	<4.1%	ND	<12,2%	<3.1%	ND	ND	<2%	<2%	ND

Table A.1 Factsage Modeling and XRD Verification for deposition Strategy Chem II at 1000 W, ND=not detected, *= overlap with Ti_2N/ not resolved, **=overlap with NiTi/not resolved, No database= no peak patterns at room temperature. 100 represents 100 wt.% Ti6Al4V-0 wt% Inconel 625, 80 represents 80 wt.% Ti6Al4V-20 wt.% Inconel 625 (Cont.).

Chem I	$MoNi_4$	$NbFe_2$	Ni_3Al	Fe(bcc)	$NbCo_3$	Ni_3Ti	$Ni_{24}Cr_{20}Mo_{12}$	FeTi	Cr_5Al_8	$AlNbTi_2$	V_5Al_8	$Mo_{0.84}Ni_{0.16}$	Co_2Ti
Factsage													
[100]+ [90] XRD	ND	ND	ND	ND	ND	ND	NDB	**	ND	<6%	ND	ND	ND
Factsage													
[90]+ [80] XRD	ND	<6.9%	ND	ND	ND	ND	NDB	**	ND	<1%	ND	<2%	<2%
Factsage													
[80]+ [70] XRD	ND	<11%	<7%	ND	ND	ND	NDB	**	ND	ND	ND	<4%	<9%
Factsage													
[70]+ [60] XRD	ND	<7.9%	<7.9%	ND	ND	<23.8%	NDB	**	ND	ND	<15.8%	<2%	<6.9%
Factsage													
[60]+ [50] XRD	ND	<7%	<6%	ND	ND	<23%	NDB	**	ND	ND	<10%	<3%	<7%
Factsage		0.12	45.27		30.17	4.85							
[50]+ [0] XRD	ND	<8.2%	<6.1%	ND	ND	<39.8%	NDB	**	ND	ND	<4.1%	<2%	<6.1%

Table A.2 Factsage Modeling and XRD Verification for deposition Strategy Chem III at 1000 W, ND = not detected, *= overlap with Ti_2N/ not resolved, **= overlap with NiTi/not resolved, No database (NDB) = no peak patterns at room temperature. 100 represents 100 wt.% Ti6Al4V-0 wt% Inconel 625, 80 represents 80 wt.% Ti6Al4V-20 wt.% Inconel 625.

Chem II	Ti_3Al	Ti-α	$NiTi_2$	V	Cr	Mo	Fe_2Ti	$NbCr_2$	$NbCo_2$	Cr_3Mn_5	AlNi	CoAl	NiTi	Ni
Factsage	30.55	42.37	18.2	4.6	1.56	0.21	0.02	0.52	0.52	0.67				
[80] +[20] XRD	*	<86%	<9%	**	ND	ND	ND	ND	ND	ND	ND	ND	ND	ND
Factsage	17.18	13.60	48.0	1.20	6.2	3.10	5.43	2.34	0.02	0.15	0.66	0.29		
[60] +[40] XRD	*	<85%	<15%	**	ND	ND	ND	ND	ND	ND	ND	ND	ND	ND
Factsage			47.7	1.30	4.86	2.40	4.14	4.50	1.54	1.23	5.26	0.94	24.17	
[40] + [60] XRD	*	<47%	<40%	**	ND	ND	<4.2857	ND	ND	ND	ND	ND	ND	ND
Factsage				0.40	11.2	3.91	5.36	4.98	0.08	0.49	3.33	1.08	45.10	
[20] +[80] XRD	*	<50%	<11%	**	ND	ND	ND	<5%	ND	ND	ND	ND	ND	ND
Factsage				0.37	15.0			5.07	0.14	2.42				17.8
[0]+ [100] XRD	*	ND	<79.2%	**	ND	<0.9%	ND	ND	ND	ND	ND	ND	<3%	ND

Table A.2 Factsage Modeling and XRD Verification for deposition Strategy Chem III at 1000 W, ND = not detected, *= overlap with Ti_2N/ not resolved, **= overlap with NiTi/not resolved, No database (NDB) = no peak patterns at room temperature. 100 represents 100 wt.% Ti6Al4V-0 wt% Inconel 625, 80 represents 80 wt.% Ti6Al4V-20 wt.% Inconel 625 (Cont.).

Chem II	$MoNi_4$	$NbFe_2$	Ni_3Al	Fe(bcc)	$NbCo_3$	Ni_3Ti	$Ni_{24}Cr_{20}Mo_{12}$	FeTi	Cr_5Al_8	$AlNbTi_2$	V_5Al_8	$Mo_{0.84}Ni_{0.16}$	Co_2Ti
Factsage													
[80] +[20]													
XRD	ND	ND	ND	ND	ND	ND	NDB	ND	ND	ND	ND	<5%	ND
Factsage													
[60] +[40]													
XRD	ND	ND	ND	ND	ND	ND	NDB	ND	ND	ND	ND	ND	ND
Factsage													
[40] + [60]													
XRD	ND	<4%	ND	ND	ND	ND	NDB	ND	ND	<2%	ND	ND	ND
Factsage						22.89							
[20] +[80]													
XRD	ND	ND	ND	ND	ND	ND	NDB	**	<21%	ND	<9%	<4%	ND
Factsage	22.95	0.14	15.90	0.10	0.76	11.04	7.32						
[0]+ [100]													
XRD	ND	ND	<1%	ND	ND	ND	NDB	**	<11.9%	ND	<4%	ND	ND

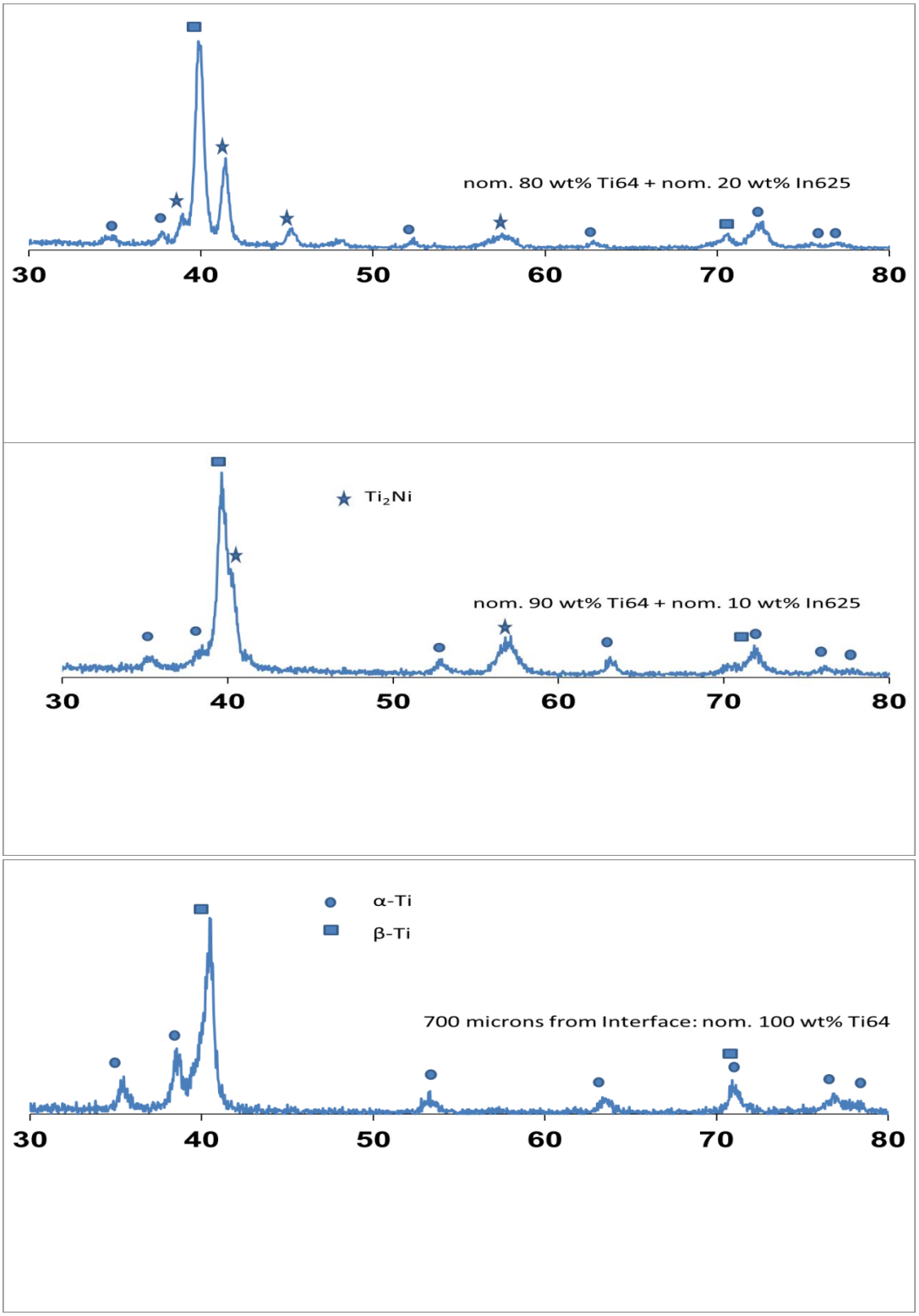

Figure A.4 XRD patterns measured perpendicular to the laser scanning direction in the compositionally graded material for chem II_at 1000 W. Note: all the compositions are nominal and calculated from measured data.

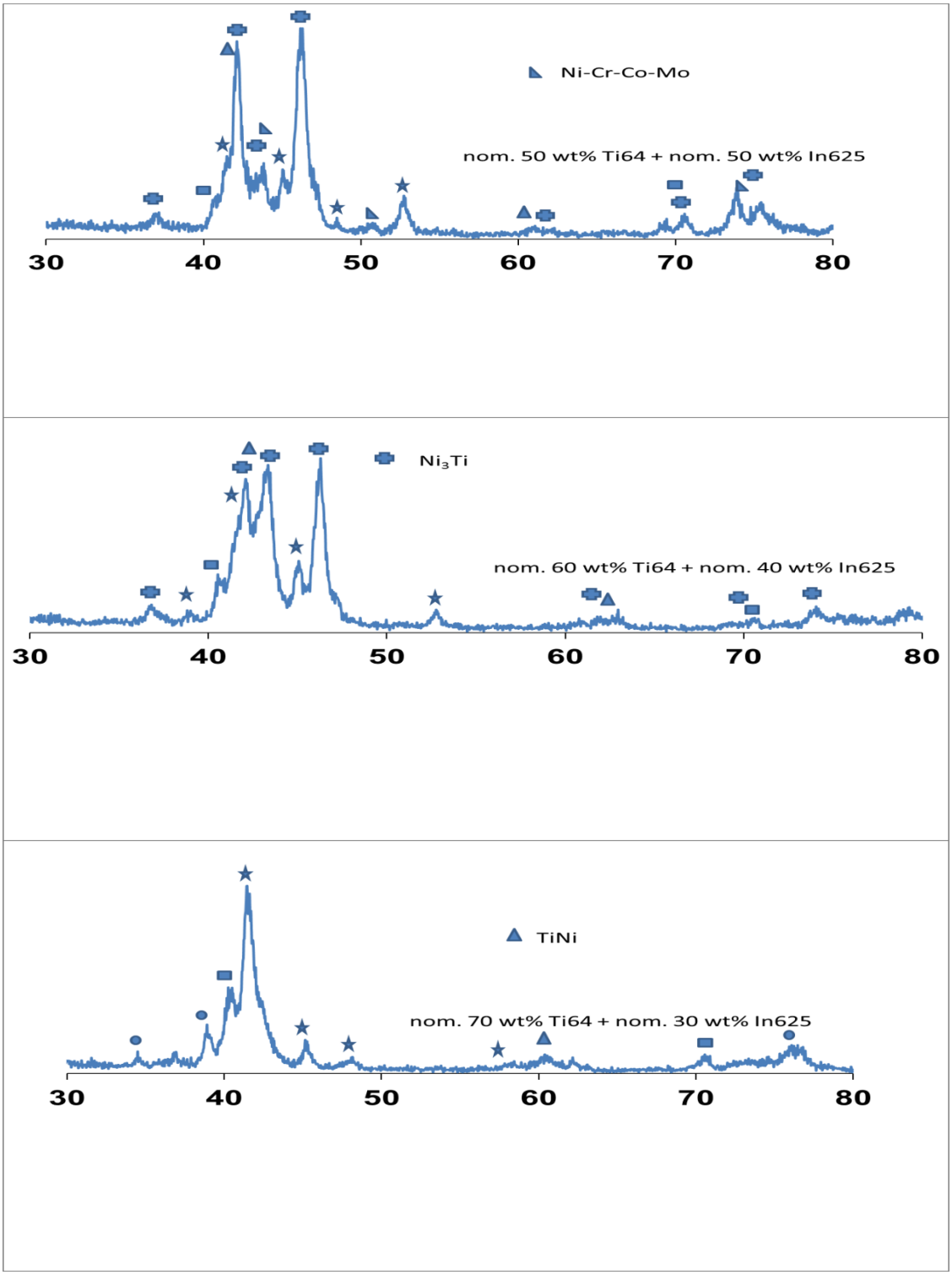

Figure A.4 XRD patterns measured perpendicular to the laser scanning direction in the compositionally graded material for chem II_at 1000 W. Note: all the compositions are nominal and calculated from measured data (Cont.).

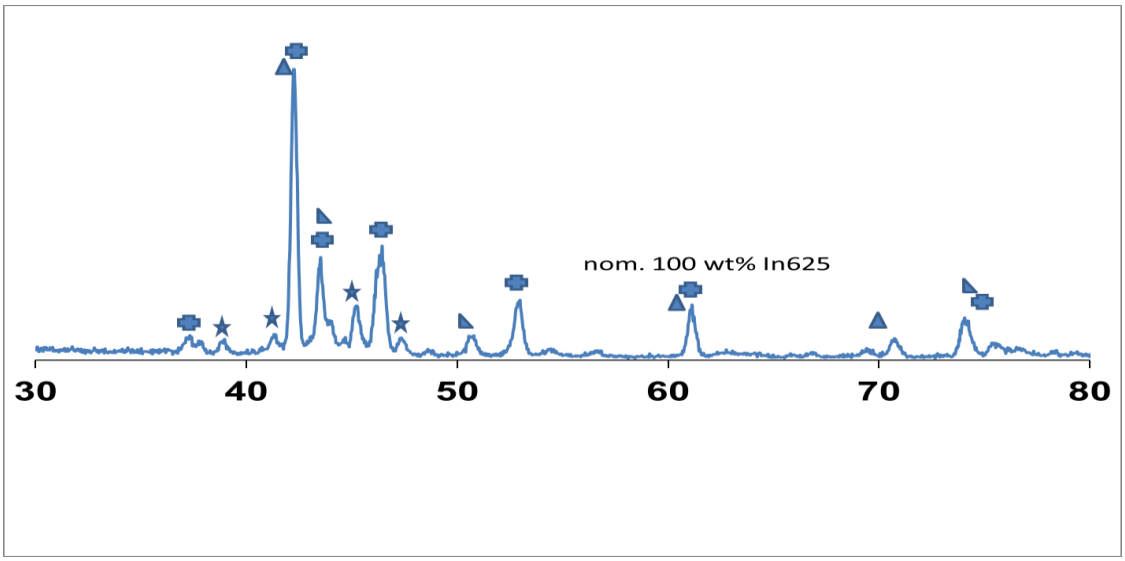

Figure A.4 XRD patterns measured perpendicular to the laser scanning direction in the compositionally graded material for chem II at 1000 W. Note: all the compositions are nominal and calculated from measured data (Cont.).

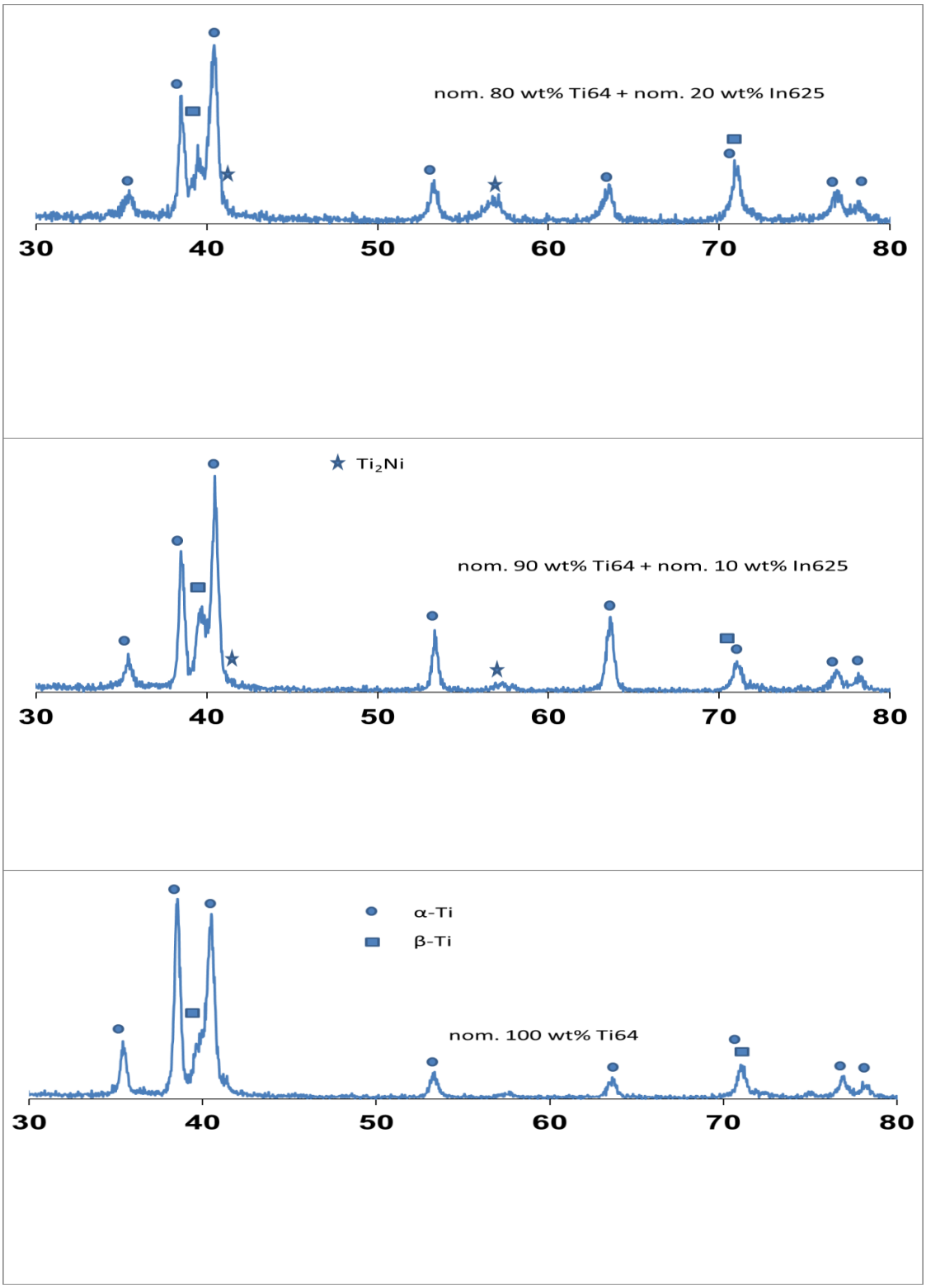

Figure A.5 XRD patterns measured perpendicular to the laser scanning direction in the compositionally graded material for chem II at 500 W. Note: all the compositions are nominal and calculated from measured data.

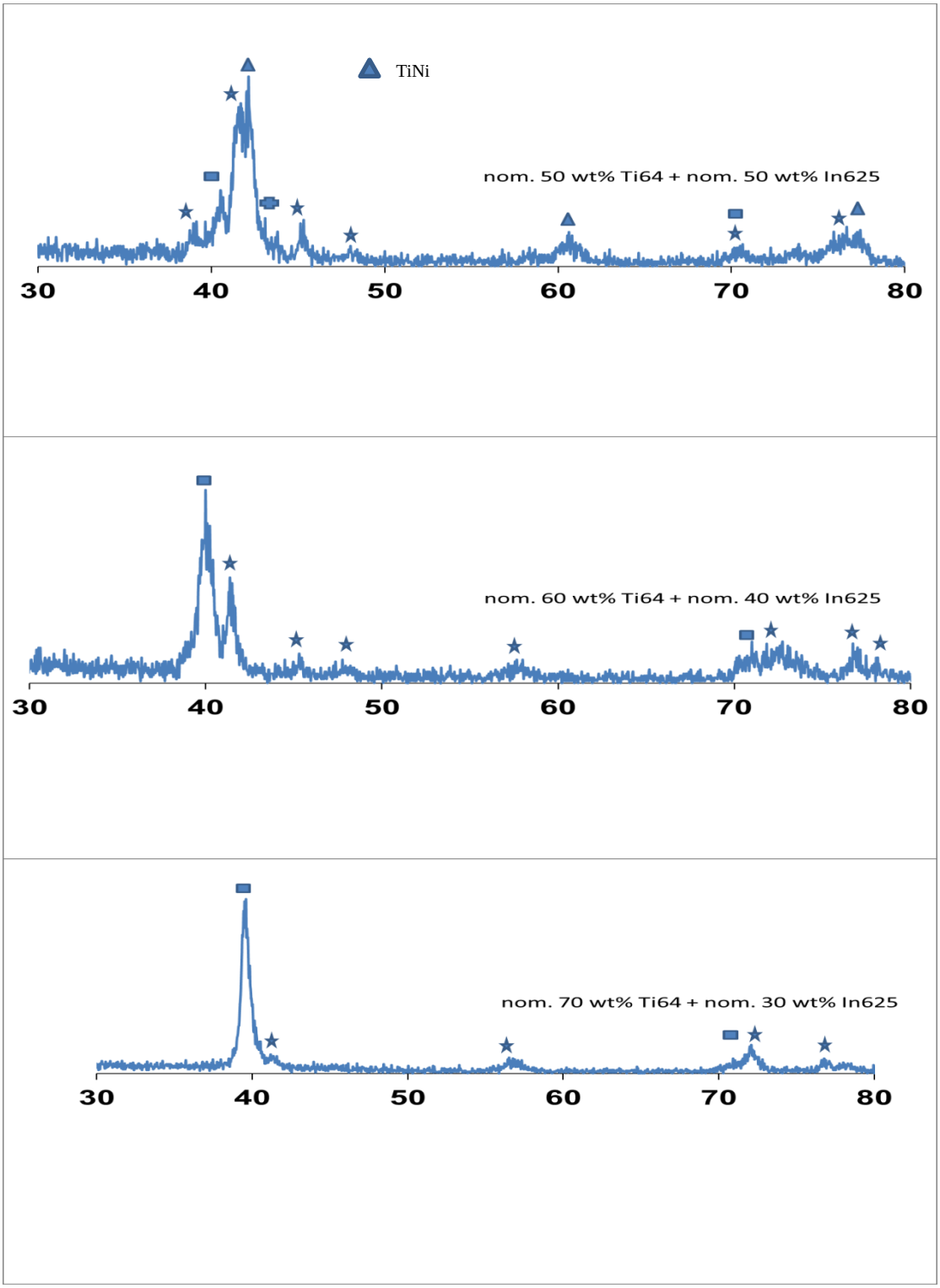

Figure A.5 XRD patterns measured perpendicular to the laser scanning direction in the compositionally graded material for chem II at 500 W. Note: all the compositions are nominal and calculated from measured data (Cont.).

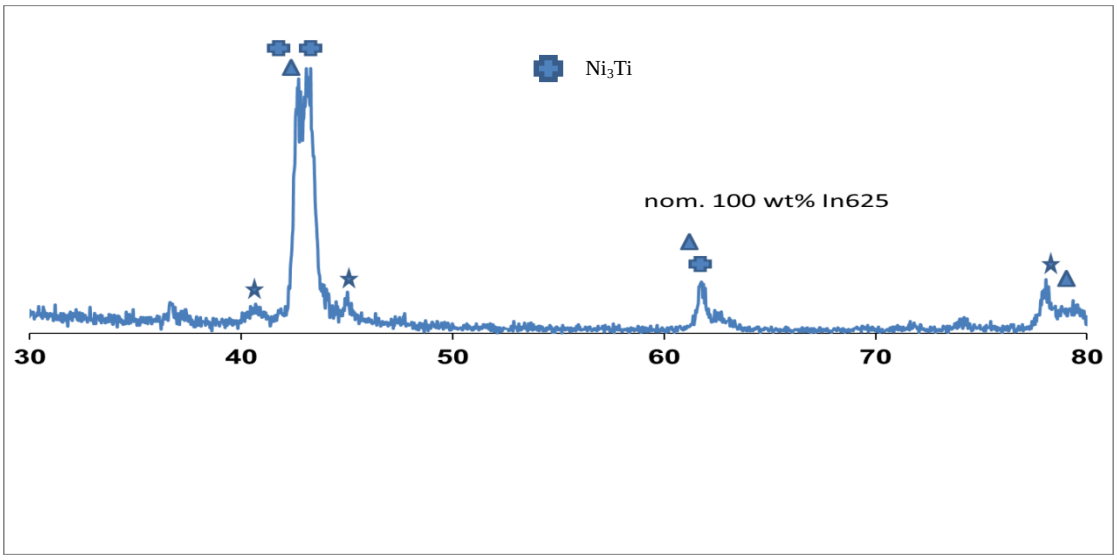

Figure A.5 XRD patterns measured perpendicular to the laser scanning direction in the compositionally graded material for chem II at 500 W. Note: all the compositions are nominal and calculated from measured data (Cont.).

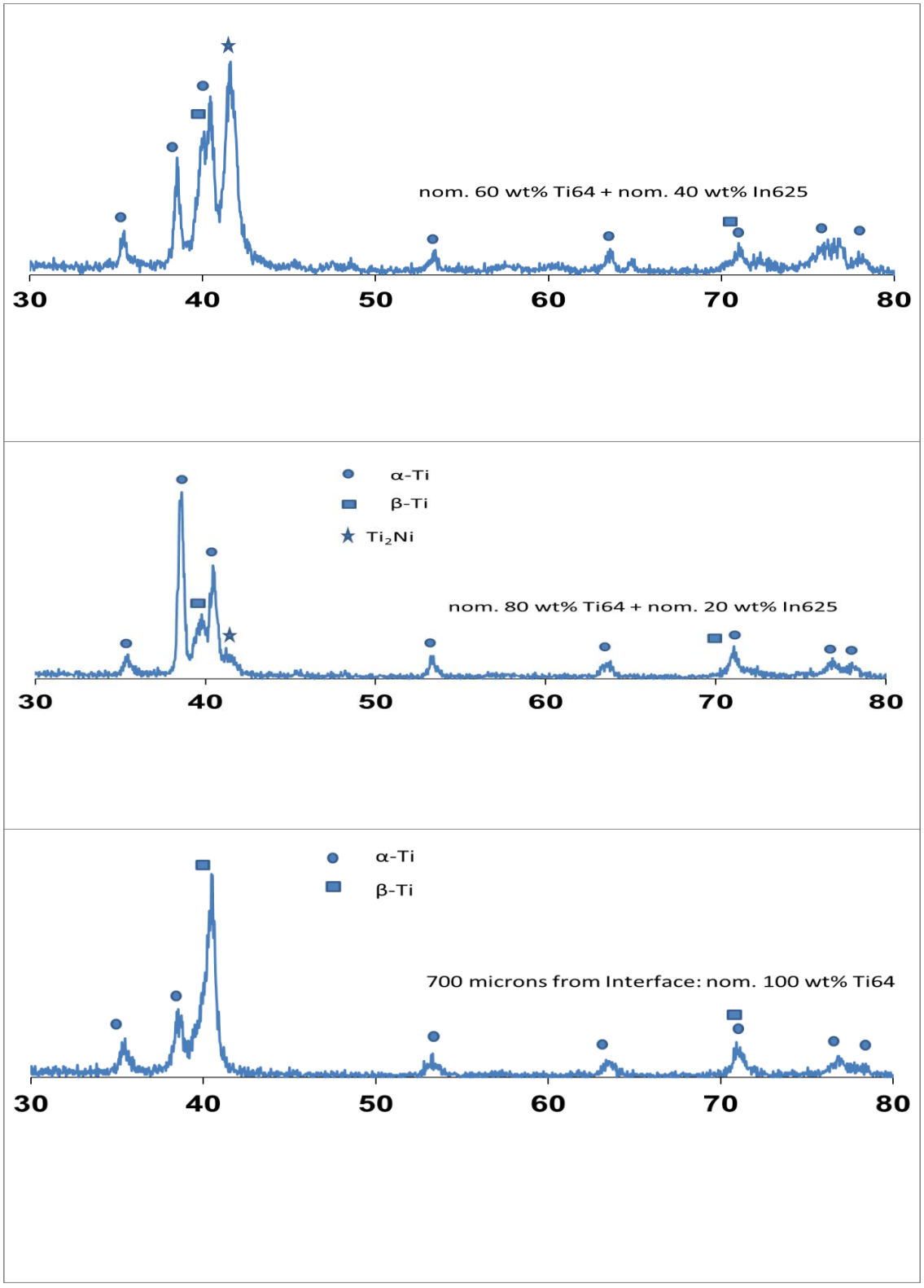

Figure A.6 XRD patterns measured perpendicular to the laser scanning direction in the compositionally graded material for chem III at 1000 W. Note: all the compositions are nominal and calculated from measured data.

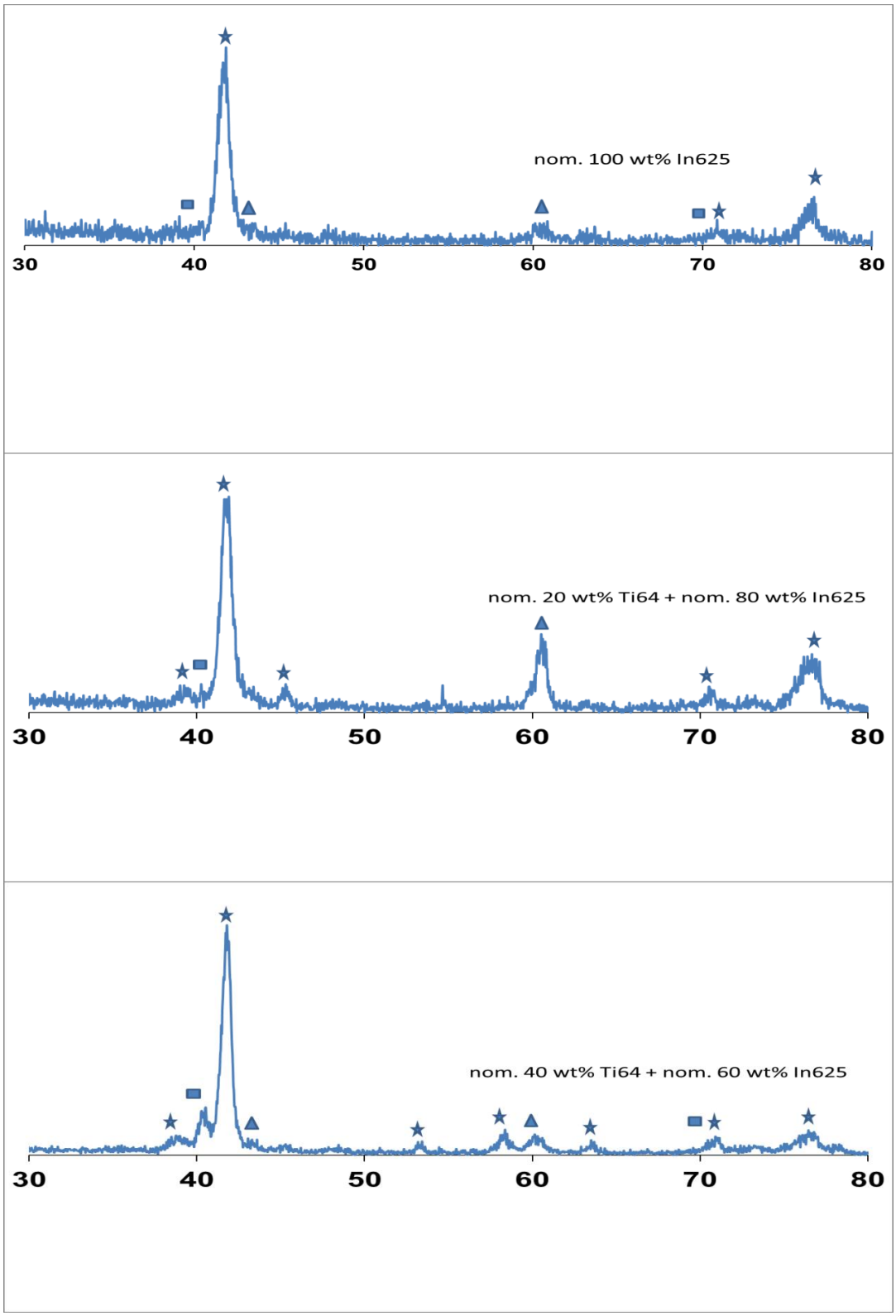

Figure A.6 XRD patterns measured perpendicular to the laser scanning direction in the compositionally graded material for chem III at 1000 W. Note: all the compositions are nominal and calculated from measured data (Cont.).

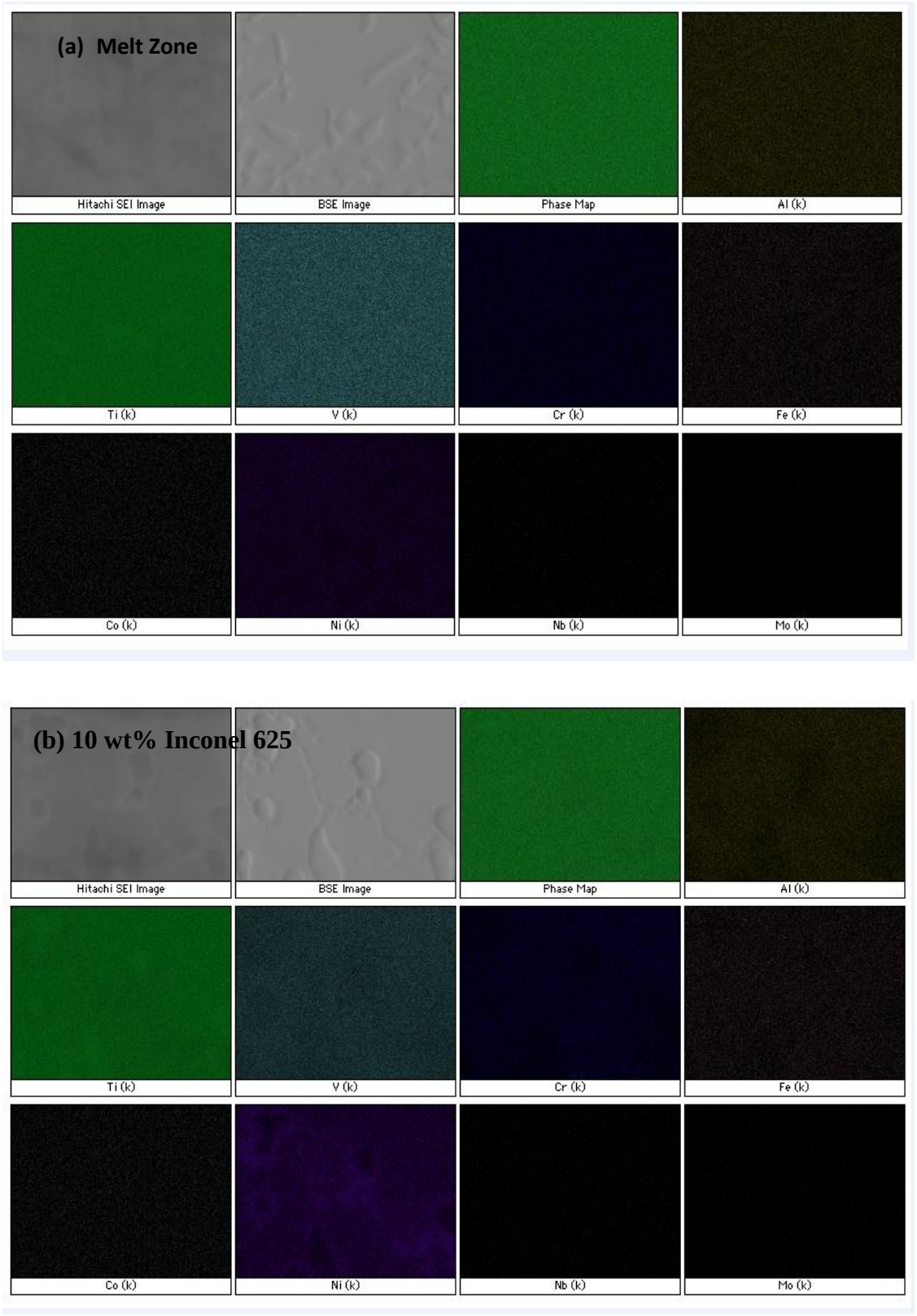

Figure A.7 X-ray elemental maps of Chem II showing elemental distribution along the composition gradient. Note: all the compositions are nominal and calculated from measured data.

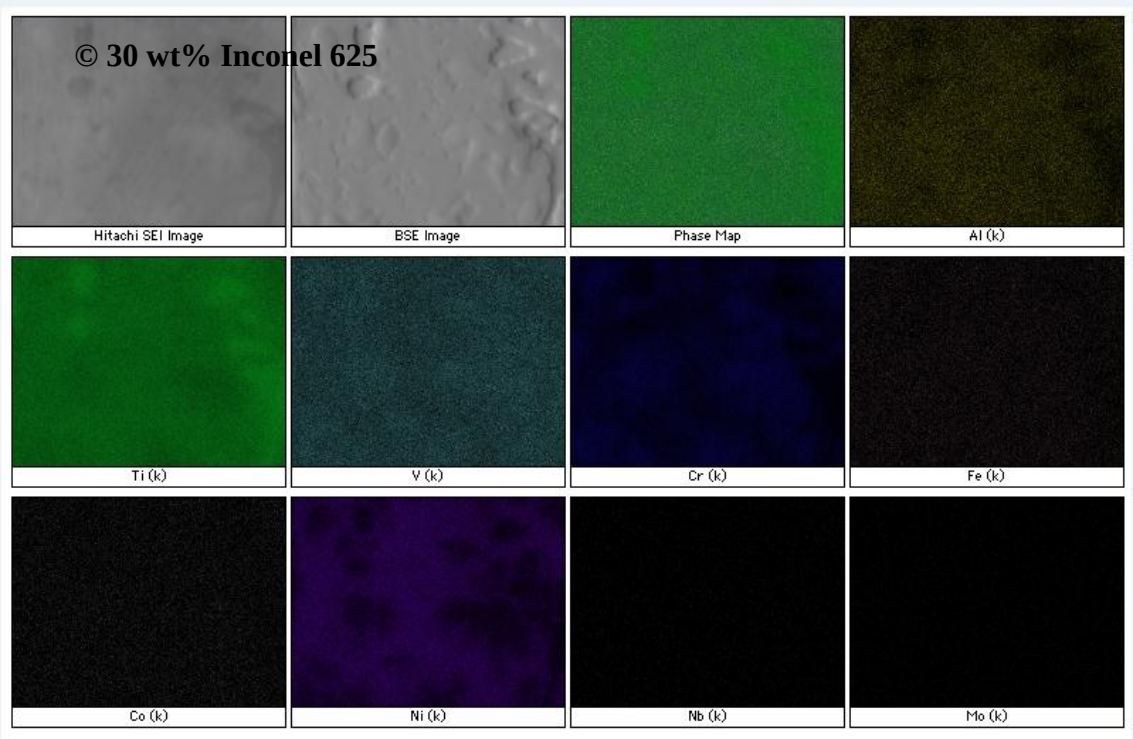

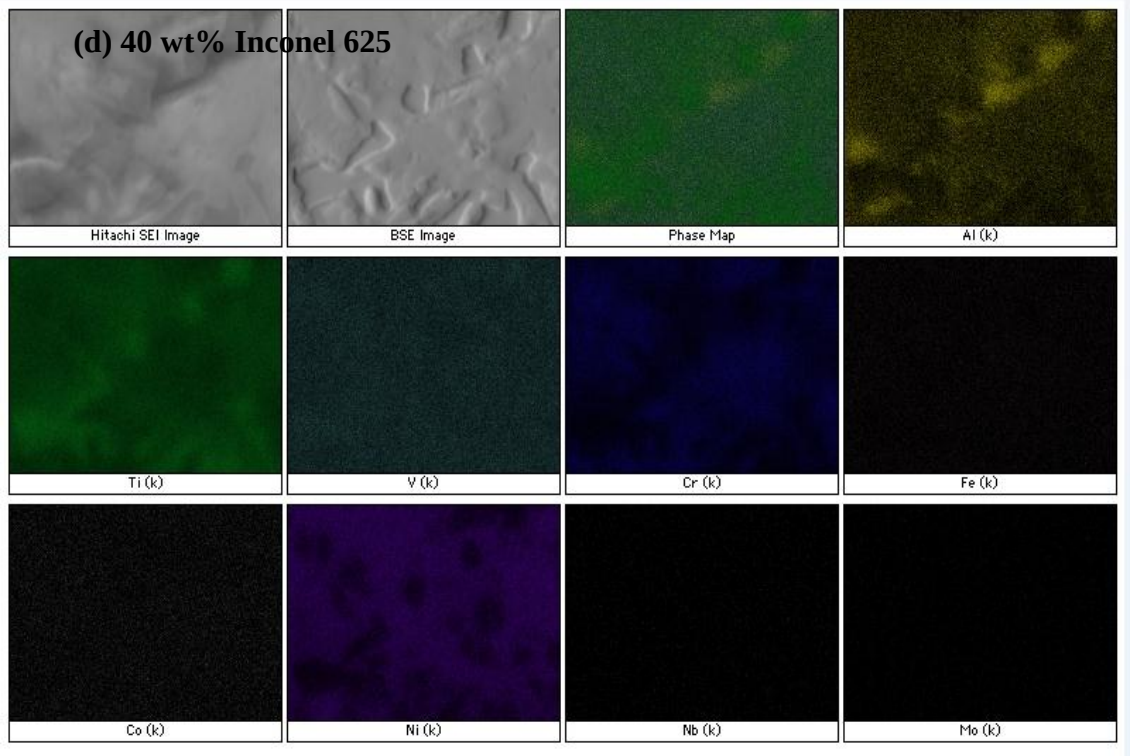

Figure A.7 X-ray elemental maps of Chem II showing elemental distribution along the composition gradient. Note: all the compositions are nominal and calculated from measured data (Cont.).

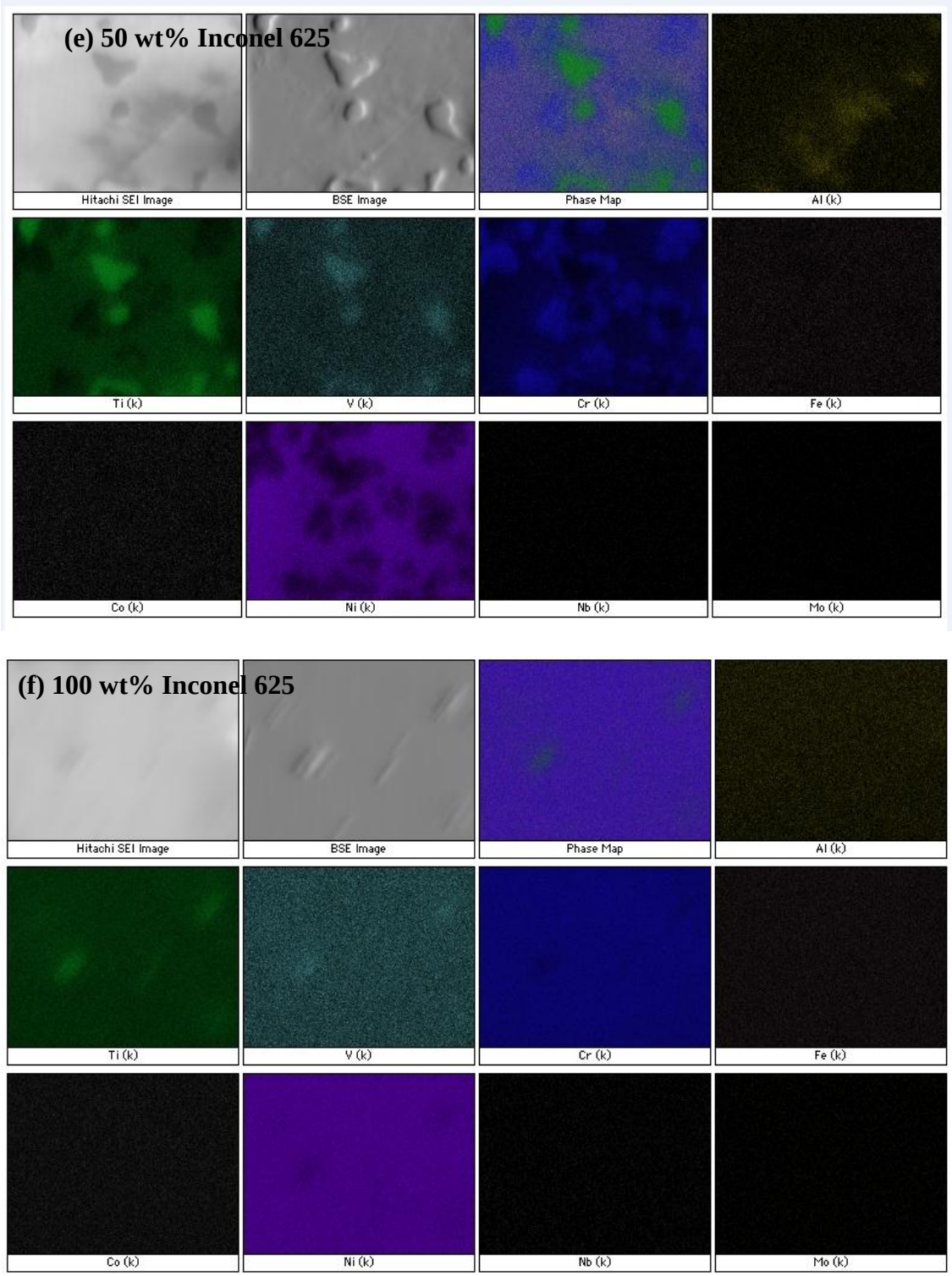

Figure A.7 X-ray elemental maps of Chem II showing elemental distribution along the composition gradient. Note: all the compositions are nominal and calculated from measured data (Cont.).

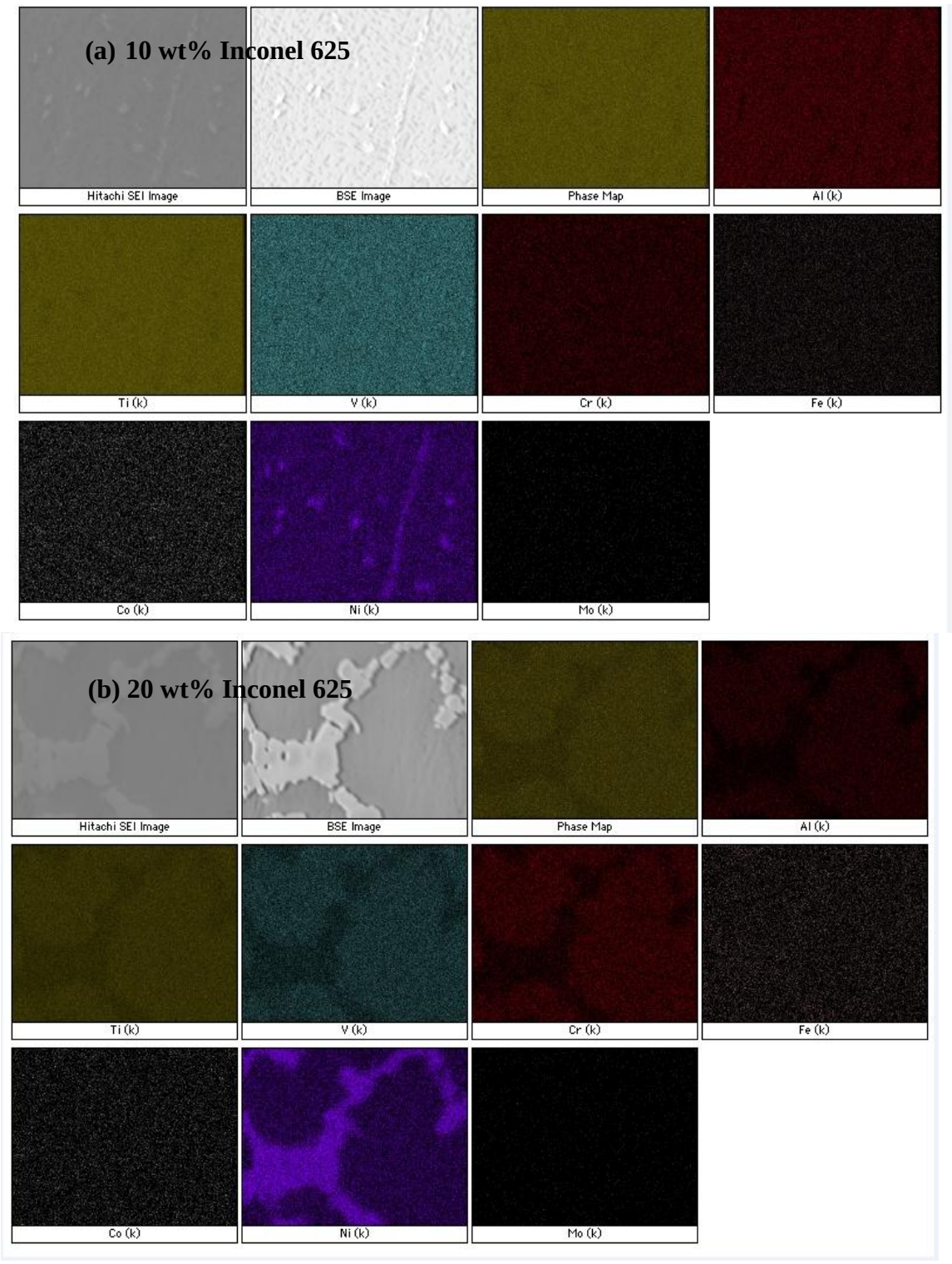

Figure A.8 X-ray elemental maps of Chem III showing elemental distribution along the composition gradient. Note: all the compositions are nominal and calculated from measured data.

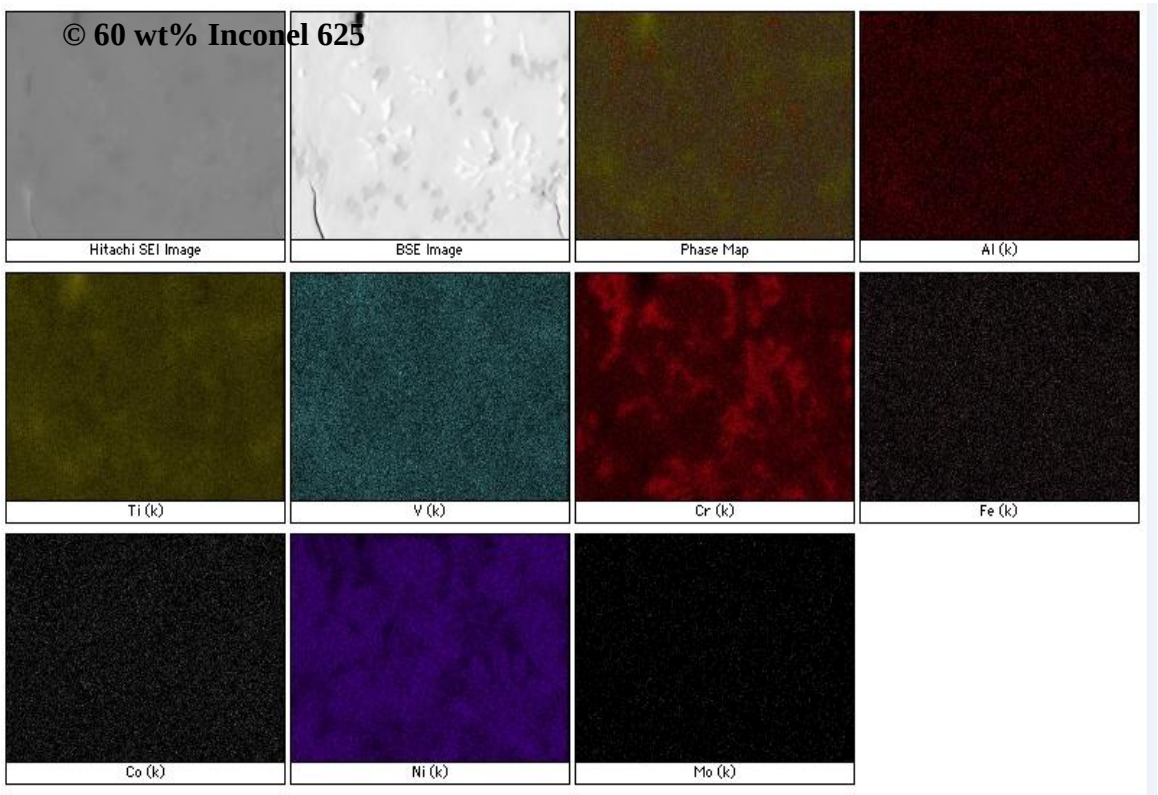

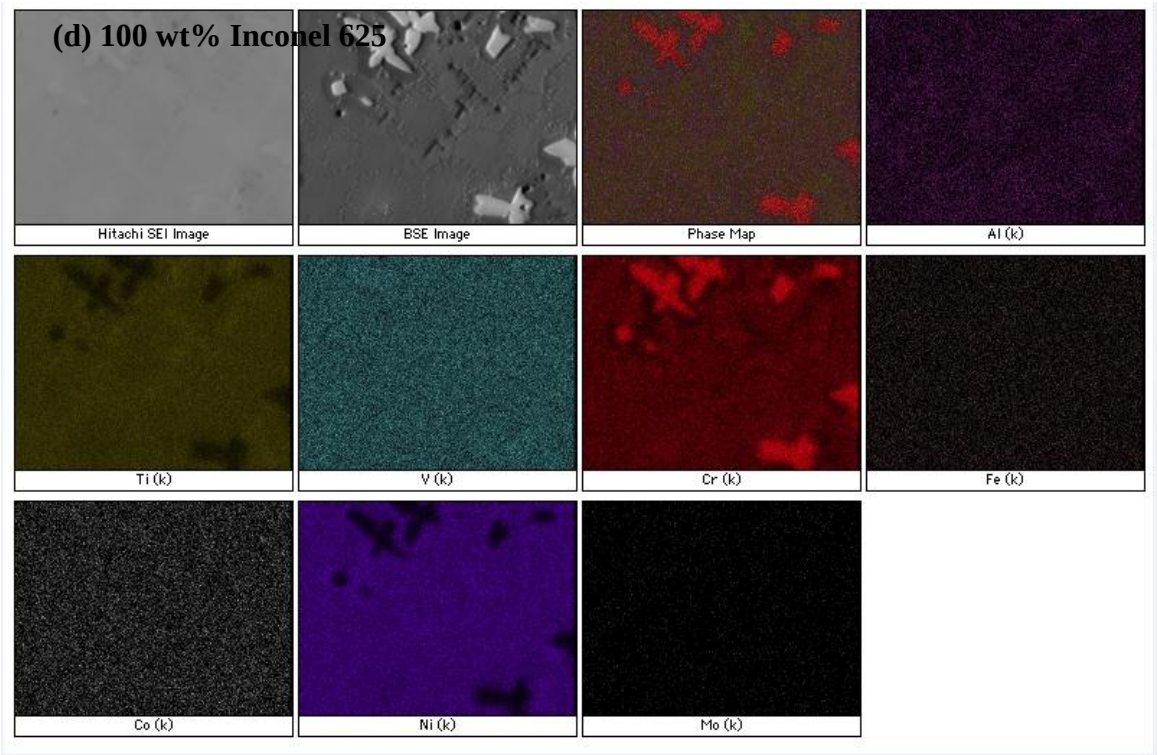

Figure A.8 X-ray elemental maps of Chem III showing elemental distribution along the composition gradient. Note: all the compositions are nominal and calculated from measured data (Cont.).

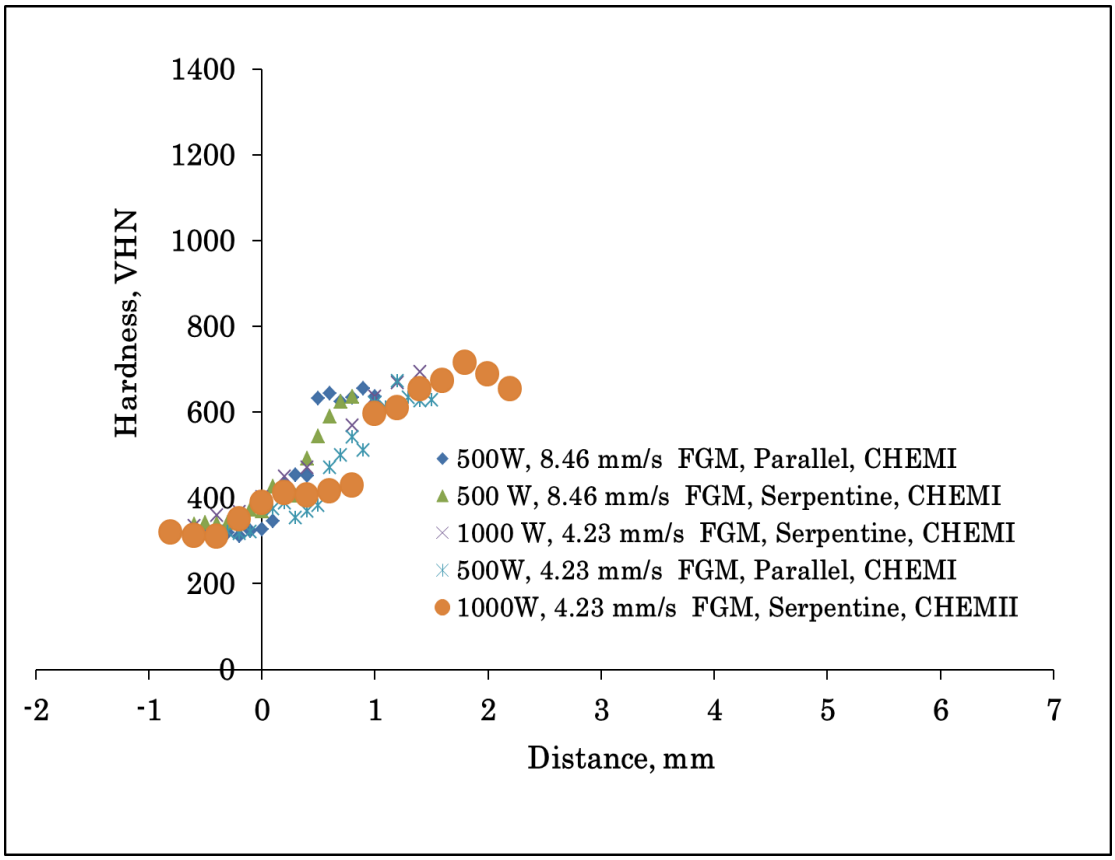

Figure A.9 Hardness values of the functionally graded material measured along the composition gradient, *0 mm = means initial substrate-deposit interface.

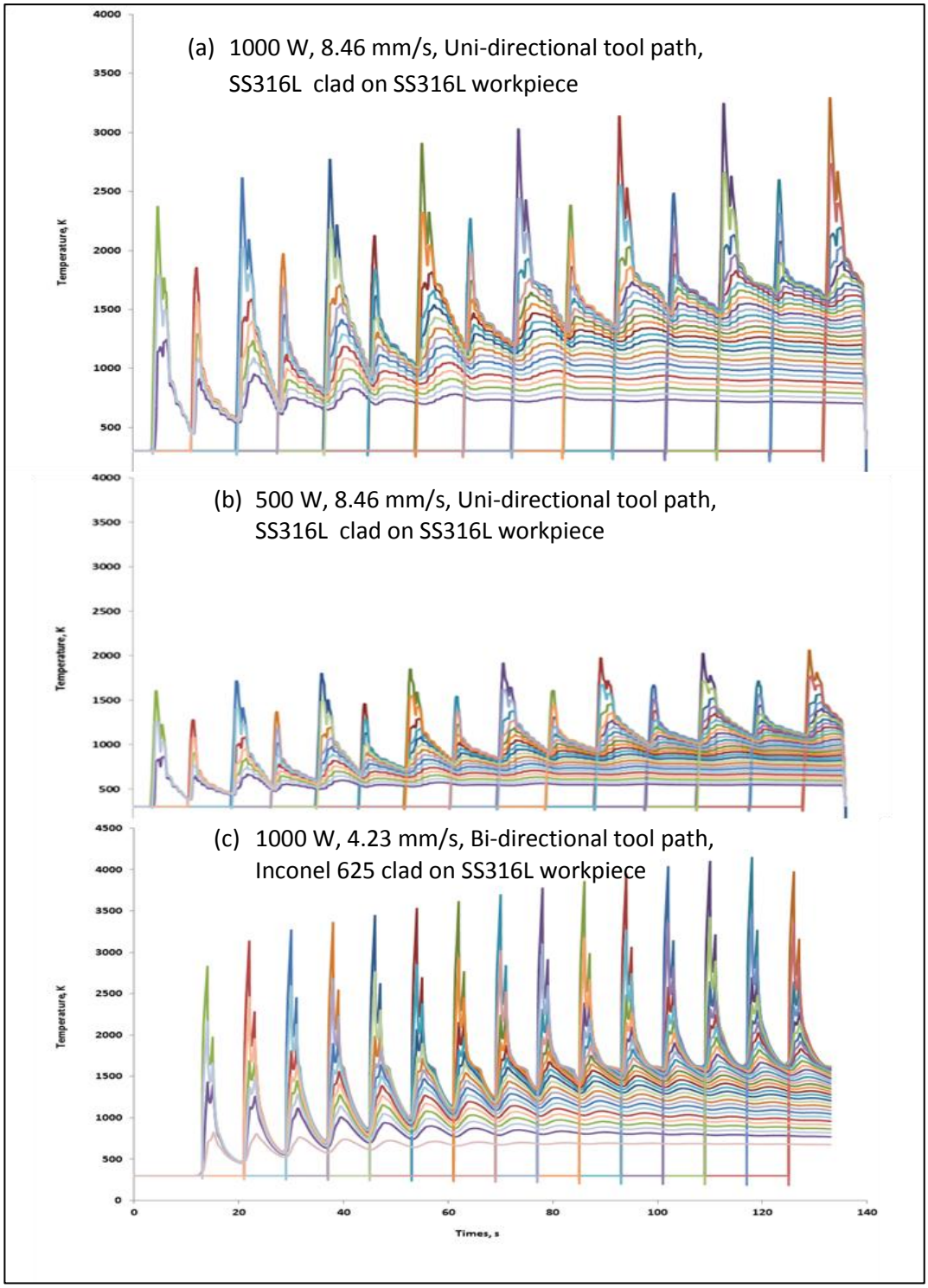

Figure A.10 Peak temperature history calculated for each layer of thin wall at the end of deposition.

BIBLIOGRAPHY

[1] www.wikipedia.org, Accessed on 2nd February, 2011.Search term = Functionally Graded Materials.

[2] G. K. Lewis, E. Schlienger, Materials and Design, 21 (2000), p 417.

[3] W. M. Steen, V.M. Weerasinghe, P. Monson, Proceedings of SPIE, 650 (1986), p 226.

[4] N. I. S Hussein, I.R. Pashby, D.G. McCartney, International Journal of Manufacturing Technology and Management, 17(4) (2009), p 419.

[5] R. Lahoz, J. A. Puertolas, Journal of Alloys Compounds, 381(2004), p 130.

[6] X. Lin, T. M. Yue, H. O. Yang, W.D. Huang, Materials Science and Engineering A, 391 (2005), p 325.

[7] M. S. Domack, J. M. Baughman, Rapid Prototyping Journal, 11 (2005), p 41.

[8] X. Xu, X. Lin, M. Yang, J. Chen, W. Huang, Journal of Alloys and Compounds, 480 (2009), p 782.

[9] X. Lin, T. M. Yue, H. O. Yang, W.D. Huang, Metallurgical & Materials Transactions A, 38 A (2007), p 127.

[10] H. C. Chen, A. J. Pinkerton, L. Li, Int J Adv Manuf Technol (2010), DOI 10.1007/s00170-010-2791-3.

[11] J. Mazumder, A. Schifferer and J. Choi, Materils Research Innovation, 3:1999, p 118.

[12] J. Mazumder, J. Choi, K. Nagarathnam, J. Koch and D. Hetzner, Journal of the Minerals, Metals and Materials Society, 49 (5), 1999, p 55.

[13] Y. T. Pei, V. Ocelik, J. Th. M. De Hosson, Acta Materialia, 50(8), 2002, p 2035.

[14] W. Liu, and J. N. DuPont, Proc. 13th Solid Freeform Fabrication Symposium, Austin USA, 2002, p 124.

[15] B. Kloosterman, B. J. Kooi, and J. Th. M. De Hosson, Acta Mater. 46, 1998, p 6205.

[16] Zheng, J.E. Smugeresky, Y. Zhou, D. Baker, and E.J. Lavernia, Metallurgical and Materials Transactions A, 39A, 2008, p 1196.

[17] K. A. Mumtaz and N. Hopkinson, Journal of Materials Science, 42, 2007, p 7647.

[18] X. Liu, and H. M. Wang, Applied Surface Science, 252, 2006, p 5735.

[19] X. C. Li, J. Stampf, and F. B. Prinz, Materials Science and Engineering A, 282, 2000, p 86.

[20] Processes and mechanisms of welding residual stress and distortion by Zhili Feng, copyright of CRC press.

[21] L. Sexton, S. Lavin, G. Byrne, and A. Kennedy, Journal of Materials Processing and Technology, 122(1), 2002, p 63.

[22] R.R. Unocic and J.N. Dupont, Metallurgical and Materials Transactions B, 35B, 2004, p 143.

[23] Felde, T. Reti, K. Zoltan, L. Costa, R. Colaco, R. Vilar, and B. Vero, Proceedings from the 1st International Surface Engineerung Congree and the 13th IFHTSE Congress, 2002, p 237.

[24] Miyamoto, S. Fujimori, and K. Itakura, Section F ICALEO, 1997, p 1.

[25] R. Noecker, Advanced Materials and Processes, 22, 2003, p 12.

[26] Kelbassa, A. Welsheit, K. Wissenbach, V. Hermes, Proc. of the 2nd Pacific International Conference on Applications of Lasers and Optics, 2006, p 208.

[27] C. Yao, B. xiu, X. Zhang, J. Huang, J. Fu, and Y. Wu, Optics and Lasers In Engineering, 47, 2009, p 807.

[28] J. Beuth, and N. Klingbeil, Journal of the Minerals, Metals and Materials Society; 53, 2001, p 36. J. Liu, and L. Li, Optics & Laser Technology, 37, 2005, p 287.

[29] F. Meriaudeau, F. Truchete, Journal of Laser Applications, 8, 1996, p.317.

[30] J. Lin, Optics and Laser Technology, 31(3), 1999, p 251.

[31] J. Lin, Journal of Materials Processing Technology, 105(1), 2000, p 17.

[32] J. Pinkerton, and L. Li, Journal of Laser Applications, 15(3), 2003, p 172.

[33] J. Pinkerton, and L. Li, 'Journal of Engineering Manufacture, 218(4), 2004, p 363.

[34] J. Pinkerton, and L. Li, 'International Journal of Machine Tools and Manufacture, 44(6), 2004, p 573.

[35] J. Pinkerton, and L. Li, Annals of the CIRP, 52(1), 2003, p 181.

[36] W. Hofmeister, M. Griffith, and M. Ensz, J. Smugeresky, Journal of the Minerals, Metals and Materials Society, 53(9), 2001, p 30.

[37] M. L. Griffith, M. E. Schlienger, and L. D.Harwell, Materials & Design, 20(2), 1999, p 107.

[38] M. Picasso, C. F. Marsden, and J. D. Wagniere, Metallurgical Transactions B, 25(2), 1994, p 281.

[39] F. H. Kaplan, and G. Groboth, Trans. ASME, Journal of Manufacturing. Science & Engineering, 123, 2001, p 609.

[40] S. M. Kelly, and S. Kampe, Metallurgical and Materials Transactions, 35A, 2004, p 1861.

[41] P. A. Kobryn, E.H. Moore, and S.L. Semiatin, Scripta Materialia, 43, 2000, p 299.

[42] D. H. Abbott, and F. G. Arcella, Advanced Materials & Processing, 153(5), 1998, p 29.

[43] X. Wu, and J. Liang, J. Mei, and C. Mitchell Materials and Design, 25(2), 2004, p 137.

[44] M. Gaumann, C. Bezencon, P. Canalis, W. Kurz, Acta Materialia, 49(6), 2001, p 1051.

[45] L. Wang, S. D. Felicelli, and P. Pratt, Materials Science and Engineering A, 496, 2008, p234.

[46] Vasinonta, and J.L. Beuth, and M.L. Griffith, Journal of Manufacturing. Science and Engineering, 129, 2007, p 101.

[47] P. Aggarangsi, J. L. Beuth, and M. Griffith, SFF Symposium, Austin, 2003, 207, p196.

[48] W. Hofmeister, M Wert, J. Smugersky, J. A. Philliber, M. Griffith, and M. Ensz, Journal of the Minerals, Metals and Materials Society,51(7), 1997,p 150.

[49] F. Kong, and R. Kovacevic, Metallurgical and Materials Transaction B, 41, 2010, p1310.

[50] H. U. Weiwei, K. Jinwu, and H. Tianyou, Tsinghua Science and Technology, 14, 2009, p154.

[51] V. Neela, and A. De, 2007 Abaqus India Regional Users' Meet, 2007, p1.

[52] L. Costa a, R. Vilar, T. Reti, and A.M. Deus, Acta Materialia, 53, 2005, p 3987.

[53] W. Hu. J. Kang, J. Ma, T. Huang, D. Li, A. Zhang, Advanced Materials Research, 148-149, 2011, p157.

[54] M. Labudovic, D. Hu, and R. Kovacevic, Journal of Materials. Science, 38, 2003, p 35.

[55] Y. P. Yang, and S. S Babu, Melting in the World, 54(9-10), 2010, p 298.

[56] S. Zekovic, and R. Kovacevic, Tribology in industry, 28(1&2), 2006, p9-14.

[57] P. Rangaswamy, M.L. Griffth, M.B. Prime, T.M. Holden, R.B. Rogge,J.M. Edwards, and R.J. Sebring, Materials. Science and. Engineering. A, 399, 2005, p 72.

[58] P. Rangaswamy, T.M. Holde, R. Rogge, and M.L. Griffith, Journal of Strain Analysis for Engineering Design, 38, 2003, p 519.

[59] R.J. Moat, A.J. Pinkerton L. Li P.J. Withers, and M. Preuss, Materials Science and Engineering A, 528, 2011, p 2288.

[60] A.M. Kamara, S. Marimuthu, and L. Li, Journal of Manufacturing Science and Engineering, Transactions of the ASME, 133 (3), 2011, p1.

[61] P. Pratt, S. D. Felicelli, L. Wang, and C. R. Hubbard, Metallurgical and Materials Transactions A: Physical Metallurgy and Materials Science, 39 (13), 2008, p 3155.

[62] M.L. Griffith, M.E. Schlienger, L.D. Harwell, M.S. Oliver, M.D. Baldwin, M.T. Ensz, J.E. Smugeresky, M. Essien, J. Brooks, C.V. Robino, W.H. Hofmeister, M.J. Wert, and D.V. Nelson, Journal of Materials Design, 20, 1999, p 107.

[63] P.J. Maziasz, E.A. Payzant, M.E. Schlienger, and K.M. McHugh, Scripta Materialia, 39, 1998, p 1471.

[64] A Capriccioli, and P. Frosi, Fusion Engineering and Design, 84, 2009, p 546.

[65] L. Borjesson, and L. Lindgren, Journal of Engineering. Materials and Technology, 123 (1), 2001, p106.

[66] L. R. sheng, L. Wei-jun, X. Fei, and W. Hua-bing, Transactions of Nonferrous Metals Society of. China, 18, 2008, p691.

[67] http://www1.asminternational.org/PortletTemplate.cfm, Accessed on 22nd September, 2013.

[68] I.A.Roberts, C.J.Wang, R.Esterlein, M.Stanford, and D.J.Mynors, International Journal of Machine Tools & Manufacture, 49, 2009, p 916.

[69] D. Deng, Materials and Design, 30, 2009, p 359.

[70] J.-Y. Chen, K. Conlon, L. Xue, and R. Rogge, Materials Science and Engineering A, 527, 2010, p 7265.

[71] G.P. Dinda, A. K. Dasgupta, and J. Mazumder, Materials Science and Engineering A, 509, 2009, p 98.

[72] L. F. Guo, T. M. Yue, and H. C. Man, Journal of Laser Applications, 16(4), 2004, p. 229.

[73] F.J. Kahlen, and A. Kar, Journal of Laser Applications, 13, 2001, p60.

[74] J. Spencer, Zeitschrift Fur Metallkunde, 87(7), 1996, p.535.

[75] G. Eriksson and K. Hack, Metallurgy Materials Transaction B, 21B, 1990, p1013.

[76] Ansara, Journal of Alloys and Compounds, 247, 1997, p20.

[77] H.L. Lukas, E.-Th. Henig, and B. Zimmermann, CALPHAD, 1, 1977, p225.

[78] R.H. Davies, P. Nash and B. Sundman, Applications of Thermodynamics in the synthesis and processing of materials, eds. P. Nash and B. Sundman, TMS, Warrendale, PA, 1995.

[79] Sundman, B. Jansson, and J.-O. Andersson, CALPHAD, 9, 1985, p153.

[80] C.W. Bale, E. Bélisle, P. Chartrand, S.A. Decterov, G. Eriksson, K. Hack, I.-H. Jung, Y.-B. Kang, Melançon, A.D. Pelton, C. Robelin, S. Petersen, CALPHAD, 33, 2009, p 295.

[81] C.W. Bale, P. Chartrand, S.A. Degterov, G. Eriksson, K. Hack, R. Ben Mahfoud, J. Melanqon, A.D. Pelton and S. Petersen, CALPHAD, 26(2), 2002, p. 189.

[82] C.W. Bale, A.D. Pelton, W.T. Thompson, F*A*C*T 2.1 _ User's Manual, Ecole Polytechnique de Montreal/Royal Military College, Canada, July 1996.

[83] U. R. Kattner, Minerals, Metals and Materials Society (JOM), 49(12), 1997, p.14.

[84] E. Gheribi, C. Robelin , S. Le Digabel , C. Audet , and A. D. Pelton, Journal of Chemical Thermodynamics. 43, 2011, p.1323.

[85] M. Ritoni, M. Martins, F. C. Nascimento and P. R. Mei, Defect and Diffusion Forum, 312-315, 2011, p 56.

[86] S. Aminorroaya, M. Reid and R. Dippenaar, Modeling and Simulation in Materials Science and Engineering, 19, 2011, p 1.

[87] E. Gheribi, C. Robelin, S. Le Digabel, C. Audet, and A. D. Pelton, Journal of Chemical Thermodynamics, 43, 2011, p 1323.

[88] M. Dehmas, J. Kovac, B. Appolaire, E. A. Gautier, B. Denand, and J. Da C. Teixeira, Solid State Phenomena, 172-174, 2011, p 396.

[89] J. Bursˇı´k, P. Bro, and J. Popovi, Intermetallics, 14, 2006, p 1257.

[90] R. P. Martukanitz, S. S. Babu, U.S. Government under contract DE-AC05-00OR22725, p 1.

[91] X. Lin, T.M. Yue, H.O. Yang, and W.D. Huang, Acta Materialia 54, 2006, p 1901.

[92] M. L. Griffith, M. T. Ensz, J. D. Puskar, C. V. Robino, J. A. Brooks, J. A. Philliber, J. E. Smugeresky, and W. H. Hofmeister, Proceedings of Solid Freeform Fabrication Symposium, University of Texas, Austin, TX, 1996, p. 125.

[93] S. M. Kelly, and S. Kampe, Metallurgical and Materials Transactions, 35A, 2004, p 1861.

[94] P. A. Kobryn, E.H. Moore, and S.L. Semiatin, Scripta Materialia, 43, 2000, p 299.

[95] R. Cottam, and M. Brandt, Physics Proceedings, 12, 2011, p 323.

[96] R. Banerjee, P.C. Collins, D. Bhattacharyya, S. Banerjee, and H.L. Fraser, Acta Materialia, 51, 2003, p 3277.

[97] P.C. Collins, R. Banerjee, S. Banerjee, and H.L. Fraser, Materials Science and Engineering A, 352, 2003, p 118.

[98] R. Banerjee, P.C. Collins, and H.L. Fraser, Metallurgical and Materials Transactions A, 33A, 2002, p 2129.

[99] K. I. Schwendner, R. Banerjee, and P. C. Collins, C. A. Brice, and H. L. Fraser, Scripta Materialia, 45, 2001, p 1123.

[100] J. D. Majumdara, I. Manna, A. Kumar, P. Bhargava, and A.K. Nath, Journal of Materials Processing Technology, 209,2009, p 2237.

[101] F.J. Kahlen, A. Von Klitzing, A. Kar, P. Christensen, P. Denney, I. Miyamoto, and K. Watkins, Proceedings of the ICALEO '99, Laser Institute of America, San Ddiego, California, LIA, 87, 1999, p129.

[102] J. Seretsky, E. R. Ryba, Welding Research Supplement, 1976, p 208.

[103] S. Chatterjee, T. A. Abhinandanan, K. Chattopadhyay, Journal of Materials Science, 41, 2006, p 643.

[104] Laser Direct Metal Deposition of Dissimilar and Functionally Graded Alloys, PhD Thesis by Kamran Shah, submitted in 2011.

[105] Dong, M. Zhong, W. Liu, M. Ma, H. Zhang, Issued for Individual use to only Mary Haug (38445), on Jan 5, 2012, Distribution Prohibited.

[106] L. Zheng, W. Xie, and Y. Li, Key Engineering Materials, 467-469 (2011), p 1372-1376.

[107] M. B. Prime, Ch. Hellwig, The Fifth International conference on Residual Stresses 1 (1997), 127.

[108] http://www.engineersedge.com/properties_of_metals.htm, Accessed on 15th March, 2013.

[109] H. I. Aaronson, G. K. Scarr, M. R. Plichta and J. P. Moore, AFSOR, 1979.

[110] T. Furhura, H. J. Lee, E. S. K. Menon, H. I. Aaronson, Metallurgical Transactions A 21 (1990), 1627.

[111] G. W.Franti, J. C. Williams, H. I. Aaronson, Metallurgical Transactions 9A (1978), 1641.

[112] V. J. Laraia, H. Heuer, Scripta Metallurgica et Materialia 25 (1991), 2803.

[113] A. Ilbagi, P. D. Khatibi, H. Henein, R. Lengsdorf, D. M. Herlach, J. of Physics 327 (2011), 1.

[114] W. Xu, D. Ma, Y. P. feng, Y. Li, Scripta Materialia 44 (2001), 631.

[115] Y. C. Liu, G. C. Yang, X. F. Guo, J. Huang, y. H. Zhou, J. of Crystal Growth 222 (2001), 645.

[116] J. H. Perepezko, W. J. Boettinger, Mater Res Soc Symp Proc 19 (1983), 223.

[117] J. C. Brachet, P. Olier, G. Brun, P. Wident, I. Tournie, C. Foucher, P. Dubuisson, J Phys. IV, 7 (1997), 561.

VITA

Syamala Rani Pulugurtha was born on December 1, 1980 in Kakinada, Andhra Pradesh State of India. She received her primary and secondary education in New Delhi, India. From 1999 to 2003, she worked towards her Bachelor of Engineering degree from Department of Metallurgical Engineering, Andhra University-Visakhapatnam, India. For a period of one year and three months she worked as Junior Research Fellow at the Advanced Research Center for Powder Metallurgy and New Materials (ARCI), Hyderabad, India.

In 2005, Syamala joined the University of Arkansas, Fayetteville, Arkansas for her M.S. in Mechanical Engineering under Dr. Deepak G Bhat. In graduate school, she held a Graduate Research Assistantship in the Surface Engineering and Materials Processing Lab. In December 2007, she received her M.S. in Mechanical Engineering from University of Arkansas. From May to November of 2007 she worked as a Process Engineer at IonBond Inc. at Bend, Oregon. After a brief period she came back to graduate school and started to work towards her Doctor of Philosophy degree in Materials Science and Engineering under Dr. Joseph Newkirk in January of 2008. She held a Graduate Research Assistantship until August of 2010 and Powder Metallurgy Fellowship until August of 2011. Since past two and half years she is holding a position as a Sr. R&D Engineer at Medtronic Inc. at Santa Rosa, CA. In August 2014, she received her PhD in Materials Science and Engineering from Missouri University of Science and Technology.